A Method for Modeling and Prediction of Ground Vehicle Dynamics and Stability in Autonomous Systems

Patrick Norman Currier

Dissertation submitted to the faculty of the
Virginia Polytechnic Institute and State University
in partial fulfillment of the requirements for the degree of

Doctor of Philosophy
in
Mechanical Engineering

Alfred L. Wicks, *Chair*
John B. Ferris
Dennis W. Hong
Samuel M. Kherat
Charles F. Reinholtz

May 6, 2011
Blacksburg, Virginia

A Method for Modeling and Prediction of Ground Vehicle Dynamics and Stability in Autonomous Systems

Patrick Norman Currier

ABSTRACT

A future limitation of autonomous ground vehicle technology is the inability of current algorithmic techniques to successfully predict the allowable dynamic operating ranges of unmanned ground vehicles. A further difficulty presented by real vehicles is that the payloads may and probably will change with unpredictably time as will the terrain on which it is expected to operate. To address this limitation, a methodology has been developed to generate real-time estimations of a vehicle's Instantaneous Maneuvering Manifold. This approach uses force-moment method techniques to create an adaptive, parameterized vehicle model. A technique is developed for estimation of vehicle load state using internal sensors combined with low-magnitude maneuvers. An unscented Kalman filter based estimator is then used to estimate tire forces for use in determining the ground/tire coefficient of friction. Probabilistic techniques are then combined with a combined-slip pneumatic trail based estimator to estimate the coefficient of friction in real-time. This data is then combined to map out the instantaneous maneuvering manifold while applying techniques to account for dynamic rollover and stability limitations. The algorithms are implemented in MATLAB, simulated against TruckSim models, and results are shown to demonstrate the validity of the techniques. The developed methodology is shown to be a novel approach that is capable of addressing the problem of successfully estimating the available maneuvering manifold for autonomous ground vehicles.

Acknowledgments

Does it really take a village to raise a doctor? Probably, so I will therefore apologize in advance to those of you who may deserve a mention here but will not receive one. If you are one of those people, thank you for whatever it was that you did and I omitted.

That said, I must start the specific acknowledgments with my family. First to my parents: thank you for being the level-headed, caring, hard-working people that you are. I may be terrible at expressing it but I know that you did all of the dirty work necessary for me to writing this today and I appreciate it every moment of every day. To my grandparents: you were the ones who really inspired my passion for education. This degree is for you and I hope that I can use it to inspire others the way you inspired me. And, of course, my sisters: you may have contributed more than you will every realize.

To Caterpillar, in particular Sam Kherat and Ramadev Hukkeri: it may have been a rougher road than any of us would have liked, but I really do appreciate all of the support you provided. I could not have done it without you and I hope we can collaborate again.

To the other grad students: Florin Marcu who was the brother I never had, Dan Knost who first planted the idea for this work in my head, the whole DARPA Challenge crew who initiated me into the strange and wonderful world of autonomy, Phillip Tweedy who helped me discover how to conquer the impossible, John Bird who raced me to the end (I won), and all of the others through the years. You all made grad school an experience that I will never forget and that changed me forever.

To my committee: Dennis Hong, John Ferris, Corina Sandu, and particularly Charles Reinholtz. Thank you for your time, your feedback, and your support.

And finally, to Dr. Wicks: I may rarely have listened to you and I'm pretty sure that we irritated the hell out of each other at times, but outside of my family I'm not sure there is anyone I respect more. Signal processing will never be my thing, but what I learned outside of a classroom from you will influence me far longer than anything I ever could have learned within. It is because of you this degree is worth more than a piece of paper.

** Unattributed photos and figures by author.*

Contents

List of Figures

List of Tables

Chapter 1

Introduction

They who can give up essential liberty to obtain a little temporary safety, deserve neither liberty nor safety.

–Benjamin Franklin, 1775 [1]

1.1 Motivation

Expansion of autonomous systems beyond the research stage into useful real-world applications requires that an Unmanned Ground Vehicle (UGV) be capable of operating safely at high-speeds in uncertain environments. These environments may include difficult features such as low-traction areas, undulating terrain, and deformable surfaces. Additionally, to be useful, real UGVs must be capable of carrying substantial payloads with magnitudes often approaching or exceeding that of the unladen mass of the vehicle; the masses and distributions of these payloads can also be uncertain and sometimes dynamic. An autonomous UGV must also incorporate knowledge of its own dynamics in order to efficiently follow trajectories in stable dynamic regions while avoiding those

in dynamically unstable regions. The results of insufficient consideration of knowledge in any of these areas are potentially catastrophic, resulting in damage to the surrounding environment or loss of the vehicle as illustrated in Figure 1.1 or by Urmson in the Defense Advanced Research Projects Agency (DARPA) Grand Challenge [2].

Figure 1.1: Virginia Tech's Rocky rolls over as a result of attempting a dynamically infeasible maneuver. This rollover occurred during evaluation testing for the DARPA Grand Challenge

Most current autonomous systems deal with difficult environmental or dynamic situations at the motion planning level by either navigating around problem areas or slowing the vehicle to a speed at which the limited knowledge can be applied safely. Autonomous systems must also compensate for the inherently imperfect information that represents the best knowledge obtainable of their environments [3]. Even if every effort is made to avoid difficult situations, the uncertain nature of environmental data means that it is possible for the UGV to unintentionally enter a dangerous environment. An example of this type of situation is an UGV encountering an undetected batch of black ice on a roadway, resulting in a rapid change in the dynamic handling characteristics and stability margins of the vehicle. Human drivers often encounter this situation but a properly trained driver

can detect the situation and apply a proper corrective action such as steering into the skid and not braking. An autonomous system based on a simple dynamic or kinematic model cannot determine the proper action in conditions such as these that exceed the assumptions used in formulating the model. In these types cases, the suddenly invalidated model can cause the autonomous controller to apply normally valid control actions that result in a worsening of the situation due to the invalidation of the models by the unexpected environmental changes. An example of this would be a controller applying braking to slow a vehicle while on black ice; this control action would be valid in on a normal road surface but could result in a loss of controllability in this case due to the low friction condition present in the environment.

Since safety cannot be compromised, if the autonomous system cannot successfully predict its safe dynamic operating region the allowable dynamic operating region must be restricted to ensure safety. Generally, this results in a significant reduction of the allowable operating speeds. For commercial applications such as mining, low-speed operation is unacceptable as a primary motivation for autonomy is to meet or exceed manned vehicle productivity. In military environments vehicle speed and terrain traversability can be essential to completion of the mission and survival of the UGV. It would be highly desirable for these types of applications to develop the capabilities of autonomous systems so that vehicle dynamics uncertainties are not the limiting operational factor.

Due to these concerns, efficient operation in high-performance regions on uncertain terrain is predicated on an understanding of the complex non-linear dynamics exhibited by ground vehicles under these conditions. Knowledge of these dynamics and the dynamic limits of the vehicle is critical for safe, efficient operation in uncertain environments with uncertain payloads. Despite this need, a comprehensive method for incorporating complex non-linear ground vehicle dynamics into autonomous path planning and control does not currently exist.

This research is an attempt to begin the process of addressing this gap in autonomous systems research. The problem will be outlined, relevant literature will be reviewed, and a solution methodology will be proposed. Results will be presented indicating the possibilities that this work could lead to a substantial increase in the capabilities of autonomous systems to model and predict vehicle states and dynamic stability limits.

1.2 Background

Autonomous vehicle technology is rapidly developing, but the fundamental difference between human controlled (manned or tele-operated) and automatically guided vehicles remains is the ability of humans to diagnose and adapt to changing or unexpected operating conditions versus the relative rigidity of autonomous controllers. For this reason, most high-speed UGV research to date has focused on operations in relatively benign environments, namely paved roads, open tracks, and relatively smooth open fields or has been restricted to low-speeds. Many large scale off-road autonomous navigation projects such as the DARPA PerceptOR program, XUV DEMO III program, and extraplanetary rover research are largely focused on the perception and planning aspects; difficult terrain surfaces are either avoided or traversed at low speeds [4] [5]. High-speed autonomous vehicles have been demonstrated, notably by Volkswagen and BMW, but these demonstrations have been, as of 2011, limited to well-known, highly accurately modeled vehicles under tightly controlled circumstances.

Probably the best known event involving high-speed operation on unknown terrain was the DARPA Grand Challenge (DGC) series. Both the 2004 and 2005 DGCs required vehicles to traverse an unknown cross-country course at high-speed. A review of the technical papers demonstrates that terrain information was used to plan paths around difficult surfaces and non-linearities encountered in the surfaces were handled by feedback

control. Advanced vehicle dynamics integration was largely neglected [6]. However, it should be noted that the courses for the DGC consisted primarily of well groomed, hard packed roads where the terrain surface was largely uniform and unchallenging [7]. However, situations did occur where vehicle dynamics became significant [2]. In testing, the Red Team rolled their vehicle, Sandstorm, while operating at high-speed. Due to an error in the planned path, the vehicle attempted to execute a hard turn beyond its dynamic capabilities. The team's recommended solution to this occurrence is implementation of a better model of the robot safety margins in order to provide control limiting [2].

One of the fundamental problems in autonomous systems research is the inherent uncertainty present in measurements of the environment [3]. Even when extensive high quality sensor data exists it is impossible to state with certainty that the environment is completely known. While this difficulty applies to all aspects of autonomy, the most significant aspect in relation to this research is the uncertainty with regards to terrain conditions, particularly its slope and COF.

It is important to note here the distinction between the terms uncertain and unknown. The term uncertain in indicates that knowledge about the measured state exists but that its accuracy cannot be precisely determined, although it may be possible to quantify statistical bounds on the accuracy. In contrast, the term unknown describes a region in which no usable data about the state exists; this may occur either due to physical unobservability or due to the inability of the sensing system to collect and process data on the specific state in question. An unknown state can be said to possess an infinite uncertainty.

While completely unknown terrain is by definition highly uncertain, it is also possible for a large degree of uncertainty to exist in terrain that is well mapped. The mapping process will inherently contain a degree of uncertainty, although this may be well quantified. Additionally, even if the *a priori* data is in fact precisely accurate it can be extremely dangerous to assume that this is the case without constant verification. Outside of the

laboratory, this verification will require additional sensor readings that induce additional uncertainty in the system. Rapid temporal changes in terrain uncertainty can also occur in many real-world situations, for example a sudden rain storm can change a well mapped unpaved road into a highly uncertain muddy environment due to rapid changes in COF. To enable high-speed operation, it is necessary to quantify and handle this uncertainty.

At this point it is also important to note that the terms high-speed and low-speed are relative terms and cannot be quantified numerically in the general case. For a Formula One race car, as an example, a longitudinal speed of 100 km/h is considered a very low speed whereas that same speed would be unfeasibly high (and extraordinarily dangerous) for a loaded mining haul truck. High-speed operation can qualitatively be connoted in operational terms as movement at speeds similar to that at which an efficient human operator would command in the current operating environment to rapidly complete the desired task. A more rigorous definition for purposes of this work would define low-speed as the maneuvering region in which quasi-static motion constraints can be considered valid. The corollary to this would define high-speed as the regime in which dynamic effects must be considered in order to accurately define motion constraints, often in a non-linear fashion. It is also important to note that the line between high and low-speed operation is not static, even for a single vehicle. Changes in payload, vehicle configuration, or environmental conditions can result in rapid shifts in the regimes. In extreme cases, these shifts may even effectively eliminate the low-speed region.

One of the difficulties to the expansion of vehicle dynamics into autonomy is the difficulty of accurately modeling the vehicle itself. Despite the fact that a considerable amount of literature and expertise including a number of commercial modeling packages are available, autonomy integrators often do not have easy access to the data required to develop an accurate model as the vehicles are often converted from existing platforms without access to the Original Equipment Manufacturer (OEM) design specifications. The process

to develop such a model can be highly labor intensive and involve extensive testing and specialized equipment that make it economically undesirable to conduct. Furthermore, a fixed parameter model only represents the vehicle in a single configuration and may not accurately represent the actual load state and operational conditions encountered.

In light of these difficulties, most current UGV applications rely on simple linear kinematic models [8] [9]. Kinematic models differ from true dynamic models in that they are time-invariant and do not take into account the time delays that occur between state transitions in real systems and the coupling that results. While vehicle handling can be represented as a linear system, this limits the effective operating range and accuracy of the model to the low-speed operating regime since real vehicles behave in a highly non-linear manner as the edge of the operating high-speed range is approached [10]. It should be noted that for many applications the vehicles do not operate outside of the low-speed range in which the linear kinematic models are applicable. If operation under these conditions can be guaranteed, then use of simplified models is easily justifiable as more complex dynamic models are unlikely to significantly improve prediction performance in the low-speed linear kinematic range. However, many realistic commercial applications will require expansion into the high-speed regime.

The motivation behind the integration of more advanced dynamic models into autonomous systems is to expand the effective safe operational envelope of UGVs. Even if the vehicle may never be intended to leave the low-speed region, uncertainties in the operating environments of most real applications mean that operation outside of the intended range may occur. As has been noted, it is also possible for UGVs to become dynamically unstable even in environments with low uncertainties when the limits of the vehicle platform are exceeded. If these limits are not well known, prudence demands that the limits be underestimated, reducing vehicle performance. It is therefore important to be able to predict the stable operating range of the vehicle in real-time so that the vehicle can be

operated efficiently and safely at speeds high enough to be useful in real applications.

1.3 Scope of Work

The primary goal of this research is to develop a generalized methodology for modeling, estimating, and predicting the dynamics and stability of four-wheeled Ackerman steered wheeled vehicles to enable autonomous operation in high-speed regimes on uncertain terrain with uncertain payloads. The methodology incorporates a parameterized non-linear vehicle model and a state estimator to calculate and update a performance envelope that defines the dynamic stability limits of the vehicle in real-time. The final desired output is an Instantaneous Maneuvering Manifold (IMM) that describes in terms of a 4-D space the possible ranges of longitudinal and lateral maneuverability that are within the dynamic limits of the vehicle given its current state. A key feature of this methodology is that it requires a minimal amount of integration effort, utilizes generally available sensors, and is capable of adapting to changes in payload and terrain conditions.

This work focuses on a general class of four-wheeled, pneumatic-tired, Ackerman-steered wheeled vehicles. Although this does not fully encompass the possible space of vehicle configurations, the class of vehicles represents the dominant configuration of vehicles used in real applications. The modeling techniques employed are restricted to those that predict overall vehicle response; calculation of internal stresses, analysis of ride characteristics, improvement of suspension response, and derivation of theoretical models are deemphasized. This approach is consistent with the goal of this research being to develop a method for guidance of existing vehicles, not to create tools to aid design of new vehicles.

As noted, the primary goal of this work is to develop a method for estimating maneuvering manifolds. A significant capability required to achieve this mission is the ability

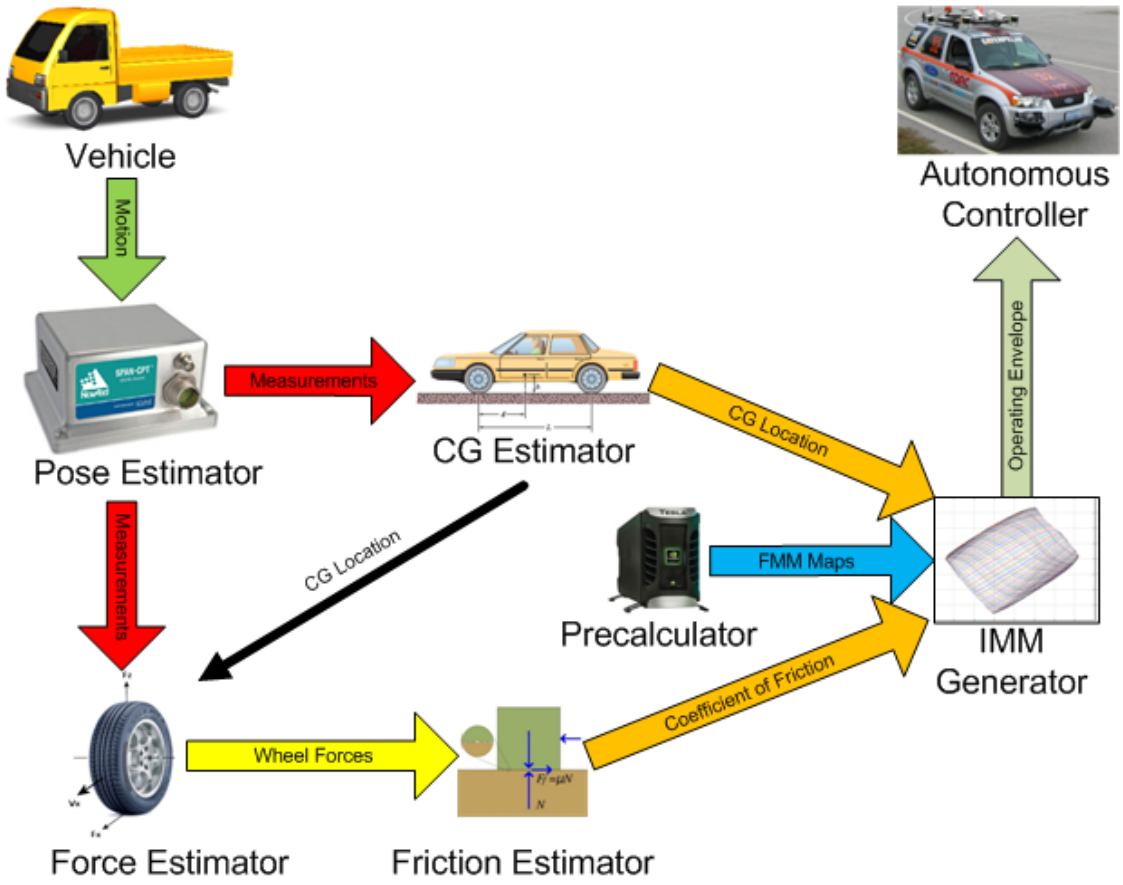

Figure 1.2: Overall structure of components. The goal of this work is to take vehicle data, estimate the CG location, estimate the friction coefficient, and use this information to generate an Instantaneous Maneuvering Manifold that defines the safe operating envelope for the vehicle to an autonomous controller.

to estimate states and parameters. Many of the states and parameters required have very specific conditions for observability and/or very low signal-to-noise ratios; this makes creation and validation of a robust state estimator extremely difficult. As the main goal of this work is to develop the IMM mapping techniques, state and parameter estimation will be performed, but creation of a fully robust and realistically deployable parameter estimation structure is considered beyond the scope of this work and will be left for future work.

Additionally, the scope is restricted to analysis of vehicle dynamics and the use of proprioceptive sensors. The problems of mission intelligence, motion planning, external

sensing, low-level control, and other aspects of autonomy are addressed only insofar as necessary to elucidate their connections to the vehicle dynamics systems. For the purposes of this work, it will be assumed that terrain information is available and the autonomous system is always capable of planning a safe and efficient path towards a goal. Given the state-of-the-art in autonomous systems at the time of this writing (2011), these may be somewhat generous assumptions but, as it would be considered impolitic for this author to solve all of the problems of autonomous systems, these assumptions are necessary to restrict the scope of the work.

1.4 Contributions

Due to the requirement that doctoral work enhance the state-of-the-art of knowledge in the field, it is necessary to enumerate clearly the expected contributions of this work:

1. Development of a combined-slip handling model abstraction technique using the Force-Moment Method to handle uncertain Center of Gravity locations, mass, and ground/tire coefficient of friction

2. Development of a technique for Center of Gravity (CG) estimation using low-magnitude excitation maneuvers and proprioceptive sensors.

3. Development of a Unscented Kalman Filter (UKF) based method for real-time estimation of horizontal and vertical tire forces proprioceptive sensors.

4. Development of a method for friction estimation in combined-slip conditions with application of probabilistic filtering techniques.

5. Development of a set of cohesive stability metrics and a method for application to predict safe dynamic vehicle operating regions.

6. Development of a method for real-time prediction of Instantaneous Maneuvering Manifolds for prediction of stable vehicle operating manifolds for autonomous ground vehicles.

The result of this work will be the development of an integrated approach for autonomous vehicle adaptive modeling and stability prediction with potential applications to non-linear control. These contributions are posited to be novel work that adds significantly to the state-of-the-art in the field of Unmanned Ground Vehicle navigation and control.

Chapter 2

Literature Review

If I have seen further it is only by standing on the shoulders of Giants.

–Sir Isaac Newton, 1676 [11]

Before a methodology can be developed to achieve the goals of this work, it is necessary to research and evaluate the previous work in the field. The relevant work can be divided into a number of categories: autonomous systems, vehicle modeling, state estimation, vehicle stability, and vehicle control. Examples from the literature in each of these areas will be summarized and their relevance to this work analyzed.

2.1 Autonomous Systems

Unmanned Ground Vehicles have a long history of operating off-road on uncertain terrain surfaces. The predominant approach to these problems has been algorithmic from the autonomous motion planning perspective. While this approach is certainly logical from the standpoint that avoiding difficult situations is preferable to handling them, it provides little margin for error. Most UGV applications to date have focused on the sensing and

motion planning aspects of the problem while neglecting any rigorous treatment of vehicle dynamics.

As a result, comparatively little literature exists outlining the vehicle dynamic aspects of the autonomous navigation problem. It is known that the National Robotics Engineering Center's CRUSHER program has attempted to use machine learning techniques to aid in terrain traversal but, as this is a military program, very little information is publicly available [4]. Some work in the area of high performance autonomous vehicle control has been done by the German auto manufacturers Volkswagen and BMW but, while both companies have demonstrated high-performance autonomous driving on learned courses, little scholarly information about the techniques employed appears to exist.

Off-road guidance is also an active research area, but this research focuses on the sensing and path planning aspects of the problem while the vehicles are operated at low speeds [5]. Even well known robotic events, such as the DGCs have taken place in an environment where the condition of the terrain and the dynamics of the vehicles were not major factors [7]. However, a large number of techniques exist for autonomous motion planning. Many of these are capable of taking kinematic and dynamic characteristics into account. Several techniques will be outlined, but the techniques presented are not intended to comprise an exhaustive listing.

The problem of planning and tracking trajectories for non-linear systems using reduced order models is addressed by Bottasso *et al.* [12]. They propose a method for maneuvering multi-body dynamics problems using a multi-layered structure with a reduced order model tuned through use of a neural network. The proposed structure includes a *strategic layer* responsible for defining high level goals, a *tactical layer* responsible for planning optimal trajectories to meet the goals defined by the strategic layer, and a *reflexive layer* that produces the control signals necessary to track the planned trajectory [12]. The reduced order reference model is augmented with a neural network that can be trained

to reduce errors between the reduced and full-order models. The problem can then be cast as a non-linear programming problem and solved using the reduced order model to find the optimal steering conditions [12].

Frazzoli *et al.*address the importance of considering a vehicle's dynamic constraints while planning motion [13]. The algorithm uses a rapidly expanding random tree search algorithm that converges kinematically while still accounting for the dynamic constraints. To accomplish this, the motion planning algorithm is decoupled from the low-level control. The motion planning algorithm can then operate primarily in a kinematic regime [13].

An example of this type of structure is the trajectory search algorithm implemented by Bacha *et al.*for autonomous motion planning in the DARPA Urban Challenge [14]. A cost map is created using obstacle data and a motion profile is specified. The search algorithm then performs a heuristic search through a family of pre-computed clothoid trajectories that were generated using a kinematic bicycle model of the vehicle and a basic map of rollover stability limits. The search process is iterative and proceeds in segments, simulating the motion of the vehicle along the path. The best path is chosen and transmitted to a low-level vehicle interface for execution [14].

2.2 Vehicle Modeling

Modeling of four wheeled, Ackerman steered vehicles of the type dominant in the world today has been studied extensively for the last 50 years. The dynamics and characteristics are well understood and well validated models have been developed for many applications. Additionally, standard terminology and coordinate systems have been developed. This paper will use the Society of Automotive Engineers (SAE) standard coordinate system.

2.2.1 Bicycle Model

A common formulation of basic vehicle handling compresses that lateral dynamics such that a four-wheel vehicle can be represented as a two-wheel vehicle; this formulation is known as the bicycle model. While this formulation removes the roll and pitch dynamics (which may be significant in some cases), it greatly simplifies the derivation of the equations of motion for the vehicle and produces easily implementable equations.

Equations for this model can be found in many sources, but both Milliken and Wong provide good derivations [10] [15]. The model used in both of these derivations (along with most other derivations of this model) use the small angle assumption to linearize the system and assume that the tires generate forces according to linear coefficient. The model is most often derived for the constant velocity case; in this formulation it is seen that vehicles rarely follow the path that would be predicted by a purely kinematic analysis. A vehicle that follows exactly the path predicted by a kinematic steering analysis is known as a neutral steer vehicle; if it steers a larger radius than that path it exhibits understeer or oversteer if it exhibits the converse [10]. As most real vehicles exhibit understeer behavior, an understeer coefficient is introduced to compensate for this effect. This approach can be shown to work well for operation in the linear dynamic range and is the dominant model used in autonomous vehicle development [16] [17].

Frezza *et al.*derive the equations for a fully kinematic bicycle model [8]. The difference between the dynamic and kinematic bicycle is outlined, namely that the kinematic model becomes increasingly inaccurate as the body slip angle increases. A metric for the applicability of the kinematic model is also proposed. The paper derives a control law for the decoupled kinematic state, which is greatly simplified by the assumption that heading is controlled only by the steering input and that longitudinal forces are negligible. The applicability of this control law is shown using simulations [8], but the paper fails to clearly state the derived caveat that this control law will not work outside of the kinematic range.

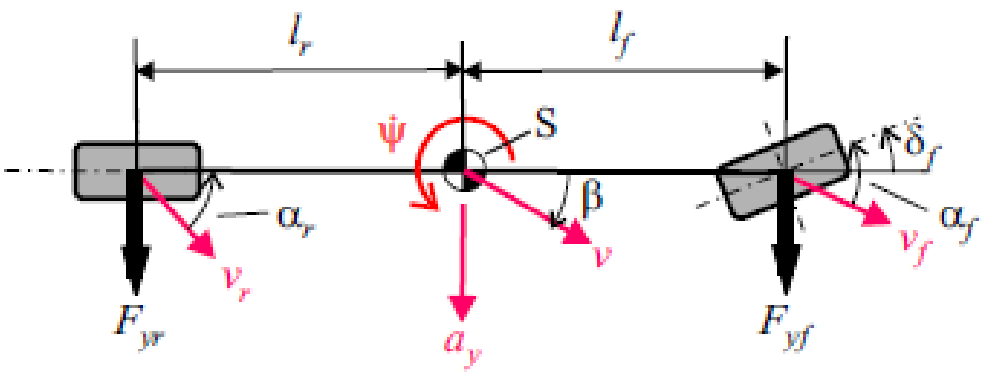

Figure 2.1: Illustration of bicycle model of vehicle handling characteristics as derived by Abdellatif and Heimann [18].

Abdellatif and Heimann present an approach for non-linear modeling of vehicle dynamics [18]. Their approach uses a modified bicycle model with a roll Degree of Freedom (DOF) and a non-linear tire model to simulate lateral driving maneuvers. The roll DOF is used to modify the effective lateral slip angles of the tires and thus modifies the lateral forces produced. To model the tire force characteristics, a simplified form of the Magic Formula tire model is used. Non-measurable parameters of the model are estimated using a non-linear technique based on Newton's method. The resultant model is shown to be more accurate than the basic, linear bicycle for estimating the lateral dynamics of the vehicle [18].

2.2.2 Full Car Model

A vehicle model that incorporates the dynamics of all four-wheels is commonly known as a full car model. Full car models can be derived for a variety of purposes. Jazar derives the equations for a full car vibrating model for use in vibrational analysis [19]. In this work, full car models such as those proposed by Will [20] and Wenzel [21] are more relevant. The advantage of the full car model over the bicycle model is that it can incorporate the roll and pitch dynamics present in real vehicles. Incorporation of these

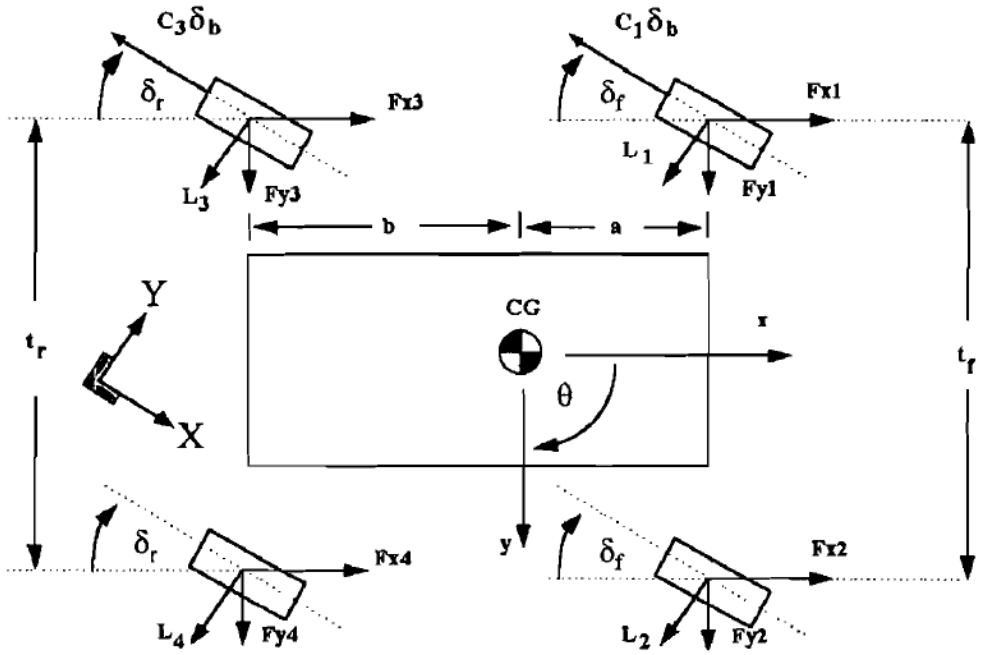

Figure 2.2: Full car vehicle handling model derived by Will and Zak [20]

dynamics allows the estimation of the normal force on each wheel [20] [21]; as will be explained in Section 2.2.4, this knowledge is critical to the accurate determination of tire forces.

Will and Zak derive a full car model for autonomous prediction and control, as shown in Figure 2.2 [20]. The model is fairly complete for the purposes of autonomous control as it includes degrees of freedom in roll, pitch, and steering in addition to lumped sprung and unsprung masses and tire forces. It does not include provisions for lateral CG offsets, wheel rotation degrees of freedom, or tire moments. The model is analyzed but is not validated against proven models or actual vehicles. Since the derivation is extensive, it is not reproduced here. The reader is advised to see the paper for the full derivation [20].

2.2.3 Multi-body Models

High accuracy multi-body vehicle dynamics models are often used for purposes of simulation. As most of these models are not appropriate for the type of implementations found in this work, the use of these models is largely restricted to validation purposes [22] [23] [20] [24]. Many commercial software packages are available to implement these types of models including the popular ADAMS and CarSIM/TruckSIM packages. Although the exact derivations of these proprietary models are not available, the commercial multi-body dynamics models are generally considered to be the most accurate vehicle models available.

2.2.4 Tire Models

Although seemingly fairly simple, the rubber pneumatic tire that is dominant among wheeled vehicles is actually extremely difficult to analyze and characterize accurately. The tire may be, however, the most important aspect of the vehicle to analyze. Ultimately, the only interaction the vehicle has with the ground is through the contact patches of the tires. All other aspects of handling can therefore be related to the effects that they have on the forces and moments generated by the tires.

It is first important to establish the terminology. In this work, tire forces, moments, and angles will be defined according to SAE standards, as shown in Figure 2.3. The terms important to the modeling in this work are defined as in [25]:

1. Slip angle (α) – Angle from the X_R axis to the velocity vector of the center of tire contact.

2. Longitudinal slip (s) – The ratio of the angular velocity of the wheel (ω) to the free rolling angular velocity (ω_0): $\frac{\omega-\omega_0}{\omega_0}$

3. Lateral tire force (F_y) – Y_R component of ground resultant force.

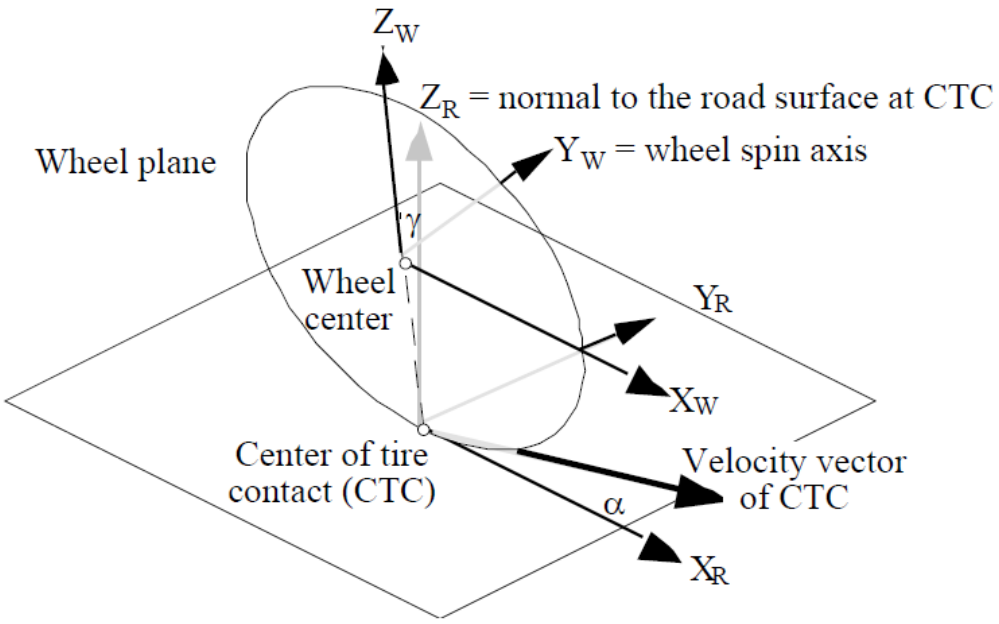

Figure 2.3: Diagram of SAE standard tire forces, moments, and angles [25].

4. Longitudinal tire force (F_x) – X_R component of ground resultant force.

5. Aligning moment (M_z) – Z_R component of ground resultant force.

Although detailed description of tire behavior is beyond the scope of this work, it is important to understand the fundamental property that a rubber tire generates forces only when deformed, as often occurs under slip conditions. This can be shown analytically using techniques such as the brush model [26]. Due to this property, tires are usually characterized in terms of the force or moment generated per unit of either longitudinal or lateral slip. A condition in which a tire is exerting only a lateral or longitudinal force is known as pure slip [10]. While pure slip is useful for analysis, in reality tires usually operate in a condition where both forces are produced, known as combined slip [10]. An important corollary to this is that a tire is only capable of providing a certain amount of total tractive force; this limit can be plotted on a diagram showing lateral versus longitudinal accelerations and is typically bounded by an ellipsoid known as the friction circle or friction ellipse [10].

The models discussed here will be formulated for the combined slip condition. Since the physical phenomena behind the generation of these forces are complex and highly non-linear, most practical tire models tend to be at least semi-empirical. Three commonly used semi-empirical tire models are the Magic Formula and TMeasy formulations.

Similarity Principle

It has been shown that tire characteristics show a large degree of similarity when properly non-dimensionalized [10] [26]. This principle can be extremely useful in the formation of efficient and accurate tire models as resultant tire forces can be shown to be functions of load, COF, and slip. The non-dimensionalization can be derived as shown by Milliken [10]:

$$\bar{F_x} = \frac{F_x}{\mu_y F_z} \tag{2.1}$$

$$\bar{F_y} = \frac{F_y}{\mu_y F_z} \tag{2.2}$$

$$\bar{M_z} = \frac{M_z}{T_z \mu_y F_z} \tag{2.3}$$

The resulting non-dimensionalized curve tends to resemble the curve shown in Figure 2.4. The curve contains three regions: a linear adhesion range, a non-linear transitional range, and a non-linear sliding range. Many simple models that approximate tire force generation by a linear coefficient neglect the two upper regions of the curve. These models work well when the tire is operating in the adhesion range, but it can be noted from the similarity equations that changes in normal load or COF can easily cause the tire to enter the non-linear part of the curve [10].

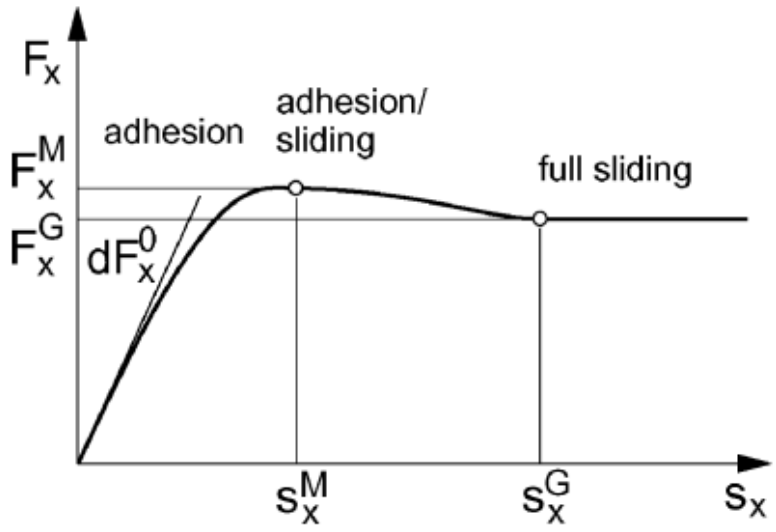

Figure 2.4: Typical tire force generation characteristic. Note the adhesion (linear), transitional, and sliding regions [27]

Brush Model

The brush model is a widely used analytical derivation of tire behavior. In the brush model, the tire is modeled as a set of bristles which are given characteristic stiffnesses to represent tire behavior [26]. The forces are generated at the contact patch between the tire and the ground and a pressure distribution is mapped to a rational function. One common function used is a parabolic distribution as proposed by Fiala [26]. A full derivation of the brush model is beyond the scope of this work, but it has been found to reasonably approximate the forces generated by real tires and is one of the primary analytical tire behavior models [26].

Magic Formula

The Magic Formula is a semi-empirical tire model that was introduced by Pacejka [26]. Called the Magic Formula because there is no true analytical methodology behind the form of the equations, the Magic Formula attempts to describe tire behavior via a formula

that captures the shape of empirical data. By taking the similarity principle into account, this formula is able to describe the shapes of the lateral, longitudinal, and aligning moment curves. Although many highly parameterized version exist, the general form of the Magic Formula is given by Pacejka as [26]:

$$y = Dsin\left[C\ arctan\left\{Bx - E\left(Bx - arctanBx\right)\right\}\right] \tag{2.4}$$

$$Y(X) = y(x) + S_V \tag{2.5}$$

$$x = X + S_H \tag{2.6}$$

where Y is the output variable (F_x, F_y, M_z), X is input variable $(tan(\alpha), S)$, B is the stiffness factor, C is the shape factor, D is the peak value, E is the curvature factor, S_H is the horizontal shift, and S_V is the vertical shift. For a full derivation and modifications for more advanced forms of the model, see [26].

TMeasy

TMeasy is another popular semi-empirical tire model that was developed by Hirschberg *et al.* [27]. As one may surmise from the name, TMeasy is intended to be simple to use while still maintaining a reasonable degree of accuracy. Similar to the Magic Formula, TMeasy is derived largely from empirical data and benefits from the similarity principle; in contrast to the Magic Formula, TMeasy uses rational polynomial functions to describe the force relationships. The TMeasy model also differs from most other approaches in that it calculates the total horizontal force first and then uses a set of equations to resolve it into components based on the slip angles [21] [27]. The equations for this decomposition can be found in [27].

2.3 State Estimation

State estimation can be considered to be one of the fundamental problems of control theory. The need for estimation grows out of the simple fact that it is usually infeasible to directly measure all of the states of interest in a system. Additionally, real systems must deal with noisy data that may give instantaneous readings for states that vary from the true value of the state. Estimation of states requires the states to be observable. A state is said to be observable if it can be uniquely determined from a set of constraints and to be unobservable if it cannot be uniquely determined from a given set of constraints [28].

Observability of a system is a property of the system model and can be determined by calculating the observability Grammian [28]. For an arbitrary continuous time system, the Grammian can be defined as:

$$O(H,F,t_0,t_f) = \int_{t_0}^{t_f} \Phi(t)^T H(t)^T H(t) \Phi(t) dt \tag{2.7}$$

for a linear dynamic system with fundamental solution matrix $\Phi(t)$ and measurement sensitivity matrix $H(t)$ [28]. For the system to be fully observable, the Grammian must be of full rank. For real systems, care must also be taken to ensure that the Grammian is not nearly singular such that small numerical errors result in the system losing observability [28].

Many techniques exist for estimation of states and handling stochastic measurements. Common methods include least squares, Kalman filtering, and neural networks. All of these methods can and have been used for the problem of estimation of vehicle states.

2.3.1 Least Squares

Discovery of the method of least squares is most often attributed to Gauss, and it was one of the first techniques to offer the potential for an optimal solution to the problem of

estimation. The method requires computation of the Grammian matrix and the basic form can be expressed as:

$$\hat{x} = (H^T H)^{-1} H^T z \tag{2.8}$$

for the linear system $Hx = z$ where $\hat{x}$ is the optimal estimate of the states [28]. The basic method can be expanded for more complex systems [28].

Vahidi *et al.*implement a recursive least squares with a multiple forgetting algorithm to obtain online estimates of mass and road grade [29]. The parameters are estimated from a model of the longitudinal dynamics of the vehicle using engine torque maps, engine rpm, and brake line pressures as the inputs. The estimation process is based on a recursive least squares algorithm; this algorithm that attempts to minimize the a loss function. In order to handle time varying parameters, such as road grade, it is necessary to rework the algorithm such that older data is weighted less heavily and is thus 'forgotten.' Due to the measurement parameters having different characteristics of noise and parameter variation, the scheme used by Vahidi implements 'multiple forgetting' in which each measurement parameter has an independent forgetting weight. Simulation testing is able to show that the multiple forgetting algorithm is clearly superior to a single forgetting implementation for all types of estimation. The estimator was then tested on a real vehicle. Convergence of results to within 5% of expected values was seen, but the estimator has difficulty maintaining stable state values especially in the presence of transients such as gear shifts. Additionally, the least squares algorithm is not inherently capable of evaluating the quality of the excitation data. Without extra logic the estimator values can wind up or become unstable in the presence of non-continuous excitation. Overall, the recursive least squares algorithm is shown to work but to lack robustness [29].

Wesemeier and Isermann use a least-squares technique and a bicycle model to estimate the longitudinal location of the CG, the mass of the vehicle, and the linear tire cornering stiffnesses [30]. The estimation is performed for various combinations of sensors and

parameters. Results were shown to be accurate to within 5% [30].

2.3.2 Kalman Filter

The Kalman Filter (KF) was initially developed by Rudolf Kalman around 1960 as a method for state estimation of linear stochastic systems [3]. The KF is a stochastic tool that represents the belief of the value of a state as a mean and a covariance. Filter operation is a two step process, the filter predicts the each of the states and then uses the measurement data to update the values. In addition to updating the states, the covariance matrix is updated to reflect the increase in knowledge. The basic KF algorithm can be presented as [3]:

$$\hat{\mu}_t = A_t \mu_{t-1} + B_t u_t \tag{2.9}$$

$$\hat{\Sigma}_t = A_t \Sigma_{t-1} A_t^T + R_t \tag{2.10}$$

$$K_t = \hat{\Sigma}_t C_t^T (C_t \hat{\Sigma}_t C_t^T + Q_t)^{-1} \tag{2.11}$$

$$\mu_t = \hat{\mu}_t + K_t (z_t - C_t \hat{\mu}_t) \tag{2.12}$$

$$\Sigma_t = (I - K_t C_t) \hat{\Sigma}_t \tag{2.13}$$

for the linear system $A_t x_{t-1} + B_t u_t + \varepsilon_t$ where x_t is the state vector, u_t is the control vector, and ε_t is a zero mean random variable that represents the process noise in the system with covariance R_t [3]. The measurement signal is represented as $z_t = C_t x_t + \delta_t$ where δ_t describes the measurement noise. The state mean estimates are represented by μ_t and the estimate uncertainty covariance is represented by the zero mean random variable Σ_t with covariance Q_t. The matrix K_t is known as the Kalman gain matrix and specifies the degree to which the measurement is incorporated into the new state estimate. A full derivation of the KF equations can be found in [3].

Anderson and Bevly demonstrate the use of a model based KF derived from a lin-

earized bicycle model to estimate yaw rate, side slip, heading and gyro bias [31]. The model proved sensitive to the accuracy of the parameterization, so residual analysis was performed to fine tune the parameters and achieve improved performance. After the parameters were tuned, the model based KF was able to accurately track the estimated parameters on both flat cornering maneuvers and a banked test track [31].

Ryu *et al.*describe a method for using a combination of Global Positioning System (GPS) and an Inertial Measurement Unit (IMU) to estimate heading angle, yaw rate, and side slip [32]. Specifically, a two antenna GPS with laterally offset antennas is used to provide an absolute heading reference. The data from these sensors is fused using a series of KFs based on a bicycle model and good results are shown for planar operating environments. In order to estimate the parameters in non-planar environments, a roll center model is developed. The parameters for this model are estimated using a least-squares technique and the combined road grade and vehicle roll are successfully measured [32]. This work is expanded in a follow-up paper to separately estimate the body roll angle and the road bank angle [33]. A disturbance observer is implemented on the roll center model and uses the multi-axis IMU measurements to successfully separate the road disturbance input from the total roll measurement. The observer is validated by comparing real vehicle test results to measured terrain data; the method is used successfully even on mostly flat terrain [33].

Extended Kalman Filter

The Extended Kalman Filter (EKF) is an extension to the original KF to allow for its use on non-linear systems. The EKF uses a Taylor series approximation to linearize the state equations about the operating point [3]. This linearization is made implicit within the filter by calculation of the Jacobian and Hessian matrices that represent the derivatives of the state and measurement transition matrices. A full derivation of the equations is not

provided here, but can be found in [3]. The EKF is a very popular tool for estimation tasks, but it does have some important limitations. The accuracy of the Taylor series approximation is heavily dependent on the local linearity of the system. Additionally, calculation of closed form solutions for the Jacobian and Hessian can be difficult for complex systems [3].

In an early application of vehicle state estimation, Ray uses an EKF to estimates states for use in Anti-lock Brake System (ABS) controller development [34]. The model is a 5-DOF bicycle model with a pitch DOF. Unlike much other work in this area, the EKF in this work is tested under application of high braking forces. Simulation testing shows that the estimator is capable of estimating tire forces and slip angles accurately given perfect parameters. The results hold even at extremely high longitudinal slips seen in high brake situations. The estimator is then used to implement a Proportional-Integral (PI) controller and it is shown that, in simulation, the state estimates are sufficient for control [34].

Best, *et al.*compare the performances of an EKF and a linear KF in estimating states of a 4-DOF handling model [35]. These observers were compared against a higher fidelity 6-DOF model with Pacejka tire model using a sensor suite that consists of three orthogonal accelerometers. The results show that the EKF implementation is clearly superior for state estimation, although both implementations can still be considered suboptimal [35].

Hodgson and Best develop an EKF based method for state and parameter estimation of a simple vehicle model [36]. The model is based on the single track bicycle model but also includes a simple form of the nonlinear Pacejka tire model. The filter is tested in both static and adaptive forms. In the adaptive form, up to two of the four Pacejka parameters are varied to allow the model to conform to inaccuracies in the tire model. The method is demonstrated successfully in both simulation and real vehicle tests with the adaptive model showing improved performance [36].

Samadi *et al.*outline a method for using a 7-DOF vehicle model to estimate the veloc-

ities, yaw rate, and tire forces from accelerometer and wheel speed sensor measurements [37]. The model equations are formatted into an EKF with a Gauss-Markov stochastic component to account for measurement noise. The EKF is then implemented using a square root algorithm that is more numerically stable than standard algorithms [37] [38]. The method is capable of closely tracking simulation models and is fairly insensitive to measurement noise [37].

Venhovens and Naab illustrate the use of KFs for three separate automotive applications: adaptive cruise control, lane keeping assist, and state estimation [39]. In the context of this work, the latter is the most relevant. In contrast to many other implementations, the state estimation formulation uses a 4-wheel model to estimate lateral acceleration and side slip using only wheel speed sensors. Although this method is greatly affected by wheel slip, good results are obtained by careful formulation of the measurement and state equations. By assuming that the side slip angle changes slowly relative to the measurement update rate, performance is further enhanced by using the side slip angle from the previous iteration to apply a correction to the sensor measurements. The method is also able to show good results in varying environmental conditions, such as low-friction surfaces [39].

Wenzel *et al.*use a higher fidelity 4-wheel vehicle model to implement an EKF based state estimator as a virtual sensor [24]. The higher fidelity model allows for the estimation of a large number of states including: roll, pitch, yaw, vertical tire forces, lateral slip angles, longitudinal slip angles, and velocities. Additionally, this model takes into account that the mass and location of the CG can change as a result of the addition of cargo or passengers. The implementation makes use of only stock vehicle sensors: accelerometers, wheel speed sensor, and steering sensors as inputs to the model. Although use of tire models is discussed this implementation does not attempt to estimate tire parameters, instead relying on knowledge of tire models from manufacturer testing. The results show good correlation to both multi-body model simulations and real vehicle test data, but

the behavior of virtual sensors in feedback control systems is left as future work [24]. Complete details of Wenzel's work can be found in [21].

Dual Extended Kalman Filter

The Dual Extended Kalman Filter (DEKF) is an expansion of the EKF proposed by Wan and Nelson for use in simultaneous parameter and state estimation [40]. The DEKF separates the prediction and correction phases for the parameter phases of the parameter and state parts of the filter. A bootstrapping technique is used where the parameter estimates are predicted, these estimates are used to update the state predictions, and then the measurement updates are performed by both segments as shown in Figure 2.5 [22]. The principal of the dualization of the DEKF could also be applied to other variants of the filter, such as the UKF, although no example of this implementation has been found in the literature.

Wenzel *et al.*propose the use of a DEKF for combined state and parameter estimation [22]. The model and equations are similar to those found in [24], but a DEKF is implemented for increased performance. The parameters are implemented in the first prediction stage and the estimated states in the second prediction stage. Separating the parameters from the states allows for the deactivation of the parameter estimator if static parameters are desired or insufficient excitation exists. Computationally, separate EKFs can also be more efficient due the square properties of the matrices. Additionally, by updating the parameters first, more accurate parameter estimates are used in the state estimator, leading to lower covariances [22].

Unscented Kalman Filter

The UKF is another type of extension to a KF for use with non-linear systems. The UKF differs from the EKF in that a technique known as the unscented transform is used to

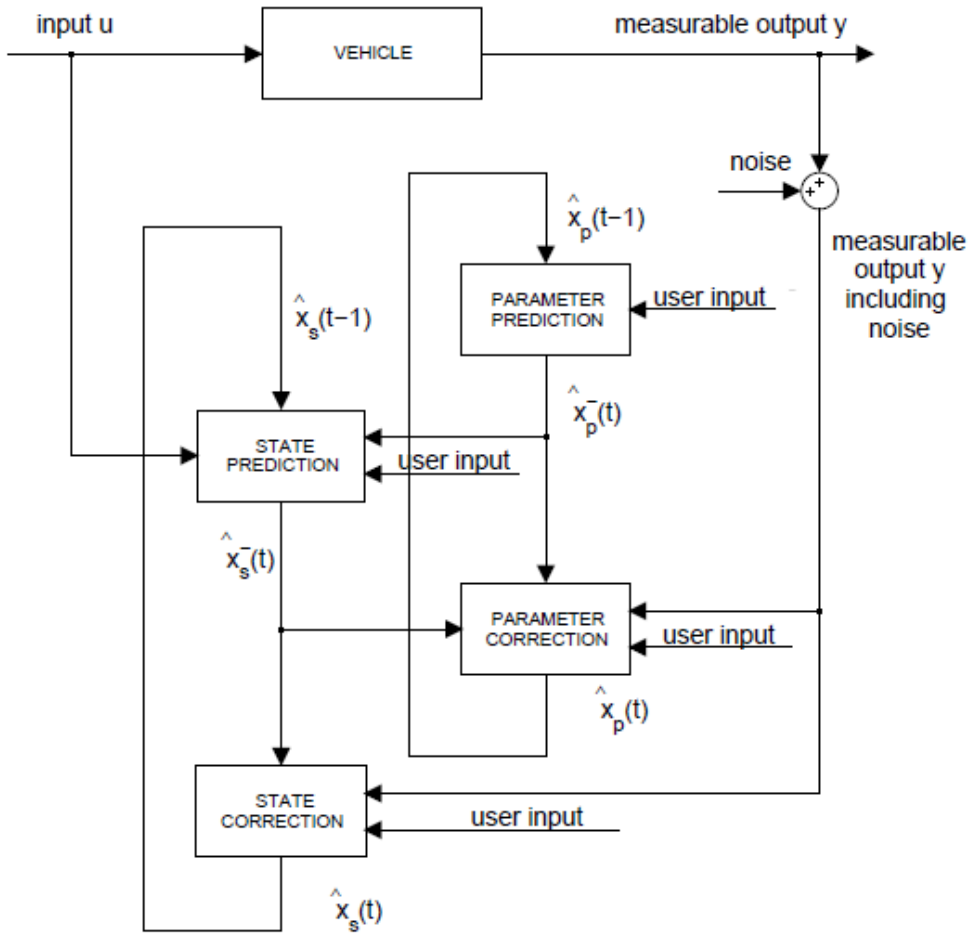

Figure 2.5: DEKF state flow diagram [21].

linearize the system. The unscented transform uses sigma points chosen along the primary axis of the covariance matrix to approximate the non-linear function. This method can often provide a better estimate of the function than the Taylor approximation for highly uncertain functions because it takes the stochastic distribution into account. The UKF also does not require the computation of Jacobian or Hessian matrices, which may be difficult in complex systems. Overall, the UKF tends to be slightly less computationally efficient than the EKF, but is often able to achieve greater accuracy, especially for highly non-linear or highly uncertain systems [3].

Brunke and Campbell apply a UKF to the problem of state estimation on an Unmanned Aerial Vehicle (UAV) [41]. The UKF is recommended for use in state estimators due to its lower susceptibility to initial states and tuning and the elimination of the requirements to calculate Jacobian and Hessian matrices. It is also shown that the UKF is capable of estimating state and model parameters of an aircraft and that it can be used to adapt the flight controller for damage [41].

2.3.3 Neural Networks

Yim and Oh model the lateral dynamics of a vehicle using a real-time recurrent neural network [42]. The neural network consists of six external input neurons, four external output neurons, and four hidden layer neurons. The network learns through the use of real-time recurrent learning algorithm of a type that has been shown to be generally applicable to dynamic systems. The network was then trained using a hybrid approach that combines initial open-loop training followed by closed-loop training. In the open-loop stage, the network is used only for short term prediction with the goal of stabilizing the weights. The closed-loop stage introduces feedback of the network output so that the network can be used for long-term prediction, further refining the weights. The network was trained using data from a Daewoo Leganza that was driven at a variety of steering angles over a course using a magnetic wire for position measurement. After training, different data sets were input into the network to evaluate its capability over non-trained data [42]. Although the authors describe the results as good, the correlation between the predicted and actual states on some of the data sets is notably less accurate than those obtained from many of the other methods described here. The paper also illustrates a difficulty in the use of neural networks: their lack of an algebraic representation inhibits control design. An evolutionary, partially fuzzy lateral control scheme is suggested as a solution [42].

2.3.4 Other Techniques

Kiencke and Daiss use a non-linear bicycle model to estimate lateral dynamics [43]. The model is used to design an observer via pole placement techniques that can estimate the lateral acceleration, yaw rate, and front and rear slip angles. Testing using a real vehicle shows that both non-linear and linear forms of the observer can provide reasonable estimates of the lateral acceleration and yaw rate when the vehicle is operated at lateral accelerations below 0.4g on dry pavement. However, since the bicycle model does not include roll dynamics, the estimates must be corrected using a roll measurement. It is also shown that the non-linear observer provides significantly better estimates of the slip angles than the linear observer and that the results from the non-linear observer closely match results from a high-order model [43].

Bae *et al.*demonstrated the feasibility of using data from either a single or dual-antenna GPS receiver to estimate road grade, mass, and parasitic drag forces on heavy trucks [44]. The GPS provides a pitch estimate from either carrier phase analysis with the dual antennas or a ratio of vertical to horizontal velocity from the single antenna. This data is combined with a map of steady-state engine torque and a drive train model that includes the torque multipliers generated by the torque converter, transmission, and final drive to form the inputs for a recursive linear estimator. The input data is low-pass filtered, and the estimator is disabled in poor GPS but no attempt is made to incorporate error estimates into the estimator. The results show that this method is capable of rapidly converging the mass estimate to a tolerance as tight as $\pm 2\%$ of the measured value. The testing was conducted with road grades of less than 3 degrees, but even with small grades, incorporation of the road grade into the estimator is shown to make a significant difference in the results. The method is also capable of estimating non-observable parasitic drag forces such as rolling resistance and aerodynamic drag [44].

Stephant *et al.*compare four different techniques for estimation of vehicle side slip and

lateral forces: a linear Luenberger observer, an extended Luenberger observer, and EKF, and a sliding-mode observer [45]. The estimators are compared for three different sensor sets: yaw rate only, speed only, and yaw rate plus speed. The non-linear observers are shown to be superior to the linear observers and, for most sensor configurations, the non-linear observers are shown to be roughly equivalent in performance at low accelerations. At higher accelerations, the linearizations in the models cause all of the techniques to diverge rapidly [45].

Solmaz *et al.*use an unusual technique to estimate vehicle parameters [46]. The technique involves creating an array of static models that span a multi-variable parameter space. The parameter space is chosen such that it includes all expected values for the actual vehicle parameters. The parameters are then estimated by a model switching technique that iterates through the models until the performance of the chosen model most closely matches the measured values. While the paper was able to show some reasonable results, the technique requires a dramatic trade-off between resolution and computational power [46]. The computational requirements at even low levels make this technique infeasible for implementation in most systems.

Ouladsine *et al.*implemented a sliding mode observer to estimate vehicle parameters [47]. The observer is used to estimate tire longitudinal forces, vehicle side slip angle, and vehicle velocity. The use of sliding modes is intended to allow for accurate determination due to the insensitivity of sliding modes to unknown inputs and rapid convergence characteristics. The results show the expected good convergence and ability to determine states even in the presence of high levels of noise [47].

2.3.5 Friction Estimation

Hahn *et al.*propose a method for identifying the road-tire COF from the lateral dynamics of the vehicle [48]. The method uses measurements from a differential GPS unit and a

yaw rate gyroscope to perform a regression based on an adaptive control law. One of the major drawbacks to measuring friction coefficients is discussed: the magnitude of the excitations needed for estimations increases as the COF increases. The validity of the method is demonstrated in both simulation and testing on a Navistar truck cab. In both cases, the estimator is able to converge to the value of the COF with a time constant of approximately one second [48].

Wang *et al.*demonstrate the feasibility of measuring the road-tire coefficient by measuring longitudinal slip [49]. The method uses a measurement of the slip-slope product of the Magic Formula tire model obtained by analyzing GPS, accelerometer, and wheel encoder data. A recursive least-squares algorithm is used to estimate the slip-slope. To ensure both fast convergence and steady state stability, a change detector is used to switch the least-squares gains when a transient event is detected. The algorithm was implemented on a snowplow and demonstrated the ability to measure the COF during both acceleration and braking. One drawback to this method, however, is that the excitation levels in the acceleration and wheel encoder data are not high enough in constant velocity situations to produce an estimate; an acceleration or braking condition is required for proper excitation [49].

Hsu proposes a method for estimating ground-tire friction using model-based methods [50]. These methods rely on estimating the required steering aligning moment using steering torque as a measure of COF. The major factor in determining the aligning moment is the pneumatic trail that results from the geometrical offset between the tire contact patch and the steering linkages. The interesting part about this method is the strong relationship exhibited between pneumatic trail and maximum tire force. This relationship allows the method to be used to accurately predict the limits of adhesion at an excitation level much lower than required for many other methods. Hsu's results show that the friction limit can often be found even when the vehicle is operating at tire forces around 50%

of the peak force [50].

For further information on tire and friction modeling, the reader is referred to the excellent survey paper by Li *et al.* [51].

2.4 Vehicle Stability

Due to the non-holonomic constraints present in an Ackerman steered vehicle and the limits imposed by tire tractive capabilities, it is possible for a vehicle to enter an unstable portion of the operating space or even to leave the operating space entirely. To prevent these occurrences, many methods have been proposed for both metrics and control schemes.

2.4.1 Rollover Stability

Rollover can be defined as an overturning of a vehicle about its longitudinal axis. Rollover tends to be a highly dynamic event and a variety of models and metrics have been proposed to predict its occurrence.

Putney applied a simplified rigid body model to the problem of rollover prevention in an autonomous vehicle [52]. The model consists of a rigid block on a banked surface. Rollover was predicted when the moments due to the centripetal acceleration exceeds the moment due to the vehicles weight about the outside tire. A safe maneuvering range for the current vehicle state is calculated and actuation commands are limited to prevent violation of these limits [52].

Odenthal *et al.*use steering and braking control to prevent rollover of human controlled road vehicles [53]. The vehicle is modeled using a bicycle model extended with roll dynamics. A rollover metric is derived by calculating the relative lateral load transfer between the left and right wheels. This metric is used to predict the proximity of the

vehicle to rollover and a controller is developed that uses active steering and braking control to reduce the value of the metric [53].

Whitehead *et al.*implemented a an electronic stability controller to detect and intervene to prevent rollover [54]. The controller was implemented on a scaled testbed equipped with an IMU and GPS. The testbed was then run through a series of fishhook maneuvers with differing CG locations to reveal the effectiveness of the controller [54].

Lambert analyzes the effects of vehicle parameters on the rollover propensities of passenger vehicles [55]. Rollover propensity is judged using a measure known as the static stability factor that is largely dependent on the ratio of the track width to the CG height. The effects of CG height, track width, understeer gradient, suspension stiffness, and friction coefficients are analyzed using CarSim models of vehicles. CG height, understeer gradient, and friction coefficients were found to have the strongest relationships with rollover propensity [55].

A rollover metric known as the Force-Angle Stability Metric (FASM) is presented by Papadopoulos *et al.* [56] and Peters *et al.* [57]. Papadopoulos proposes the FASM based on the principle that the angle of the vector representing the resultant force on the CG must not exceed the angle between the CG and the nearest ground support. It is shown that the metric can be used to successfully predict and prevent rollover of mobile manipulators [56]. Peters extends the FASM for use with four-wheeled vehicles by calculating the moments about the axes connecting the tire contact points of each of the wheels. Additionally, the moments and support polygon are modified to account for the mass of the wheels and movements of the suspension. Simulation and empirical testing using a dynamic fishhook maneuver shows that the metric can provide an accurate measure of rollover and parameter sensitivity studies indicate that knowledge of both the unsprung mass and CG location are significant factors in the calculation [57].

Chen and Peng propose a method known as Time to Rollover (TTR) for rollover pre-

diction [58]. The TTR approach calculates the time until wheel liftoff by simulating a very fast model forward in time. As future control states are not known for human driven vehicles, the assumption is made that the control inputs will remain constant. In order to be able to rapidly simulate the rollover conditions, a simple model that trades accuracy for speed is used. To compensate for the low-order model, a neural network is implemented to compensate. The neural network compensated TTR improved performance, but as is often the case with neural networks, the gains were maximized in the vicinity of the training data set [58]. This work is expanded by Yu *et al.*who use the TTR paradigm to develop an active roll-stabilizing controller [59].

Dahlberg addresses the issue of rollover from an energy perspective [60]. The dynamic rollover threshold is contrasted with the steady state rollover threshold. It is analytically demonstrated using an energy metric that a rollover event can occur at a lower lateral acceleration in a dynamic event than in a steady-state situation. Rollover in both dynamic and static situations can be predicted by plotting a Roll Energy Diagram with static energy mapped to potential energy and dynamic to kinetic energy. Testing with an articulated semi-trailer with a variable CG validated the results and also indicated that rollover for articulated vehicles is dependent on longitudinal velocity as well as lateral dynamics [60].

2.4.2 Directional Stability & Controllability

Directional stability can be defined as the ability of the vehicle to maintain its yaw heading and avoid 'spinning out.' Additionally, it is important for the vehicle to maintain directional controllability: the ability to continue to follow a desired path without entering an uncontrolled slide. For front steered vehicles, directional stability is typically dictated by the tire forces at the rear wheels, while directional controllability is dictated by the forces at the front wheels [61].

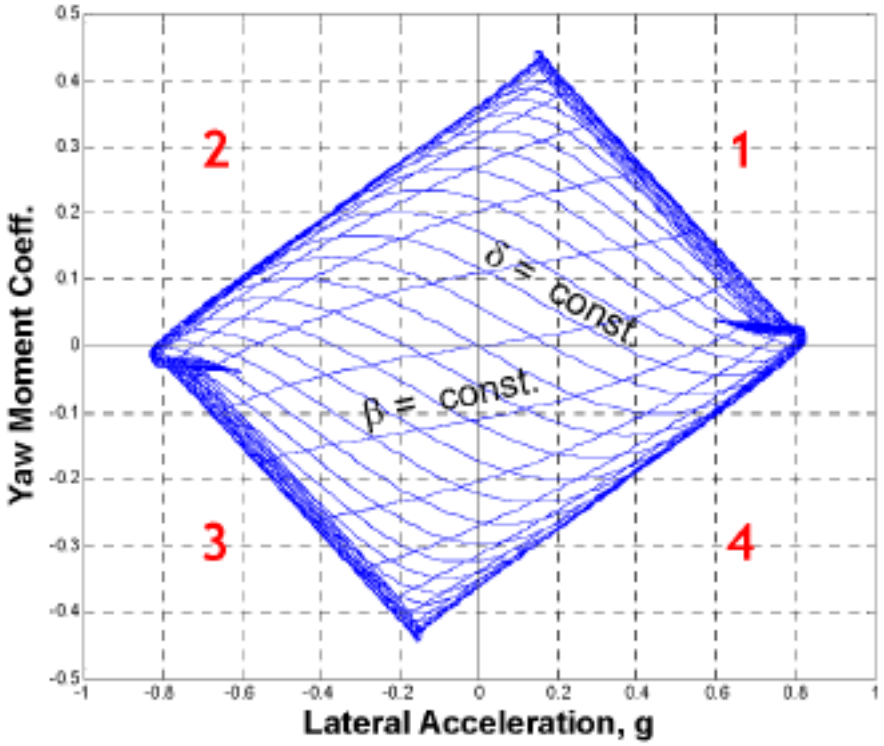

Figure 2.6: Typical Milliken Moment Method diagram showing steering angle and side slip versus yawing moment and lateral acceleration [61].

Milliken and Milliken deal with the concept of static stability by introducing the Stability Index (SI) [10]. The SI is a measure of the total steady-state directional stability at a given lateral acceleration and is defined as the derivative of the yaw moment with respect to path curvature [10]. The SI can be used as a static metric to determine directional stability.

Milliken also presents a method for analysis of static cornering stability known as the Milliken Moment Method (MMM) [10]. A MMM diagram, as shown in Figure 2.6, plots the lateral acceleration versus a non-dimensionalized yaw moment coefficient. The diagram is crossed by lines of constant steering angle (δ) and lines of constant side slip angle (β). Due to non-linearities in real vehicle handling dynamics, these lines converge to limits at the edge of the diagram.

Hoffman *et al.*demonstrate that quadrants 1 and 3 in Figure 2.6 can be used to predict front tire saturation and directional controllability while quadrants 2 and 4 can be used to predict rear tire saturation and directional stability [61]. Stability and controllability can be expressed by calculating the distance from the current operating point to the nearest boundary on the MMM diagram. The MMM diagram method is compared to a phase plane analysis of side slip and yaw rate. The results indicate that the MMM method yields similar results to phase plane analysis while being easier to analyze than phase plane methods [61].

Much of the research in the area of directional control and stability has focused on the implementation of driver assist control systems. These systems apply additional braking or steering control to a human-driven vehicle. These systems are typically designed to to minimize error in either yaw rate or side slip but typically are designed to operated in real time based on a reference model and thus do not estimate stability or controllability. Although the techniques used in many of these implementations are not applicable to this work, they are described here for completeness.

Anwar presents a method for enhancing yaw stability based on a generalized predictive control method [62]. The method uses a full-car handling model to predict yaw rate error. Differential braking is applied according to a control law to stabilize the vehicle around the desired yaw rate. The method was shown to enhance the stability of a vehicle on a snow covered surface [62].

Karbalaei *et al.*use fuzzy logic to implement a direct yaw rate controller using active front steering and differential braking [63]. The fuzzy controller uses a set of rules to determine the corrective steering angle and braking moment to apply in order to stabilize the vehicle about the desired yaw rate. Simulations show the effectiveness of this method [63].

Zhao *et al.*implement sliding mode control for yaw stabilization using differential

braking [64]. A 4-DOF vehicle model is used to estimate state variables and a sliding mode controller takes yaw rate error and side slip into account. The controller estimates the proper sliding trajectory and generates differential braking commands. Simulation results have shown the applicability of the method, but the authors did not conduct real vehicle testing [64].

Nishio *et al.*describe an estimation and control architecture for stability control [65]. In order to make the system robust to uncertain terrain environments, a non-linear tire model is combined with a switching friction state estimator and road bank estimator. The friction estimator performs a similarity analysis on the phase lag in the lateral acceleration wave form and chooses one of three friction states. Vehicle spin-out is detected by detecting the saturation of measured acceleration with respect to modeled acceleration. The side slip is then estimated using a pseudo-integral technique. The controller is designed to restrict extreme understeer and oversteer behavior by tracking side slip versus its derivative. The controller intervenes with differential braking to stabilize the vehicle when the controller criteria are met. The efficacy of the control architecture was validated in full-scale testing [65].

Liebemann *et al.*outline the concepts behind the Bosch electronic stability control system [66]. The Bosch system uses meausrements of lateral acceleration, forward velocity, and steering angle to recognize potentially dangerous situations. In yawing situations, the system applies controls to the center differential and wheel brakes to balance the drive torque and reduce the likelihood of loss of directional control. Additionally, the system detects potential rollover states and applies similar inputs to mitigate the rollover propensity [66].

2.5 Vehicle Control

In order for an autonomous vehicle to be able to navigate, it must have a vehicle controller that is capable of tracking the trajectories determined by the high level path planning systems. For UGVs, this means both accurate longitudinal and lateral control. As shown in analysis of the basic vehicle models, longitudinal and lateral control can often be largely decoupled for vehicles operating in the linear range [17]. However, as the goal of this work is to produce a controller that can operate stably and efficiently in the non-linear dynamic range, existing work on both coupled and decoupled controllers will be outlined.

Early work in the area of autonomous path tracking, such as that of DeSantis [67], focused on an operational domain in which side slip could be neglected and linear dynamics applied. In these cases, path tracking controllers could rely on simple vehicle models that decoupled the lateral and longitudinal dynamics. Under these conditions, linear control techniques such as Proportional-Integral-Derivative (PID) can provide adequate performance [67]. Further work in this area began to look at nonlinear controllers and more advanced control techniques. Freund and Mayr used compensator to decouple the dynamics and an observer to estimate unobservable states [68]. With these elements in place, the controller could be designed using pole placement techniques that increase the overall stability and performance of the controller [68].

Alleyne analyzes a variety of possible actuation methods for autonomous or semi-autonomous obstacle avoidance maneuvers: four-wheel steering, front wheel steering, four wheel brake steering, front wheel brake steering, and rear wheel brake steering [69]. A 7-DOF non-linear model is used to simulate each of the actuation types under control of a linear-quadratic controller. An obstacle avoidance maneuver was simulated using each actuation mode. Combined modes were not tested. The results are analyzed based on a maximum actuator effort criteria that measures the portion of the available tire force used for control. As might be expected, the two and four wheel steering actuation modes

yielded the best results in terms of the lowest maximum actuator effort to achieve the maneuver. Alleyne recommends the use of front wheel steering as the primary actuator for maneuvering and strongly recommends against using rear wheel brake steering due to the high actuator effort required [69].

2.5.1 Lateral Control

Wang *et al.*show the feasibility of path tracking using a yaw rate based sliding mode controller [23]. Since most autonomous motion planning algorithms output commands in terms of trajectories, the first module is a desired yaw rate generator that converts the trajectory coordinates into a target yaw rate for the controller to follow. The vehicle is modeled using a simplified full car model and a sliding mode control law is derived. The controller is validated in simulation against a high-fidelity, multi-body CarSim model and is compared to a position error based control system. At a constant speed of 50 km/h, the yaw rate based control architecture significantly outperforms the position error architecture. The yaw rate controller is also shown to be capable of tracking trajectories when the initial state is not located on the trajectory [23].

Peng and Tomizuka develop a lateral controller to lane centers under varying load, speed, and road conditions [70]. A controller is developed using a 6-DOF model and frequency-shaped linear quadratic control theory to design a feedback controller. To improve ride and performance characteristics, a lateral cornering stiffness estimator was implemented and its results were used to implement a gain-scheduling scheme. The composite controller was shown to yield good results with respect to lane tracking performance while maintaining acceptable ride quality [70].

Boada *et al.*designed a fuzzy logic controller to control the yaw rate of a vehicle using differential braking [71]. The controller is not designed for autonomy or path tracking, rather as a dynamic stability aid. The fuzzy controller uses the error in the desired slip

angle and yaw rate and the yawing moment as categories for fuzzification. Membership in these categories is defined to be negative big, negative medium, negative small, none, positive small, positive medium, or positive big according to membership functions. After evaluation of the fuzzy rules, the output is defuzzified and scaled to produce a desired yaw moment for the brakes to apply. Simulation using an 8-DOF model shows that application of the control improves the yawing performance and yaw stability of the vehicle [71].

2.5.2 Longitudinal Control

Kachroo *et al.*outline an architecture for a switched multi-mode longitudinal controller supervised by a fuzzy expert system [72]. Four separate controllers are implemented: PID, PI, sliding mode, and fuzzy. A separate fuzzy expert system monitors the control variables and switches between the controllers according to a set of fuzzy rules. Although seemingly complex and unwieldy, the strategy was successfully demonstrated in simulation [72].

Hedrick introduces a multiple sliding surface technique for longitudinal control of multiple vehicles [73]. The method is primarily designed to avoid the necessity of differentiating sparsely represented functions. The technique uses an upper sliding surface for speed and spacing control and a lower sliding surface to control the actual application of the throttle and brakes. An adaptive from of the algorithm is also introduced, primarily to account for the unknown values of parasitic drag forces. The effectiveness of this control strategy was demonstrated in the California PATH DEMO'97 [73].

2.5.3 Input/Output Linearization

Smith *et al.*develop a non-linear gain optimized controller for high-g lateral control [74]. A linear bicycle model is used to define the control states and an 8-DOF non-linear model is used to optimize the feedback gains. In order to achieve optimal control, the controller

is designed around two target speeds: 15 m/s and 30 m/s. The controllers were then tested in emergency single and double lane change maneuvers. The system was shown to be robust to changes in tire cornering stiffness and changes in mass. However, the controller showed poor performance with either low coefficients of friction or road elevation changes [74]. Considering the limited operating range of the derived controller, this approach is not recommended for future use.

Javid *et al.*control a simple autonomous vehicle through a feedback linearization scheme [75]. A simplified dynamic model of the vehicle is constructed and the parameters are determined by using a least squares technique to fit data offline. The feedback linearization scheme controls the trajectory in Cartesian coordinates uses the third derivatives of the x and y coordinates to linearize the feedback in terms of the control torques. A simple linear controller is then implemented to generate the control signals. The performance of the feedback linearized controller is shown to be superior to a linear PID controller in simulation. Experimentation shows that the simplified vehicle model failed to capture some aspects of the dynamics, resulting in performance significantly worse than shown in simulation. However, the feedback linearization controller is still able to maintain stable control of the vehicle [75]. Similar feedback linearization techniques are applied by Eghtesad and Necsulescu to a research vehicle with good results at low speeds [76].

2.5.4 Model Predictive Control

Falcone *et al.*develop a Model Predictive Controller (MPC) strategy for combined braking and steering control [77]. The model is a simplified full car model with a Pacejka tire model. The MPC has authority over the steering angle and the individual brakes on each of the four wheels. The primary goal of the controller is lateral control to follow a Cartesian path, but since the MPC can apply braking, longitudinal speed is also affected.

Simulation of a double lane change maneuver shows that tracking performance is best when a low weight is applied to longitudinal speed maintenance, enabling the controller to brake more aggressively [77]. These results illustrate the inherent coupling of lateral and longitudinal control in vehicle maneuvering.

Kim *et al.*compare a MPC to an input/output linearized controller [78]. The drawbacks of the linearization approach are highlighted in that it requires a smooth operating region. Due to aspects such as actuator saturation, non-holonomic constraints, and vehicle dynamic limits, the linearization based controller can produce non-optimal control trajectories. Since the MPC incorporates these limitations into the model, the control output can more closely match the capabilities of the vehicle. These differences are highlighted by testing on a three-wheeled autonomous vehicle. The input/output linearized controller produces trajectories that can result in loss of wheel-ground contact, resulting in rollover. With proper tuning, the MPC is able to produce trajectories that are more dynamically stable [78].

Rodic and Vukobratovic describe a method for automatic guidance of a generic vehicle [79]. Recognizing the inherent coupling between lateral and longitudinal control, a non-adaptive integrated dynamic controller capable of pure position or position/force control was developed. Because the accuracy of MPC algorithms depends on the accuracy of the model parameters, a practical stability test was used to set the control gains [79]. Practical stability is the concept that sufficient conditions exist for the system to be shown to be stable in the practical operating range. Practical stability does not guarantee asymptotic stability but for complex systems it is much easier to show that practical stability criteria exist than to prove asymptotic stability [80].

The practical stability tuning test consists of intentionally introducing parameter error into the model so that the gains can be tuned to ensure robustness to likely error sources. To account for additional sources of error and unmodeled dynamics, a neural network

based compensator was added to the controller. The neural network was trained using a back propagation method using the practical stability test parameter variations and fine tuned in closed loop mode. The addition of the neural compensator increases the robustness of the controller and allows for adaptation to changing dynamics [79]. Extensive proof of the practical stability of the system for both types of control laws is provided and a procedure for automatic checking of the practical stability conditions is introduced [80]. The total method presented is an adaptable, integrated dynamic controller that can be shown to be practically stable [79] [80].

For further discussion of MPC techniques, the reader is referred to the survey paper by Mayne *et al.* [81].

2.6 Literature Summary

Although many programs have resulted in successful operation of autonomous systems in off-road environments on uncertain terrain surfaces, research to date has largely focused on the motion planning and perception aspects of the problem. Very little literature exists to describe approaches to advanced vehicle dynamic implementations into UGV systems.

Vehicle dynamics modeling has been extensively studied for over 50 years and the fundamental dynamics are well understood. The most common vehicle handling models used in autonomous systems are based single track bicycle model. Many formulations of the bicycle model exist, but the most common approximates the dynamics as being linear and time invariant. This approach works well when the vehicle is operating in low-performance regimes, but can break down as operation nears the limits. Additionally, the bicycle model is fundamentally incapable of modeling roll dynamics and most formulations do not capture the coupling between the lateral and longitudinal dynamics.

More sophisticated models capture the dynamics of the full car by approximating

it as a four-wheeled system with roll and pitch motions. This formulation allows the calculation of normal forces on each wheel. Normal forces are used in the formulation of tire models due to the similarity principle. Tire models such as the Magic Formula and the TMeasy models use semi-empirical formulations to predict the non-linear tractive forces and moments generated by tires based on the vertical loads, COF, slip angles, and slip ratios. Most existing formulations of vehicle models make the assumption of uniform terrain environments, namely paved roads. The effects of terrain superelevation are usually neglected and a constant COF is usually assumed.

State estimation is also an extensively studied problem with two dominant techniques: least squares and Kalman filtering. The least squares technique, especially weighted forms of it, has been applied to estimation of vehicle states. The disadvantage of the least squares method is that it lacks well integrated methods for dealing with uncertainties of individual measurements, especially when excitation levels are low. The Kalman filter and extensions such as the EKF and UKF provide a method to estimate states based on stochastic data. Various forms of the KF have been successfully applied to vehicle state estimation. Combined state and parameter estimation can also be performed using forms such as the DEKF. Other techniques such as neural networks and classical observers have also been applied to state estimation.

Vehicle stability can be divided into two major parts: rollover stability and directional stability/controllability. Rollover stability metrics for road vehicles relying on lateral load transfer and overturning moments have been derived and validated. Additionally, some researchers have proposed the use of a Time to Rollover metric to provide a rational basis for warning of likely rollover events. The directional part of stability has been extensively studied, but much of the work in the field has focused on real-time control, not prediction. It has been shown, however, that directional stability relies largely on the force producing capability of the rear tires and that controllability relies heavily on the front tires. The

Stability Index has been proposed as a stability metric and the use of MMM diagrams has been demonstrated as an approach to prediction of both stability and controllability loss.

Although control design is outside the scope of this work, various control techniques have been applied to autonomous vehicles. Almost all current autonomous controllers separate lateral and longitudinal control; this separation ignores the inherent coupling due to the vehicle dynamics but works reasonably well as long as the vehicle is not operated outside of its low-performance linear range. More advanced techniques such as MPC, input/output linearization, and neural networks have also been tested, but no standard method for coupled autonomous vehicle dynamic control currently exists.

Although a broad base of the literature has been surveyed, many of the topics do not have direct application in this work. Fascinating as they may be, the autonomy and control sections of the literature represent areas that are beyond the scope of this work and are included for completeness. The aspects of the literature review that find direct application include the vehicle modeling, tire modeling (particularly the Fiala model), UKF-based state estimation, and the stability metric formulations. As will be seen in later chapters, work from the literature was further developed and integrated to create a novel method for estimation of stable vehicle operating envelopes with uncertain parameters.

Chapter 3

Vehicle Modeling

Determine that the thing can and shall be done, and then we shall find the way.

–Abraham Lincoln, 1848 [82]

The first step in developing the desired methodology for estimating a IMM is to establish a method for modeling the handling characteristics of a vehicle. Desirable characteristics for the model will be laid out, a model will be developed, and the modeling technique used in this work will be explained in detail. Finally, the output of the model will be compared to those of other well established models to demonstrate its efficacy.

3.1 Model Characteristics

Before a model can be developed, it is necessary to define the characteristics which are required to produce the desired result. The ultimate goal of this work is to produce a real-time estimate of a IMM for a standard Ackerman-steered vehicle. An additional goal is to formulate the model so that the specific vehicle configuration is abstracted as much as possible from the estimation and manifold mapping algorithms. A level of abstraction

allows easy transition of the techniques between vehicles by reducing the dependence of the high level algorithms on specific vehicle data. The logical starting point is to define the parameters of the manifold that will be the ultimate output of the model.

3.1.1 Coordinate Frames

Prior to discussions of models or manifolds, it is necessary to define the coordinate system in which they will be expressed. In the autonomy domain, the position and orientation of a vehicle is typically expressed in one of two coordinate frames: a globally referenced inertially-fixed frame (global frame) or a rotating frame affixed to the vehicle body (vehicle frame) [14]. The vehicle frame is capable of translating and rotating with respect to the global frame. The global frame is typically defined with the Z-coordinate normal to the surface of a reference spheroid (representing the Earth) and the X-axis oriented to point to geographic north. This definition will be used here although the global frame is relevant mainly for us with navigation and path planning purposes that are beyond the scope of this work. Therefore, unless stated otherwise, all coordinates in this work will be expressed in terms of the vehicle frame.

The vehicle frame in this work will be defined in terms of the standard definitions used by SAE. This frame is oriented as shown in Figure 3.1 with the x-axis pointing forward aligned the longitudinal axis, the y-axis pointing to the right, and the z-axis pointing downward. Rotations are defined as positive counter-clockwise with rotation about the x-axis termed roll, about the y-axis termed pitch, and about the z-axis termed yaw [10].

It is customary to place the origin of the vehicle frame at the CG of the vehicle. However, in this work the assumption is made that the CG location is variable and not necessarily known. To solve this problem, the origin of the vehicle frame will instead be placed at the center of the rear axle of the vehicle as defined by the lateral midpoint of the centers of ground contact of the rear wheels at nominal ride height. This placement

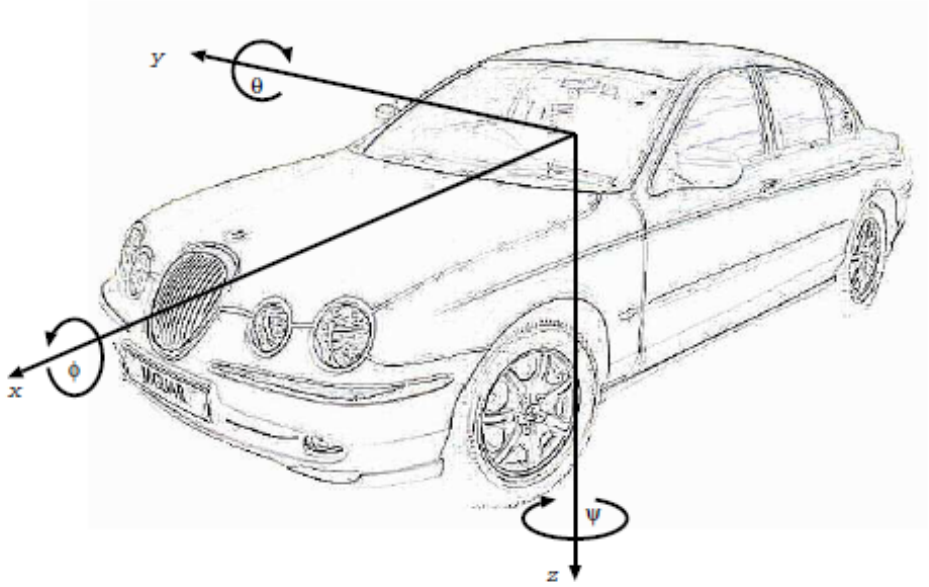

Figure 3.1: SAE standard automotive coordinate frame [21].

is commonly used in the autonomy domain as it simplifies the definition of vehicle paths and is typically considered the center of navigation [9]. It should be noted that this placement at nominal ground level will usually result in the frame being located outside of the physical constraints of the vehicle body.

For cases in which it is desirable to express terms with respect to the CG, an additional cg frame will also be defined. This frame is located at the CG of the total vehicle and is oriented identically to the vehicle frame. The translational offset between the cg frame and the vehicle frame will be used as the definition of the location of the CG.

It is also often convenient to define additional coordinate frames located at the center of the contact patch of each of the four wheels. These frames are located at translations from the vehicle frame defined by the track width and wheel base. The z-axes of the tire frames are aligned with the z-axis of the vehicle frame, but the tire frames are free to rotate about the z-axis with wheel rotation. An overview of the vehicle-centric coordinate frames can be seen in Figure 3.2.

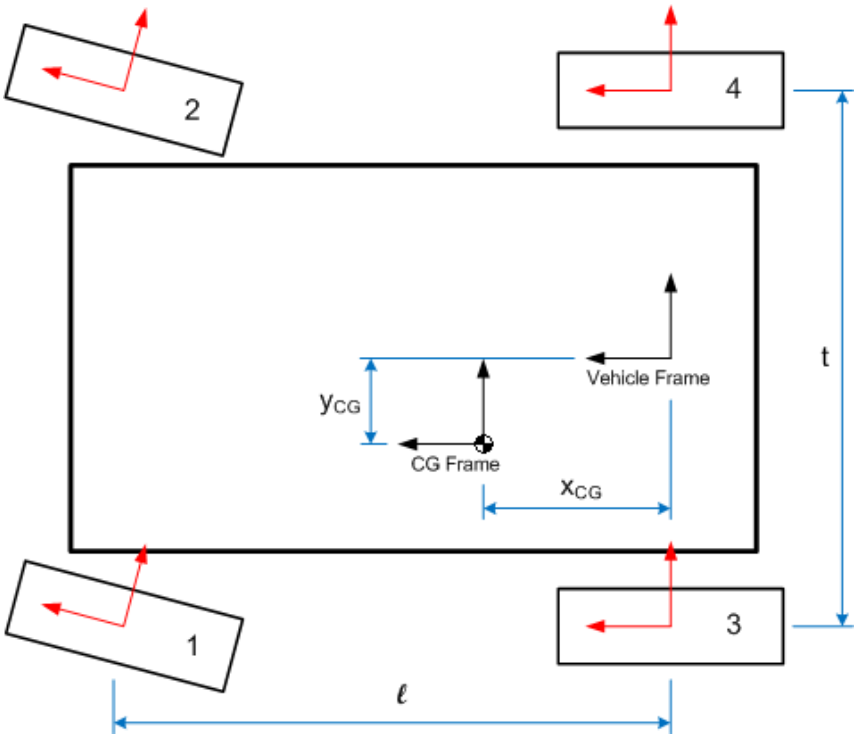

Figure 3.2: X-Y plane schematic view of the vehicle coordinate frames. Note vehicle frame, CG frame, and the wheel frames and wheel reference numbers.

3.1.2 Instantaneous Maneuvering Manifold

The concept of the Instantaneous Maneuvering Manifold (IMM) is an attempt to encapsulate the potential maneuvering space of a vehicle into a minimal set of variables that could be used by a motion planning algorithm to produce navigation commands. Ideally the maneuvering envelope would express the set of possible paths bounded the dynamic and kinematic vehicle constraints and the relationship of these variables to the physical control inputs.

It is a basic principle of macroscopic Newtonian physics that the path of a body through space is determined as a result of a time history of its orthogonal velocities, which are in turn determined by the accelerations created through the actions of external forces on the body. Since this work is concerned with ground vehicles, this problem can be simplified with the assumption that the vehicle is constrained through its wheels to

contact a ground plane of arbitrary orientation. Application of this assumption eliminates motion in the z-axis of the wheels relative to the ground. It is of course possible for vehicles to become airborne with one or more wheels as a result of dynamic maneuvers. However, this rather exciting operational state is well beyond the expected operational range of most UGVs at present and will not be considered in this work.

In terms of the coordinate frames defined above, the vehicle path is the trace of the motion of the vehicle frame relative to the global frame. Since the global frame is also affixed to the ground plane, the path can be expressed in terms of the 2-D global X-Y plane. Since this work is concerned with vehicle state and not global paths, it is more convenient to disregard the global positioning of the vehicle and instead express the path in terms of the instantaneous trajectory of the vehicle frame with respect to the global frame.

The instantaneous state of the vehicle with regards to maneuvering is referred to as its posture and can be expressed by assuming that the vehicle is moving along a curved path with an arbitrary center at a certain speed [83]. At steady state, this will result in a trace on the global X-Y plane of a circle over time. Real vehicles, however, are typically driven in non-steady-state conditions and thus it is necessary to introduce allow for variable rates of change of path speed and curvature. If the derivatives of these rates are assumed to be practically infinite, as is commonly done, these four variables will uniquely define a global path in terms of instantaneous posture [9].

The resultant maneuvering space can then be defined in terms of four instantaneous vehicle frame variables: path curvature, curvature rate, path speed, and path acceleration. If a 4-D manifold can be constructed to enumerate the relationships between these variables, it would contain the information necessary for a path planning algorithm to determine the optimal combination for the desired global path.

Most Ackerman-steered vehicles are not configured to allow for direct control of path

curvature or speed. The commonly available control inputs are a front-wheel steering angle (usually controlled by a hand wheel) and wheel torque (usually controlled by pedals linked to the engine or brake system). It is therefore also necessary to ensure that a mapping function exists to transform the path variables into appropriate control variables that can be manipulated by a control system.

3.1.3 Fundamental Assumptions

As with any engineering problem, it is necessary to make certain assumptions in order to formulate a tractable problem. For clarity and completeness, these fundamental assumptions must be defined before a model can be derived.

Vehicle Configuration

1. The vehicle has four wheels and is laterally symmetrical about its x-axis with regards to configuration
2. All forces produced by the vehicle act through the tires to the ground
3. The tires exhibit characteristics common to standard rubber bias or radial ply pneumatic tires
4. The vehicle is steered only via the front wheels through a linkage of known configuration
5. The contributions of suspension and tire compliances are much greater than that of the vehicle frame stiffness
6. The wheels are connected to the sprung mass through a suspension system whose characteristics are known
7. The unladen mass and static weight distribution are known

8. Vehicle configuration parameters are time-invariant

These assumptions in general represent a standard four-wheel, Ackerman-steered, pneumatic-tired vehicle of the type defined in the scope. This type of vehicle configuration is dominant in the world today and is used in the vast majority of real-world applications. The assumptions are intended to represent the type of information that is generally available to integrators of autonomous systems. Basic vehicle dimensions can be measured easily and techniques exist to extract information on suspension and weight distribution [10].

Most vehicles in production today are dimensionally laterally symmetrical, but significant differences often exist between the configurations of the front and rear axles. This lack of longitudinal symmetry can have a large impact on maneuvering characteristics, and thus longitudinal symmetry cannot be assumed [10]. Vehicles with more than two axles and multi-axle steering exist but will not be included in the scope of this work due to their relative production scarcity and the difficulties inherent in modeling multi-axle vehicles [84] [85]. Similarly, articulated vehicles will be excluded due to their vastly different maneuvering dynamics and highly-specialized nature [86].

As with all structures, the frame of any real vehicle is not infinitely rigid and possesses a characteristic stiffness in response to load. If the frame stiffness is high enough compared to the stiffnesses of the suspension components, it becomes reasonable to model the frame as a rigid body. Unfortunately, this rigid-body assumption cannot be said to be accurate for all vehicles [87]. This deflection can be particularly noticeable on very stiffly sprung vehicles (such as race cars) or vehicles with weak structures (such as convertibles). Results from Sampo, et al., indicate that the key factor determining the impact of frame stiffness on handling is the ratio of frame stiffness to suspension roll stiffness [87]. For vehicles with a frame/roll stiffness ratio above 5, a rigid frame assumption is valid [87]. However, it should be noted that even for vehicles with ratios as low as 1, the error in load

transfer distribution is less than 5% [87].

Vehicle frames are complex structures and deriving an accurate model of the stiffness typically requires either a finite-element model or an experimental modal analysis. Techniques exist for performing these type of analyses, but they require either highly detailed design information or specialized experimental equipment [88] [89]. In many cases this level of data and equipment will not be available to autonomy integrators who are not OEM manufacturers.

The high stiffness of the frame of most vehicles relative to the suspension indicates that the impact of a rigid-frame model on calculated wheel loads will be small for most vehicles. Due to the complexities involved with modeling frame stiffnesses and the lack of available data, a rigid-frame assumption will be used in this work. This assumption will undoubtedly reduce the accuracy of the modeling, but is necessary to bring the problem with in the bounds of the computational, technical, and temporal resources available. Expansion of the models to incorporate frame flexibility will be left as future work.

The assumption that vehicle parameters are time-invariant is not strictly true for real vehicles. Some parameters, such as wheelbase, are unlikely to change with time but others, such as stiffnesses or tire parameters, may change gradually with time due to factors such as wear and fatigue. This wear, especially for the tires, may be significant over long time scales and may impact maneuvering performance. However due to the long time scales (on the order of thousands of hours of operation) associated with such wear, it is necessary for purposes of expediency to leave the incorporation and validation of time-variant vehicle parameters as future work [90].

Environmental Assumptions

1. The vehicle will be operating in combined-slip conditions

2. Payloads of unknown mass and distribution may be dynamically applied to the

sprung mass

3. The vehicle will be operating on terrain that is generally locally smooth

4. Terrain will not exhibit large scale changes in bank or grade

5. Time-variant terrain-tire interaction can be characterized by a dynamic coefficient of friction

6. Aerodynamic forces are small and can be neglected

The core principle that differentiates this work from previous work in the field is the assumption that the maneuvering environment can and will be time-variant. In order to restrict the scope for tractability, some bounds must be placed on the dynamic nature of the environment.

The first assumption, that the vehicle will operate in combined-slip conditions (i.e. coupled longitudinal and lateral acceleration), may seem obvious, but the astute reader will note that a very high percentage of vehicle modeling techniques rely on the assumption of uniaxial slip. Secondly, it is anticipated that changes in vehicle mass and CG will occur due to the addition of payloads to the sprung mass. The masses and distribution of these payloads will not be known *a priori*, but the magnitude of the payload will be bounded by the cargo capacity of the vehicle.

The most important assumptions required to restrict the scope of the work are those related to the operational terrain surfaces. For purposes of this work, it will be assumed that the terrain profiles are locally smooth enough to maintain contact between the ground and wheel at all four wheels. This assumption would tend to exclude operation in extreme off-road environments or cases in which the vehicle is required to traverse large discrete objects such as ditches or logs. While it may be necessary for vehicles to operate in this type of environment for some mission types, it is unlikely at present that the vehicle would

do so at high-speed. The primary operating environments considered for this work will be areas in which high-speed operation is more likely to be conducted: paved roads, unpaved roads, unimproved but clear trails, and open fields. Another aspect of this assumption is that the environment will be assumed to be planar: to restrict the scope for tractability, changes in terrain bank or grade will not be present and the vehicle will be assumed to be operating on a generally flat, level surface.

As the goal of this research is to characterize handling and not soil characteristics, advanced terramechanics techniques, such as those cited in the literature, taking into account factors such as wheel sinkage, soil shear strength, and soil adhesion are considered beyond the scope of this work [91]. Instead, the terrain surface will be characterized in terms of a single coefficient of friction value that can be used by tire models to predict the forces relevant to handling.

Aerodynamic forces can have a significant effect on vehicles, particularly those traveling at high absolute speeds and those equipped with aerodynamic surfaces [10]. However, as aerodynamic forces are generally related to the square of the vehicle's velocity, these forces become much less significant as absolute speed decreases. Accurate modeling of aerodynamic forces on vehicles is a difficult procedure that often requires a wind tunnel for verification [10]. Therefore for the purposes of this work, in which the vehicles will be modeled at relatively low absolute speeds, aerodynamic forces will be considered to be small and will not be modeled.

3.1.4 Key Parameters

Given the assumptions and desired model attributes, some key model parameters can be identified, as outlined in Table 3.1. These parameters capture most of the key characteristics of the vehicle as they relate to maneuvering. As noted in the third column, some of these parameters are known *a priori* and are assumed to be time-invariant. The parameters

that are time-variant will need to be estimated using the methods described in Chapter 4.

Table 3.1: Key Model Parameters

Symbol	Parameter Name	Variable?
C_α	Linear tire cornering stiffness	No
C_S	Linear tire traction coefficient	No
c_{ϕ_n}	Roll damping coefficient of axle-n	No
c_ψ	Pitch damping coefficient	No
k_{ϕ_n}	Roll stiffness coefficient of axle-n	No
k_ψ	Pitch stiffness coefficient	No
I_n	Moment of inertia about n-axis	Yes
ℓ	Wheelbase length	No
M	Mass of total vehicle	Yes
m_s	Mass of sprung mass	Yes
m_{us_n}	Mass of unsprung mass of axle-n	No
t_n	Track width of axle-n	No
μ	Tire-ground coefficient of friction	Yes
x_{CG}	Longitudinal CG offset from vehicle frame	Yes
y_{CG}	Lateral CG offset from vehicle frame	Yes
z_{CG}	Vertical CG offset from vehicle frame	Yes
z_{RC}	Roll center height from vehicle frame	No

3.2 Vehicle Model

The goal of a vehicle model is to provide a mathematical approximation of the behavior of a real vehicle with respect to the key parameters identified in Table 3.1. The model will be based on a simplified 4-wheel representation of a vehicle with separate sprung and unsprung masses similar to the model formulated by Will and Zak [20]. This representation was selected as the simplest representation capable of capturing the critical dynamics of sprung mass weight transfer in response to accelerations.

The model has a total of 11 DOF: translation in x, y, and z, rotation in θ, steering of the front wheels (δ), rotation of the sprung mass in ϕ and ψ, rotations of the wheels (ω_n), and location of the CG in x_{CG}, y_{CG}, and z_{CG}. The choice of these DOF for the model

allows for all of the desired characteristics which are of particular relevance to this work: variable CG location, mass, and lateral and longitudinal weight transfer. For comparison, the model by Will and Zak possesses four DOF and a complicated multi-body model such as VehicleSim may have in excess of 200 [20] [92].

3.2.1 Tire Model

Ultimately, the forces affecting vehicle motion can be related to the the forces generated at the contact patches of the tires. It thus becomes extremely important to select a tire model that can accurately predict these forces and is compatible with the overall goals of the vehicle model.

The tire model selected for this work is the combined-slip Fiala model as described by Hsu [50]. This model can be analytically derived from the brush tire representation, a full derivation of the which was performed by Pacejka and will not be repeated here in the interest of conciseness [26]. The Fiala model is widely used in the literature and its efficacy has been demonstrated. As noted in the literature review, the Magic Formula is considered to be the most accurate model currently available [26]. However, the Magic Formula model is defined by a large number of parameters whose physical realization is not always clear; it thus does not lend itself to the desired online estimation techniques and accurate parameter values are typically not available to parties without specialized test equipment.

The Fiala model, while possibly less accurate than the Magic Formula, is defined in terms of the physically recognizable parameters of vertical load (F_{z_n}), slip angle (α_n), slip ratio (S_n), cornering stiffness (C_α), traction coefficient (C_S), and COF (μ) [50]. Techniques exist for measuring or estimating these physical quantities (see Chapter 4) thus meeting the overall goal of model adaptability. Although it is beyond the scope of this work to demonstrate, it is possible that over a wide range of operating conditions an

adaptable Fiala model may be more accurate than a static parameter version of the Magic Formula.

The combined-slip version of the Fiala model is developed here. Combined-slip indicates that the model is valid for conditions of simultaneous longitudinal and lateral tire slip. A combined-slope model is important for real vehicle operations as the maximum force the tire is capable of generating is a function of both the lateral and longitudinal forces. This relationship is often referred to as the friction circle or more properly the friction ellipse as the maximum force characteristic will generally trace an ellipse in the lateral force vs longitudinal force plane, although in reality this ellipse will likely be distorted due to the properties of real tires [10].

The two key outputs of the tire model are the lateral and longitudinal forces produced at the contact patch. The form of the equations given here is taken from Hsu, but may be found in other references [50]. The longitudinal force equation is augmented with a linear rolling resistance coefficient to enable modeling of the resistance in the tire due to deformation while rolling.

$$F_{x_n} = C_S \left(\frac{S_n}{1+S_n} \right) \frac{F}{f} - C_{rr} F_{z_n} \tag{3.1}$$

$$F_{y_n} = C_\alpha \left(\frac{\tan \alpha_n}{1+S_n} \right) \frac{F}{f} \tag{3.2}$$

where

$$F = \begin{cases} f - \frac{1}{3\mu F_{z_n}} f^2 + \frac{1}{27\mu^2 F_{z_n}^2} f^3, & f \leq 3\mu F_{z_n} \\ \mu F_{z_n}, & f > 3\mu F_{z_n} \end{cases} \tag{3.3}$$

$$f = \sqrt{C_S^2 \left(\frac{S_n}{1+S_n} \right)^2 + C_\alpha^2 \left(\frac{\tan \alpha_n}{1+S_n} \right)^2} \tag{3.4}$$

The polynomial representation of the contact patch area used in the brush model can be seen in Eq. 3.3, as is the piecewise representation that limits the maximum force to to the product of the coefficient of friction and vertical force. It should also be noted that Eq. 3.4 represents the friction ellipse that occurs as a result of combined slip conditions. These equations will reduce to the standard single-axis Fiala equations if either of the slip quantities is set to zero.

A normalized resultant force profile from the Fiala model is plotted in Figure 3.3. Note that the initial segment of the profile that occurs at low slip values has a slope that is proportional to the stiffness coefficient (C_α or C_S). This linear region is then followed by a transitional region in which the proportionality begins to break down until it reaches a peak value. Due the definition of the piecewise function in Eq. 3.3 the force remains constant at slip values beyond the maximum. For real tires the force in this sliding region would begin to decrease gradually from the peak [26]. However, as other constraints will generally limit the operation of most autonomous vehicles to the linear and transitional ranges, this deviation from real tire behavior is of limited significance to this work.

3.2.2 Maneuvering Dynamics

In the absence of aerodynamic and other external body forces, the maneuvering dynamics of the vehicle will be determined by the forces generated between the four tires and the ground. To account for these forces, the vehicle model will consider the forces at each of the four wheels rather than compressing the two axles into a bicycle model.

As the vehicle is only in contact with the ground at the contact patches of the four tires, the maneuvering dynamics are dictated by the forces generated by the tires. As can be noted by observation from Eq. 3.1 and Eq. 3.2, these forces are dictated by the slip ratios, S_n, and slip angles, α, of the tires. The slip ratio defines the ratio of the actual speed of rotation of the tire to the speed of a free-rolling (i.e. non-force generating) tire

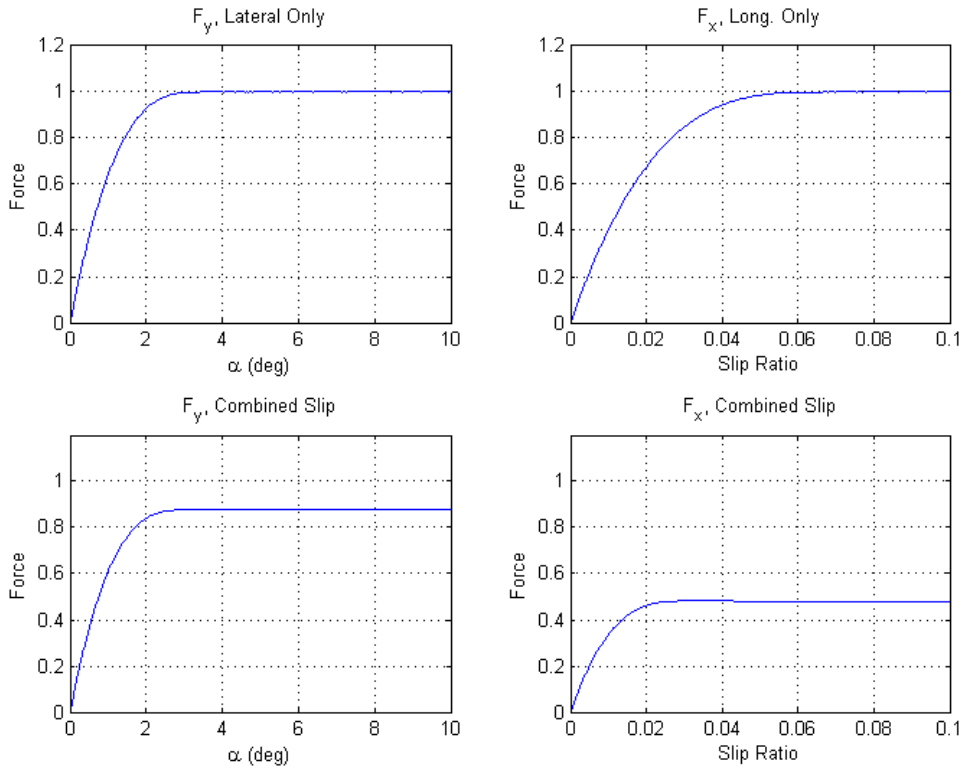

Figure 3.3: Non-dimensionalized Fiala force profile. Note lateral and longitudinal profiles for simple slip (top) and combined slip (bottom) cases. A limitation of the Fiala model is the lack of roll-off above maximum force generation.

and is commonly defined as [10]:

$$S_n = \frac{R_{e_n}\omega_n - V_x}{V_x} \tag{3.5}$$

The slip angles of the tires are a function of both the kinematics and dynamics of the vehicle. The slip angle can be defined as the angle between the direction of orientation of the tire and the direction of travel. Several methods exist for calculating slip angles, but a

common and reasonably accurate approximation is given by [93]:

$$\beta = atan\left(\frac{V_y}{V_x}\right) \tag{3.6}$$

$$\alpha_1 = -\delta + atan\left(\frac{V_x\beta + (\ell - x_{CG})\dot{\theta}}{V_x - 0.5(t_F + y_{CG})\dot{\theta}}\right) \tag{3.7}$$

$$\alpha_2 = -\delta + atan\left(\frac{V_x\beta + (\ell - x_{CG})\dot{\theta}}{V_x + 0.5(t_F - y_{CG})\dot{\theta}}\right) \tag{3.8}$$

$$\alpha_3 = -atan\left(\frac{-V_x\beta + (x_{CG})\dot{\theta}}{V_x - 0.5(t_R + y_{CG})\dot{\theta}}\right) \tag{3.9}$$

$$\alpha_4 = -atan\left(\frac{-V_x\beta + (x_{CG})\dot{\theta}}{V_x + 0.5(t_R - y_{CG})\dot{\theta}}\right) \tag{3.10}$$

A marginally more accurate alternative formulation is also presented by Kiencke that accounts for the change in contact patch position due to caster effects, however this formulation is significantly more complex to implement [93]. Note that β calculated in Eq. 3.6 is the body slip angle of the vehicle.

Calculation of the slip ratios and slip angles allows use of Eq. 3.1 and Eq. 3.2 from the tire model to calculate the resultant longitudinal and lateral forces from the tires. The individual tire forces can then be summed to determine the overall force acting on the vehicle:

$$F_x = \sum_{n=0}^{4} F_{x_n} cos(\delta_n) + F_{y_n} sin(\delta_n) \tag{3.11}$$

$$F_y = \sum_{n=0}^{4} F_{x_n} sin(\delta_n) + F_{y_n} cos(\delta_n) \tag{3.12}$$

Additionally, the yawing moment due to the forces can be calculated by taking the cross

products of the forces and their moment arms:

$$\begin{aligned} N = &[0.5t_F cos(\delta) + (\ell - x_{CG})sin(\delta)]\,F_{x_1} - [0.5t_F cos(\delta) - (\ell - x_{CG})sin(\delta)]\,F_{x_2} \\ &+ 0.5t_R F_{x_3} - 0.5t_R F_{x_4} + [(\ell - x_{CG})sin(\delta) - 0.5t_F cos(\delta)]\,F_{y_1} \\ &+ [(\ell - x_{CG})sin(\delta) + 0.5t_F cos(\delta)]\,F_{y_2} - x_{CG}F_{y_3} - x_{CG}F_{y_4} \end{aligned} \tag{3.13}$$

In order to determine the desired yaw terms from the yawing moment, it is necessary to calculate the rotational moment of inertia about the yaw (z) axis. Since this value cannot be easily measured without specialized equipment, it is necessary to approximate this value. One method for doing this is to use the dynamic index, which is defined as [21]:

$$DI = \frac{r_z^2}{x_{CG}(\ell - x_{CG})} \tag{3.14}$$

The dynamic index for most vehicles is approximately equal to one, with high performance vehicles typically slightly lower [21]. From the dynamic index, a reasonable approximation of the moment of inertia can be calculated as:

$$I_z = m_s x_{CG}(\ell - x_{CG})DI \tag{3.15}$$

These forces can then be used to calculate the motion variables of the vehicle in the $x-y$ plane. Application of Newton's Second Law allows for calculation of the changes in the velocities due to the forces:

$$\dot{V}_x = \frac{F_x}{M} + V_y\dot{\theta} \tag{3.16}$$

$$\dot{V}_y = \frac{F_y}{M} - V_x\dot{\theta} \tag{3.17}$$

$$\ddot{\theta} = \frac{N}{I_z} \tag{3.18}$$

The velocity in each direction can then determined by integration and the position and heading by double integration:

$$V_x = \int \dot{V}_x dt + v_{x_0} \tag{3.19}$$

$$V_y = \int \dot{V}_y dt + v_{y_0} \tag{3.20}$$

$$\dot{\theta} = \int \ddot{\theta} dt + \dot{\theta}_0 \tag{3.21}$$

$$X = \int V_x dt + X_0 \tag{3.22}$$

$$Y = \int V_y dt + Y_0 \tag{3.23}$$

$$\theta = \int \dot{\theta} dt + \theta_0 \tag{3.24}$$

3.2.3 Internal Dynamics

Dynamic redistribution of normal forces between the four wheels can have a great impact on the handling dynamics of the vehicle. Since tire lateral and longitudinal forces have a strong dependence on normal force, the distribution of normal forces has a large impact on overall handling characteristics, especially at high accelerations.

A major aspect of the weight transfer is governed by the the interactions between the sprung and unsprung masses through the suspension. The connection involved in the suspension can be complex due to the variety of possible suspension geometries and the possible inclusion of additional linkages such as anti-roll bars. One key property of the suspension linkages that influences the dynamics is the roll center, which is defined as the point at which a lateral force applied to the sprung mass does not create a rolling moment [10]. The roll centers can be determined kinematically for the front and rear suspensions and are connected by a virtual roll axis about which the sprung mass rolls. It should be noted that for many geometries the roll center will actually move slightly in response to suspension jounce. However for purposes of this work the roll center will be

considered a static location with respect to the vehicle frame.

To simplify and generalize suspension characteristics, the attachment between the unsprung and sprung mass will be modeled as a series of revolute joints. One joint is placed at each roll center with its axis aligned with the roll axis. A third revolute joint is placed at the pitch center with its axis oriented parallel to the vehicle y-axis. The most significant effect of the internal vehicle dynamics is the weight transfer between the four wheels. This transfer can be be separated into two orthogonal parts: longitudinal and lateral.

Under a planar assumption, longitudinal weight transfer is caused by accelerations due to the throttle and braking inputs. The magnitude of this transfer can be calculated by taking moments about the front tire contact patches, as shown by Milliken [10]:

$$\Delta W_{x_F} = -\frac{(z_{CG} + R_e) m_s g A_x}{\ell} \tag{3.25}$$

$$\Delta W_{x_R} = \frac{(z_{CG} + R_e) m_s g A_x}{\ell} \tag{3.26}$$

A lateral offset of the CG will affect the distribution of the longitudinal load transfer. The effects of the lateral CG offset can be compensated by calculating a normalized coefficient for each wheel [10]:

$$C_{x_1} = \frac{1}{2} - \frac{y_{CG}}{0.5 t_F} \tag{3.27}$$

$$C_{x_2} = \frac{1}{2} + \frac{y_{CG}}{0.5 t_F} \tag{3.28}$$

$$C_{x_3} = \frac{1}{2} - \frac{y_{CG}}{0.5 t_R} \tag{3.29}$$

$$C_{x_4} = \frac{1}{2} + \frac{y_{CG}}{0.5 t_R} \tag{3.30}$$

Lateral weight transfer occurs due to lateral accelerations acting on the CG and is influenced by the height of the CG, the location of the roll centers, the suspension compliances, and the lateral offset of the CG. The effect of the roll centers causes the lateral

load transfer to be governed by a characteristic height that is the distance between the CG and the roll axis at the longitudinal location of the CG:

$$H = z_{CG} + R_e - \frac{z_{RC_F} x_{CG} + z_{RC_R}(\ell - x_{CG})}{\ell} \tag{3.31}$$

The effect of lateral acceleration can then be derived by taking moments about one side of the vehicle, as shown by Milliken [10]:

$$\Delta W_{y_F} = \frac{k_{\phi_F} m_s g A_y H}{t_F (k_{\phi_F} + k_{\phi_R} - m_s g A_y y_{CG} - m_s g H)} + m_s g A_y \frac{x_{CG} x_{RC_F}}{\ell t_F} \tag{3.32}$$

$$\Delta W_{y_R} = \frac{k_{\phi_R} m_s g A_y H}{t_F (k_{\phi_F} + k_{\phi_R} - m_s g A_y y_{CG} - m_s g H)} + m_s g A_y \frac{(\ell - x_{CG}) x_{RC_R}}{\ell t_R} \tag{3.33}$$

The total instantaneous weight distribution can be found by first calculating the static weight distribution:

$$F_{z_1 s} = \frac{C_{x_1} m_s g x_{CG}}{\ell} + m_u g \tag{3.34}$$

$$F_{z_2 s} = \frac{C_{x_2} m_s g x_{CG}}{\ell} + m_u g \tag{3.35}$$

$$F_{z_3 s} = \frac{C_{x_3} m_s g (\ell - x_{CG})}{\ell} + m_u g \tag{3.36}$$

$$F_{z_4 s} = \frac{C_{x_4} m_s g (\ell - x_{CG})}{\ell} + m_u g \tag{3.37}$$

The effects of the dynamic weight transfers can then be applied:

$$F_{z_1} = F_{z_1 s} - \Delta W_{y_F} - C_{x_1} \Delta W_{x_F} \tag{3.38}$$

$$F_{z_2} = F_{z_2 s} + \Delta W_{y_F} - C_{x_1} \Delta W_{x_F} \tag{3.39}$$

$$F_{z_3} = F_{z_3 s} - \Delta W_{y_R} + C_{x_1} \Delta W_{x_R} \tag{3.40}$$

$$F_{z_4} = F_{z_4 s} + \Delta W_{y_R} + C_{x_1} \Delta W_{x_R} \tag{3.41}$$

These values yield the expected normal force on each wheel given the CG location under conditions of lateral and longitudinal acceleration.

3.3 Modeling Technique

The ultimate goal of this research is to produce a IMM that can be updated in real-time. To provide maximum usefulness for higher level components autonomy components such as motion planners, this manifold should be expressed in a form that indicates both the limits of maneuvering performance as well as information about intermediate states. The equations generated from the vehicle model are formulated to express the state of the vehicle at single values of the relevant input variables. Additionally due to the coupling between internal and maneuvering dynamics, these equations must typically be solved using iterative numerical techniques. The combination of these factors makes solving for the grid of input states required to generate a manifold in real-time computationally infeasible. To solve this difficulty, a method of representing offline precalculated maneuvering dynamics will be developed.

3.3.1 Force-Moment Method

The Force-Moment Method (FMM) (also known as the MMM) as described by Milliken is a method for representing the steady-state forces and moments acting on a vehicle due to a set of input variables in a format useful for maneuvering analyses [10]. For an extensive discussion of the FMM, the reader is directed to Milliken's excellent volume *Race Car Vehicle Dynamics* [10].

As shown in Figure 3.4, a plot of the output of an FMM implementation displays a representation of lateral force on the abscissa and yawing moment on the ordinate for lines of multiple steering angles (δ) and body slip angles (β). The plot in Figure 3.4 was calcu-

lated for a constant velocity and longitudinal acceleration, but if the FMM analysis can be conducted across a range of velocity and acceleration values, the result can be transformed into the desired manifold variables. An important property of the FMM diagram is that the maximum/minimum β lines on the diagram correspond to the Directional Controllability Metric (DCM) and the maximum/minimum δ lines correspond to the Directional Stability Metric (DSM).

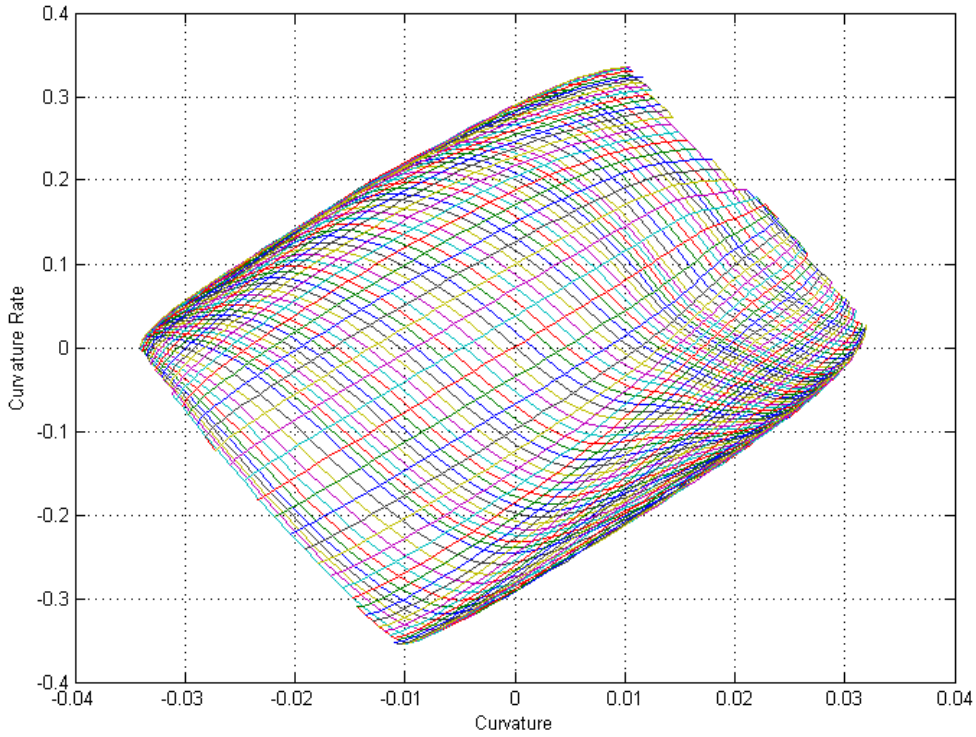

Figure 3.4: Example FMM diagram

The proposed method uses the vehicle model equations to generate FMM maps of the IMM for a set of variables. This set represents the variables that will be estimated using the techniques in Chapter 4 and includes tire coefficients, CG location, mass properties, and COF. The manifold maps will be generated offline using a MATLAB implementation and then stored in a data structure for use on the vehicle in real-time. These maps will

then be used with the interpolation techniques developed in Chapter 5 to generate real-time representations of the IMM based on the current state estimates. By precalculating the maps and then using computationally less intensive interpolation techniques online, real-time generation of the manifolds becomes feasible.

3.3.2 Implementation

To generate the FMM maps, the steady-state vehicle model equations were implemented in MATLAB. Use of a commercial multi-body vehicle modeling package, such as VehicleSim, to generate the maps was considered. The FMM technique represents the vehicle in a steady-state condition; at steady-state most of the advantages of a multi-body model are negated as the number of effective DOF drops significantly at steady-state. It is also challenging to set up a multi-body to generate the data due to the difficulty in initializing all of the model states correctly. When using a multi-body model for steady-state data, it is generally necessary to allow the model to initialize a set of inputs and allow the model to stabilize; this requires a large amount of computing time when implemented across a wide range of values and maneuvers. Use of a MATLAB implementation based on the vehicle model developed above allows for direct calculation of the operating points of interest with far less computing time. It will be shown in Section 6.1 that the results of the MATLAB implementation are of acceptable accuracy when compared to VehicleSim.

Force-Moment Solving

The first step in the code uses steering angle (δ), body slip angle (β) as independent variables to solve for a grid of values of lateral force (F_y) and yawing moment (N). The values for the independent variables are selected to produce a sufficiently dense grid in the $F_y - N$ plane to allow for accurate interpolation between points. Experimentation showed that a variable density grid yielded the best balance between execution time and

data density. For δ, angles were varied by 1° between the maximum kinematic steering angle and 10°, by 0.5° between 5° and 10°, and by 0.25° between 0° and 5°; this was mirrored about zero for negative values. Since values of β are generally lower than those of δ, the range was reduced to between $\pm 1/2$ of the maximum kinematic steering angle with the same ranges of resolution. This grid spacing was found to give good results for the vehicle configurations tested but might need to be adjusted if an unusual vehicle were to be modeled.

Since there is a non-linear interdependence between the lateral accelerations generated at an operating point and the load transfer at that point, it is necessary to use an iterative numerical solver to simultaneously solve for the values of the forces and the lateral and longitudinal load transfers. The built-in MATLAB function `fsolve` was found to give good results in numerically converging the system when using a `trust-region-dogleg` algorithm that is specifically designed to solve non-linear systems. This algorithm uses a Powell dogleg procedure to construct a combined Caucy and Gauss-Newton step for each iteration of the function, details of which can be found in the MATLAB documentation [94]. Other algorithms, such as `Levenberg-Marquardt`, were tested but were found to yield poor convergence due to the non-linearities present in the system.

The anonymous function input to `fsolve` was constructed using an input vector composed of the longitudinal weight transfer (ΔW_x), resultant lateral acceleration (A_y), and longitudinal slip ratio (S). This input vector, along with other required parameters, can be used to calculate an estimated vertical load distribution which can then be used as in input to the tire model to calculate the resultant forces. To account for the drive configuration of the vehicle the slip ratio is multiplied by a scale factor. For example on a Rear Wheel Drive (RWD) vehicle, this scale factor would be one for the rear wheels and zero for the front wheels under positive acceleration. In braking conditions, the scale factor would be the normalized brake proportion for each wheel. This slip ratio scaling is simplistic in

that it does not take into account drive torque distribution due to final drive configuration. Additionally, the brake factors are used for all negative accelerations; this is not strictly correct due to the effects of engine braking. The vehicles in this work used this distribution to simplify the modeling, but the method of implementation would allow for a more sophisticated scaling if engine and drive torque characteristics are known.

The weight transfer and slip ratios are combined with a vector of slip angles as inputs to the tire model. The slip angles (α_n) used are δ_i for the front wheels and β_i for the rear wheels where i is the current loop iteration. The output forces from the tire model equations are used to construct the minimization expressions.

$$\sum_{n=1}^{4} (F_{x_n} \cos\alpha_n + F_{y_n} \sin\alpha_n)/W - \Delta W_x \ell/(z_{CG}) \tag{3.42}$$

$$\sum_{n=1}^{4} (F_{x_n} \sin\alpha_n + F_{y_n} \cos\alpha_n)/W - A_y \tag{3.43}$$

$$\sum_{n=1}^{4} (F_{x_n} \cos\alpha_n + F_{y_n} \sin\alpha_n)/W - A_{x_i} \tag{3.44}$$

When the results of these expressions are equal to zero, the weight transfer and tire force generation characteristics are in balance and the system can be said to have converged. Due to numerical scaling issues, it was found that better convergence was achieved when the lateral acceleration input was scaled by a factor approximately equal to the weight of the sprung mass. For the vehicles tested, `fsolve` usually converges to a solution in less than 10 iterations and typically does not converge beyond 20 iterations. To speed overall code execution, a 20 iteration limit was established. Solution points that that do not converge are flagged for removal from the solution set at a later step.

The results of the converged numerical solution are used to calculate the FMM pa-

rameters.

$$F_y = \sum_{n=1}^{4} \left(F_{x_n} \sin\alpha_n + F_{y_n} \cos\alpha_n\right) \tag{3.45}$$

$$\begin{aligned} N = {} & \textstyle\sum_{n=1}^{2} \left(F_{x_n}(\ell - x_{CG}) \sin\alpha_n + F_{x_n} t_n \cos\alpha_n + F_{y_n}(\ell - x_{CG}) \sin\alpha_n + F_{y_n} t_n \cos\alpha_n\right) \\ & + \textstyle\sum_{n=3}^{4} \left(F_{x_n} x_{CG} \sin\alpha_n + F_{x_n} t_n \cos\alpha_n + F_{y_n} x_{CG} \sin\alpha_n + F_{y_n} t_n \cos\alpha_n\right) \end{aligned} \tag{3.46}$$

The forces and moments are then repeated over a range of values of longitudinal acceleration. This iteration through A_x is necessary due to the non-linear relation between the tire lateral and longitudinal forces and is the reason for the requirement of a combined-slip tire model [10]. Creation of maps for cases other than the basic 'road load' or $A_x = 0$ case allows for accurate modeling of the vehicle in realistic driving maneuvers. In many autonomous systems, vehicle stability limits are rarely reached except in situations such as obstacle avoidance when it is unlikely that a constant speed will be maintained. As can be seen in Figure 3.5, the force-moment envelope can change dramatically due to the total force limitations defined by the friction ellipse.

Once the force-moment maps are calculated for the range of accelerations, they can then be transformed into the desired variables for the manifold definition by introducing speed. It is intuitively obvious that the maneuverability manifold of a vehicle changes as a result of speed with maneuverability generally decreasing at higher speeds. Under the assumptions used in deriving this model, however, the force generating characteristics of the tires are speed independent, allowing the use of the same force-moment map across all speeds. The maneuverability dependence on speed occurs in the transformation between force-moment coordinates and curvature-curvature rate coordinates.

The curvature (κ) can be calculated directly from the lateral force using the assump-

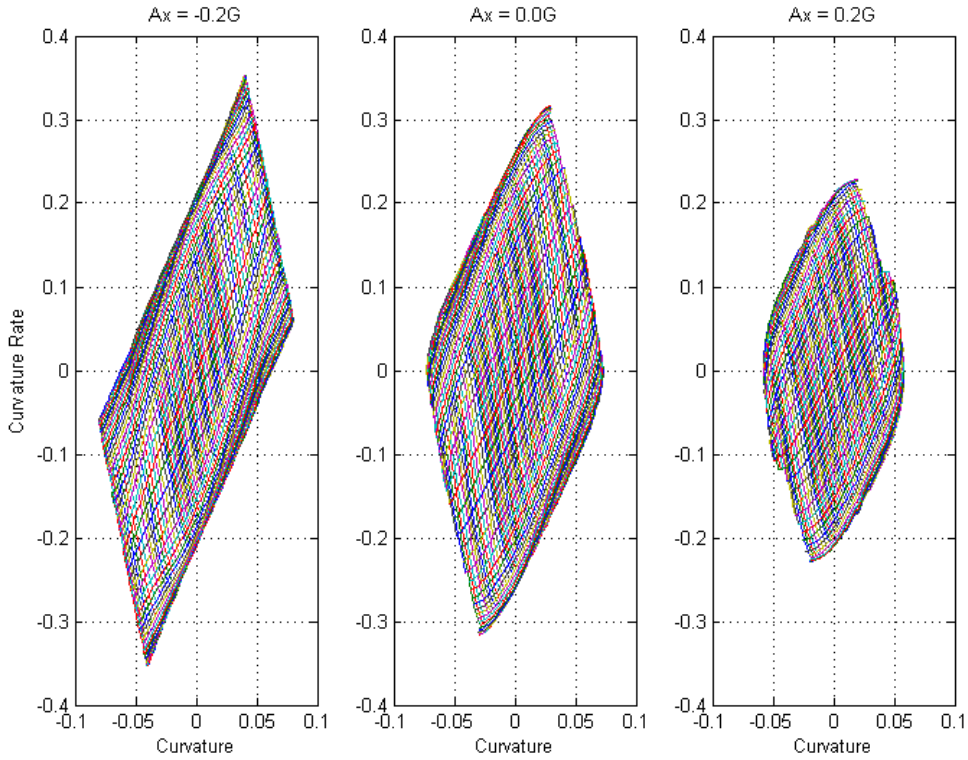

Figure 3.5: FMM map for range of A_x. Note that the maneuvering area changes significantly as A_x is varied from $-0.2G$ (left) to $0.2G$ (right).

tion that all of the lateral force is required to react the centripetal force:

$$\kappa = \frac{F_y}{V_i^2 M} \tag{3.47}$$

Since the yaw moment of inertia is an estimated parameter and is allowed to vary, the turning moment cannot be resolved immediately into a static value of curvature rate ($\dot{\kappa}$). Instead the moment is non-dimensionalized by Eq. 3.48 to produce a quantity (C_n) that can be converted into a curvature rate at a later stage:

$$C_n = \frac{N}{W\ell} \tag{3.48}$$

Once the yaw moment has been determined for a specific vehicle configuration using Eq. 3.15, an expression can be derived to transform C_n into a curvature rate:

$$\frac{N}{I_z} = \frac{C_n W \ell}{I_z} = \ddot{\theta} = \frac{d}{dt}(V_x \kappa) \tag{3.49}$$

$$\frac{C_n W \ell}{I_z} = \dot{V}_x \kappa + V_x \dot{\kappa} \tag{3.50}$$

$$\dot{\kappa} = \left(\frac{C_n W \ell}{I_z} - \dot{V}_x \kappa \right) \frac{1}{V_x} \tag{3.51}$$

After calculation of the curvatures, it becomes desirable to convert the constant α_f and α_r lines used to generate the map into the more useful coordinates of δ and β. To perform this conversion, the $\kappa - \hat{\dot{\kappa}}$ space is resampled using the MATLAB `interp1` function to perform a piecewise cubic hermitian interpolation on each variable. Since the vehicle frame is located at the rear-axle, α_r and β become identically equal. To calculate δ, kinematics can be used to derive [10]:

$$\delta = \arctan(\ell / R) + \alpha_r - \alpha_f \tag{3.52}$$

The final step in the MATLAB FMM implementation is to perform a clean-up of the 2-D maneuvering envelopes. It is possible for a vehicle, once it passes its frictional limits, to achieve a state with the same curvature and curvature rate at a higher set of slip angles. This state can be visualized if one considers that it is sometimes possible for a skilled driver to navigate a corner either in a controlled turn below the limit or in a slide at a more extreme angle. While these states may be valid, they are generally undesirable for autonomous vehicle operation and can cause numerical issues in solvers. Therefore an algorithm is applied to remove all points at which the total force is greater than or equal to the COF times the vehicle weight, which represents states in which the vehicle is in a four-wheel slide. Additionally, the maximum slip angles that represent inflection points

are identified and data beyond the inflection point are eliminated along with points at which the numerical solver did not converge. An example of the raw versus clean data is shown in Figure 3.6.

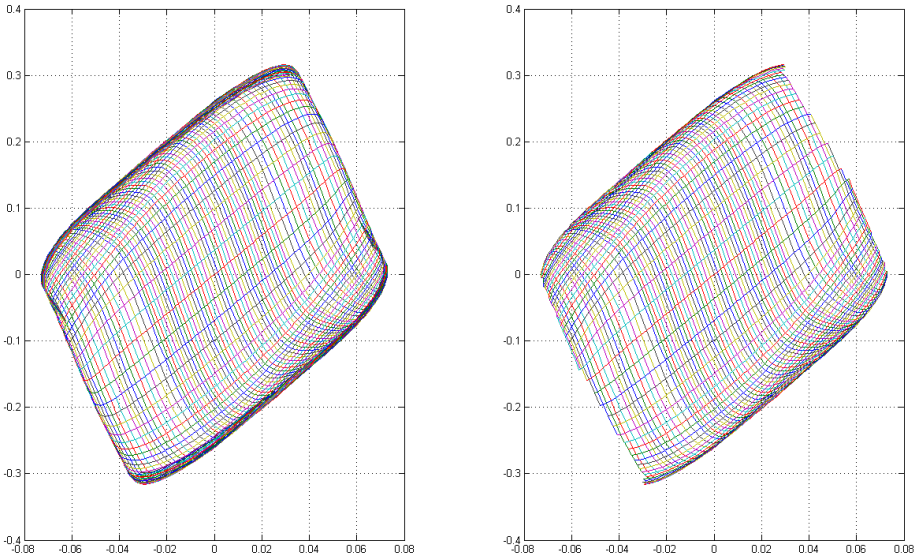

Figure 3.6: Example of raw (left) versus cleaned (right) FMM data. Note the overlap of the δ and β lines on the upper and lower edges of the raw data plot.

3.4 Modeling Summary

The vehicle model formulated in this chapter is intended to provide an adaptable representation of a standard four-wheeled, Ackerman-steered vehicle. The model can be expressed in terms of FMM maps calculated across different ranges of variables. These maps will be used in Chapter 5 to develop a method for predicting IMMs. The validity of the model will be tested against simulation and the results shown in Chapter 6.

Chapter 4

Parameter Estimation

I, at any rate, am convinced that [God] does not throw dice.

–Albert Einstein, 1936 [95]

A key concept in this work is the idea that critical parameters of most real autonomous vehicles cannot be known *a priori*. In many cases, these parameters are dictated by the terrain that the vehicle is operating on and necessarily change with time as the vehicle traverses into new areas. In other cases, these parameters are dictated largely by vehicle payloads. In realistic environments the magnitude and distribution of these payloads will be known only with a significant degree of uncertainty. To address this issue, it is desirable to define a method for estimating the key parameters of the vehicle from a knowledge of dynamics and use of the internal sensors.

They key parameters required for implementation of the IMM are the load state of the vehicle and the condition of the tire-ground interface. The load state will be defined by the total mass of the vehicle and the location of the CG in the x, y, and z axes. It will be assumed that the vehicle has been sufficiently characterized such that the mass and load distribution of the empty vehicle are known and that these parameters can be

upper-bounded by knowledge of maximum realistic values. The tire-ground interface will be characterized by a single coefficient of friction parameter that defines the maximum available tire force for a a given normal force.

4.1 Estimation Overview

The goal of parameter estimation in this work is to fuse the large amount of data available from the sensors on autonomous systems to produce an estimate of the parameters relevant to IMM generation. This task can be separated into three parts: determination of CG location, estimation of the forces acting at the wheels, and estimation of the COF at the tire/ground interface.

4.1.1 Measured States

Due to the requirements of autonomous navigation it can generally be assumed that, as a consequence of removing the operator, an autonomous vehicle will be equipped with a much greater array of sensors than those found on a manned vehicle. These sensors will also typically have much greater accuracies and lower uncertainties than those on manned vehicles. To a large extent, this integrated sensor suite removes many of the restrictions faced by researchers cited in Section 2.3 as many states can be measured directly enough to obviate the need for a dedicated observer.

For purposes of this work, it will be assumed that the vehicle is equipped with the following sensors: 6-axis IMU, GPS, steering angle sensor, and wheel encoders. Further, it is assumed that the IMU and GPS data is fused into a comprehensive Pose-Estimation System (PES). Although many of these sensors are complicated and expensive, they are typically required for autonomy and are generally found on autonomous vehicles [2] [7] [14] [96]. The states assumed to be available from these sensors are enumerated in

Table 4.1.

Table 4.1: Measured Vehicle States

Symbol	Parameter Name	Sensor
A_x	Longitudinal acceleration	IMU
A_y	Lateral acceleration	IMU
δ	Steering angle	Encoder
V_x	Longitudinal velocity	PES
V_y	Lateral velocity	PES
ω_n	Rotational velocity of wheel-n	Encoder
z_{wn}	Suspension displacement for wheel-n	SPS
ϕ	Sprung mass roll angle	PES
ψ	Sprung mass pitch angle	PES
θ	Yaw angle	PES
$\dot{\phi}$	Sprung mass roll rate	IMU
$\dot{\psi}$	Sprung mass pitch rate	IMU
$\dot{\theta}$	Yaw rate	IMU
τ	Steering torque	Actuator

Additionally, the task of force estimation is greatly eased by the use of Suspension Position Sensor (SPS)s. This sensor measures the linear displacement between the sprung and unsprung masses at each wheel. This type of sensor is becoming increasingly available on OEM vehicles as part of systems such as Dynamic Stability Control (DSC) and semi-active suspension and is often implemented through use of a rotary or linear potentiometer as shown in Figure 4.1. These sensors are also typically fairly easy to retrofit onto existing vehicles. Knowledge of the suspension displacement, combined with knowledge of the suspension compliance characteristics allows much more direct observation of the normal forces, especially in static or quasi-static motion states, as shown in Section 4.2.2.

4.1.2 Vehicle Parameters

In order to estimate the desired temporally varying parameters, certain key parameters of the autonomous vehicle can be known *a priori*, as outlined in Table 4.2. In most cases, it is reasonable to assume that the configuration of the unloaded vehicle can be known

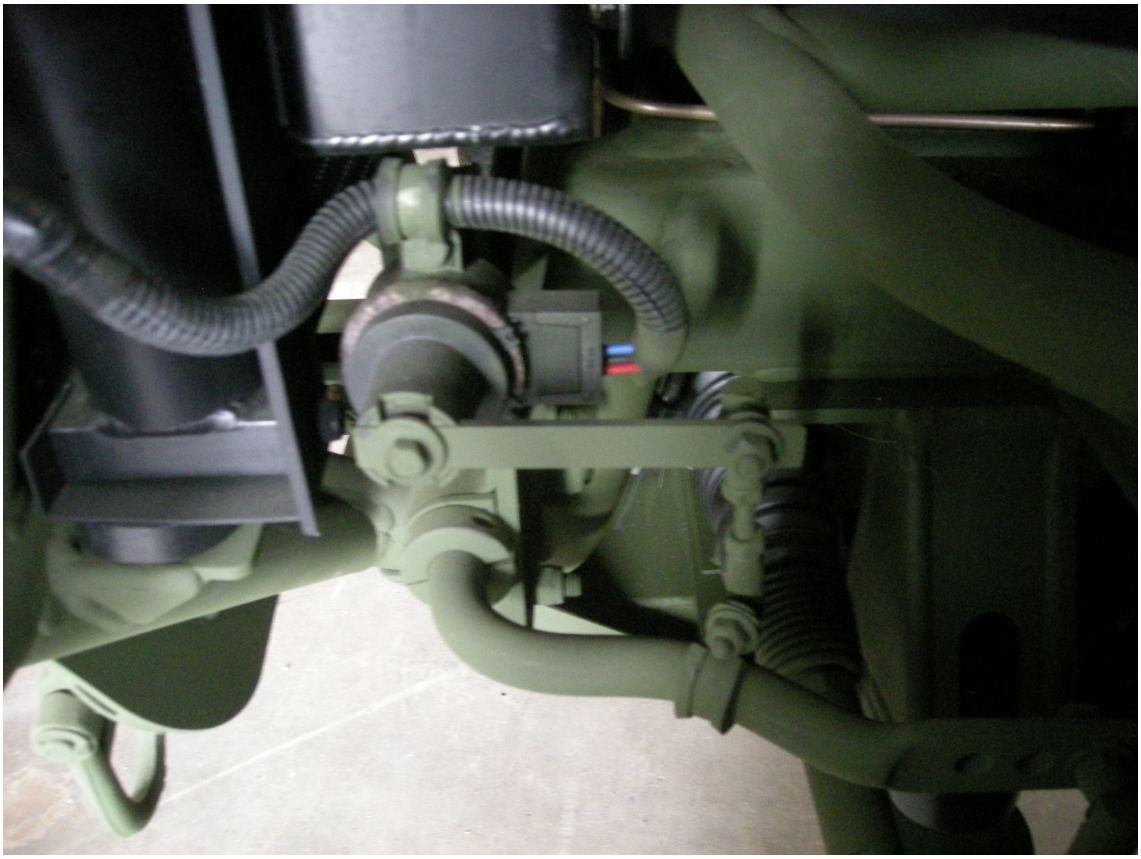

Figure 4.1: Example of a suspension position sensor on an OEM vehicle.

fairly precisely. These parameters can be separated into three groups: tire parameters, suspension parameters, and mass parameters.

Tire Parameters

As discussed in Chapter 3, tire parameters will be represented using a combined-slip Fiala model. This model relies on two linear coefficients of tire performance, a cornering stiffness C_α, and traction coefficient C_S. The cornering stiffness determines the generation of lateral forces per unit of slip angle and the traction coefficient determines the longitudinal forces per unit of slip angle, resulting in force profiles such as that shown in Figure 3.3. These parameters are typically also dependent on tire normal loads [26].

These parameters would ideally be obtained through use of a tire test rig, as shown in

Table 4.2: Known Vehicle Parameters

Symbol	Parameter Name
C_α	Linear tire cornering stiffness
C_S	Linear tire traction coefficient
c_ϕ	Roll damping coefficient
k_ϕ	Roll stiffness coefficient
ℓ	Wheelbase of vehicle
M_e	Mass of the empty total vehicle
m_{s_e}	Mass of the empty sprung mass
t_n	Track width of axle-n
x_{CG_e}	Longitudinal empty vehicle CG offset from vehicle frame
y_{CG_e}	Lateral empty vehicle CG offset from vehicle frame
z_{CG_e}	Vertical empty vehicle CG offset from vehicle frame
z_{RC}	Roll center height from vehicle frame

Figure 4.2, in which the slip angles, slip ratios, and tire loads can be varied and the forces measured precisely. In practice, such data and test rigs are often not available and the coefficients must be estimated from performance data. Several methods for performing this type of estimation on real vehicles are presented in Section 2.3.

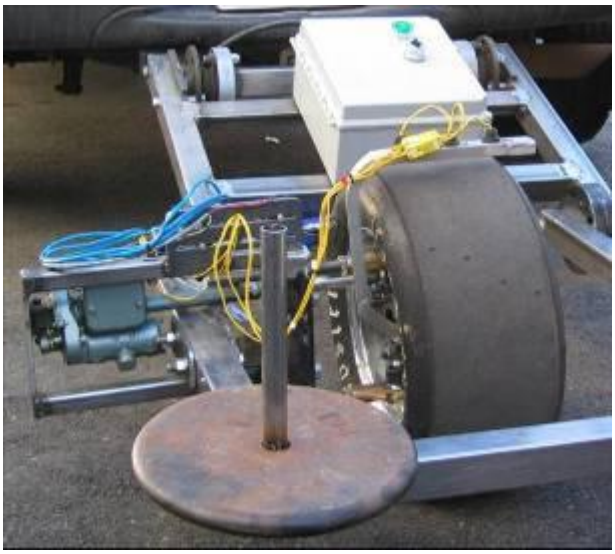

Figure 4.2: Example of a tire test rig for determining tire parameters [97].

The VehicleSIM model used for this work uses a much more sophisticated Pacejka tire model to simulate tire performance. As a result, the linear Fiala tire parameters on

the simulated model are unknown. To determine these parameters, the vehicle was run through a series of maneuvers designed to isolate the particular parameters. To test cornering stiffness, the vehicle was driven in a 500-ft circle at a constant speed of 40kph to generate conditions of constant lateral force and constant slip angle. To test the dependence on friction coefficient, the test was repeated using different simulated coefficients of friction. The cornering coefficient can then be calculated by applying:

$$C_\alpha = -\frac{F_y}{\alpha F_z} \tag{4.1}$$

The resulting data points are plotted in Figure 4.3 for each individual wheel. Note that except at extremely low COFs, where the vehicle is not really capable of maintaining the maneuver, the cornering coefficient can be considered independent of friction coefficient. It can be noted, however that there is a dependence on normal load. This dependence is roughly linear ($R^2 = 0.84$) and thus the cornering coefficient can be approximated for wheel-n by:

$$C_{\alpha_n} = 16000\, N/rad \left(\frac{F_{z_n}}{Mg}\right) \tag{4.2}$$

To determine the traction coefficient, a similar procedure was used. The vehicle was drive in a straight line and then it was braked from 50-0 kph in 15 seconds. Tests were performed over a range of COFs to test friction dependency. The traction coefficient can then be calculated using:

$$C_{S_n} = \frac{F_x}{SF_z} \tag{4.3}$$

The resulting traction coefficient is plotted as a function of COF in Figure 4.4 for the individual wheel loads. No results were obtained at extremely low COFs due to the wheels

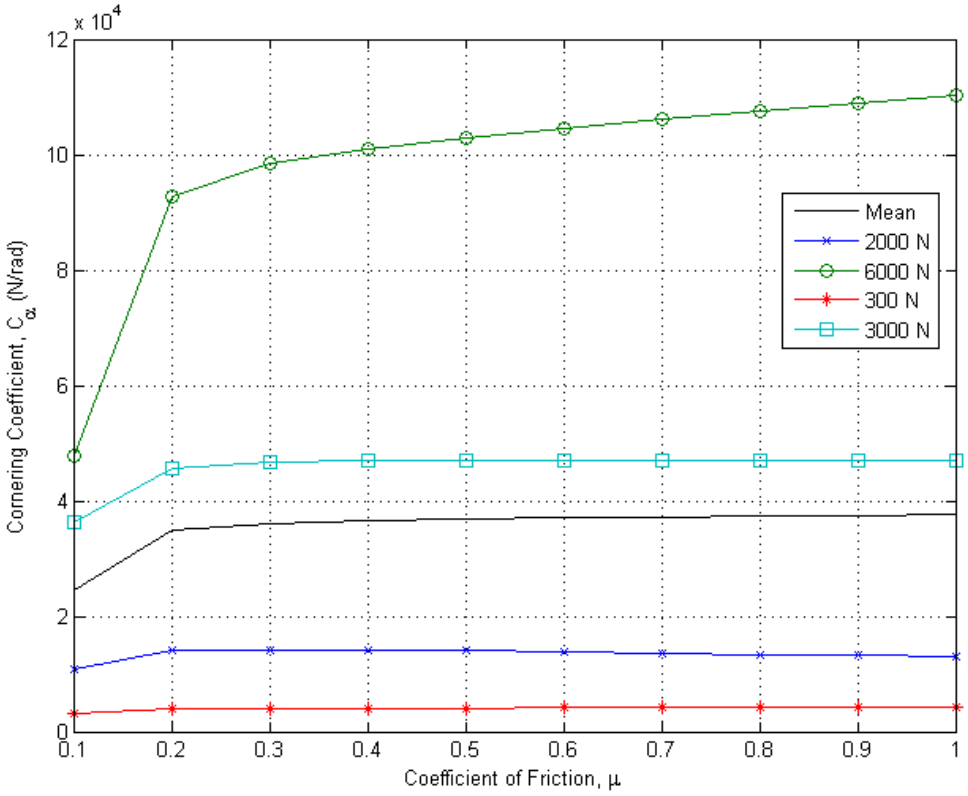

Figure 4.3: Plot of C_α vs. μ for individual wheel loads from estimation test.

locking and the vehicle entering a sliding state, rendering the slip ratio undefined. It can be noted that within the valid range, the dependence on friction coefficient is slight and will thus be neglected. The dependence on normal load is almost perfectly linear ($R^2 = 0.99$) and thus the traction coefficient for the simulated set of tires can be approximated for wheel-n by:

$$C_{S_n} = 28000\,N\left(\frac{F_{z_n}}{Mg}\right) \tag{4.4}$$

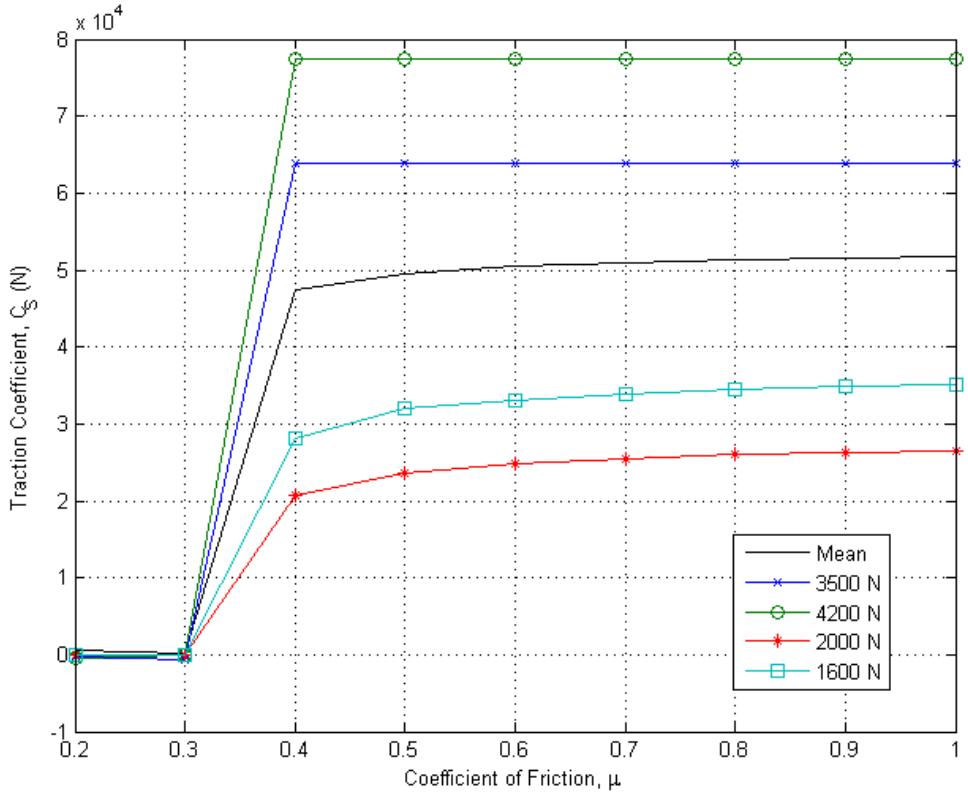

Figure 4.4: Plot of C_S vs. μ for individual wheel loads from estimation test.

Suspension Parameters

Determination of suspension parameters is very heavily dependent on the exact suspension configuration of the vehicle. Common configurations include independent configurations such as dual wishbones and McPherson struts and coupled configurations such as beam axles. Many vehicles utilize different configurations on the front and rear. Due to the extreme range of possible configurations, an example will be provided but all possible options will not be discussed. For further discussion of suspension configurations, the reader is referred to Milliken [10].

One of the key suspension parameters is the roll center. The roll center can be defined as the point at which a lateral force applied to the sprung mass does not induce roll [10].

Typical vehicles will have differing roll center heights in the front and rear. The line connecting these points is known as the roll axis and for purposes of this work will be modeled as a revolute joint coupling the sprung and unsprung masses. In most real configurations, the locations of the roll centers are not static and change with roll and jounce movement of the suspension. However, for purposes of this work a reasonable approximation will be achieved by assuming a constant roll center height and centerline location of the roll center for both ends of the vehicle.

The roll can be determined kinematically by first determining the location of the instant center of the suspension linkages. A line can then be plotted from the center of tire contact to the instant center. The intersection of these lines for both sides of the suspension determines the roll center location. An example of this kinematic determination is shown in Figure 4.5. For the VehicleSIM model used, determination of the roll center was unnecessary as the static roll center location is an input used to determine suspension deflection characteristics.

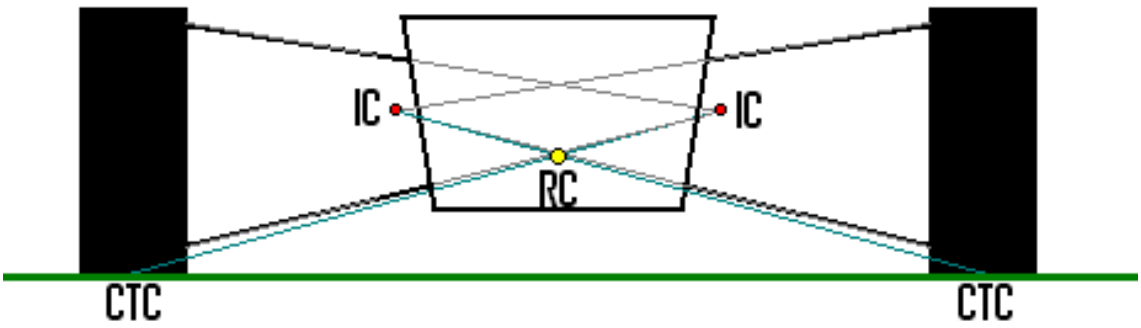

Figure 4.5: Determination of the kinematic roll center for a short-long arm suspension.

Another important characteristic of the suspension system is the values of the springs and dampers that connect the sprung and unsprung masses. In conjunction with the suspension kinematics, these components largely control the movement and force transfer

between the sprung mass and the wheels. In a real suspension system, the effective values of the compliance and damping are determined by many factors including: main springs, primary dampers, tire compliances, tire damping, bushing compliances, suspension link compliances, and frame compliance. As noted in Chapter 3, the effects of most of these factors are small. Since it is assumed that a detailed analytic model of these components is not available, only the effects of the main springs, shock absorbers, and tire compliances will be considered.

The most accurate method for determining the characteristics of the these components is the remove them from the vehicle and test them on dedicated test rigs, as shown in Figure 4.6. Determination of these values for vehicles in which suspension disassembly is not practical and for which OEM values are not available is theoretically possible by analyzing performance data. However, development of these techniques is beyond the scope of this work and will be left for future work.

Once the values of the physical springs and dampers are known, it is necessary to convert these values into effective roll values. The first step in this conversion is to correct for the installation ratio of the suspension to produce a ride rate. The installation ratio is caused by the fact that springs and dampers are typically mounted inboard of the wheels. Thus, a suspension deflection at the wheel results in a smaller deflection at the location of the force component and can be corrected, as derived by Milliken [10]:

$$k_{w_s} = k_s(IR)^2 \tag{4.5}$$

$$c_w = c_s(IR)^2 \tag{4.6}$$

The wheel rate due to the main spring must then be combined with the tire rate to generate

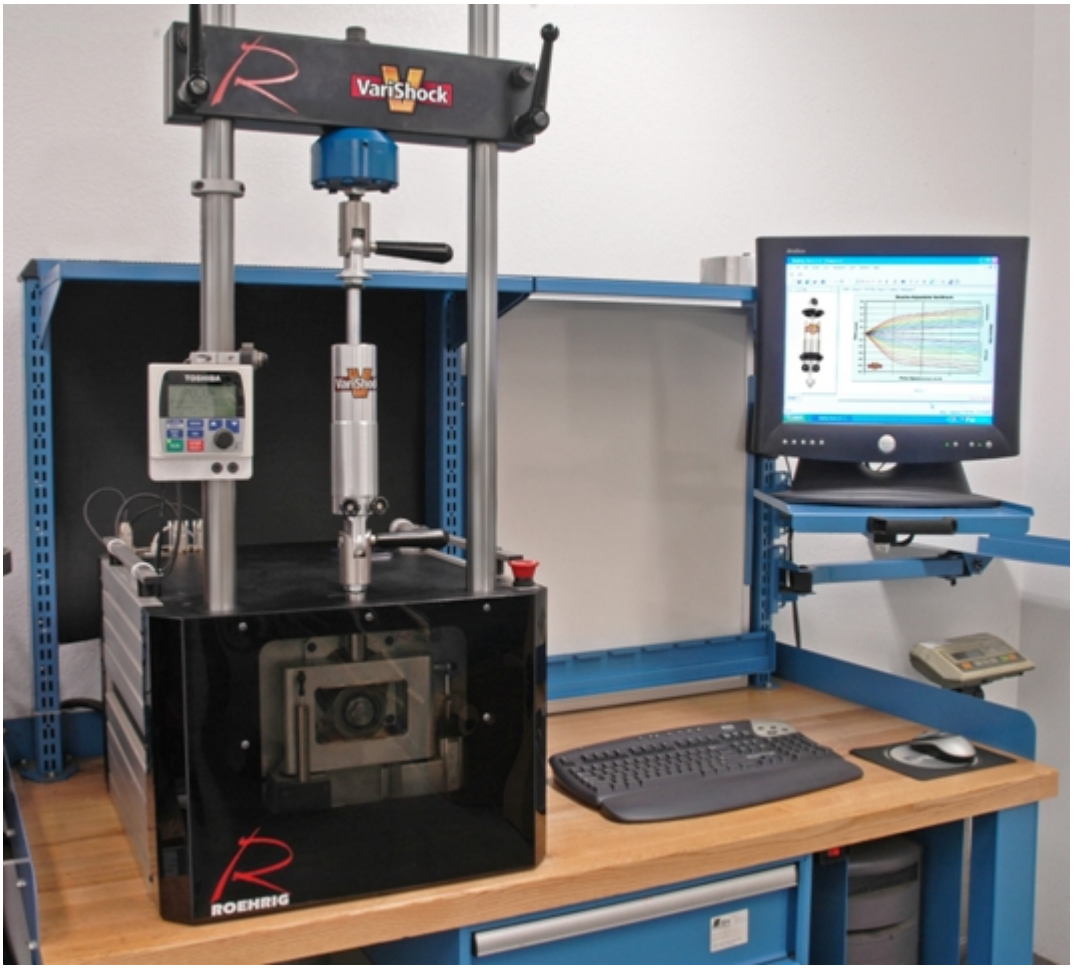

Figure 4.6: Example of a damper dynamometer [98]

a total ride rate using the standard formula for springs in series as given by:

$$\frac{1}{k_w} = \frac{1}{k_{w_s}} + \frac{1}{k_t} \tag{4.7}$$

These rates can then be transformed kinematically into a total roll rate by using the small angle approximation and the formula, derived by Will and Zak, given by [20]:

$$k_\phi = \frac{1}{2}\left(k_{w_1} t_F^2 + k_{w_2} t_R^2\right) \tag{4.8}$$

$$c_\phi = \frac{1}{2}\left(c_{w_1} t_F^2 + c_{w_2} t_R^2\right) \tag{4.9}$$

Mass Parameters

The mass parameters of the unladen vehicle are important to provide lower bounds on the estimated mass and CG parameters. Determination of the unladen mass is trivial provided a scale of sufficient capacity is available as the vehicle can simply be weighed in its lightest configuration. Measurement of the CG location is more involved, but is straightforward provided a set of four wheel scales can be obtained. A full description of the procedure can be found in Milliken, but it generally involves using wheel weights on level ground to calculate the x_{CG} and y_{CG} locations followed by raising one end of the vehicle to induce load transfer sufficient to calculate z_{CG} [10].

4.1.3 Estimated Parameters

The key vehicle parameters to be estimated are determined by the inputs to the IMM formulation. These parameters, as identified in Table 4.3, represent the expected time varying components of the autonomous system. The mass and CG parameters are expected to change as the cargo load in the vehicle changes. The magnitude and distribution of this cargo cannot be known *a priori*, however it can be assumed in most cases that the cargo load will not change significantly unless the vehicle is at rest. The primary exception to this assumption would be changes in fuel load; this can be considered negligible except in situations such as ultra-high performance racing that are beyond the scope of this work. In contrast to the mass parameters, it is expected that the coefficient of friction may vary rapidly and independently of vehicle state.

4.1.4 Estimation Structure

To achieve the estimation goals outlined above a structure was developed to integrate the various desired aspects. The estimation tasks are divided into three main parts: force es-

Table 4.3: Estimated Vehicle Parameters

Symbol	Parameter Name
m_c	Mass of cargo on sprung mass
μ	Tire-ground coefficient of friction
x_{CG}	Longitudinal CG offset from vehicle frame
y_{CG}	Lateral CG offset from vehicle frame
z_{CG}	Vertical CG offset from vehicle frame

timation, CG estimation, and friction estimation. Figure 4.7 shows the data flow between the three main parts. The outputs from the CG estimation and friction estimation blocks are applied to generate the IMMs using the methods outlined in Chapter 5.

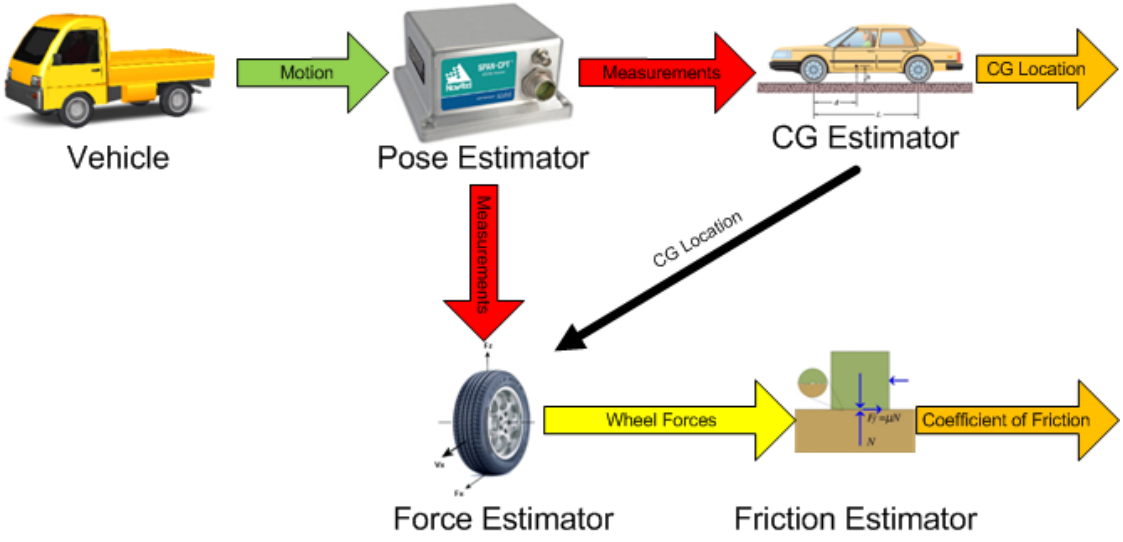

Figure 4.7: Diagram of estimation structure showing the different components. The output of the total estimation system is the location of the CG and the current estimate of the COF.

4.2 Force Estimation

In order to estimate the desired parameters, it is necessary to have knowledge of both the normal forces acting on the tires and the lateral and longitudinal forces generated by the tires. While it is possible to construct transducers capable of measuring these forces

directly, such devices are typically extremely expensive and are really only suitable for experimental vehicles [99]. It is therefore desirable to develop a method for estimating these forces using more readily available sensors.

4.2.1 Unscented Kalman Filter

In real applications, noise-free data sets do not exist and a method must exist to handle noise in both the measurements and the process itself. The standard methodology for deriving a best estimate of a variable in a noisy environment is the Kalman filter. Other methods exist, as outlined in Section 2.3, but a variant of the Kalman filter known as the Unscented Kalman Filter has been selected for force estimation. The primary advantage of the UKF over the other major non-linear form of the Kalman filter is that the UKF is a 'derivative-free' filter in that it does not require direct analytical computation of the derivatives in the Jacobian. This is advantageous for the force estimation problem as the derivatives of the relevant equations are difficult to derive analytically.

The UKF is a non-linear extension of the basic linear Kalman filter. The UKF takes its name from the unscented transform used to approximate the variable distributions. This transform uses deterministic 'sigma points' to probe the covariance of the variable Gaussians. The significant difference between the unscented transform and Monte Carlo type transforms is that the sigma points are determined deterministically. For a Gaussian with dimension n, estimated mean $\hat{x}$ and covariance Σ, a total of $2n+1$ sigma points are generated [3].

$$\chi^{[0]} = \bar{x} \tag{4.10}$$

$$\chi^{[i]} = \bar{x} + \left(\sqrt{(n+\lambda)\Sigma}\right)_i \; for\; i = 1,...,n \tag{4.11}$$

$$\chi^{[i]} = \bar{x} - \left(\sqrt{(n+\lambda)\Sigma}\right)_{i-n} \; for\; i = n+1,...,2n \tag{4.12}$$

The parameter λ is set based on scaling parameters chosen to control the distribution of the sigma points from the mean. The standard form for λ is given by [3]:

$$\lambda = \alpha^2(n+\kappa) - n \tag{4.13}$$

where α is usually chosen to be a small positive number $(0.1 < \alpha < 0.001)$ and κ is typically chosen such that $\kappa = 3-(2n+1)$ [100]. Also associated with the sigma points are weights that are used to recover the mean and covariance estimates. These weights are typically given by [3]:

$$\omega_m^{[0]} = \frac{\lambda}{n+\lambda} \tag{4.14}$$

$$\omega_c^{[0]} = \frac{\lambda}{n+\lambda} + (1-\alpha^2+\beta) \tag{4.15}$$

$$\omega_m^{[i]} = \omega_c^{[i]} = \frac{1}{2(n+\lambda)} \; for \; i = 1,...,2n \tag{4.16}$$

where β is a parameter used to represent knowledge about the underlying distribution. For a Gaussian distribution, which is inherently assumed for an UKF, $\beta = 2$ can be shown to be the optimal choice [3].

The non-linear state transition function, $f(x)$, and measurement function, $h(x)$ can then be evaluated at each sigma point. The weights are then applied by [3]:

$$\hat{x}_t = \sum_{i=0}^{2n} w_m^{[i]} f(\chi_{t-1}^{[i]}) \tag{4.17}$$

$$\hat{\Sigma}_t = \sum_{i=0}^{2n} w_c^{[i]} (f(\chi_{t-1}^{[i]}) - \hat{x}_t)(f(\chi_{t-1}^{[i]}) - \hat{x}_t)^T + P_t \tag{4.18}$$

$$\hat{z}_t = \sum_{i=0}^{2n} w_m^{[i]} h(\chi_{t-1}^{[i]}) \tag{4.19}$$

$$\hat{S}_t = \sum_{i=0}^{2n} w_c^{[i]} (h(\chi_{t-1}^{[i]}) - \hat{z}_t)(h(\chi_{t-1}^{[i]}) - \hat{z}_t)^T + Q_t \tag{4.20}$$

where P_t represents the estimated process noise and Q_t represents the estimated measurement noise. This determines the unscented transform estimate of the state transition and measurement distributions.

Once the state transition and measurement estimates have been computed, the optimal UKF estimate can be calculated by computing the Kalman gain [3]:

$$K_t = \Sigma_t S_t^{-1} \tag{4.21}$$

Note that the matrix inversion required in this step is most computationally expensive operation in the application of the UKF. As a result of this inversion, the computational complexity of the UKF scales roughly with the number of states as O^3 [3]. This gain is then applied to the measurement innovation, $(z_t - \hat{z}_t)$, to produce the new estimated mean [3]:

$$x_t = \hat{x} + K_t(z_t - \hat{z}_t) \tag{4.22}$$

The covariance can then be updated to produce a new covariance estimate [3]:

$$\Sigma_t = \hat{\Sigma}_t - K_t S_t K_t^T \tag{4.23}$$

Note: The UKF equations in this section are obtained from Thrun's and Haykin's works. More complete derivations of these equations can be found in those works [3] [100].

4.2.2 UKF Formulation

Implementation of the UKF-based force estimator first requires definition of a state vector. The states of interest are the lateral, longitudinal, and vertical forces at the wheels of

the vehicle. Unlike the standard linear Kalman filter, the UKF does not require all variables to be contained within the state vector. This allows for the selection of a minimal representation of the state vector consisting of only the desired states. The choice of a minimum state vector reduces the computational requirements of the implementation as the computational complexity of the UKF scales with O^3 of the number of states.

Another important consideration for the selection of the state vector is its usage in friction estimation. As the generation of tire forces is partially regulated by the COF, it becomes possible for a positive feedback loop to form in the overall parameter estimation structure where an increase in the estimated COF causes the estimated tire forces to increase, resulting in a further increase in the COF. This interconnection can result in a divergent estimator that produces physically unrealizable estimates for the COF. It is therefore desirable to develop a force estimator that does not depend on the COF.

The prediction-update structure of the Kalman filter lends itself well to the use of a relatively simple model in the prediction stage. Although this will result in prediction errors, the measurement update can be used to correct for these errors, particularly if the iteration rate of the UKF is significantly faster than the dynamics of the system. Therefore, to achieve the goal of a COF independent state transition model, a simple bicycle representation will be used for prediction of the lateral and longitudinal forces while a four-wheel model will be used for prediction of the vertical forces. This representation leads to the state vector:

$$x = \begin{bmatrix} x_1 \\ x_2 \\ x_3 \\ x_4 \\ x_5 \\ x_6 \\ x_7 \\ x_8 \end{bmatrix} = \begin{bmatrix} F_{x_F} \\ F_{x_R} \\ F_{y_F} \\ F_{y_R} \\ F_{z_1} \\ F_{z_2} \\ F_{z_3} \\ F_{z_4} \end{bmatrix} \tag{4.24}$$

where the subscripts F and R represent the front and rear wheels of the bicycle representation and the F_{z_n} represent the weights on the individual wheels of the four-wheel model.

Once the state vector has been defined, the UKF requires definition of two functions: a state transition function, $f(x,u)$, and a measurement function, $h(x,u)$. The state transition function calculates the predicted change in the state vector due to the dynamics of the system and the measurement function calculates the expected value of the measurements to allow calculation of the innovation. Both functions are dependent on both the state vector, x, and the exogenous input vector, u, that provides a mechanism for incorporating additional information not contained within the state vector.

The astute reader will note that the state vector does not include any of the measured states such as the accelerations and velocities as are commonly included in similar observers implemented in the literature. Normally the inclusion of such states is required in order to filter and correct for biases present in real sensor readings. This exclusion is possible due to the assumption that the autonomous vehicle is already performing these tasks as part of the PES. This is a generally safe assumption as a PES is a requirement for

autonomous navigation. It can therefore be assumed that, for the purposes of force estimation, the measurements from the PES are the most accurate available measurements of the states that they represent and that further processing is unlikely to significantly improve the estimates. Therefore, the measured states, outlined in Table 4.1, form the exogenous input vector:

$$u_t = \begin{bmatrix} u_{1_t} \\ u_{2_t} \\ u_{3_t} \\ u_{4_t} \\ u_{5_t} \\ u_{6_t} \\ u_{7_t} \\ u_{8_t} \\ u_{9_t} \\ u_{10_t} \\ u_{11_t} \\ u_{12_t} \\ u_{13_t} \\ u_{14_t} \\ u_{15_t} \\ u_{16_t} \\ u_{17_t} \end{bmatrix} = \begin{bmatrix} A_{x_t} \\ A_{y_t} \\ V_{x_t} \\ V_{y_t} \\ \dot{\theta}_t \\ \dot{\phi}_t \\ \dot{\psi}_t \\ \theta_t \\ \phi_t \\ \psi_t \\ \tau_t \\ \omega_{1_t} \\ \omega_{2_t} \\ \omega_{3_t} \\ \omega_{4_t} \\ \delta_t \\ A_{u_t} \end{bmatrix} \tag{4.25}$$

It is important to note that the u vector is expressed in the CG coordinate frame, not the measurement frame. Before the vector is constructed, it is first necessary to transform the acceleration and velocity components from one frame to the other. These transformations

can be performed by applying the standard rigid body vector transform equations [101]:

$$V_{CG} = \omega \times r + V_{RA} \tag{4.26}$$

$$A_{CG} = \omega \times (\omega \times r) + A_{RA} \tag{4.27}$$

where r is the vector between the two coordinate frames defined by $r = -[x_{CG}, y_{CG}, z_{CG}]$ and all other quantities are vectors. Also note that the transverse acceleration is neglected as no measurement of the angular acceleration is available and that the Coriolis term is assumed to be zero.

State Transition Function

As previously noted, the state transition function for force estimation is based on a hybrid bicycle/four-wheel model representation of the vehicle. The vertical force estimation component relies on the model developed in Section 3.2 to calculate the vertical forces at each wheel. Specifically, Eqs. 3.25-3.41 can be reformulated with the substitutions:

$$A_x = u_1 \tag{4.28}$$

$$A_y = u_2 \tag{4.29}$$

$$F_{z_1}, ..., F_{z_4} = x_5, ..., x_8 \tag{4.30}$$

This set of equations produces a quasi-static approximation of the true state transition function for weight transfer. Due to the implementation method using the exogenous input vector to provide current input values, the output of these transition equations produces the desired result: the state of the vertical forces at time t.

The state transition function for the longitudinal and lateral forces without inclusion of the COF requires use of a bicycle representation. The bicycle model, as shown in

Figure 2.1, combines the front and rear wheels on each side of the vehicle to produce a single track representation. This representation is useful when the states of the individual tires are unable to be or not desired to be separated from the total axle forces.

In this case it is not necessary to fully develop a detailed model, such as those in Section 2.2.1. Instead two exogenous control inputs, the desired acceleration, A_u, and the steering angle, δ, will be used to predict the vehicle states. The desired acceleration can be obtained from either direct measurements of the pedal inputs or the output of the autonomous speed controller and is considered to be an indication of the total longitudinal force. If this value is obtained from direct measurements of the pedal positions, it is necessary to know the (probably non-linear) transfer function between the pedal position and the resulting acceleration. As this information would typically already be encoded in the autonomous speed controller, use of an output from this module is recommended.

Once the desired acceleration, A_{u_t} has been obtained, the value can be simply multiplied by the estimated mass, M, to obtain an estimated total longitudinal force, $\hat{F}_{x_t}$. It then becomes necessary to estimate the distribution of the force between the front and rear axles. This distribution is heavily dependent on the drive configuration of the vehicle and whether engine torque or braking torque is being applied to the wheels. Assuming the drive configuration is known, the force distribution can be estimated by the piecewise function:

$$\hat{F}_{x_{F_t}} = \begin{cases} (1-\eta_B)\hat{F}_{x_t}\left(\frac{F_{z_{1_{t-1}}}+F_{z_{2_{t-1}}}}{Mg}\right), & A_{u_t} \leq A_{u_{crit}} \\ (1-\eta_D)\hat{F}_{x_t} - C_r\left(F_{z_{1_{t-1}}}+F_{z_{2_{t-1}}}\right), & A_{u_t} > A_{u_{crit}} \end{cases} \tag{4.31}$$

$$\hat{F}_{x_{R_t}} = \begin{cases} \eta_B\hat{F}_{x_t}\left(\frac{F_{z_{3_{t-1}}}+F_{z_{4_{t-1}}}}{Mg}\right), & A_{u_t} \leq A_{u_{crit}} \\ \eta_D\hat{F}_{x_t} - C_r\left(F_{z_{3_{t-1}}}+F_{z_{4_{t-1}}}\right), & A_{u_t} > A_{u_{crit}} \end{cases} \tag{4.32}$$

where η_B represents the front/rear brake proportionality and η_D represents the drive torque

fraction for engine torque. Both values are allowed to vary between zero and unity with a RWD vehicle having $\eta_D = 1$, a Front Wheel Drive (FWD) vehicle having $\eta_D = 0$ and All Wheel Drive (AWD) vehicles having intermediate values depending on the drive configuration. The value $A_{u_{crit}}$ determines the point at which the change is made from applying engine torque to brake torque. Due to engine braking effects, this value is slightly less than zero for most vehicles but can be approximated by $A_{u_{crit}} = 0$ if it is unknown. This representation is not fully robust for all possible conditions. In particular, it may produce incorrect results on vehicles with complex AWD systems or cases in which the COF varies between the wheels. However, this approximation is reasonably accurate for the operating conditions assumed to be within the scope of this work.

The lateral forces are approximated based on the steering angle input, δ_t. Using a standard kinematic bicycle model, the approximate path curvature of the vehicle can be determined by [10]:

$$\kappa = \frac{\tan(\delta_t)}{\ell(1 + KV_{x_t}^2)} \tag{4.33}$$

where K is referred to as the stability factor or understeer gradient. This coefficient represents the tendency of the vehicle to steer a path curvature greater than that indicated by strict kinematics and can be determined experimentally or analytically derived as shown by Milliken [10]:

$$K = \frac{M}{\ell}\left[\frac{\frac{-(\ell - x_{CG})C_{\alpha_F} + x_{CG}C_{\alpha_R}}{C_{\alpha_F} + C_{\alpha_R}}}{\left(-(\ell - x_{CG})C_{\alpha_F} + C_{\alpha_F}\left(\frac{-(\ell - x_{CG})C_{\alpha_F} + x_{CG}C_{\alpha_R}}{C_{\alpha_F} + C_{\alpha_R}}\right)\right.}\right] \tag{4.34}$$

This curvature can then be used to determine the lateral acceleration and total lateral force:

$$\hat{A}_{y_t} = \kappa V_{x_t}^2 \tag{4.35}$$

$$\hat{F}_{y_t} = \hat{A}_{y_t} M \tag{4.36}$$

Since lateral force generation is controlled primarily by the lateral slip angle, the total force can be proportioned between the two axles as a function of slip angle:

$$\hat{F}_{y_{F_t}} = \begin{cases} 0, & \alpha_F + \alpha_R = 0 \\ \hat{F}_{y_t}\left(\frac{\alpha_F}{\alpha_F + \alpha_R}\right), & \alpha_F + \alpha_R \neq 0 \end{cases} \tag{4.37}$$

$$\hat{F}_{y_{R_t}} = \begin{cases} 0, & \alpha_F + \alpha_R = 0 \\ \hat{F}_{y_t}\left(\frac{\alpha_R}{\alpha_F + \alpha_R}\right), & \alpha_F + \alpha_R \neq 0 \end{cases} \tag{4.38}$$

The last step in formulating the estimates of longitudinal and lateral axle forces is to take into account the coordinate transformation necessary between the tire frame and the vehicle frame due to the steering angle. The final output of tire forces from the state transition function is thus:

$$x_{1_t} = \hat{F}_{x_{F_t}} cos(\delta_t) + \hat{F}_{y_{F_t}} sin(\delta_t) \tag{4.39}$$

$$x_{2_t} = \hat{F}_{x_{R_t}} \tag{4.40}$$

$$x_{3_t} = \hat{F}_{x_{F_t}} sin(\delta_t) + \hat{F}_{y_{F_t}} cos(\delta_t) \tag{4.41}$$

$$x_{4_t} = \hat{F}_{y_{R_t}} \tag{4.42}$$

Measurement Function

The measurement function relates the states to measurable outputs that can then be compared to the measurement vector to generate the measurement innovation. The measure-

ment vector, z, contains significant measurements at the current time and is defined as:

$$z = \begin{bmatrix} z_1 \\ z_2 \\ z_3 \\ z_4 \\ z_5 \\ z_6 \\ z_7 \\ z_8 \\ z_9 \\ z_{10} \end{bmatrix} = \begin{bmatrix} A_x \\ A_y \\ V_x \\ V_y \\ \dot{\theta} \\ \dot{\phi} \\ z_{w_1} \\ z_{w_2} \\ z_{w_3} \\ z_{w_4} \end{bmatrix} \tag{4.43}$$

The z vector needs to be expressed in CG coordinates for convenience and thus must be transformed using Eqs. 4.26-4.27.

The measurement equations can then be formed based on the equations from Section 3.2, starting with the accelerations and velocities:

$$z_{1_t} = \frac{x_{1_t} + x_{2_t}}{M} - u_{4_t} u_{5_t} \tag{4.44}$$

$$z_{2_t} = \frac{x_{3_t} + x_{4_t}}{M} \tag{4.45}$$

$$z_{3_t} = u_{3_t} + \left(\frac{x_{1_t} + x_{2_t}}{M} \right) dt \tag{4.46}$$

$$z_{4_t} = u_{4_t} + \left(\frac{x_{3_t} + x_{4_t}}{M} - u_{3_t} u_{5_t} \right) dt \tag{4.47}$$

where dt is the time interval represented by a single iteration. The yaw rate equation can

then be formulated:

$$z_{5_t} = u_{5_t} + \left(\frac{0.5t_F x_{1_t} + 0.5t_R x_{2_t} + (\ell - x_{CG}) x_{3_t} - x_{CG} x_{4_t}}{I_z} \right) dt \tag{4.48}$$

The roll rate equation can be derived as shown by Rajamani [102]:

$$z_{6_t} = \frac{-(z_{CG} - z_{RC} + R_e) m_s A_y}{k_\phi - (z_{CG} - z_{RC} + R_e) m_s g} \tag{4.49}$$

Finally, the SPS equations can be formulated using the suspension compliances as shown by Hahn [48]:

$$z_{7_t} = \frac{x_{5_t} - c_\phi \left(0.5t_F \dot{\phi} + (\ell - x_{CG}) \dot{\psi} \right)}{k_\phi} \tag{4.50}$$

$$z_{9_t} = \frac{x_{6_t} - c_\phi \left(0.5t_F \dot{\phi} + (\ell - x_{CG}) \dot{\psi} \right)}{k_\phi} \tag{4.51}$$

$$z_{9_t} = \frac{x_{7_t} - c_\phi \left(0.5t_F \dot{\phi} + (\ell - x_{CG}) \dot{\psi} \right)}{k_\phi} \tag{4.52}$$

$$z_{10_t} = \frac{x_{8_t} - c_\phi \left(0.5t_F \dot{\phi} + (\ell - x_{CG}) \dot{\psi} \right)}{k_\phi} \tag{4.53}$$

Noise Characteristics

Uncertainty in a Kalman filter is represented by two characteristic noise sets: the process noise, P, and the measurement noise, Q. The process noise is the less intuitive of these sets as it represents an expected uncertainty in the state transition function outputs and is difficult to accurately quantify. In practice, the process noise is often used more as gain that can be tuned than as a true statistical measure. A good estimate of the process noise can often be formed by taking the expected range of each variable as the standard

deviation and then squaring it to form a variance [21]:

$$\hat{P} = diag\begin{bmatrix} 1000 \\ 1000 \\ 1000 \\ 1000 \\ 1000 \\ 1000 \\ 1000 \\ 1000 \end{bmatrix}^2 = diag\begin{bmatrix} 1\text{E}^6 \\ 1\text{E}^6 \\ 1\text{E}^6 \\ 1\text{E}^6 \\ 1\text{E}^6 \\ 1\text{E}^6 \\ 1\text{E}^6 \\ 1\text{E}^6 \end{bmatrix} \tag{4.54}$$

Experimentation with filter performance yielded better results when the process noise terms were tuned. In general for an UKF, decreasing the process noise increases the confidence in the state transition function and decreases confidence in the measurement. Tuning these noise terms can be especially effective in cases such as this one where some of the states are directly additive in the measurement function and are thus the effects of each one are difficult to separate mathematically. As a result, the following process noise matrix yielded better convergence:

$$P = diag\begin{bmatrix} 1 \\ 1 \\ 100 \\ 1 \\ 1000 \\ 1000 \\ 1000 \\ 1000 \end{bmatrix}^2 = diag\begin{bmatrix} 1 \\ 1 \\ 1\text{E}^4 \\ 1 \\ 1\text{E}^6 \\ 1\text{E}^6 \\ 1\text{E}^6 \\ 1\text{E}^6 \end{bmatrix} \tag{4.55}$$

The measurement noise set is more easily visualized as it represents the statistical uncertainty in the sensor measurements. The values used in this work are based on a NovAtel SPAN-CPT integrated GPS/IMU system. The SPAN-CPT combines three-axis fiber-optic gyros with 3-axis MEMS accelerometers and a dual frequency L1/L2 band GPS receiver. The system uses an internal Kalman filter to fuse the GPS and IMU data into a single best estimate of vehicle pose. Although the price of this system is, at the time of this writing, approximately $25,000 it is actually considered a mid to low-grade Inertial Navigation System (INS) for autonomous vehicle use and is thus a good baseline for this work. Noise values for the accelerometers and gyros were obtained from the SPAN-CPT user manual [103]. Values for the velocity and angular position quantities were obtained by logging the `INSCOV` output from the NovAtel unit while mounted on Virgnia Tech's Rocky vehicle (which, unlike in Figure 1.1, was upright at the time of testing).

$$Q = diag \begin{bmatrix} 2\text{E}^{-4} \\ 2\text{E}^{-4} \\ 3\text{E}^{-2} \\ 3\text{E}^{-2} \\ 2\text{E}^{-5} \\ 2\text{E}^{-5} \\ 1\text{E}^{-2} \\ 1\text{E}^{-2} \\ 1\text{E}^{-2} \\ 1\text{E}^{-2} \end{bmatrix} \tag{4.56}$$

The actual MATLAB code implementation of the UKF used the ReBEL toolkit from the Oregon Health and Science University [104]. To provide additional noise suppression,

a 5-sample moving average filter was implemented on the 40Hz state outputs. This filter ensures that the dynamics of the estimate are not faster than the true dynamics of the system. Detailed results showing the performance of the UKF-based friction estimator are shown in Chapter 6, but the estimator proved capable of estimating the forces to a degree of accuracy sufficient for use in estimation of the CG and COF, as shown in Figures 4.8 and 4.9.

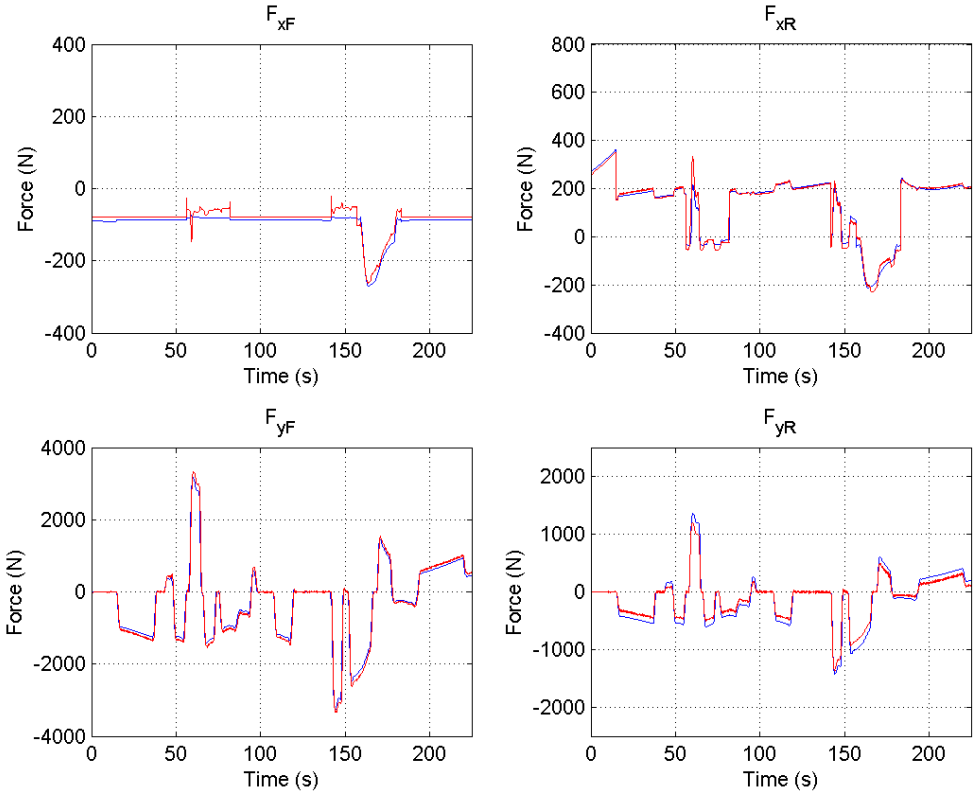

Figure 4.8: VehicleSim results of UKF tire force estimator on road course. Note that the estimated force (red) closely matches the actual force (blue)

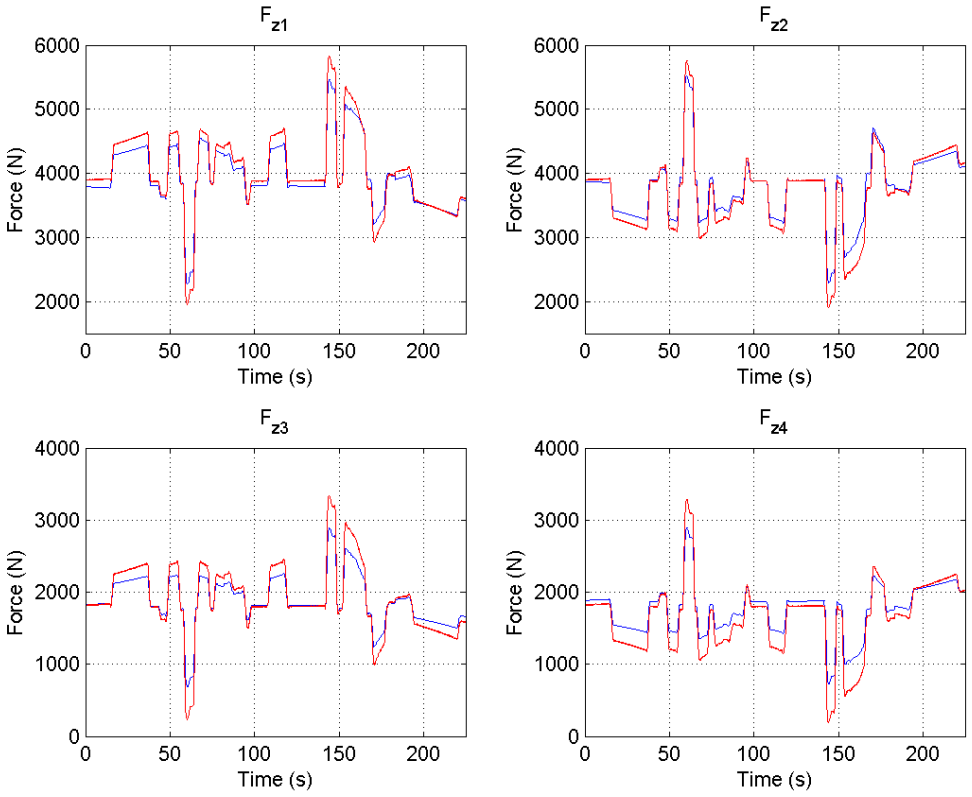

Figure 4.9: VehicleSim results of UKF normal force estimator on road course. Note that the estimated force (red) closely matches the actual force (blue)

4.3 CG Estimation

An important aspect of this work is the ability to estimate the loading condition of the vehicle. While it is assumed that the empty configuration is known *a priori*, the cargo state is not and cannot be similarly known. It is therefore necessary to develop a method for estimating the mass and distribution of the vehicle's cargo using the available sensor information. One key assumption, as previously stated, is that the mass of the vehicle will only change significantly when the vehicle is stopped. In practical terms this is not much of a constraint as, except fuel consumption, ground vehicles are rarely loaded or unloaded while in motion.

Estimation of the CG is a more complicated problem than it may initially appear. The

addition of SPSs makes measurement of the lateral and longitudinal location of the CG almost trivial when at rest, but the vertical location is unobservable under such conditions. When the vehicle is in motion, the vertical CG location can become observable, but only under conditions of sufficient excitation. A further complication is that the measurements of the accelerations used to observe this location are not in the CG coordinate frame. Transformation of these accelerations, as given by Eq. 4.27, requires knowledge of the CG location. This interconnection combined with the generally relatively low excitation levels in normal driving causes serious observability issues if continuous CG estimation is desired, especially if the mass is also unknown. Examples in the literature rely on high excitation maneuvers to successfully implement techniques such as Kalman filters and other observers for estimation of CG location [21] [30] [29]. Preliminary efforts by the author to implement similar methods in non-continuous excitation driving cases similarly yielded poor results.

As a result of these difficulties, it was decided to develop a method that exploits both the inherent controllability of autonomous vehicles and the assumption of CG change only at rest. When the vehicle is at rest, the mass can easily be calculated using the SPSs. If this value changes beyond a specified tolerance, the vehicle can be commanded to perform a non-hazardous, low-speed prescribed maneuver upon resumption of motion that can be used to recalculate the 3D location of the CG. This CG value can then be held until the vehicle again comes to rest. Experimentation has shown that with the technique described below, a simple, low-magnitude S-curve maneuver, shown in Figure 4.10, is normally sufficient to make an accurate determination of the CG location.

4.3.1 Estimator Formulation

The CG estimation method requires commanding the vehicle to execute a maneuver, storing the sensor measurements, and then running a least-squares analysis to determine the

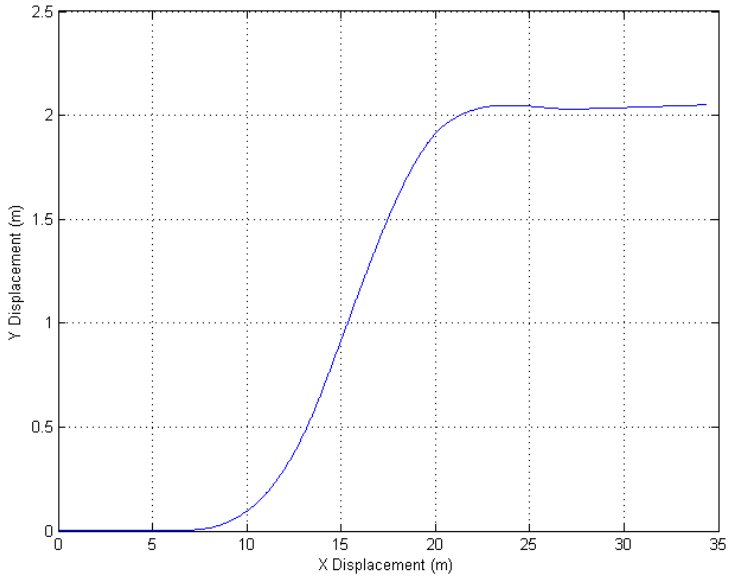

Figure 4.10: Proposed CG determination maneuver. note that the lateral displacement is only 2m over a travel distance of 20m.

most likely set of mass and CG parameters. Although this method is intended for autonomous vehicles, it is applicable to manned-vehicles as well provided that the driver can execute a similar maneuver. Simulation in VehicleSIM has shown that best results are obtained when the determination maneuver contains excitation in both directions, i.e. a left and a right turn of approximately equal magnitude. Outside of NASCAR, this requirement is actually desirable as it returns the vehicle to nearly its original course. The method does not, however, appear to be highly sensitive to the exact speed or steering configuration of the maneuver, as shown in Section 6.2.2.

The key sensor data to record during this maneuver are given in Table 4.4. Note that these data do not include the velocity due to the method being not directly dependent on vehicle velocity. Since the relevant equations are non-linear, a measurement function, $z = h(x,u)$, similar in form to that used for the UKF, is then created to calculate the estimated values of the observations for different configurations of the mass and CG.

Using m_c to represent the cargo mass, the 'state' vector for this function is given by:

$$x = \begin{bmatrix} x_1 \\ x_2 \\ x_3 \\ x_4 \end{bmatrix} = \begin{bmatrix} m_c \\ x_{CG} \\ y_{CG} \\ z_{CG} \end{bmatrix} \tag{4.57}$$

The observation vector is given by:

$$z = \begin{bmatrix} z_1 \\ z_2 \\ z_3 \\ z_4 \\ z_5 \end{bmatrix} = \begin{bmatrix} F_{z_1} \\ F_{z_2} \\ F_{z_3} \\ F_{z_4} \\ \phi \end{bmatrix} \tag{4.58}$$

The exogenous input vector is given by:

$$u = \begin{bmatrix} u_1 \\ u_2 \\ u_3 \\ u_4 \\ u_5 \\ u_6 \\ u_7 \end{bmatrix} = \begin{bmatrix} A_x \\ A_y \\ \phi \\ \psi \\ \dot{\phi} \\ \dot{\psi} \\ \dot{\theta} \end{bmatrix} \tag{4.59}$$

Inside the function, the exogenous input vector is converted to current CG coordinates using Eq. 4.27 with the substitution $r = -[x_2, x_3, x_4]$. The weight transfer equations given by Eqs. 3.25-3.41 can then be applied with the substitutions $A_x = u_1$ and $A_y = u_2$ to

Table 4.4: CG Estimation Data

Symbol	Parameter Name	Sensor
A_x	Longitudinal acceleration	IMU
A_y	Lateral acceleration	IMU
F_{z_n}	Estimated vertical wheel force for wheel-n	UKF
ϕ	Sprung mass roll angle	PES
ψ	Sprung mass pitch angle	PES
$\dot{\phi}$	Sprung mass roll rate	IMU
$\dot{\psi}$	Sprung mass pitch rate	IMU
$\dot{\theta}$	Yaw rate	IMU

produce $\hat{z}_1, ..., \hat{z}_4$. The final output, $\hat{z}_5$, can be produced by taking linearized moments about a roll plane representation of the vehicle:

$$\sum M_{CG} = \phi k_\phi - \phi(z_{CG} - z_{RC_F} + R_e)m_s g + (z_{CG} - z_{RC_F} + R_e)m_s A_y \tag{4.60}$$

$$\hat{z}_5 = \phi = \frac{(z_{CG} - z_{RC_F} + R_e)m_s A_y}{k_\phi - (z_{CG} - z_{RC_F} + R_e)m_s g} \tag{4.61}$$

4.3.2 Estimator Solver

To solve for the estimated CG location, an error function is defined as the squared difference between the output of the measurement function and the actual measurements:

$$e = (z - \hat{z})^2 \tag{4.62}$$

It can be seen that when Eq. 4.62 is minimized by varying the CG position vector, x, the resulting estimate will be optimized. To perform this optimization, a numerical solver can be used. In this particular implementation MATLAB's `fsolve` function was used. Since the system is non-square, i.e. the number of inputs and outputs are different, the standard trust-region dogleg algorithm will not work. Instead, a Levenberg-Marquardt solver algorithm was selected due to its robustness in handling non-square, non-linear systems. The mass and CG location of the empty vehicle are used as initial guesses.

Given adequate excitation, this method proved to be able to converge rapidly to an accurate CG estimation under a wide variety of loading conditions. It also proved far more robust to a wide range of excitation parameters and was able to converge to a solution of acceptable accuracy at far lower levels of excitation than other attempted methods. Further results are presented in Chapter 6.

4.4 Friction Estimation

The problem of estimating the coefficient is important for operations in realistic environments due to the dramatic effect it can have on the handling characteristics of the vehicle. Ideally, the autonomous vehicle would be equipped with a sensor capable of looking ahead and reliably measuring the COF. Unfortunately, although some research has been performed in this area, at the present time such sensors do not exist. It is therefore necessary to rely on friction estimates that can be obtained using proprioceptive sensors.

Due to the COF's influence on tire forces, it becomes possible to use this knowledge to produce friction estimates. Research has been performed on using lateral and longitudinal tire dynamics to derive friction estimates, but the most promising work to date involves exploiting the influence of the COF on pneumatic trail [48] [49] [51] [50]. The pneumatic trail method will be developed in this work but a more complete description of other methods can be found in Section 2.3.5. It is significant to note in reviewing the literature that there is a significant lack of work in applying friction estimation techniques to the type of combined-slip conditions that exist in realistic drive cycles.

Hsu demonstrated that the pneumatic trail, the distance at behind the Center of Tire Contact (CTC) at which tire force generation is centered due to tire deformation, scales roughly linearly with the COF [50]. As illustrated in Figure 4.11, the primary effect of the variation in pneumatic trail is on the torque required to be applied by the steering system

to maintain the desired steering angle. If this torque can be measured or estimated, it is possible to construct a COF estimator using the pneumatic trail effect.

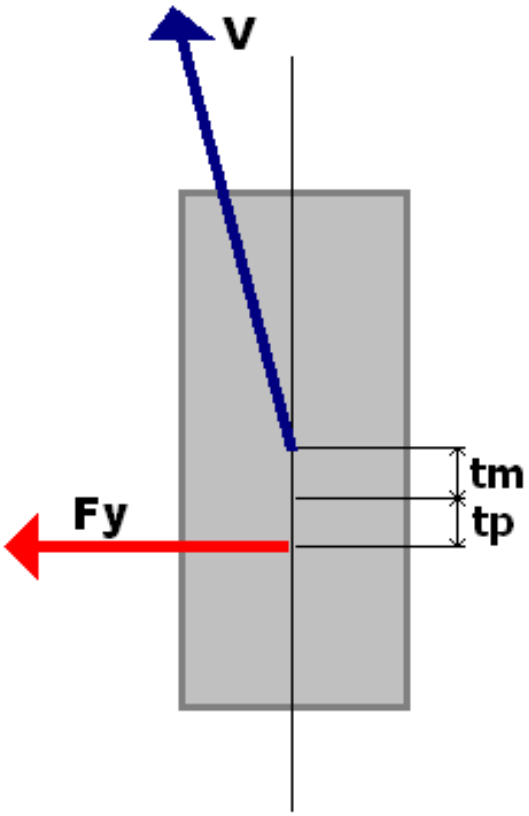

Figure 4.11: Effect of pneumatic trail on steering torque. Note that the point at which the lateral force acts is offset by a distance equal to the combined mechanical (t_m) and pneumatic (t_p) trails.

4.4.1 Equation Formulation

From the diagram in Figure 4.11, summing the moments about the kingpin yields:

$$\sum M_{kingpin} = \hat{F}_y(t_m + t_p) + \tau \tag{4.63}$$

$$t_p = -\frac{\tau}{\hat{F}_y} - t_m \tag{4.64}$$

where t_p is the pneumatic trail length, t_m is the mechanical trail due to suspension geometry, and τ is the steering torque. This is a simplified representation as other effects, such as jacking torque, may exist, but Hsu demonstrated that these effects can be neglected in this application [50]. The mechanical trail is a function of the suspension linkage geometry, primarily caster and kingpin inclination and can be determined from a kinematic linkage analysis or measured experimentally. Mechanical trail is usually dependent on steering angle, but the effect is small and so this dependency will be neglected.

The dependency of the pneumatic trail on COF can be represented, as shown by Hsu, as a linear function of $\hat{F}_y$, $\hat{F}_z$, and μ [50]:

$$t_p = t_{p0} - \frac{t_{p0}\hat{F}_y}{\mu \hat{F}_z} \tag{4.65}$$

This representation differs from that used by Hsu in that the estimated values of the lateral and normal forces are used. In Hsu's derivation, a first-order approximation of the Fiala model is used to calculate the forces [50]. The use of the estimated forces extends the formulation to include the effects of longitudinal forces present in combined slip conditions due to the incorporation of of the longitudinal component in Eq. 4.41.

Combining Eq. 4.64 and Eq. 4.65 and substituting the appropriate values from Section 4.2 yields an expression for the estimated COF:

$$\hat{\mu} = \begin{cases} \dfrac{t_{p0}\hat{F}_{y_F}}{\left[-\left(\frac{\tau}{\hat{F}_{y_F}}\right) - t_m - t_{p0}\right]\left(\hat{F}_{z_1}+\hat{F}_{z_2}\right)}, & t_p > 0 \\ \dfrac{\tau}{t_m\left(\hat{F}_{z_1}+\hat{F}_{z_2}\right)}, & t_p \leq 0 \end{cases} \tag{4.66}$$

The piecewise nature of this equation corrects for the fact that Eq. 4.65 allows for negative values of t_p. In the physical system, it is impossible for the total trail length to decrease to less than the value of the mechanical trail. At this point the aligning moment degenerates into the simple ratio given.

4.4.2 Bayesian Histogram Filter

Two major problems exist with friction estimation from Eq. 4.66: the result is noisy and the result falls off as excitation decreases. Obviously, the first of these problems can be addressed by applying a proper filtering technique. The second problem , as can be seen in Figure 4.12, is more difficult to address. It is necessary to implement a method that is capable of maintaining a value in the periods of low excitation that occur whenever the vehicle is traveling straight or nearly straight. It is of course possible to just naively assume that the COF does not change during these periods and hold the last observed value, but this can be a dangerous assumption. One also must take into account that in maneuvers of small lateral magnitude an observation may be achieved but that the true COF may in fact be significantly higher.

Bayesian Statistics

These issues of observability and uncertainty can be addressed by introducing the mathematical construct of Bayesian statistics. Introduced by Thomas Bayes in the 18th century, Bayesian statistics allows the representation of knowledge in a non-binary form. In the Bayesian domain, knowledge is represented by a Probability Density Function (PDF) that contains the likelihood of occurrence of a different outcomes within the belief space, represented as $p(x)$ and is known as a prior distribution. Another important concept is that of the posterior probability distribution, $p(x|y)$, that represents the probability of a state x given knowledge of the prior density of y. Bayes's innovation was the production of the Bayes rule that allows for the calculation of posterior distributions given knowledge of the inverse posterior probability [3]:

$$p(x|y) = \frac{p(y|x)p(x)}{p(y)} \tag{4.67}$$

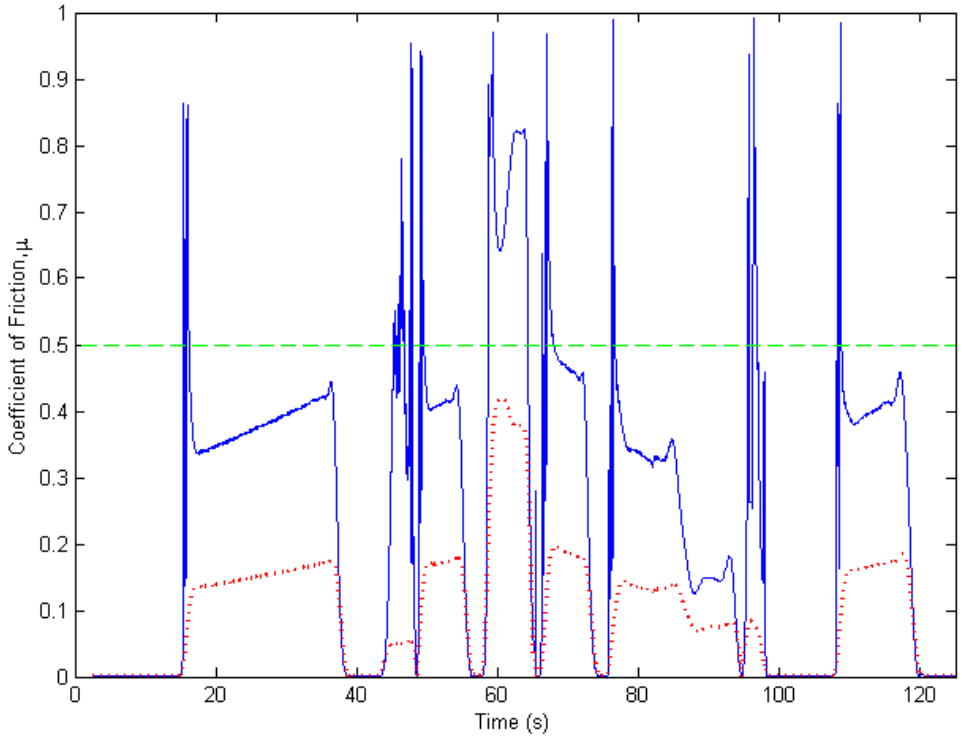

Figure 4.12: Unfiltered output from friction estimator (solid blue). Data are shown in combined slip conditions with estimated excitation levels (dotted red) and the true coefficient of friction (dashed green).

The importance of this rule is that it allows for the calculation of the posterior of a state, $p(x|y)$, given knowledge of the posterior distribution of a measurement, $p(y|x)$.

The Bayes rule also allows for formulation of a Bayesian filter with prediction and update stages similar to those of a Kalman filter. The general algorithm for the Bayes filter is given by [3]:

$$\overline{bel}(x_t) = \int p(x_t|u_t, x_{t-1}) bel(x_{t-1}) dx_{t-1} \tag{4.68}$$

$$bel(x_t) = \eta\, p(z_t|x_t) \overline{bel}(x_t) \tag{4.69}$$

Further discussion and expansion of Bayesian statistics is considered beyond the scope of

this work as the prescribed implementation can be constructed from these principles. For further reading on this topic the reader is referred to the excellent *Probabilistic Robotics* by Thrun, *et al.* [3].

Bayesian Friction Estimation

The form of Bayesian statistics used to address the issues with friction estimation is the Bayesian Histogram Filter (BHF). The BHF is a discrete version of the classic Bayes filter in which the domain space is partitioned into a number of discrete bins and then propagated through the discrete form of the Bayes filter algorithm [3]:

$$\bar{p}_{k,t} = \sum p(X_t = x_k | u_t, X_{t-1} = x_i) p_{i,t-1} \tag{4.70}$$

$$p_{k,t} = \eta\, p(z_t | X_t = x_k) \bar{p}_{k,t} \tag{4.71}$$

The partitioning of the friction space for this implementation is justifiable in the physical sense. Extremely accurate determination of the COF is doubtful given the uncertainties and approximations in the estimation methodology. It is also difficult to intuitively correlate COFs to actual terrain surfaces. Furthermore, the difference in operating envelope between, for example, $\mu = 0.7$ and $\mu = 0.8$ is not large. As a result, the friction space will be partitioned into the four bins given by Table 4.5, each of which can be roughly correlated to common terrain surfaces [105].

Table 4.5: Friction Space Partitions

COF Range	Likely Terrain Surface
$0.75 - 1.0$	Dry paved road
$0.50 - 0.75$	Wet paved road or hard unpaved road
$0.25 - 0.50$	Soft unpaved road or snow
$0.0 - 0.25$	Wet mud or ice

To form the BHF, two beliefs are established for each bin: the probability that the

maximum COF is contained within the bin (bel_{in}) and the probability that the maximum COF is not contained within the bin (bel_{out}). For each time step, the probability that the maximum COF is within the bin is established from the output of Eq. 4.66 by a piecewise function and its inverse:

$$P_{in_i} = \begin{cases} 0.01, & \mu_{l_i} \geq 2\hat{\mu} \\ 0.25, & \mu_{l_i} > \hat{\mu} \\ 0.90, & \mu_{l_i} \leq \hat{\mu} \leq \mu_{u_i} \\ 0.35, & \mu_{u_i} < \hat{\mu} \\ 0.05, & \mu_{u_i} \leq 2\hat{\mu} \end{cases} \tag{4.72}$$

$$P_{out_i} = 1 - P_{in_i} \tag{4.73}$$

where μ_{u_i} and μ_{l_i} represent the upper and lower bounds to the bin, respectively and $\hat{\mu}$ represents the current time step estimate of the COF. These values were chosen somewhat arbitrarily but represent a high confidence in the measurement when within the bin and a slightly greater confidence that the COF is underestimated than that it is overestimated.

Another key aspect of the friction BHF is the inclusion of another probability: the probability that the current estimate is actually in the observable range. This probability is an attempt to address the issues of observability that plague friction estimation by producing a quantity that can be interpreted as a confidence that the estimated value is actually correct based on the current excitation levels. An estimate of the excitation level can be formed by the ratio of the lateral force at the front tires to the normal force on the front tires:

$$\gamma = \frac{\hat{F}_{y_F}}{\hat{F}_{z_1} + \hat{F}_{z_2}} \tag{4.74}$$

This excitation estimate can then be used to generate a probability for each bin that the

range it represents is observable and its inverse:

$$P_{obs} = \begin{cases} 0.01, & \mu_{l_i} > 4\gamma \\ 0.3, & \mu_{l_i} \leq 4\gamma \\ 0.85 - 0.55\left(\frac{\mu_{l_i} - 2\gamma}{\gamma}\right), & \mu_{l_i} \leq 3\gamma \\ 0.99 - 0.14\left(\frac{\mu_{l_i} - \gamma}{\gamma}\right), & \mu_{l_i} \leq 2\gamma \\ 0.99, & \mu_{l_i} \leq \gamma \end{cases} \tag{4.75}$$

$$P_{unobs} = 1 - P_{obs} \tag{4.76}$$

As can be seen in Figure 4.13, this function was chosen to represent a high confidence when the COF estimate is within two times the value of the excitation level and to ramp off linearly thereafter. This corresponds to the results presented by Hsu which show that pneumatically trail friction estimation performance drops off rapidly when the true friction coefficient exceeds twice the excitation level [50].

As the friction estimate has no predictable expected dynamics due to the lack of future terrain information, the prediction stage of the BHF becomes trivial ($\overline{bel} = bel$) and can be neglected. The measurement update can then be formulated according to:

$$\tilde{bel}_{in_i} = P_{in_i} P_{obs_i} \overline{bel}_{in_i} + P_{out_i} P_{unobs_i} \overline{bel}_{out_i} \tag{4.77}$$

$$\tilde{bel}_{out_i} = P_{out_i} P_{obs_i} \overline{bel}_{out_i} + P_{in_i} P_{unobs_i} \overline{bel}_{in_i} \tag{4.78}$$

The new estimate can then be normalized into a PDF by:

$$bel_{in_i} = \frac{\tilde{bel}_{in_i}}{\tilde{bel}_{in_i} + \tilde{bel}_{out_i}} \tag{4.79}$$

$$bel_{out_i} = \frac{\tilde{bel}_{out_i}}{\tilde{bel}_{in_i} + \tilde{bel}_{out_i}} \tag{4.80}$$

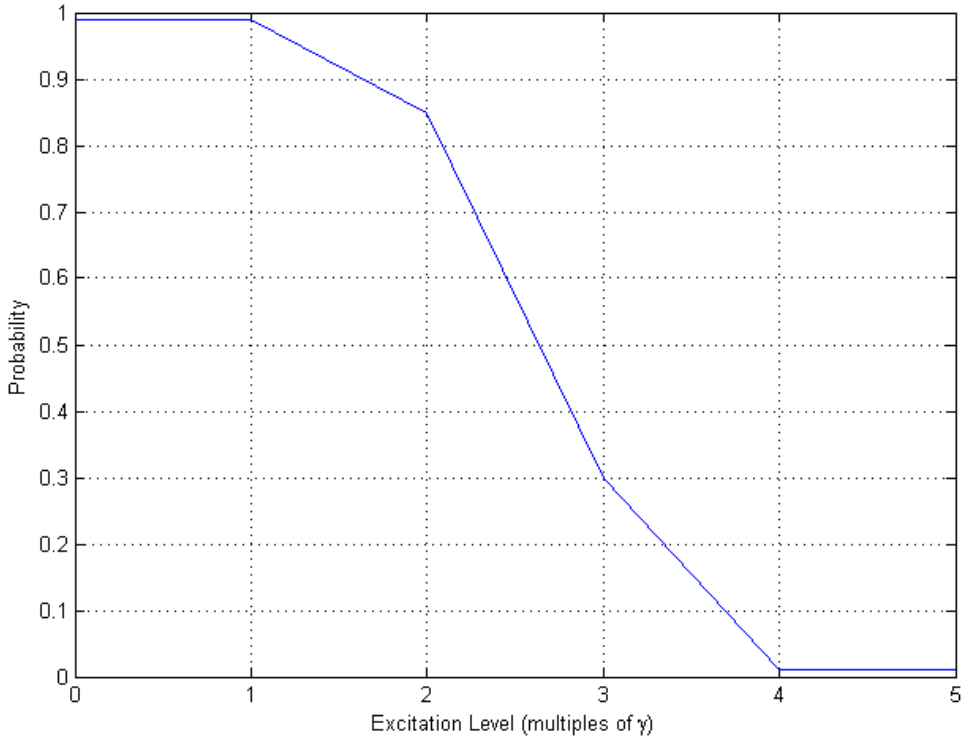

Figure 4.13: Probability of observation of COF for estimated excitation level.

The final output of the friction BHF is derived by selecting the bin with the maximum probability that the COF of friction is within its bounds:

$$\mu = max(bel_{in}) \tag{4.81}$$

One difficulty with this implementation is that it does not provide enough of a filtering effect to smooth the friction estimate and maintain an estimate during periods of low excitation. A modification is thus proposed to the BHF to add damping to the filter by performing a weighted average of the current time step value with the previous time step value. First a smoothing coefficient can be defined based on the observability PDF:

$$\zeta = 1 - \lambda P_{obs} \tag{4.82}$$

where λ is a freely chosen value that controls amount of smoothing in the filter. The choice of a smoothing coefficient based on the observation PDF means that the amount of smoothing is dependent on the excitation level. A value of $\lambda = 0.02$ was found to yield good results in this application. The selected formulation of the smoothing coefficient ensures more rapid response to sudden changes in friction coefficient when in the observable range while providing a slow decay in the measurement probabilities when the COF is not observable. Smoothing can then be added to the BHF by modifying Eqs. 4.79-4.80:

$$bel_{in_i} = \frac{(1-\zeta)\tilde{bel}_{in_i}}{\tilde{bel}_{in_i} + \tilde{bel}_{out_i}} + \zeta\overline{bel}_{in_i} \tag{4.83}$$

$$bel_{out_i} = \frac{(1-\zeta)\tilde{bel}_{out_i}}{\tilde{bel}_{in_i} + \tilde{bel}_{out_i}} + \zeta\overline{bel}_{out_i} \tag{4.84}$$

The performance difference between the smoothed and unsmoothed versions of the BHF and the unfiltered estimate is illustrated in Figure 4.14. Note that both versions of the BHF significantly outperform the raw estimate by outputting a more stable and more accurate estimate of the COF.

Another useful feature of the BHF is the ability to easily incorporate additional measurements. If an additional measurement of the COF were available from the lateral or longitudinal dynamics, it could be incorporated merely by defining additional confidence and observation functions and adding additional terms to Eqs. 4.77-4.78. An even more potentially useful addition would be the incorporation of a look-ahead friction sensor. To test this, a hypothetical look-ahead sensor was created by adding white noise to a signal containing the known COF value. This value was then time-lagged to synchronize it with the proprioceptive estimates and incorporated into the BHF. A comparison of the performance of the friction BHF with and without this look-ahead sensor can be seen in Figure 4.15. Note that this additional sensor dramatically improves the capability of the estimator, indicating that this should be an area of future research.

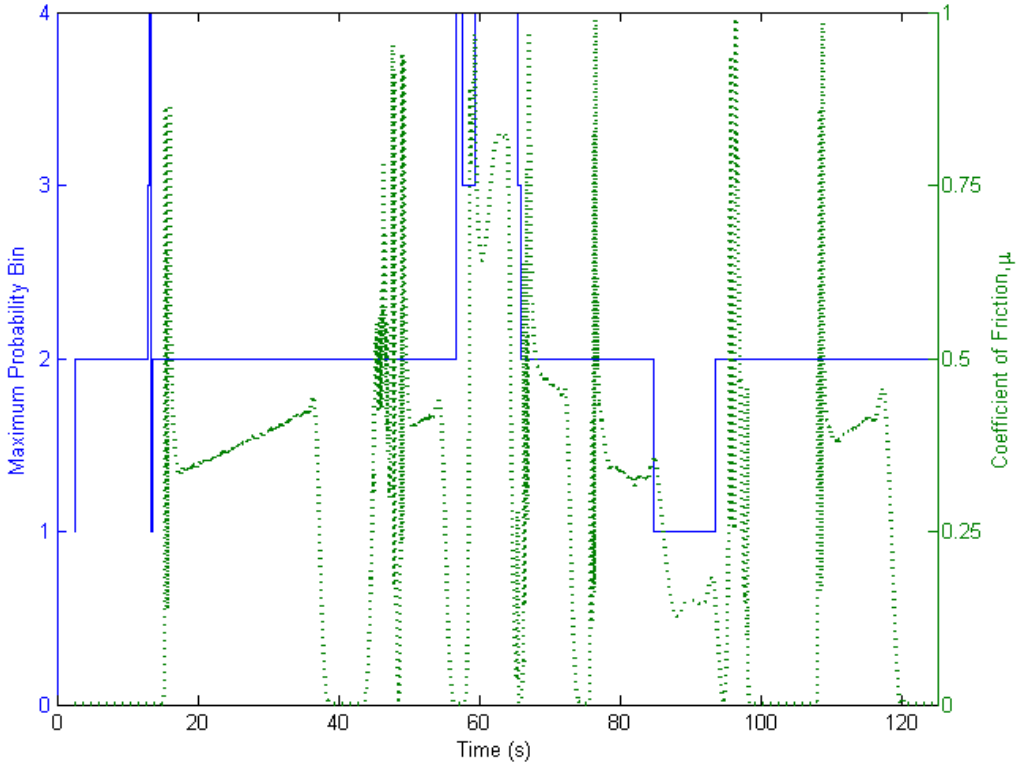

Figure 4.14: Filtered (solid blue) vs. unfiltered (dotted green) friction estimates. Note that the BHF is able to maintain an estimate near the actual value ($\mu = 0.5$) with much more stability even during periods of low excitation.

4.5 Estimation Summary

Parameter estimation is necessary to enable use of the adaptive model that is the fundamental basis of IMM generation. An UKF-based force estimator has been formulated to be capable of tracking key unobservable force states. The output from this can be used to drive a CG estimator capable of numerically determining an optimal CG estimate from a low excitation maneuver. Additionally, a friction estimation scheme has been developed using the dependency on pneumatic trail. Observability issues of this estimator are addressed by applying a BHF to stabilize and improve the estimates. The parameter estimation has been tested against the commercial VehicleSim multi-body model and results

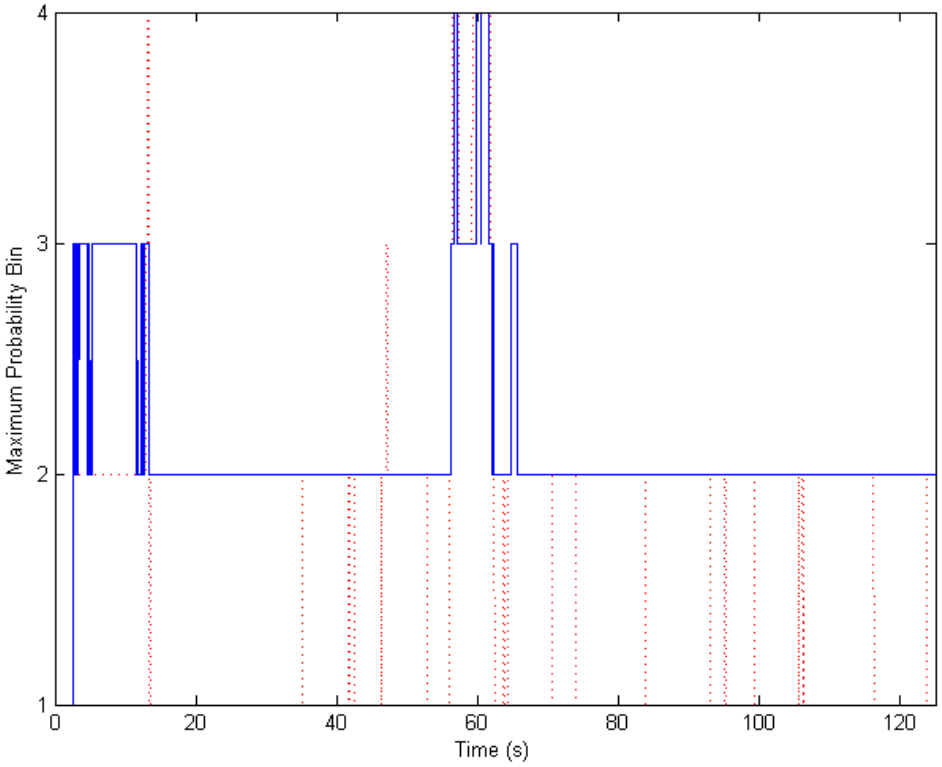

Figure 4.15: Comparison between BHF using virtual look-ahead sensor (solid blue) and proprioceptive sensors only (dotted red). This example uses $\lambda = 0.2$ to emphasize the ability of the look-ahead sensor to maintain a more accurate estimate.

can be found in Section 6.2.

It should be noted here that parameter estimation is not the primary focus of this work. Although the estimation structure presented here is capable of estimating parameters, the results may not be very robust in a real-world environment. Additionally, observability and excitation are likely to be issues in real drive cycles, particularly for friction estimation. Obviously for real implementations these may be severe limitations. However, the intent here is to demonstrate the concept of parameter generation in the context of producing the data necessary to reach to true goal of this work: generation of Instantaneous Maneuvering Manifolds. Time, equipment, and testing constraints require that implementation and validation of a fully robust state estimator be left as future work.

Chapter 5

Manifold Mapping

I cannot consent to place in the control of others one who cannot control himself.

–Robert E. Lee, 1861 [106]

The central thesis of this work is the creation of maneuvering maps using a dynamically adaptive model. After precalculation of the FMM maps and estimation of the parameters, the data necessary to create the real-time IMM is available. A methodology will be developed to quantify vehicle stability limits, compensate for dynamic effects, combine the FMM maps to create a manifold, apply the stability metrics, and handle the inherent uncertainty in the system.

5.1 Stability Metrics

Once the vehicle has been successfully modeled and parameterized, it is necessary to develop a cohesive methodology for estimating its dynamic maneuvering limits. To quantify these limits, it is necessary to define these limits in terms of numerical metrics. In the autonomy domain, there are three main modes in which a vehicle can lose its dynamic

stability: it can roll over, it can spin out (yaw instability), or it can enter a slide. The Rollover Stability Metric (RSM), Directional Stability Metric (DSM), and Directional Controllability Metric (DCM) will be defined to characterize each of these modes and the union of the three metrics will describe the unstable operating range of the vehicle.

It would be possible to combine all of these metrics without a clear differentiation. This is not done to allow for flexibility in the event that one of or more of the metrics must be exceeded. An example of such a case would be a vehicle maneuvering at high speed suddenly encountering a section of low-friction terrain, such as ice. In this situation it is possible that no valid maneuvers exist for the current state of the vehicle with the current metric limitations. In this situation it may be desirable to allow the autonomous system to systematically degrade the metric limitations until a valid maneuver does exist. Differentiating the metrics allows this degradation to occur in a manner designed to optimize vehicle survival. In most cases, a slide (DCM) is preferable to a spin (DSM) which is in turn preferable to a rollover (RSM). In such a situation it would be possible to systematically degrade the DCM limits until a valid maneuver can be found. Although this state may be undesirable, it would at least yield the safest possible trajectory in the circumstances by ensuring that the DSM and RSM are not violated.

5.1.1 Rollover Stability Metric

The Rollover Stability Metric is designed to predict the threshold at which rollover occurs. The algorithm used to estimate the proximity to the rollover envelope is based on a method proposed by Dahlberg and further developed and validated by Johansson [60] [107]. This method uses an energy formulation to determine the proximity to a critical threshold at which two wheels on one side of the vehicle lose contact with the ground. This energy (E_{roll}) has two components, a potential energy (U_{roll}) due to spring compression and gravity and a kinetic energy (T_{roll}) due to movement of the sprung mass and can be expressed

as shown by Johansson [107]:

$$U_{roll} = \frac{1}{2}\phi^2 k_\phi - m_s g(z_{CG} - z_{RC})(1 - \cos\phi) \tag{5.1}$$

$$T_{roll} = \frac{1}{2}(I_x + m_s(z_{CG} - z_{RC})^2)\dot{\phi}^2 \tag{5.2}$$

$$E_{roll} = U_{roll} + T_{roll} \tag{5.3}$$

Note that the kinetic energy term depends on roll rate and will be zero in steady-state while the potential energy term is independent of transient effects. This separation allows the RSM calculation to take place in two parts. The potential energy, which will change across the maneuvering space, can be precalculated for the FMM maps while the roll energy that depends on an instantaneous value can be calculated based on a roll rate from the state estimator. The final energy calculation is a linear superposition of the two values across the maneuvering space.

Due to its dependence on roll rate, the kinetic roll energy must be estimated in real-time. The roll rate, $\dot{\phi}$, is available as a measurement from the PES and the height of the CG, z_{CG}, is available from the CG estimator, but the value of the roll moment of inertia, I_x, of the loaded vehicle is unknown. This value can be inferred from the known empty vehicle parameters and estimates of sprung mass and CG height using the parallel-axis theorem:

$$m_{s_\Delta} = m_{s_{load}} - m_{s_{empty}} \tag{5.4}$$

$$r_\Delta = \frac{m_{s_{load}} z_{CG_{load}} - m_{s_{empty}} z_{CG_{empty}}}{m_{s_\Delta}} \tag{5.5}$$

$$I_{x_{load}} = I_{x_{empty}} + m_{s_\Delta} r_\Delta^2 \tag{5.6}$$

The critical rollover energy, E_{crit}, can be found from a moment balance for the general case by finding the minimum energy required to induce wheel liftoff. This energy can be

calculated, as shown by Johansson, by performing a moment balance with the assumption that the lateral force is equal to the maximum possible lateral force ($F_y = \mu F_z$) [107]. The critical energy can then be defined as the minimum energy that satisfies:

$$\frac{t_F + t_R}{4} F_z - z_{RC} F_y = \phi k_\phi + \dot{\phi} c_\phi \tag{5.7}$$

The assumption can be made that the critical rollover energy will occur at the point where all of the weight has been transferred to the outside wheels and where the lateral force is at the maximum level possible due to the coefficient of friction. These assumptions allow the simplification of Eq. 5.7 to [107]:

$$(\ell - \mu z_{RC}) Mg = \phi k_\phi + \dot{\phi} c_\phi \tag{5.8}$$

Note that Eq. 5.8 depends on both the COF, μ, and the roll parameters, ϕ and $\dot{\phi}$, which are estimated by the state and pose estimators. Since the value of the rollover energy that is to be minimized is dependent on the roll parameters, it becomes possible to calculate the minimum energy value for each value of the COF.

Due to the nonlinearities present in the energy equations, it becomes easiest to solve for the critical energy numerically. The problem can be recast as the system:

$$E_1 = U_{roll} + T_{roll} \tag{5.9}$$

$$E_2 = \left| \phi k_\phi + \dot{\phi} c_\phi - (\ell - \mu z_{RC}) Mg \right| \tag{5.10}$$

where U_{roll} and T_{roll} are defined by Eqs. 5.1-5.2. Assuming that the value of μ is locally fixed, this system becomes a function of the variables ϕ and $\dot{\phi}$. To satisfy the critical rollover formulation stated above, the desired solution to this system is the minimum value of E_1 for which $E_2 = 0$. This value can be approximated by applying a gradient to

the system:

$$E = \nabla E = \begin{bmatrix} 1 \\ 1\text{E}^6 \end{bmatrix} \begin{bmatrix} E_1 \\ E_2 \end{bmatrix} \tag{5.11}$$

and using the MATLAB function `fsolve` to find the minimum solution of the system of equations using the default `trust-region-dogleg` algorithm. Although this method does not guarantee an absolute minimum solution, the application of the gradient drives the moment balance equation to nearly zero and produces a reasonable result given the inherent approximations. The minimum wheel lift-off energy can then be determined as $E_{crit} = E_1/2$.

This value can be precalculated for a given vehicle configuration and used to normalize the metric to produce a value between 0 and 1 with 1 being equivalent of the vehicle state at rest on level ground and 0 predicting imminent rollover:

$$RSM \equiv \frac{E_{crit} - E_{roll}}{E_{crit}} \tag{5.12}$$

It should be reemphasized that an RSM value of zero does not necessarily indicate that the vehicle will actually rollover; instead it predicts the unstable roll condition of wheel liftoff and is somewhat more conservative than a prediction of actual rollover. Note also that this metric is valid only for untripped rollover conditions where the vehicle is not destabilized by a lateral collision with a terrain surface such as a curb. Due to the extreme complexities and unpredictabilities inherent in tripped conditions, tripped rollover will not be considered and will be left for future work.

5.1.2 Directional Stability Metric

The Directional Stability Metric is designed to predict the threshold at which loss of directional stability occurs before yaw stability is lost and the vehicle enters a spin. For a four-wheeled, front-steered vehicle, yaw instability will occur as the rear wheels approach force saturation [61]. The DSM therefore will be defined by the ratio of the total rear axle force to maximum available rear axle force. The maximum available force is defined as the value of the effective coefficient of friction times the weight on the axle. To provide consistency with the RSM, the value of this ratio is normalized, as shown in Eq. 5.13 so that a value of 1 is equivalent to the rest state of the vehicle and a value of 0 predicts imminent spin entry.

$$DSM \equiv \frac{\mu F_{z_F} - F_{y_F}}{\mu F_{z_F}} \tag{5.13}$$

It has been noted by Milliken and Hoffman that the DSM is equivalent to a normalized distance to the line of maximum absolute steering angle on an FMM diagram [10] [61]. This equivalence will be exploited for this work due to the usage of FMM modeling techniques.

5.1.3 Directional Controllability Metric

The Directional Controllability Metric is designed to predict the threshold at which loss of directional control occurs due to the vehicle entering a sliding state. The sliding state may actually be stable but is undesirable as it represents a degradation of or loss of coupling between the control inputs and the vehicle's path. For a vehicle of the type considered in this work, directional controllability is largely dictated by the level of force saturation present at the front axle [61]. Therefore, the DCM will be defined as the ratio of total front axle force to maximum available front axle force. Similarly to the DSM, this value

is normalized (Eq. 5.14) so that a value of 1 is equivalent to rest and a value of 0 indicates slide entry.

$$DCM \equiv \frac{\mu F_{z_R} - F_{y_R}}{\mu F_{z_R}} \tag{5.14}$$

Similarly to the DSM, the DCM is related to the FMM diagram. In this case the DCM is equivalent to the distance from the line of maximum absolute body slip angle and this equivalence can likewise be exploited [61].

5.2 Manifold Generation

One difficulty with the proposed technique of precalculation of FMM maps is that the number of possible combinations of the relevant variables rapidly becomes intractable. For example, using only four variables with a discretation of six values for each variable would require in excess of 1000 separate cases to be individually calculated. While this is possible provided that enough time and computational horsepower is available during precalculation, it is undesirable to store this number of results. This limitation becomes even more severe if the number of variables is increased or if the discretization resolution is increased.

5.2.1 Force Superposition

To make the generation of the IMM more computationally feasible, the principle of linear superposition can be applied. The assumption is made that the maps generated using each of the variables in reference to a baseline configuration can be linearly combined to form a resultant map that is generally equivalent to that which would be generated in a direct calculation using the true variable values. The linear superposition assumption is posited

to hold due to the ability of the FMM technique to transform the effects of each variable into a representation of forces at the wheels. It follows that if the results of all variables are expressed in terms of forces, that these forces can be linearly combined to generate a single set of resultant forces that is equivalent to that generated by direct calculation.

The set of relevant variables, outlined in Table 5.1, includes the locations of the CG in the three spatial dimensions and the coefficient of friction. Conspicuously absent from this list is the sprung mass of the vehicle. An analysis of the equations presented in Chapter 3 reveals that the mass cancels out of the equations and that the final maneuvering manifold can thus be expressed independent of vehicle mass. The force-moment calculations, therefore, are performed on a mass-normalized set of forces and moments.

Table 5.1: IMM Calculation Parameters

Symbol	Parameter Name
μ	Tire-ground coefficient of friction
x_{CG}	Longitudinal CG offset from vehicle frame
y_{CG}	Lateral CG offset from vehicle frame
z_{CG}	Vertical CG offset from vehicle frame

The effects of the CG offsets lend themselves well to application of the superposition technique. A domain for each of the three variables can be chosen based on the known empty vehicle configuration. In most cases, this domain space can be bounded by knowledge of the rated load configurations of the vehicle. A front engine truck with a rear load bed, for example, is unlikely to have a large forward shift in x_{CG} position, but may experience large deviations in the rearward direction. Use of the superposition technique, however, results in the total number of precalculations required to span the domain space being additive instead of multiplicative.

The effect of the COF, μ, is difficult to address using the superposition technique due to its impact on shrinking the available maneuvering space and the increasingly nonlinear behavior of the tires at low COF values. Due to these issues, better results can

be obtained by applying the superposition technique only to the CG position variables. Instead of attempting to superimpose μ, each of the CG variables is instead calculated for each value in the discretized COF domain. This domain is neatly defined by the bins used in the BHF used for friction estimation. For calculation purposes, the center value of each bin was used. The result of this implementation choice is an increase in the of the number of precalculations by a factor equal to the number of friction bins, but this is still far superior to direct calculation of all possible variable combinations.

At a given μ, the effect of each of the CG variables is isolated by subtracting the force profile from the precalculated profile for the empty vehicle for both the lateral force, Y, and the yawing moment, N:

$$Y_{total} = Y_{empty} + (Y_{x_{CG}} - Y_{empty}) + (Y_{y_{CG}} - Y_{empty}) + (Y_{z_{CG}} - Y_{empty}) \tag{5.15}$$

$$N_{total} = N_{empty} + (N_{x_{CG}} - N_{empty}) + (N_{y_{CG}} - N_{empty}) + (N_{z_{CG}} - N_{empty}) \tag{5.16}$$

where $Y_{n_{CG}}$ represents the precalculated force profile for the current estimated CG offset in the n direction. These equations can be simplified by inspection to:

$$Y_{total} = -2Y_{empty} + Y_{x_{CG}} + Y_{y_{CG}} + Y_{z_{CG}} \tag{5.17}$$

$$N_{total} = -2N_{empty} + N_{x_{CG}} + N_{y_{CG}} + N_{z_{CG}} \tag{5.18}$$

An example of the results of a superposition estimation of a force map are shown in Figure 5.1; it can be seen that the superimposed result closely matches a directly calculated map of the same CG offset condition. Further results are presented in Section 6.3.2.

It is important to note as well that this superposition is applied at the force-moment level, not to the final manifold result. This is due to the dependency of the curvature on velocity. By performing the superposition to the force-moment level, it becomes necessary only to precalculate and store the velocity-independent force-moment maps. These

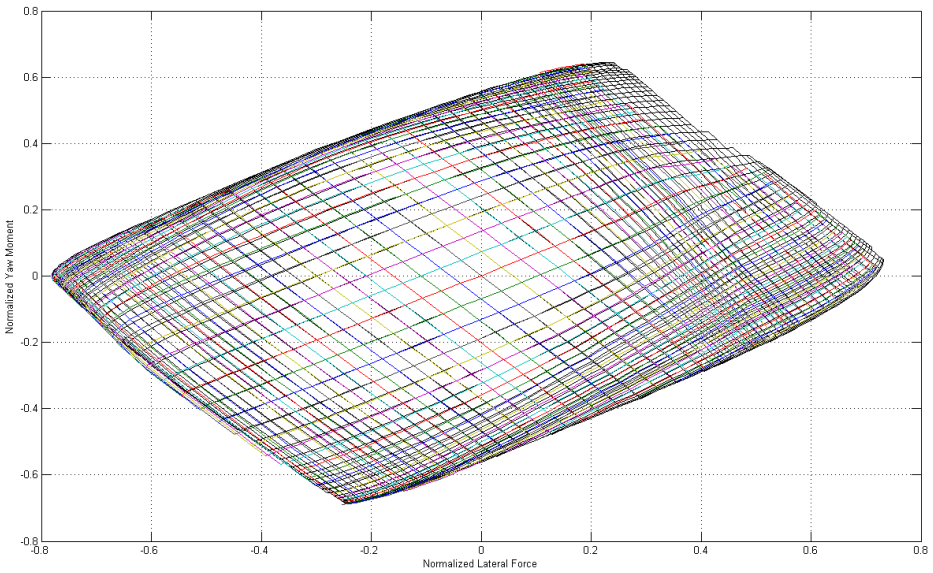

Figure 5.1: FMM force superposition. Note that the result generated by applying superposition (color) closely matches the directly calculated result (black).

can rapidly be transformed as needed to curvatures and rates at the desired velocity once the superposition has been applied.

5.2.2 Metric Masking

After the maps have been superimposed to from the final manifold output, it is necessary to apply the stability metrics to ensure that the vehicle does not attempt to operate in an unsafe region. The metrics could be incorporated into the maps at the initial calculation stage; this is not done, however, because it eliminates the flexibility to adjust the metrics programatically in response to differing conditions.

The metrics are instead applied as a masking function to the manifold: a limit is set and then the metric is mapped across the manifold space in terms of a binary one or zero. The intersection of the acceptable metric domains is then determined and used to mask the manifold. This results in a final output manifold that represents only the safe operating

region for the vehicle.

As stated in Section 5.1, some aspects of the metric calculations can be precalculated. In particular, this applies the the DCM, DSM, and the potential energy portion of the RSM. Similarly to the forces and moments, the principle of linear superposition can be applied to these metric values to compensate for the effects of CG and COF variation. However, unlike in the curvature transformations, a perusal of the metric calculation equations shows that the effects of the vehicle mass do not cancel out. It is therefore necessary to incorporate the estimate of vehicle mass from the CG estimator.

To address this issue, a discretized domain of likely mass values is formulated similarly to those created for the CG parameters. It should be obvious that this domain is lower-bounded by the empty mass of the vehicle and upper-bounded by the maximum gross vehicle weight rating. For each case of CG location and μ, the metric values are precalculated and stored for each value of the mass domain. As the metric calculations are straightforward and do not require additional numerical solver iterations these additional calculations do not add a significant amount of additional computational time, particularly when implemented in a vectorized language such as MATLAB.

The metric values for the current state can then be calculated by applying the superposition from Eqs 5.17-5.18:

$$\overline{RSM}_{total} = -2RSM_{empty} + RSM_{x_{CG},M} + RSM_{y_{CG},M} + RSM_{z_{CG},M} \tag{5.19}$$

$$DSM_{total} = -2DSM_{empty} + DSM_{x_{CG},M} + DSM_{y_{CG},M} + DSM_{z_{CG},M} \tag{5.20}$$

$$DCM_{total} = -2DCM_{empty} + DCM_{x_{CG},M} + DCM_{y_{CG},M} + DCM_{z_{CG},M} \tag{5.21}$$

Equations 5.20-5.21 produce the final estimated metric values for the DSM and DCM. For the RSM, additional steps are required to incorporate the contribution of the kinetic energy and to normalize the metric. Equations 5.2-5.3 must be calculated using the current

state estimates to produce the total rollover energy estimate. This result can then be normalized by applying the superposition technique to the precalculated critical rollover energy, E_{crit}, and applying Eq. 5.12 to produce a resultant normalized value. The validity of superposition to the metric masking problem is illustrated in Figure 5.2.

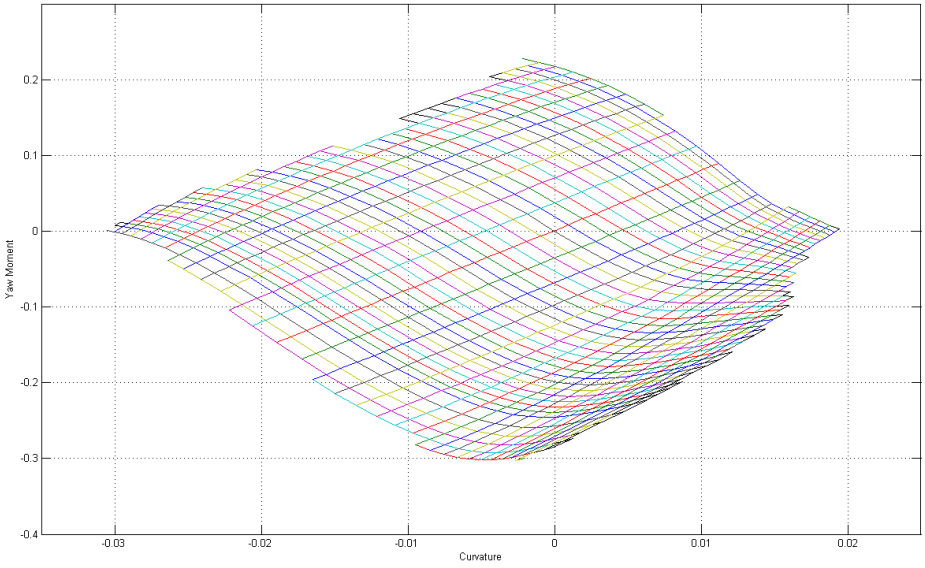

Figure 5.2: Superimposed vs. directly calculated metric mask. Note that this figure appears trivial as the superimposed metric mask (color) almost exactly overlays the directly calculated mask (black).

The final remaining step in metric application is the problem of the selection of appropriate metric thresholds. This is a difficult problem as selection of thresholds that are too conservative will result in severe restriction of the available IMM while too broad of a definition may result in an unacceptable safety risk. The appropriate balance between these two extremes can vary widely across domains. In a military combat situation, for example, a vehicle may be willing to accept a low threshold and risk a chance of rollover in order to move out of an active fire zone whereas in a more benign civilian environment operational safety and vehicle preservation concerns will likely dictate more conservative metric thresholds. Due to the operating domain specificity of the risk management, this

problem is considered beyond the scope of this work. To illustrate the results of metric masking, values will be arbitrarily selected. The results of an example of a manifold before and after metric masking with arbitrarily chosen thresholds of 0.25 for each metric are shown in Figure 5.3.

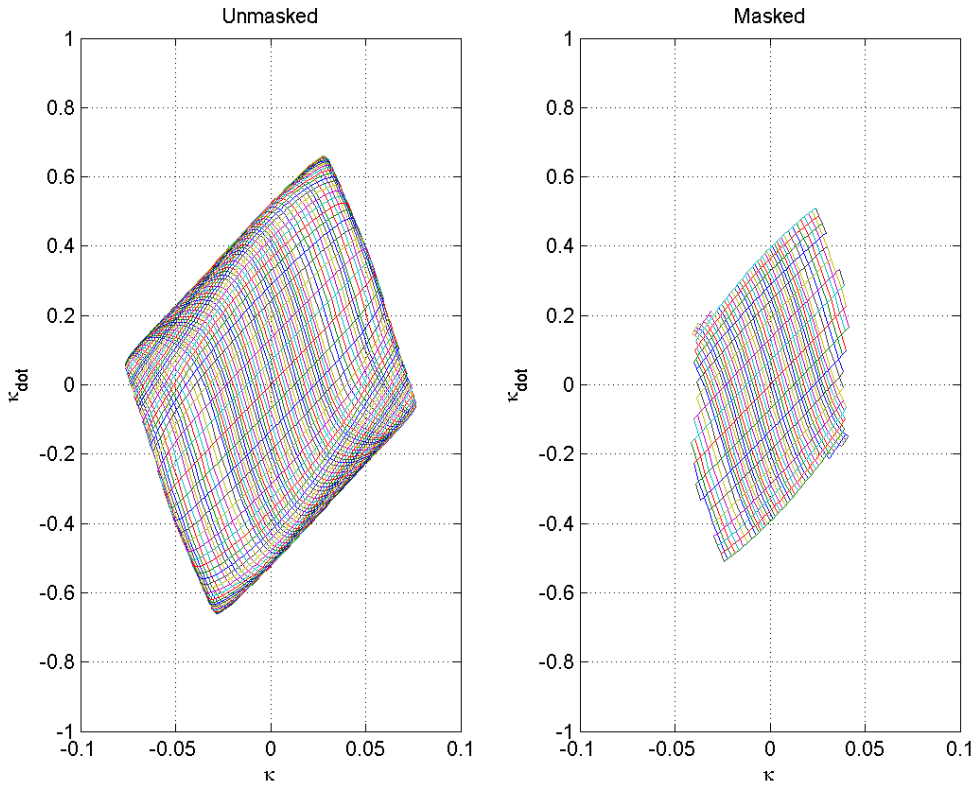

Figure 5.3: IMM before (left) and after (right) metric masking. This example represents the empty vehicle operating at a velocity of 10m/s and road load using metric values of $RSM > 0.75$, $DSM > 0.25$, and $DCM > 0.25$.

5.3 Mapping Summary

Although the various aspects of the algorithm for IMM generation have been discussed, it is instructive to restate the total algorithm. The first part of the algorithm is performed offline before the vehicle is operating.

Offline Algorithm

1. OBTAIN VEHICLE PARAMETERS
2. DETERMINE LIKELY PARAMETER SPACE
3. PRECALCULATE FMM MAPS

The main part of the IMM algorithm is intended to be performed online by the vehicle's onboard computers.

Online Algorithm

1. START STATE ESTIMATION
2. PERFORM CG ESTIMATION MANEUVER
3. STORE CG LOCATION
4. SUPERIMPOSE FMM MAPS FOR CG LOCATION
5. STORE FMM MAPS FOR LOAD STATE
6. WHILE $|V_x| > 0$
7. ESTIMATE INTERNAL STATE
8. ESTIMATE FRICTION COEFFICIENT
9. SELECT FMM FOR FRICTION COEFFICIENT
10. TRANSFORM FMM TO IMM FOR DESIRED V_x AND A_x
11. CALCULATE RSM KINETIC ENERGY AND NORMALIZE
12. APPLY METRIC MASK TO IMM

13. RETURN IMM

14. END WHILE

Application of this algorithm, presented in graphical form in Figure 5.4, allows an unmanned vehicle to predict its dynamic operating manifold based on a best estimate of the load state and tire-ground coefficient of friction. This range is bounded by metrics designed to ensure that the vehicle remains within its stable dynamic operating envelope.

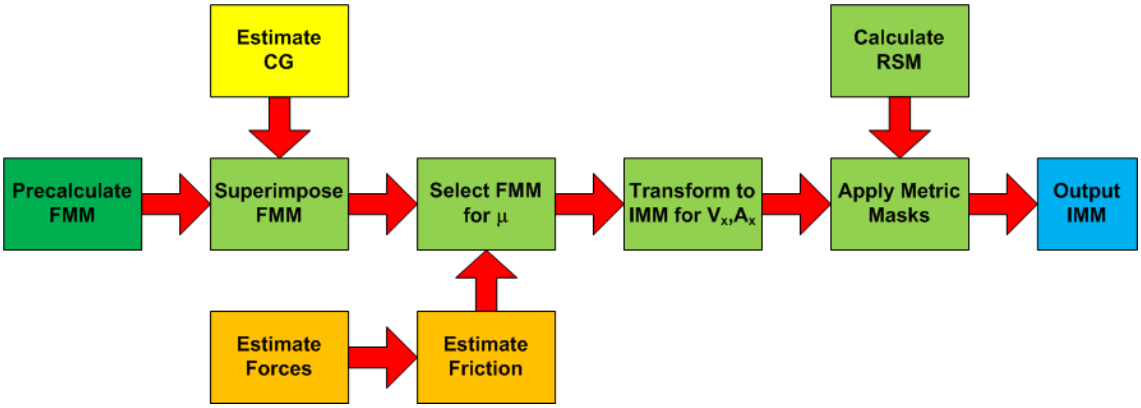

Figure 5.4: IMM generation algorithm. The precalculation step (dark green) is run offline while the light green blocks indicate steps in the online algorithmic loop. The CG estimator is run on demand when a a change in mass is detected while the orange blocks represent the force and friction estimators that are executed continuously in real-time although possibly asynchronously with the IMM loop.

Chapter 6

Results

Never tell people how to do things. Tell them what to do, and they will surprise you with their ingenuity.

–George S. Patton, 1945 [108]

A model of any system cannot be considered valid until its results are compared to similar results obtained from a source of known accuracy. The equations and methodology formulated in Chapters 3-5 were tested in simulation against known, validated commercial models to demonstrate their capabilities to produce the desired results. First the vehicle model is validated, then the state estimator is tested, then the mapping techniques are verified, and finally the ability of the overall system to generate a dynamic IMM is demonstrated.

6.1 Model Validation

Although the model in this work is derived from reputable and well proven sources, it is still necessary to demonstrate that the model, and in particular the FMM representation

of it, can be considered to be accurate. The selected source for comparison is Mechanical Simulation Corp.'s VehicleSIM model, specifically the TruckSIM implementation. This software is a commercially available multi-body dynamics modeling package and is the result of many years of research, testing, and validation. For purposes of this work, therefore, it will be assumed that the results of the of VehicleSIM solver can be considered to be accurate.

6.1.1 Test Methodology

To validate the FMM maps, a built-in TruckSIM model known as the Compact Utility Truck (CUT) was slightly modified and then recreated using FMM techniques. The CUT represents a common class of trucks and was chosen as representing a good compromise between small cars and extremely large trucks. The significant modification to the model was in replacing the motion-profile parameterized implementation of the suspension with a roll-center based representation. This modification is a standard option in TruckSIM and eases the transition of the model to the FMM representation. Full model parameters can be found in Appendix A.

Validation will be performed by using TruckSIM to simulate the CUT using a closed-loop driver model to navigate a course. The control vectors generated by the TruckSIM driver model will then be input into the Simulink model and used to simulate the same course in an open-loop fashion using the FMM representation. If the FMM model perfectly matches the TruckSIM model, the resultant path of this open-loop simulation should be identical to that generated by TruckSIM. The representation will of course not be perfect due to the lower order of the FMM model, but the magnitude of the error will provide an indication as to the accuracy of the model.

For validation purposes, a standard course will be defined and used throughout this chapter. The chosen course is a 3km road course built into the TruckSIM package. This

course includes corners of varying dimensions, as seen in Figure 6.1, and when executed with velocity profiles including positive and negative acceleration is designed to create a range of combined slip conditions. In keeping with the planar world assumption, the course does not include elevation changes. Note that although this course is intended for racing applications, racing is beyond the scope of this work and the driving used for validation is conducted at a more sedate pace.

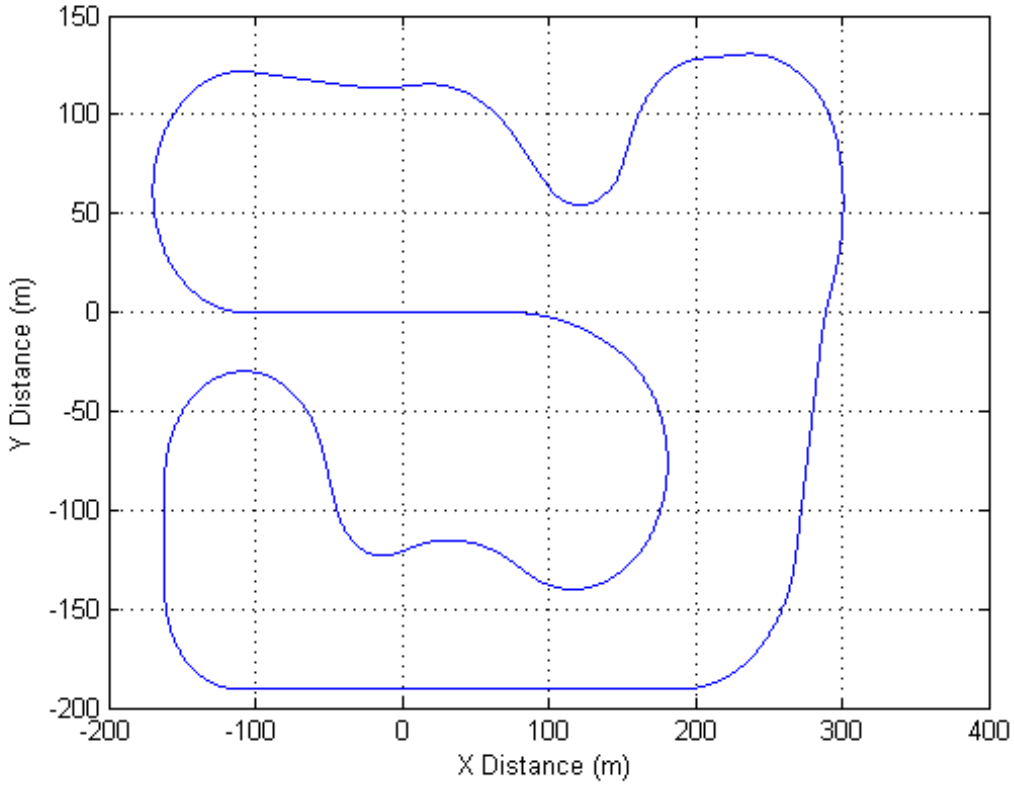

Figure 6.1: Road course used for model validation. This course has a total length of approximately 3km.

In order to conduct the validation, a Simulink model was constructed that was capable of taking a set of control inputs and using the FMM manifold to perform a motion simulation. The Simulink model, as shown in Figure 6.2, takes steering angles and longitudinal velocities as control inputs. A 4-D interpolation for β, δ, V_x, and Ax is then performed

on the curvature FMM data to produce a 1-D array of candidate curvatures for the array of β. The previous step curvature state is then used to perform a 1-D interpolation to determine the resultant value of β. The data is then combined with an array generated by a similar 4-D interpolation on the curvature rate data to solve for the current value of curvature rate. This value is then scaled by the appropriate inertias and integrated to produce a new value of curvature and to update a heading in the global frame. These values of curvature, heading, and β can then be used to solve for the the change in global position. The final output of the Simulink model is thus a path in the global frame generated as a result of control inputs that can be compared to a path generated by the same inputs in the VehicleSIM model.

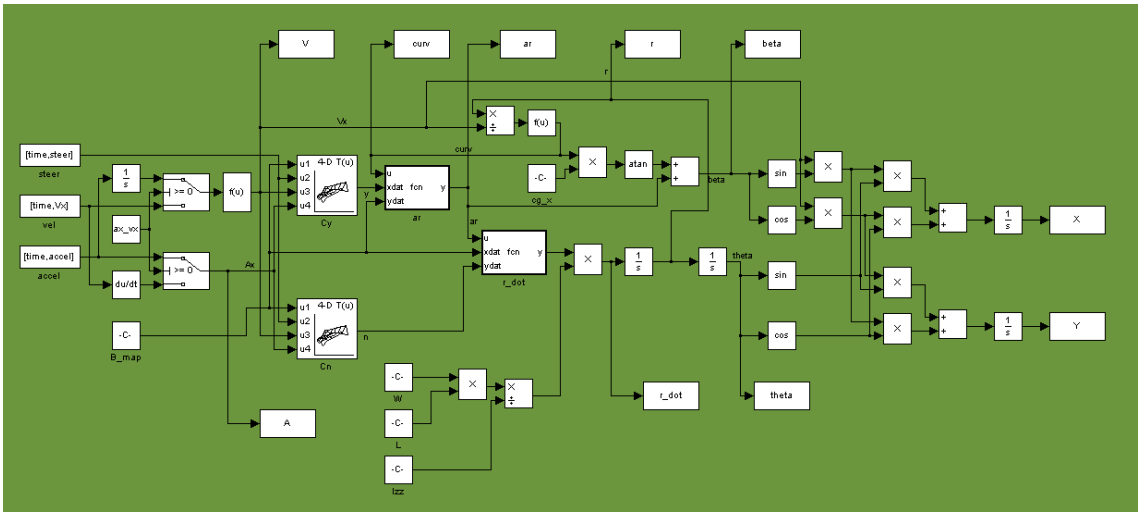

Figure 6.2: Simulink model developed to produce motion simulations from FMM representations of a vehicle.

To demonstrate that the model is accurate across the range of operating parameters, a test grid was developed as shown in Table 6.1. Differing velocity profiles were used to create a range of combined lateral and longitudinal slip conditions. The non-constant velocity profiles are shown in Figure 6.3. In all cases the parameters were set to the same values in both the TruckSIM and FMM representations.

To illustrate the need for an adaptive model, the model for the empty vehicle was

Table 6.1: Model Validation Grid

Name	Velocity Profile	μ
Case 1	30kph	1.0
Case 2	Profile 1	1.0
Case 3	Profile 2	1.0
Case 4	50% Throttle	1.0
Case 5	30kph	0.5

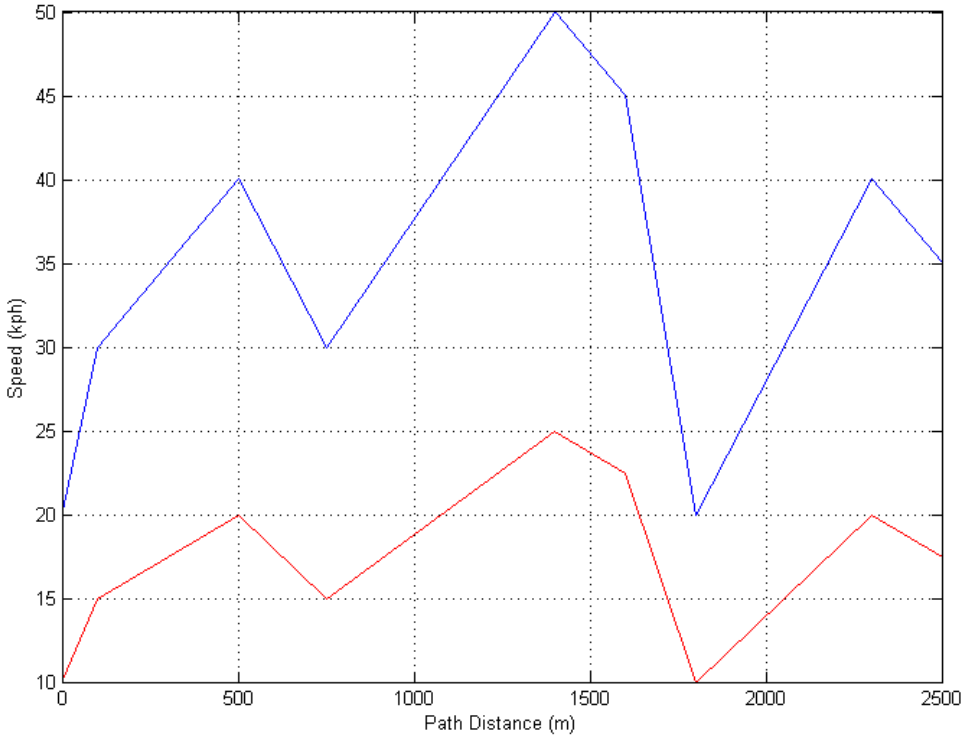

Figure 6.3: Velocity profiles for model validation. Profile 1 (red) uses velocities that are half the magnitude of Profile 2 (blue).

simulated against TruckSIM results generated using differing CG heights and masses as shown in Table 6.2. All tests were performed using the standard validation course and Velocity Profile 1.

Table 6.2: Simulation Variation Grid

Name	CG Height	Sprung Mass
Case 1	0.50m	1000kg
Case 2	0.75m	1000kg
Case 3	0.50m	1500kg
Case 4	0.75m	1500kg
Case 5	0.50m	2000kg
Case 6	0.75	2000kg

6.1.2 Comparison Results

Each case from Table 6.1 was simulated in both TruckSIM and Simulink. Results of several representative runs can be seen in Figure 6.4.

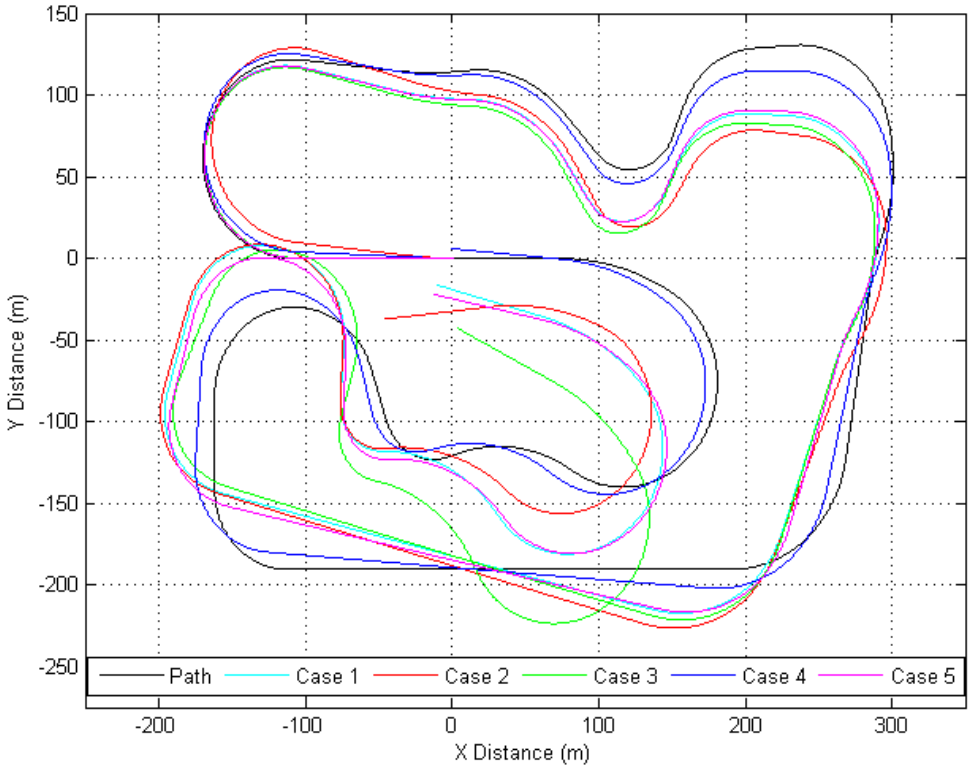

Figure 6.4: Comparison of simulation results from TruckSIM (black) and Table 6.1. Note that the Simulink model runs were conducted in an open loop form meaning that cumulative path error is not corrected.

Table 6.3: Model Validation Results

Name	Mean Path Error	Mean Relative Path Error
Case 1	41.4m	3.8%
Case 2	44.5m	5.0%
Case 3	52.2m	4.4%
Case 4	11.3m	1.7%
Case 5	38.3m	3.5%

It can be seen from the results that the open-loop implementation of the FMM model generally matches the TruckSIM simulation. Due to the open-loop nature of the FMM model implementation, the tracks from the two models will be inherently divergent as there is no mechanism for correcting accumulated error. However, despite this limitation, the FMM model produces the correct profile and the maximum offset error at the endpoint is 52.5m, which is less than 2% of the total distance traveled. The most telling statistic is probably the mean relative path error which is defined as the path error divided the total travel distance. For all cases this measurement is at or below 5% error. Considering the simplified nature of the FMM model, this result is considered acceptable for approximating vehicle performance in this application. Lower errors could likely be attained if desired by adding additional parameters into the FMM generation algorithm; this approach is supported by the method as the final FMM output format is independent of the number of parameters used to generate it.

The results from the TruckSIM model variation test are shown in Figure 6.5 and statistics are provided in Table 6.4. As a result of the differing handling characteristics, the control inputs required to produce the same handling output vary. These results show clearly the divergent error that is introduced by incorrect assumptions about the mass of the vehicle and the location of the CG. Although autonomous systems typically do not perform this type of long-range open-loop simulation, the significance of this result would be realized if the FMM model were to be used to in a feed-forward controller. Also note that the parameters varied in this result represent the best case from the handling perspective;

changes in CG height and mass would be expected to have a lower impact than changes in the lateral and longitudinal CG locations. As is shown in Section 6.3.1, these changes actually have a greater impact on stability, particularly rollover stability.

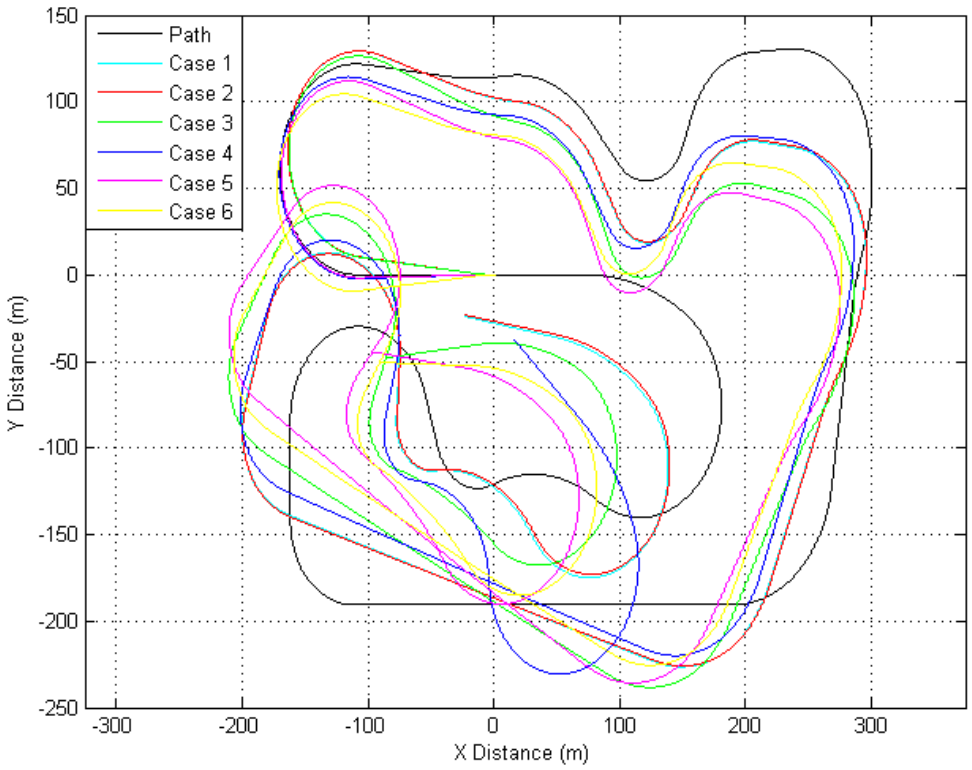

Figure 6.5: Results of TruckSIM model variation. Note that the TruckSIM models with differing parameters produce different sets of control inputs resulting in the FMM model tracks diverging from the track of the empty vehicle (cyan) and the true path (black).

Table 6.4: TruckSIM Model Variation Results

Name	Path Error	Relative Path Error	Deviation from Nominal
Case 1	47.7m	5.3%	N/A
Case 2	46.6m	5.2%	1.2m
Case 3	71.2m	7.4%	27.0m
Case 4	61.3m	5.1%	25.3m
Case 5	86.1m	7.5%	45.7m
Case 6	74.9m	7.2%	36.1m

6.2 Parameter Estimation

The implemented parameter estimation filter was tested in simulation to evaluate its ability to estimate parameters correctly. The CUT model in TruckSIM was used as the simulated test vehicle. The use of simulation is preferred fore testing the estimator due to the ability to know exactly the parameters used in the simulation.

6.2.1 Test Methodology

Using TruckSIM's built-in capability to define virtual sensors, the model was augmented with simulated sensors designed to emulate the sensor suite on an autonomous vehicle. The virtual sensors simulate an IMU, GPS, steering sensors, and wheel encoders. To simulate realistic sensor noise, noise levels were recorded on an real autonomous vehicle (Virgina Tech's Rocky) and then random noise with similar characteristics was superimposed on the noiseless TruckSIM outputs. This vehicle is equipped with a NovAtel SPAN-CPT GPS/IMU system with a dual frequency L1/L2 band GPS and a 6-axis IMU. Identified noise characteristics are shown in Table 6.5.

Table 6.5: Simulated Noise Levels

Variable	Noise σ
A_x	2E^{-4}
A_y	2E^{-4}
V_x	3E^{-2}
V_y	3E^{-2}
$\dot{\theta}$	2E^{-5}
ϕ	1E^{-2}
$\dot{\phi}$	2E^{-5}
z_{w_1}	1E^{-2}
z_{w_2}	1E^{-2}
z_{w_3}	1E^{-2}
z_{w_4}	1E^{-2}
δ	1E^{-2}

The noise was implemented by superimposing a zero-mean Gaussian noise signal with a standard deviation given by Table 6.5 onto the TruckSIM outputs. The noise signals were generated using MATLAB's `randn` function. For cases in which multiple noisy runs were made, the noise was randomly regenerated for each run.

6.2.2 CG Estimation

To test the capability of the CG estimator, the vehicle was simulated through the standard identification maneuver described in Figure 4.10. The values of each of the key CG parameters (x_{CG}, y_{CG}, and z_{CG}) were varied by 0.05, 0.1, 0.2, and 0.4 meters to discover the sensitivity of the method. These tests were conducted using the simulated noise; to remove statistical effects each test was repeated 100 times with random noise sources. Results of these tests are presented in Figures 6.6-6.8.

It is also significant to note here that results for mass estimation are not shown. In this method, the mass is determined by direct measurement of the Suspension Position Sensor and knowledge of the spring rates. Since it is assumed that the mass can only change when the vehicle is at rest and as a result of the planar world assumption, this result becomes nearly trivial and dependent only on the accuracy of the SPS and the spring rate measurements. Since these results are shown in simulation the mass result will always be correct within these bounds and will not reveal the accuracy of this measurement on a real vehicle.

The results show that the CG estimator is capable of accurately determining the value of the longitudinal location of the CG. In all cases the estimated value of x_{CG} is within 1% of the true value. Variation in this parameter does not show coupling with the other parameters in that variation in x_{CG} does not appear to change the estimates of the lateral and vertical estimates.

The estimator shows the capability to estimate the lateral CG offset nearly as accu-

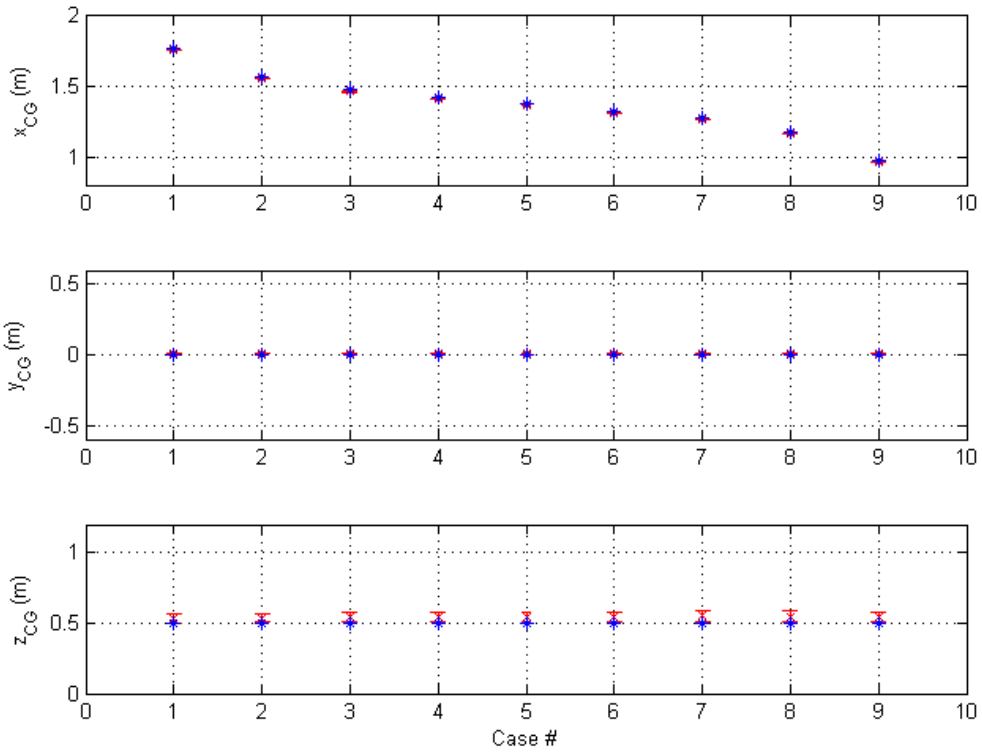

Figure 6.6: Results of CG estimation with varying x_{CG} values. The blue stars represent the true value of the parameter in TruckSIM. The red *x*s are plotted with error bars representing the 3σ value of the noise variation across the simulations. Note that in this figure the results nearly overlay the true values.

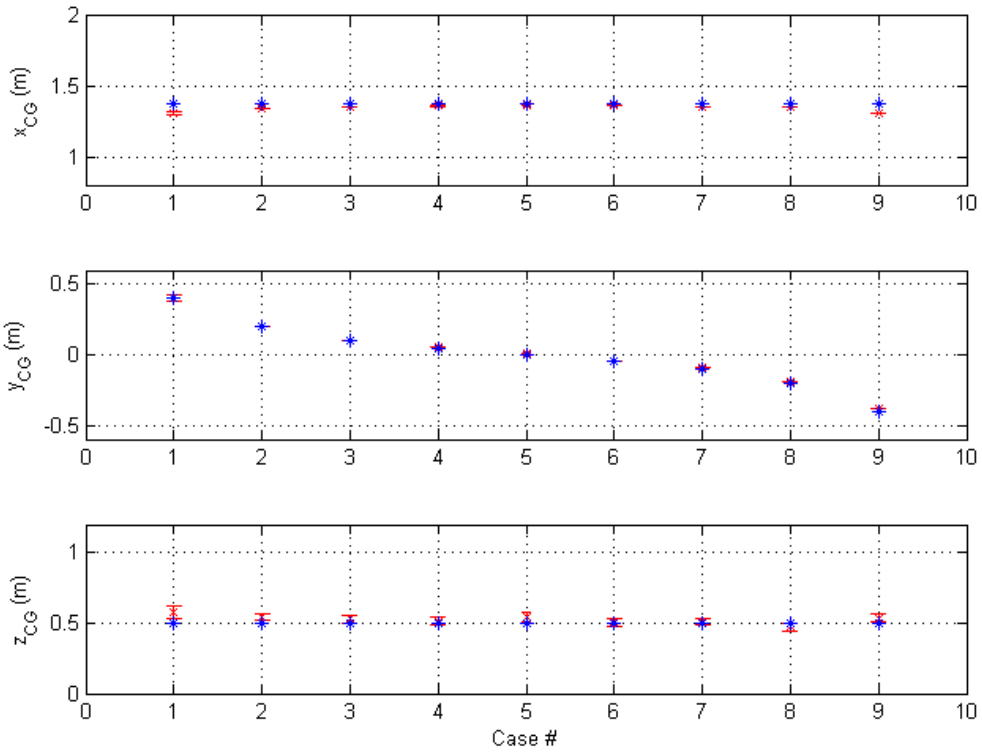

Figure 6.7: Results of CG estimation with varying y_{CG} values. The blue stars represent the true value of the parameter in TruckSIM. The red *x*s are plotted with error bars representing the 3σ value of the noise variation across the simulations. Note that in this figure the results nearly overlay the true values.

rately as the longitudinal location. Due to the smaller absolute magnitude of lateral offsets the error as a percentage varies from ¡1% to 20%, but the actual magnitude error in all cases is less than 20cm. It is interesting to note that high values of lateral offset exhibit a coupling with the longitudinal estimate. As the value of the lateral offset increases, the estimate of the longitudinal location tends to decrease below the actual value. This coupling makes sense in a physical sense as a lateral offset will induce a moment about the roll axis that will induce a weight transfer.

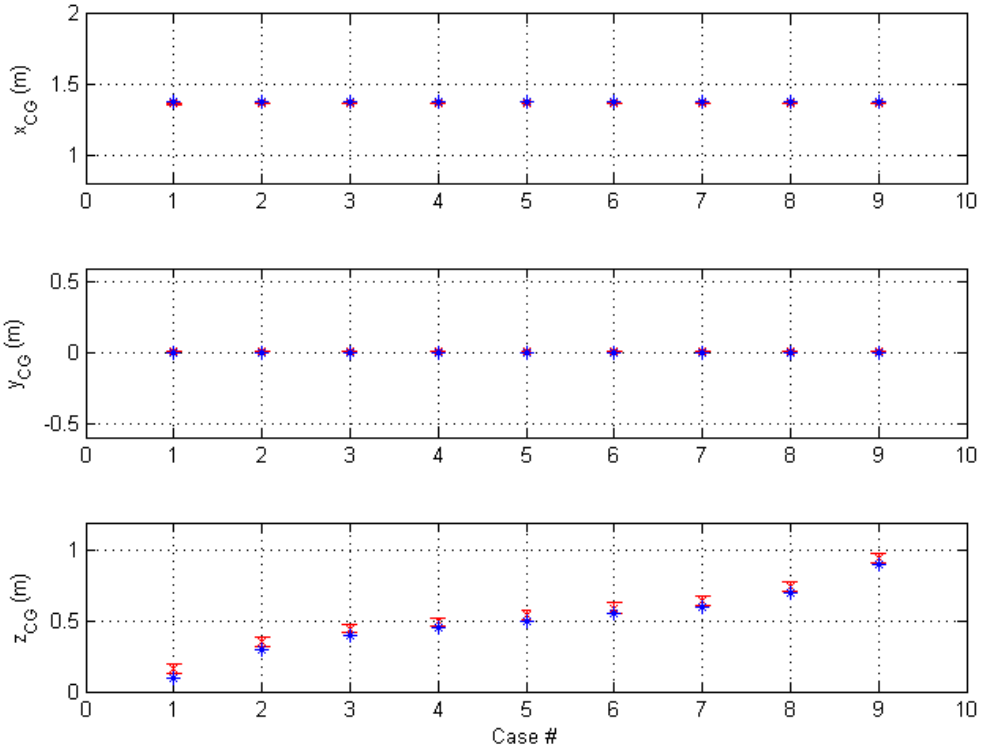

Figure 6.8: Results of CG estimation with varying z_{CG} values. The blue stars represent the true value of the parameter in TruckSIM. The red *x*s are plotted with error bars representing the 3σ value of the noise variation across the simulations. Note that in this figure the results nearly overlay the true values.

Estimates of the vertical CG position tend to be less accurate than the lateral and longitudinal estimates. This is to be expected as the vertical offset suffers from observability

problems that do not affect the horizontal measurements. The vertical CG location can only be observed when the vehicle is maneuvering while the horizontal locations can be measured at rest using the SPS measurements. As a result, the z_{CG} measurements tend to overstate the CG height by a fairly constant amount of roughly 50cm. In the context of autonomy, this offset occurs in the more acceptable direction as a higher estimate of CG height will result in a lower estimated stability and more conservative maneuver selections. No significant coupling effect were observed with variation in CG height.

A further test was conducted to determine the impact of the CG determination maneuver on the results. To test this, the vehicle was simulated using the standard maneuver at 5, 10, and 20 kph as well as a circle determined by a 20-degree steering angle at the same speeds. The tests were conducted on the empty vehicle and, as before, the tests were repeated 100 times to remove statistical effects. Results are shown in Figure 6.9.

Variations in the estimation maneuver show that capability is not significantly increased by increasing the speed of the maneuver or by changing the maneuver to a circular configuration. This would tend to indicate that the recommended 5kph maneuver provides sufficient excitation for this method to accurately determine the CG location. This result is surprising as is the overall capability of the CG estimator. Estimates of the mass and horizontal CG locations can be determined largely from the SPS measurements and should not require maneuvering to obtain accurate estimates. However, estimation of the vertical CG location requires excitation to achieve observability and the overall level of lateral acceleration excitation in the prescribed maneuver is very low. The performance of this method is most likely due to the high fidelity of the measurement from the simulated PES but could be an artifact of simulation, which raises questions as to the performance on real vehicles. Unfortunately, circumstances do not permit the application of this method to a real vehicle and validation of this method outside of simulation will be left as future work.

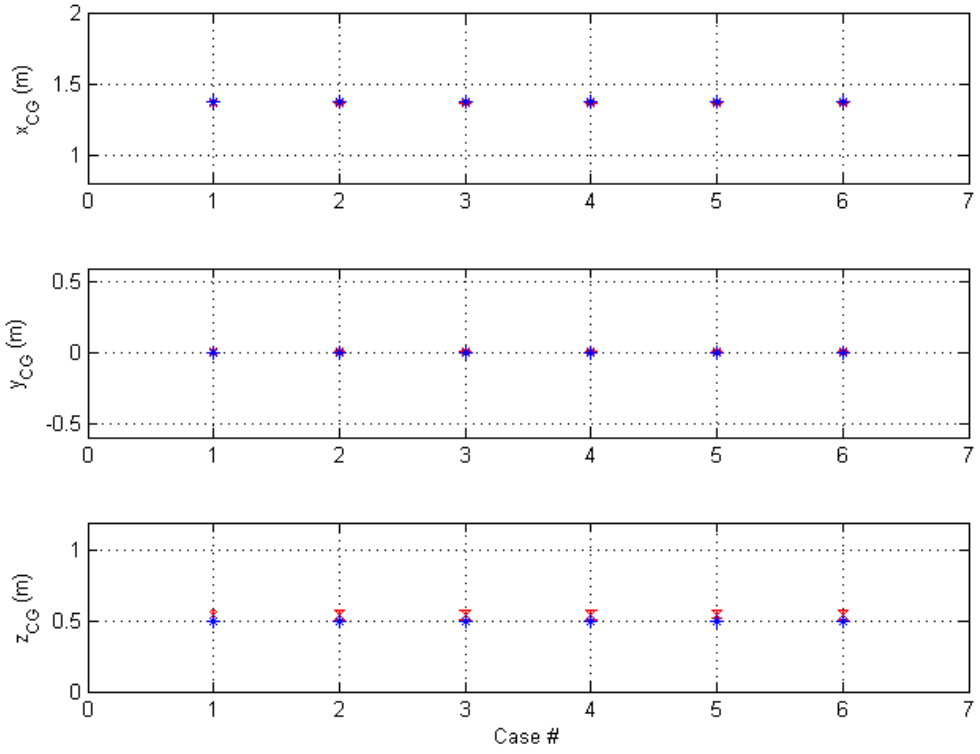

Figure 6.9: Results of variation in the CG estimation maneuver. The blue stars represent the true value of the parameter in TruckSIM. The red *x*s are plotted with error bars representing the 3σ value of the noise variation across the simulations. Note that in this figure the results nearly overlay the true values.

6.2.3 Force Estimation

To test the capability of the state estimator, the empty vehicle was simulated over the standard test course using Velocity Profile 2 and a unity COF. The higher speed velocity profile was chosen to increase the excitation levels and push the vehicle closer to its limits. To eliminate statistical effects, the state estimator was run 100 times on the simulation data using the noise levels from Table 6.5. Results of these runs are presented in Figures 6.10-6.20.

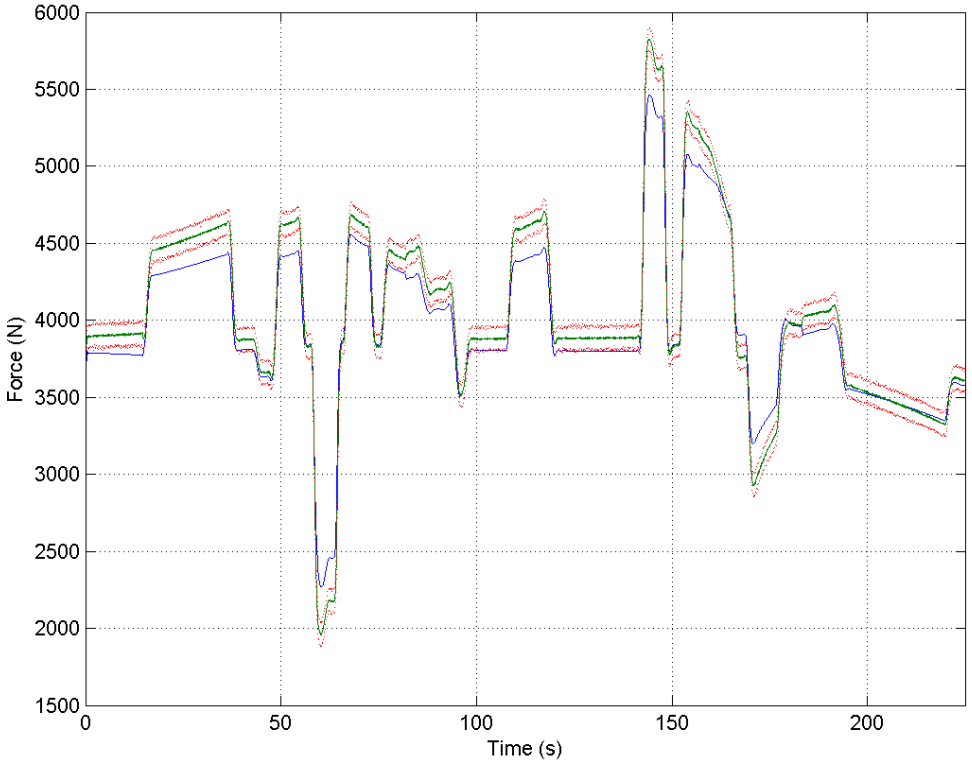

Figure 6.10: Estimated vertical force for front left wheel. Blue line represents true value of state from TruckSIM. Green line represents mean value of estimate from 100 simulations. Red dotted lines represent 3σ confidence intervals based on distribution across the simulations.

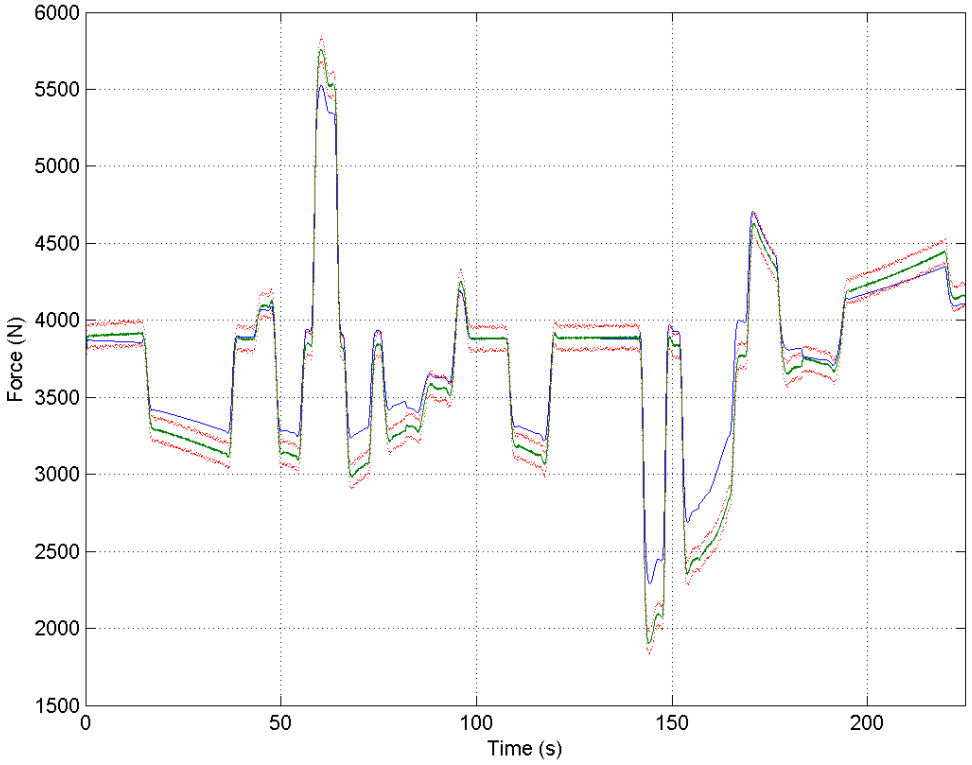

Figure 6.11: Estimated vertical force for front right wheel. Blue line represents true value of state from TruckSIM. Green line represents mean value of estimate from 100 simulations. Red dotted lines represent 3σ confidence intervals based on distribution across the simulations.

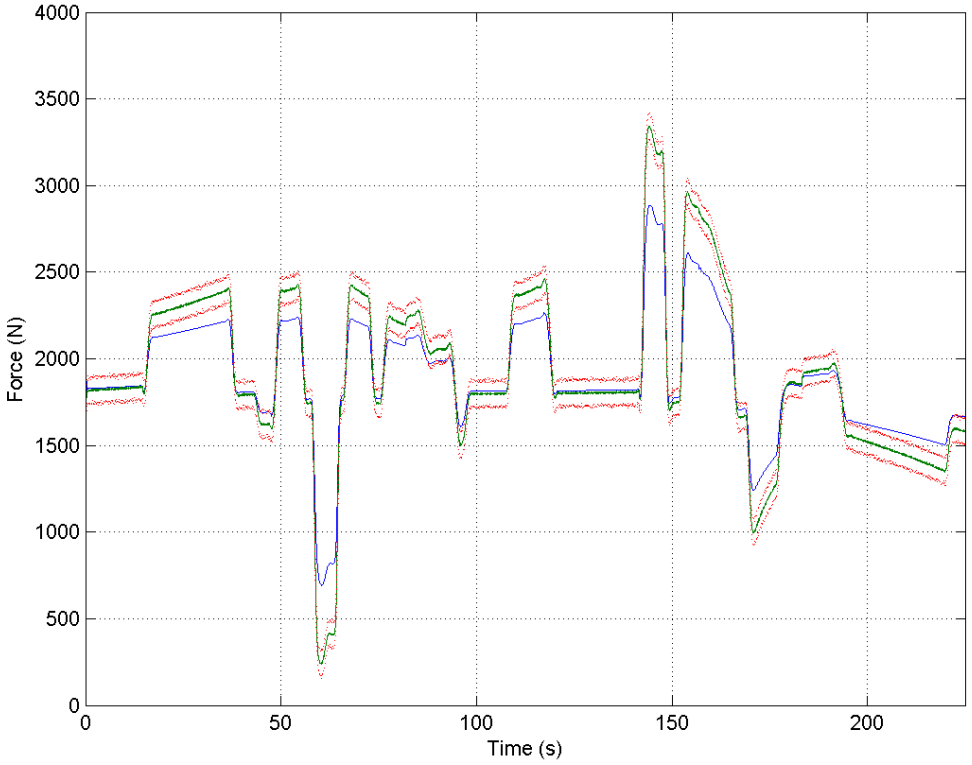

Figure 6.12: Estimated vertical force for rear left wheel. Blue line represents true value of state from TruckSIM. Green line represents mean value of estimate from 100 simulations. Red dotted lines represent 3σ confidence intervals based on distribution across the simulations.

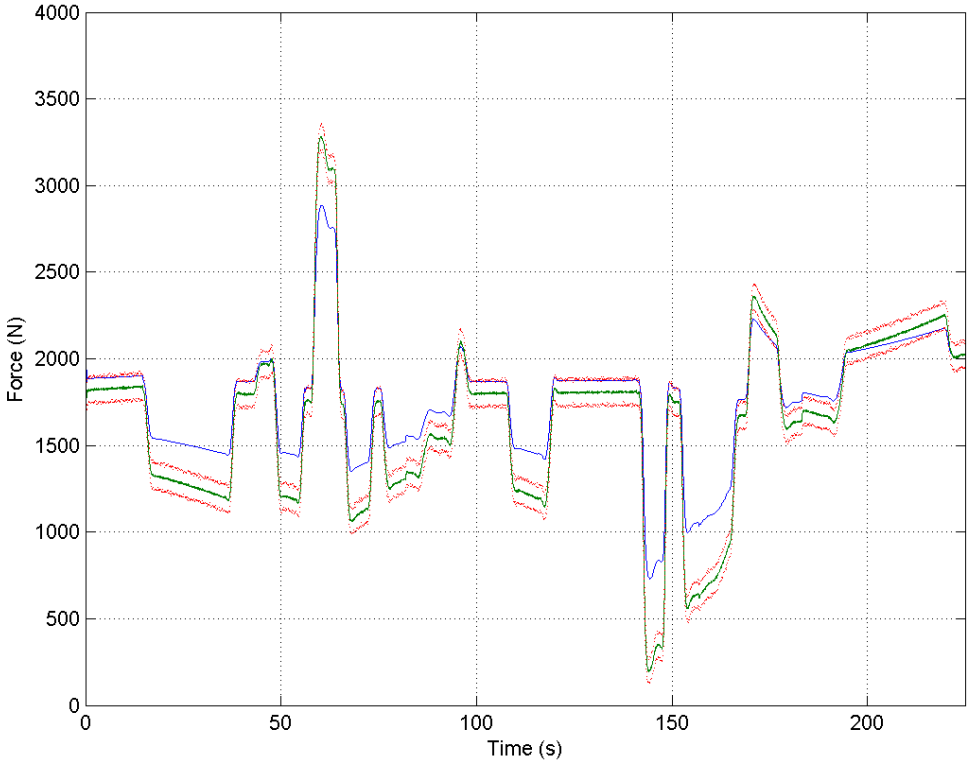

Figure 6.13: Estimated vertical force for rear right wheel. Blue line represents true value of state from TruckSIM. Green line represents mean value of estimate from 100 simulations. Red dotted lines represent 3σ confidence intervals based on distribution across the simulations.

Vertical Forces

The results show that the force estimator tends to slightly overestimate the vertical wheel forces, likely due to the simplifications in the conversion of the suspension displacement sensors to forces. To achieve higher accuracy, it would be necessary to take into account other factors such as suspension kinematics and bushing compliances. While it is certainly possible to do this, in practice addition of these factors would require extremely precise knowledge of the vehicle. If higher accuracy is required it may also be possible to calibrate out this offset on a real vehicle.

Despite the DC offset, the vertical force estimator shows a capability to successfully predict changes in the forces due to maneuvering. Largely due to the use of the SPSs, an estimate can be achieved with fairly high confidence and low noise levels, as shown by the mean error of 116N and mean standard deviation of 25N.

Since lateral load transfer is the largest component of the load transfer, it is also instructive to plot the total lateral load transfer, as shown in Figure 6.14. The lateral load transfer follows the same trend as the individual wheel weights, producing a slight overestimation while correctly estimating the proper trends.

Horizontal Forces

In addition to the vertical load, estimation of the longitudinal and lateral forces is important for friction estimation. As previously noted, the estimator uses a bicycle representation for horizontal force estimation. The results therefore are available only at each axle and not for the individual wheels as in the vertical force estimator.

Due to the RWD nature of the simulated vehicle, the only significant front axle longitudinal forces are rolling resistance, which is of low magnitude, and the braking forces, which tend to be of much higher magnitudes. As a result, the estimator is able to achieve an estimate of the front axle forces with a mean absolute error of 12N, a maximum error

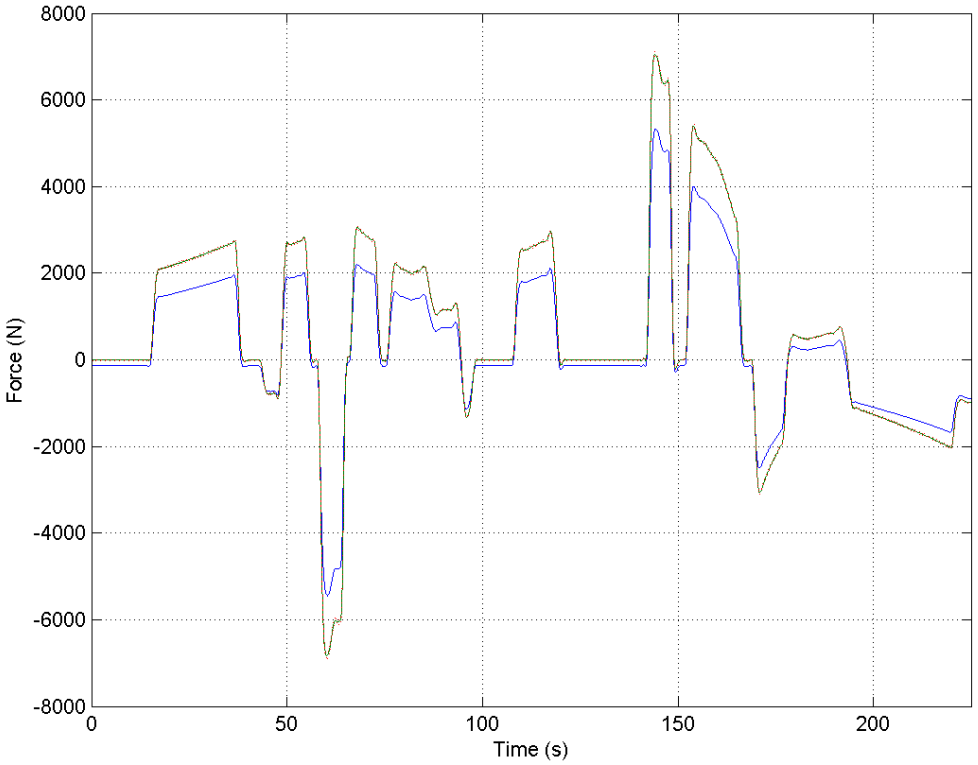

Figure 6.14: Estimated total lateral load transfer. Blue line represents true value of state from TruckSIM. Green line represents mean value of estimate from 100 simulations. Red dotted lines represent 3σ confidence intervals based on distribution across the simulations.

of 82N, and a standard deviation of 7N, as shown in Figure 6.15.

The rear axle longitudinal force estimates, shown in Figure 6.16, are significantly noisier than the front axle estimates. A portion of this increase in uncertainty can be attributed to the addition of the drive torque on this axle, for which there is no direct measurement available. The resulting estimates have a mean absolute error of 11N, a maximum error of 222N and a mean standard deviation of 14N.

As the major component of the longitudinal force in most driving conditions is generated by the rear axle on a RWD vehicle, it should be expected that the estimate of the total longitudinal force would be dominated by this component. As shown in Figure 6.17, this is generally the case. However during the hard braking maneuver that occurs from

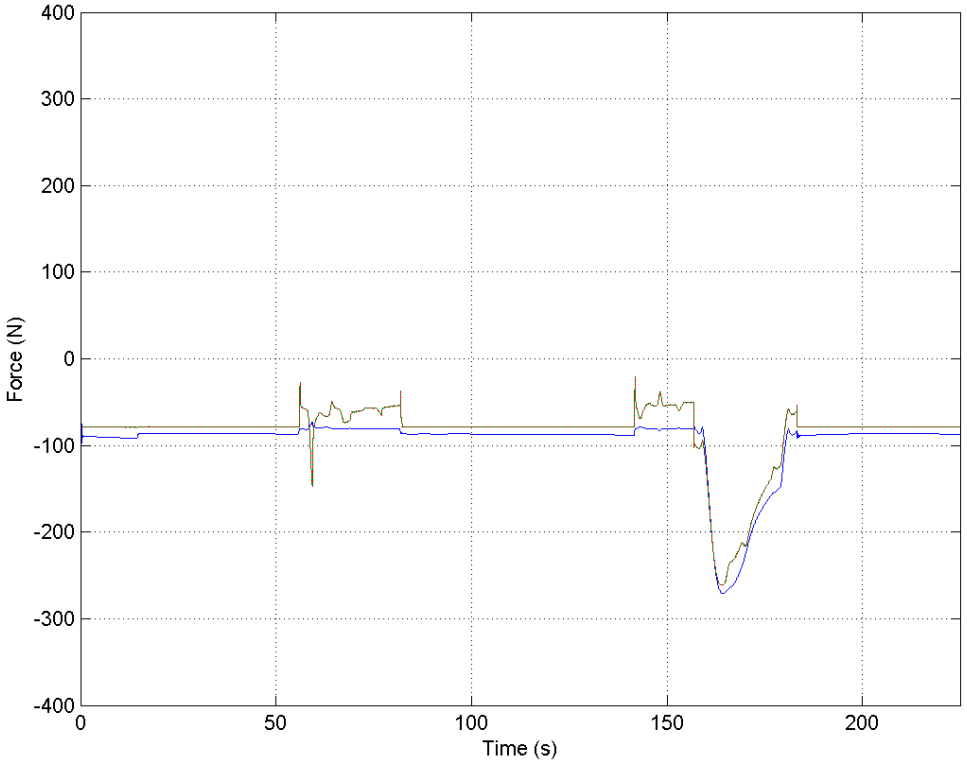

Figure 6.15: Estimated longitudinal force for the front axle. Note that this was simulated for a RWD vehicle. Blue line represents true value of state from TruckSIM. Green line represents mean value of estimate from 100 simulations. Red dotted lines represent 3σ confidence intervals based on distribution across the simulations.

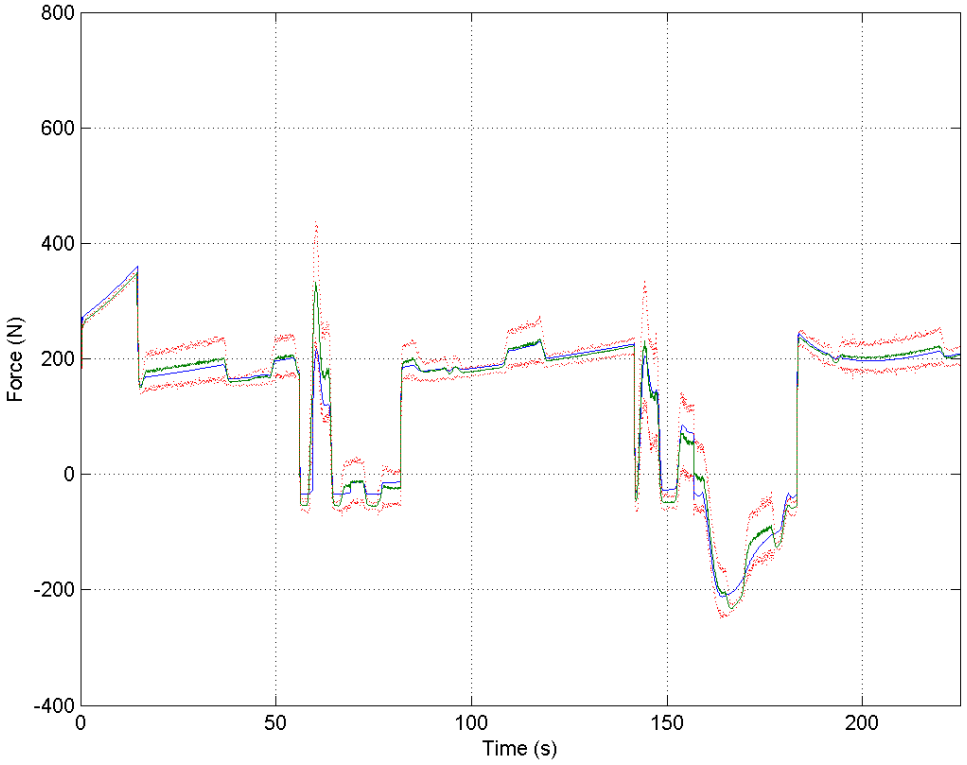

Figure 6.16: Estimated longitudinal force for the rear axle. Note that this was simulated for a RWD vehicle. Blue line represents true value of state from TruckSIM. Green line represents mean value of estimate from 100 simulations. Red dotted lines represent 3σ confidence intervals based on distribution across the simulations.

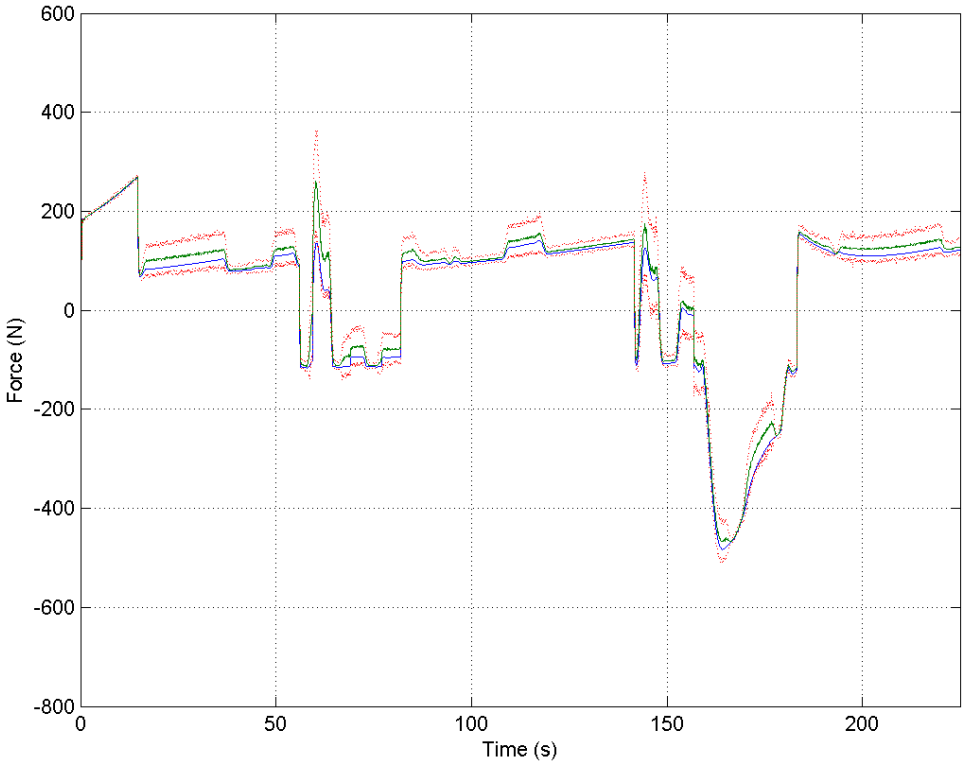

Figure 6.17: Estimated total longitudinal force. Blue line represents true value of state from TruckSIM. Green line represents mean value of estimate from 100 simulations. Red dotted lines represent 3σ confidence intervals based on distribution across the simulations.

160-180s the accuracy of the overall force estimate is increased by the contributions of the front axle. Overall, the estimator demonstrates a reasonable capability to estimate the longitudinal forces generated by the vehicle in combined slip operating conditions.

As shown in Figure 6.18, the lateral force estimator produces accurate estimates of the lateral force at the front axle with a mean absolute error of 86N, a maximum error of 914N and a standard deviation of 90N. The overall noise levels are higher than the longitudinal force estimates and the confidence intervals are larger.

The estimates of the lateral force on the rear axle, shown in Figure 6.19, are noisier than those on the front axle. This is due primarily to the lack of the strong force driver such as the steering angle present on the front axle. The mean absolute error is 70N, the

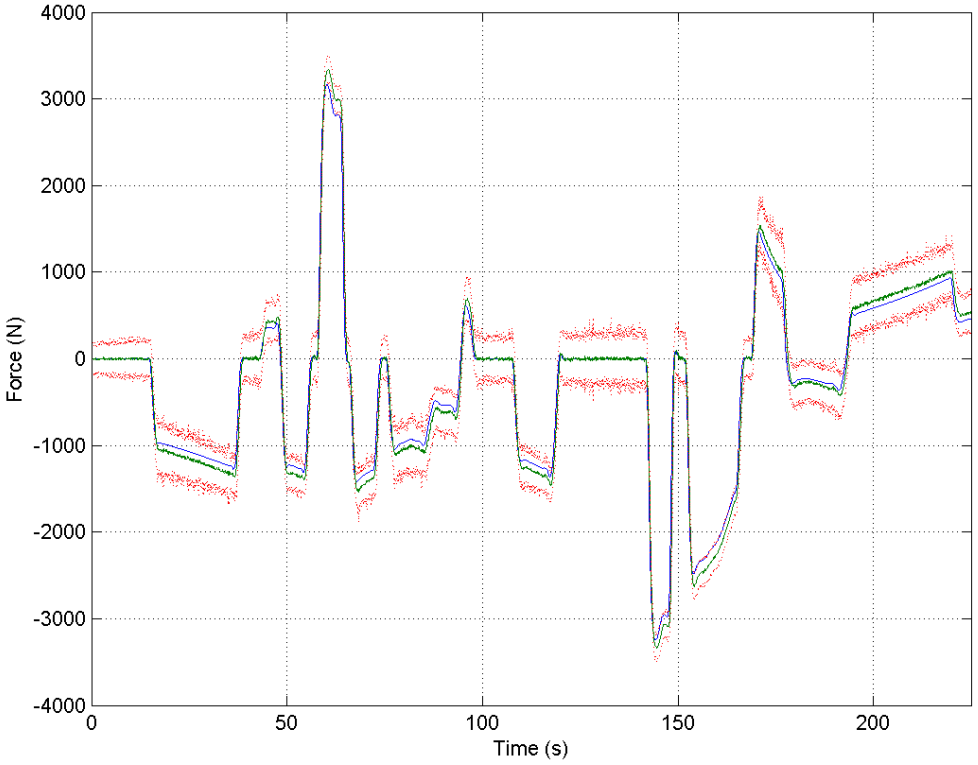

Figure 6.18: Estimated lateral force for the front axle. Note that this vehicle has front-wheel steer only. Blue line represents true value of state from TruckSIM. Green line represents mean value of estimate from 100 simulations. Red dotted lines represent 3σ confidence intervals based on distribution across the simulations.

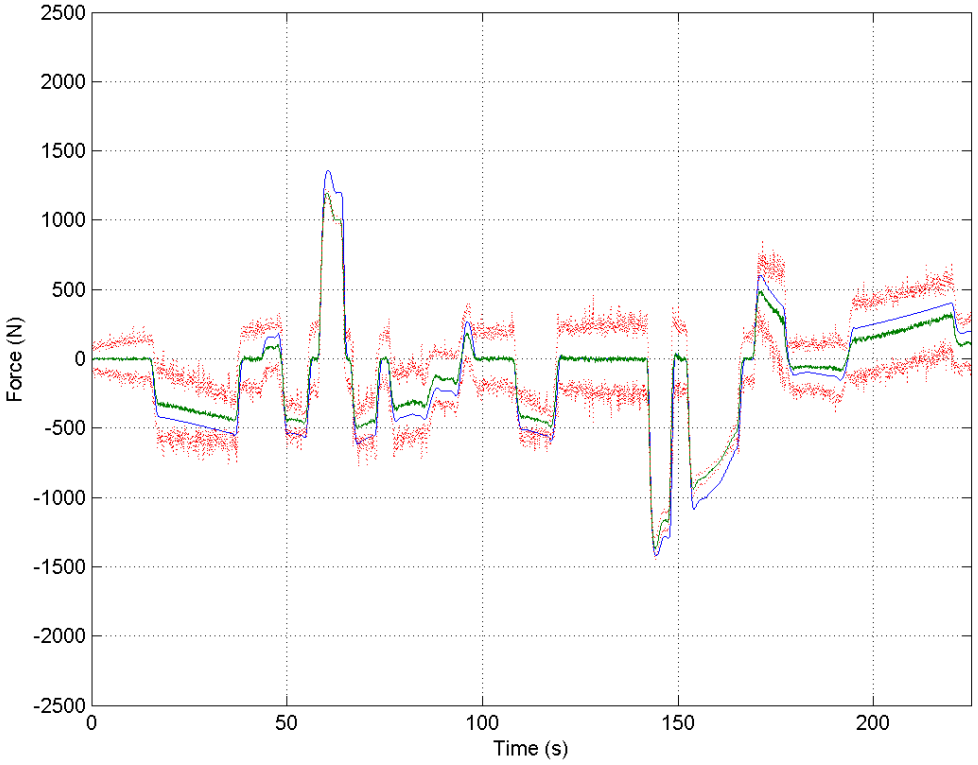

Figure 6.19: Estimated lateral force for the rear axle. Note that this vehicle has front-wheel steer only. Blue line represents true value of state from TruckSIM. Green line represents mean value of estimate from 100 simulations. Red dotted lines represent 3σ confidence intervals based on distribution across the simulations.

maximum error is 450N, and the standard deviation is 53N.

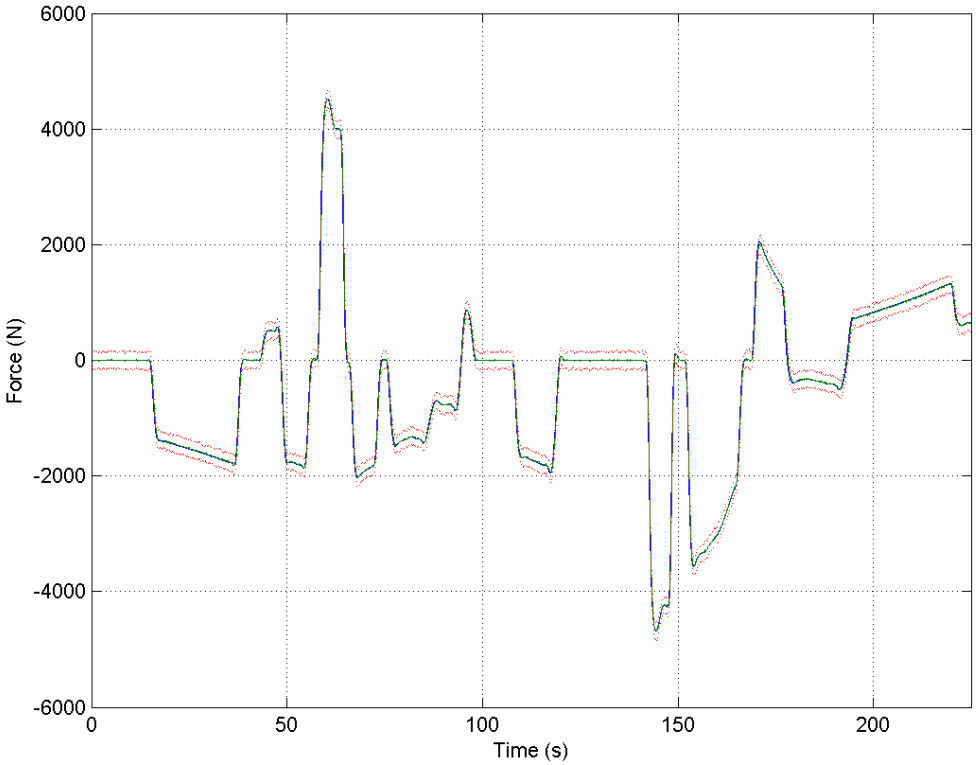

Figure 6.20: Estimated total lateral force. Blue line represents true value of state from TruckSIM. Green line represents mean value of estimate from 100 simulations. Red dotted lines represent 3σ confidence intervals based on distribution across the simulations.

The results of total lateral force estimation, Figure 6.20, show that the estimate of total lateral force is extremely accurate and much less noisy that those of either of the components. This indicates that the estimation of the total vehicle motion from which the lateral force estimates are derived is accurate, but that the distribution of this force between the two axles is much less certain. A primary driver of the uncertainty in the distribution is the lack of highly accurate dynamic slip angles. The values produced by Eqs. 3.7-3.10 are approximations that do not take into account factors such as caster change and pneumatic trail in calculating the exact location of the CTC. A more accurate approximation, such as that given by Kiencke, would likely produce more accurate distribution results [93].

Noise Sensitivity

Additionally, the impact of the simulated sensor noise levels on the estimates should be quantified. To test this, the estimation tests were rerun with noise levels one order of magnitude higher and one order of magnitude lower than the estimated realistic levels from Table 6.5. The variable representing the lateral force on the front wheels, F_{y_F} was chosen as a representative result, but other results show similar trends. The low noise result, Figure 6.21, and high noise result, Figure 6.22, can be compared to the same variable plotted in Figure 6.18.

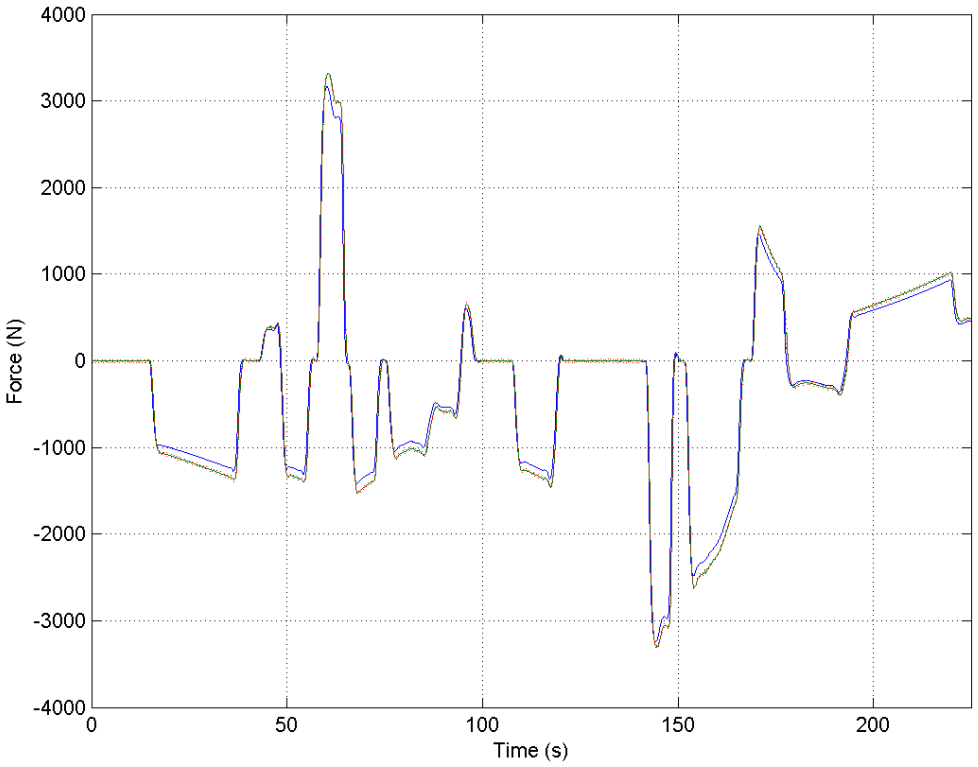

Figure 6.21: Estimated lateral force for the front axle. Note that the mean noise levels are much lower and the confidence intervals much tighter than in Figure 6.18. Blue line represents true value of state from TruckSIM. Green line represents mean value of estimate from 100 simulations. Red dotted lines represent 3σ confidence intervals based on distribution across the simulations.

The results show that, unsurprisingly, estimates using less noisy sensors produce better results. Of more interest are the results from the high noise case. The mean estimate follows the correct general trends, but the noise levels and the confidence intervals are extremely large. In practice, the values generated at this level of sensor noise would be nearly unusable, a point that emphasizes the value of the highly precise sensors present in autonomous systems.

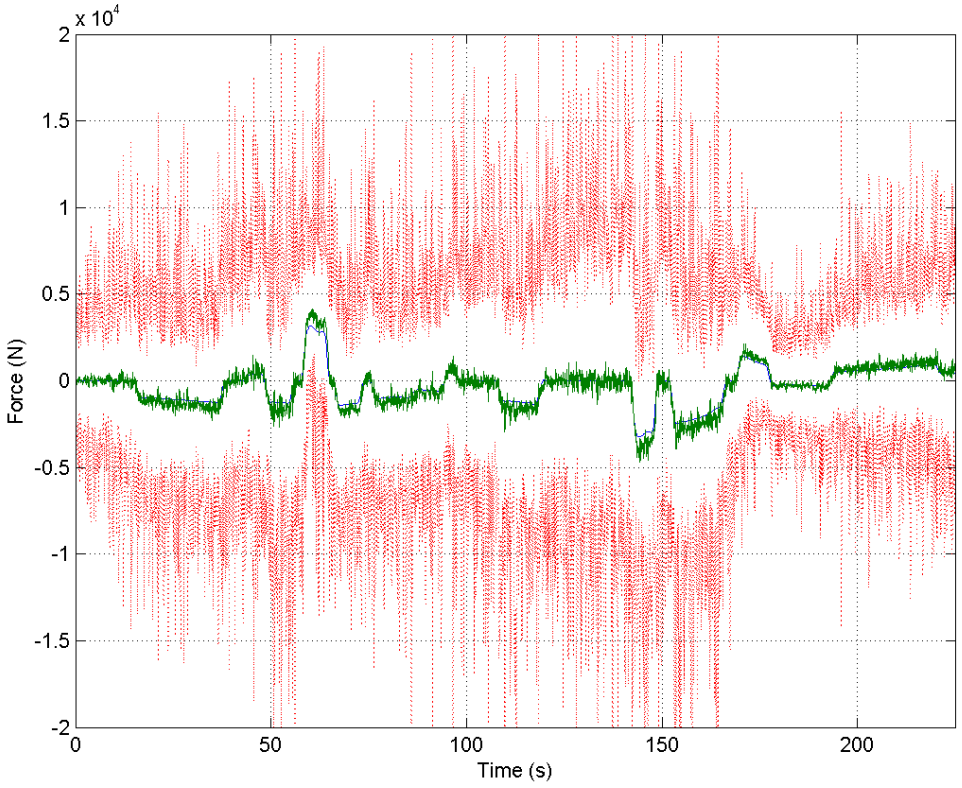

Figure 6.22: Estimated lateral force for the front axle. Note that while the mean estimate is generally correct in terms of trends, it is extremely noisy and the confidence bounds are extraordinarily high. Blue line represents true value of state from TruckSIM. Green line represents mean value of estimate from 100 simulations. Red dotted lines represent 3σ confidence intervals based on distribution across the simulations.

It is significant to note that the estimates, particularly the vertical force estimates, are likely to be significantly noisier on a real vehicle due to the presence of stochastic road

excitations. As the primary goal of this work is not to develop robust state estimation, testing with stochastic road excitations and implementation of more robust estimators is left as future work.

6.2.4 Friction Estimation

To validate the friction estimator, the vehicle was simulated over the test course under the conditions shown in Table 6.6. The higher COFs are run at two different speeds to show the impact of excitation levels on friction estimation. The friction values selected are the midpoints of the bins given in Table 4.5. The lower COFs were unable to be run at higher speeds as the vehicle could not complete the course under these conditions. As with the state estimator, the results were repeated 100 times to eliminate statistical effects. Results of these tests are shown in Figures 6.23-6.28.

Table 6.6: Friction Test Matrix

Name	Velocity Profile	μ
Case 1	Profile 1	0.88
Case 2	Profile 2	0.88
Case 3	Profile 1	0.63
Case 4	Profile 2	0.63
Case 5	Profile 1	0.38
Case 6	Profile 1	0.13

The results for Cases 1-4 show that, in general, the excitation levels are not high enough to accurately detect the COF when its value is in the upper two bins. Only in a few maneuvers did the the estimate and excitation limit reach high enough to allow the estimate to converge to the true value and this probability was rapidly degraded in subsequent maneuvers. Cases 2 and 4, which used the lower speed velocity profile, never provided sufficient excitation to achieve an accurate estimate.

Estimator performance was somewhat better in the lower friction regimes. In Case 5, excitation was still an issue due to the low operating speed. Had this speed been

slightly higher, it is likely that the estimate would have converged largely to the correct value. Case 6 had sufficient excitation across the entire run to provide an estimate. The majority of the time, the estimator was able to accurately determine the correct COF. In one increment, however, a falsely high estimate caused the filtered response to jump to a higher bin and remain at this level for an extended period. Further tuning of the parameters of the BHF may be able to reduce the frequency of this type of error.

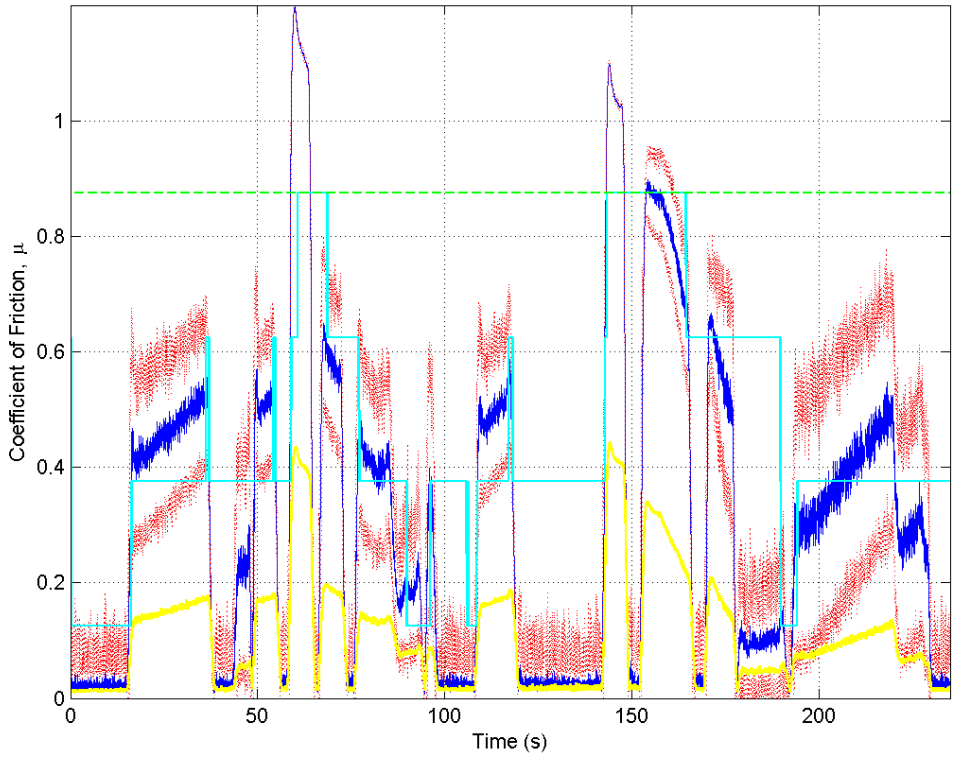

Figure 6.23: Friction estimation results for Case 1. The dark blue line represents the mean value of the pneumatic trail estimator and the red lines represent 3σ confidence intervals from 100 simulations. The light blue line is the output from the BHF estimator using the yellow estimated excitation. The green dashed line is the actual coefficient of friction.

A further test was conducted to show the capability of the friction estimator to rapidly detect changes in the COF. The vehicle was simulated driving at a constant speed of 45 kph around a 500ft radius circle, which was the maximum sustainable speed at the

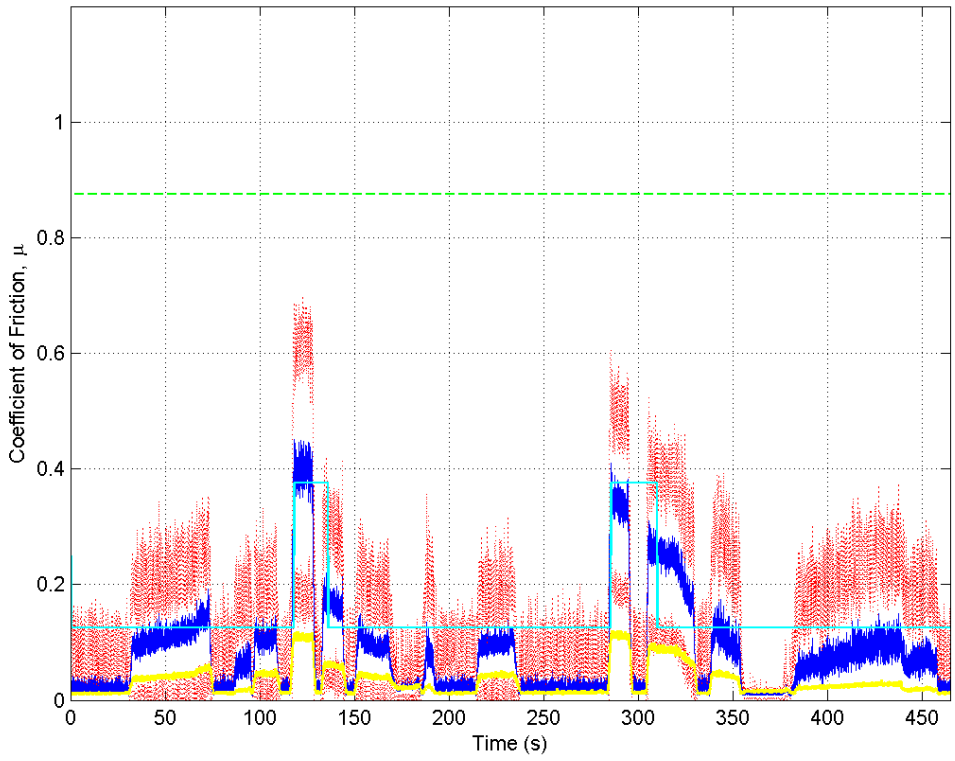

Figure 6.24: Friction estimation results for Case 2. The dark blue line represents the mean value of the pneumatic trail estimator and the red lines represent 3σ confidence intervals from 100 simulations. The light blue line is the output from the BHF estimator using the yellow estimated excitation. The green dashed line is the actual coefficient of friction.

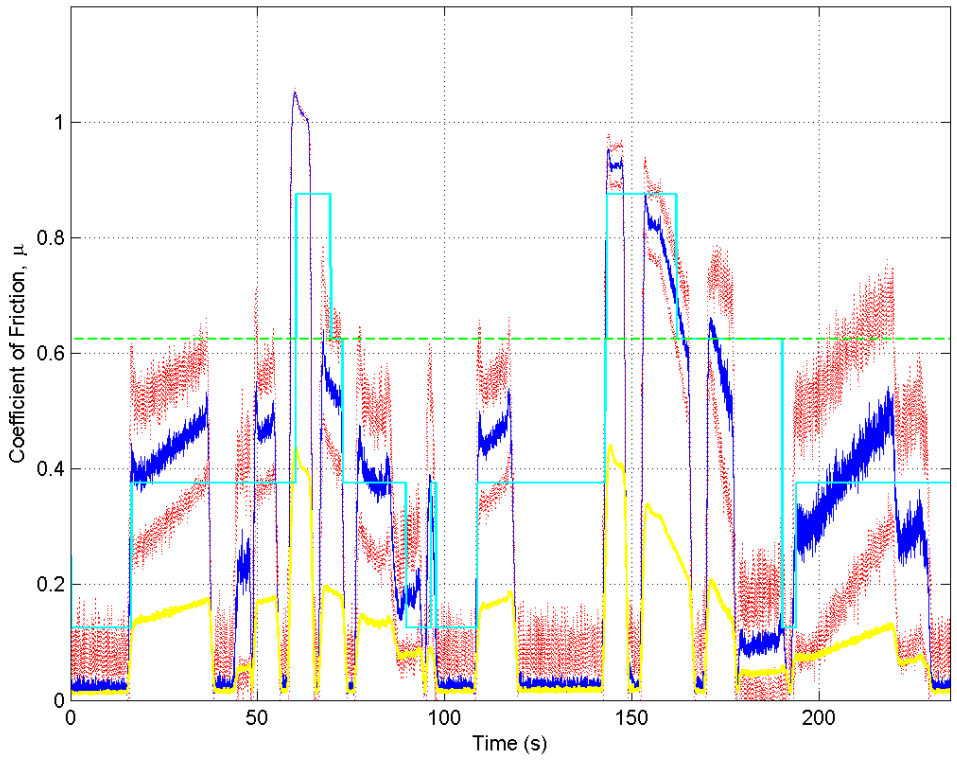

Figure 6.25: Friction estimation results for Case 3. The dark blue line represents the mean value of the pneumatic trail estimator and the red lines represent 3σ confidence intervals from 100 simulations. The light blue line is the output from the BHF estimator using the yellow estimated excitation. The green dashed line is the actual coefficient of friction.

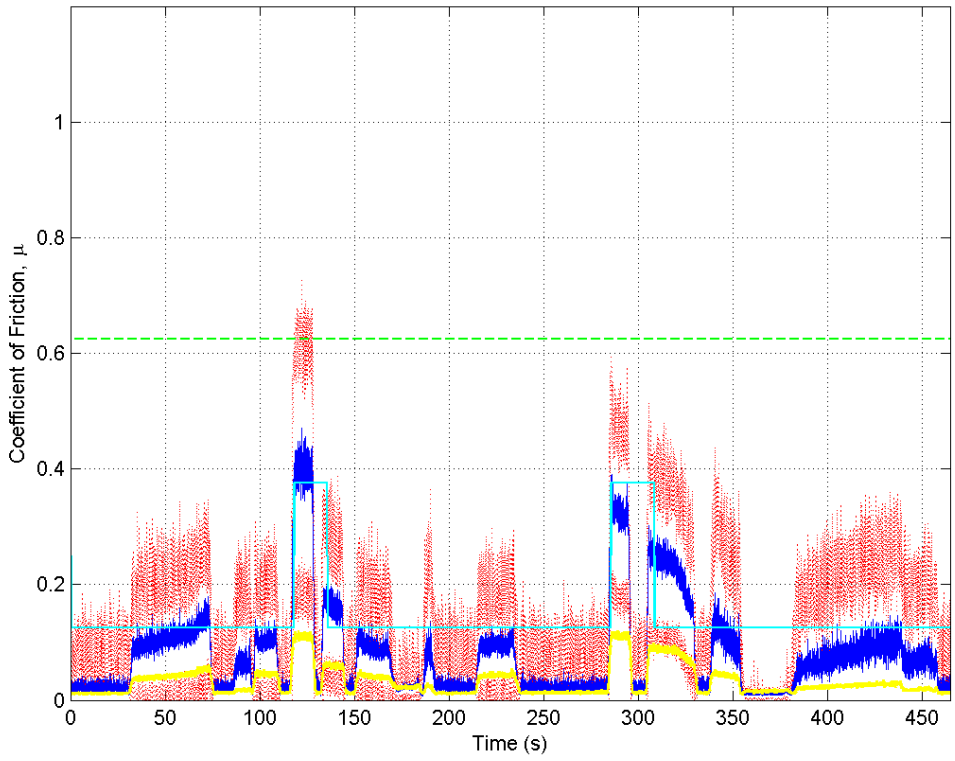

Figure 6.26: Friction estimation results for Case 4. The dark blue line represents the mean value of the pneumatic trail estimator and the red lines represent 3σ confidence intervals from 100 simulations. The light blue line is the output from the BHF estimator using the yellow estimated excitation. The green dashed line is the actual coefficient of friction.

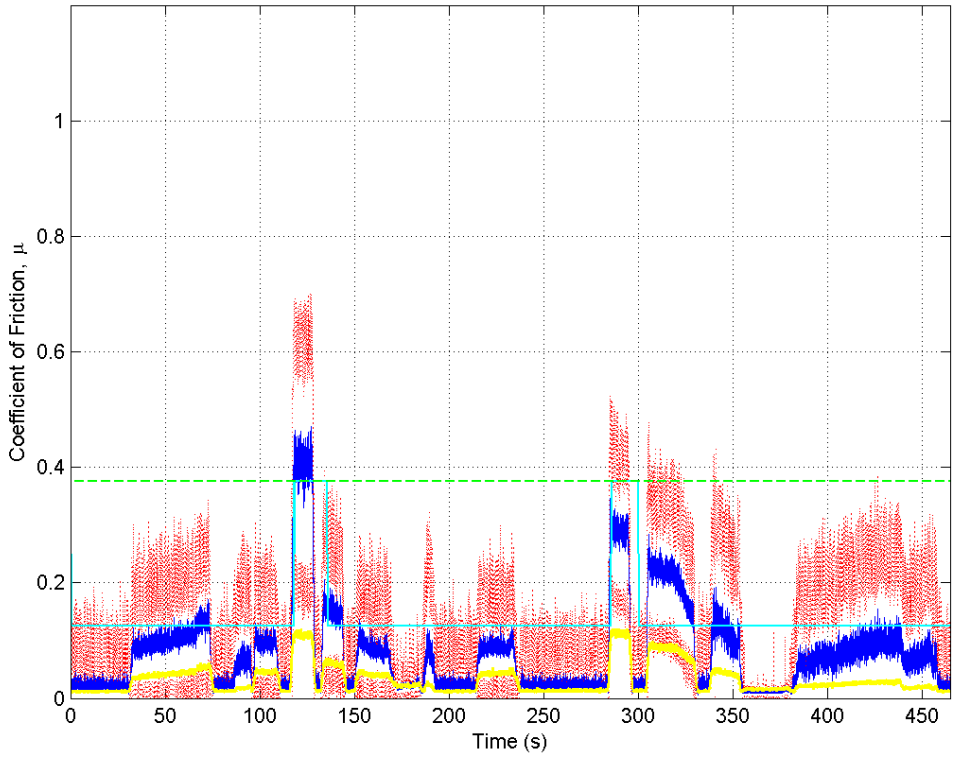

Figure 6.27: Friction estimation results for Case 5. The dark blue line represents the mean value of the pneumatic trail estimator and the red lines represent 3σ confidence intervals from 100 simulations. The light blue line is the output from the BHF estimator using the yellow estimated excitation. The green dashed line is the actual coefficient of friction.

lowest COF. The COF was varied around the circle with each quadrant having a different value. Results of this test are shown in Figure 6.29 and demonstrate that the estimator is capable of detecting changes in COF, provided that sufficient excitation is available. An additional issue raised by these results is the proper level of damping in the BHF. In this case the detection of the drop by the BHF is delayed by the damping. The proper level of damping to hold estimates in times of low excitation versus change detection performance is operationally dependent but is an important consideration in real applications. [1]

The major limitation of the friction estimator is the lack of excitation in normal driv-

[1] update me?

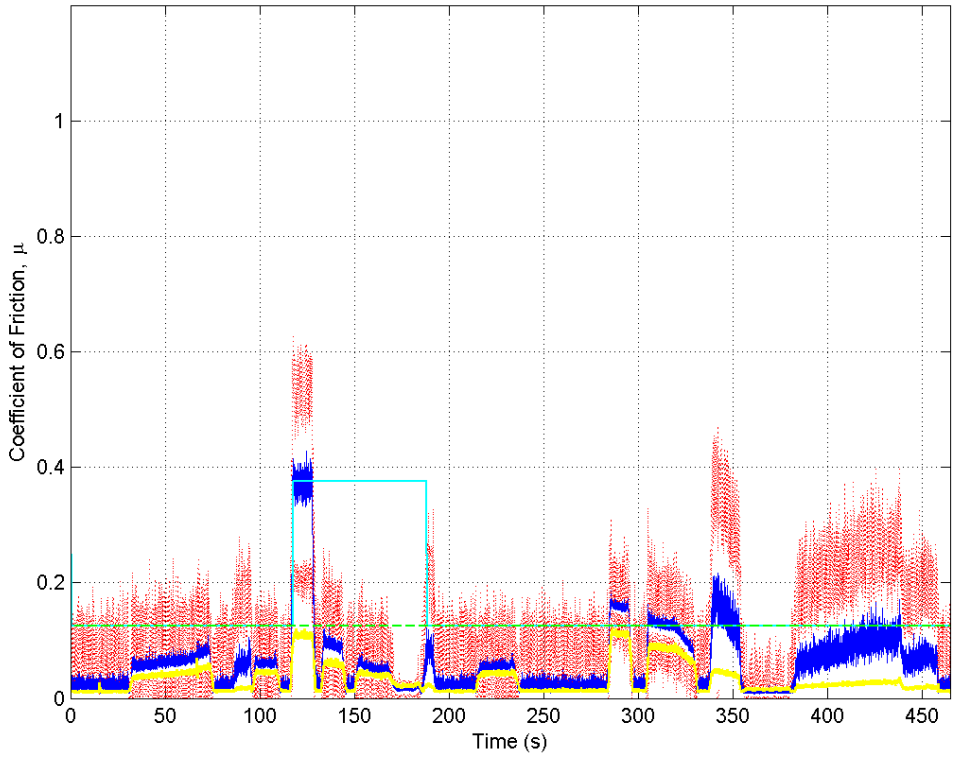

Figure 6.28: Friction estimation results for Case 6. The dark blue line represents the mean value of the pneumatic trail estimator and the red lines represent 3σ confidence intervals from 100 simulations. The light blue line is the output from the BHF estimator using the yellow estimated excitation. The green dashed line is the actual coefficient of friction.

ing conditions. The pneumatic trail technique shows better capability to operate at low excitation than other known proprioceptive methods, but this capability is still clearly insufficient to provide accurate estimates at higher values of COF. Given the high noise levels in the estimates, the ability of the BHF to filter the estimates based on excitation level and to probabilistically maintain estimates in periods of low excitation appears to be effective. Discovery of an optimal method for tuning of the BHF parameters would likely provide a further increase in real-world performance.

The majority of the time this limitation would not be likely to affect the vehicle's maneuvering performance as the required forces will not reach the friction limit. However, it

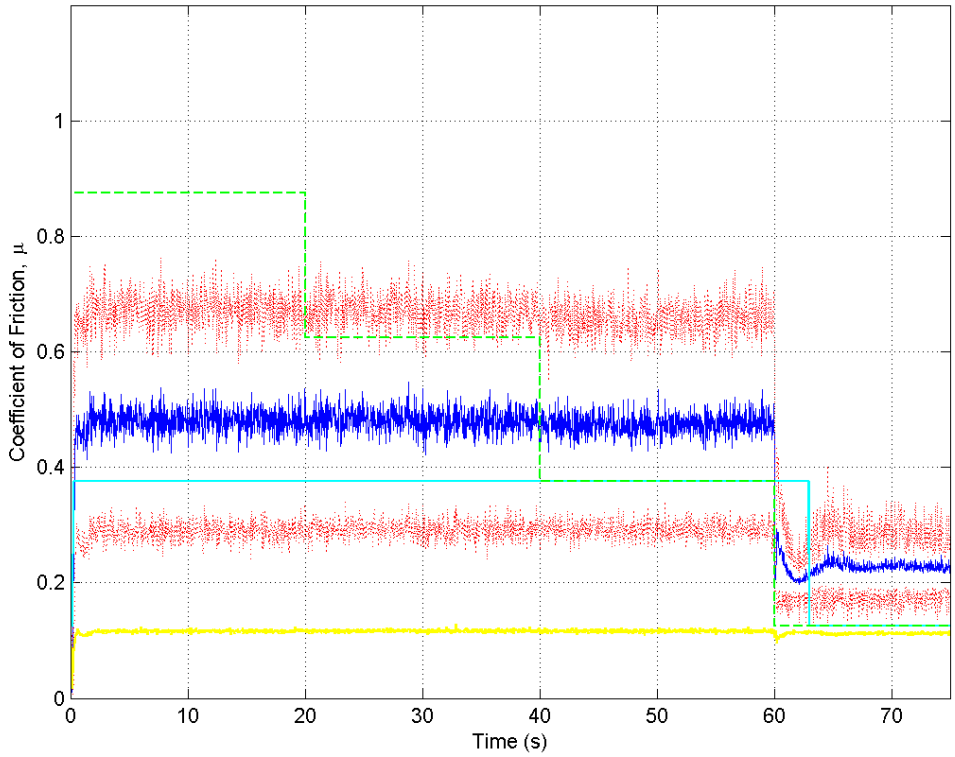

Figure 6.29: Friction change detection results. Note that the excitation is insufficient to detect the higher COFs but the estimator very quickly converges to the lower COF. The dark blue line represents the mean value of the pneumatic trail estimator and the red lines represent 3σ confidence intervals from 100 simulations. The light blue line is the output from the BHF estimator using the yellow estimated excitation. The green dashed line is the actual coefficient of friction.

would be useful to have knowledge of the true COF for purposes of planning emergency maneuvers. Clearly from these results, further research in this area would be highly desirable.

6.3 Manifold Generation

The final step in validating the proposed methods is to verify the ability to generate the IMMs. The metrics and map superposition techniques are tested and their accuracy is

compared to previous results.

6.3.1 Metric Validation

A final stage in validation of the vehicle model is an evaluation of the accuracy of the stability metrics. Due to the safety hazards involved with testing limit behavior on real vehicles, the stability metrics will be validated against results from TruckSIM. Using the CUT model, a series of standard stability tests were simulated and the metric values were calculated. The maneuvers were repeated until the vehicle reached its stability limits. In the interest of space, results are not shown for tests in which the limit was not reached. Additionally, since the goal is to validate the metrics independently of state estimation, these tests were performed on 'perfect' data from TruckSIM to eliminate the effects of statistical noise.

Fishhook Maneuver

A standard automotive testing maneuver known as a 'fishhook,' shown in Figure 6.30, is used to test the metrics in a likely rollover condition. In this maneuver, the steering is actuated in one direction and then quickly reversed in an attempt to destabilize the vehicle and induce rollover. To ensure that rollover occurs before a spin or a slide, the tests were conducted at a COF of unity. It should be noted that the RSM is designed to predict wheel lift-off, not true rollover, and thus may predict rollover in scenarios in which the vehicle is still capable of recovering stability.

As can be seen in Figure 6.31, the RSM rapidly approaches zero, indicating impending rollover conditions. The vehicle is capable of completing the maneuver at 50kph without wheel lift-off but is operating at the limits of performance, as indicated by both the RSM prediction and vertical wheel force measurements. At both 55kph and 60kph, the inside wheels break contact with the ground as shown by the wheel force measurement but the

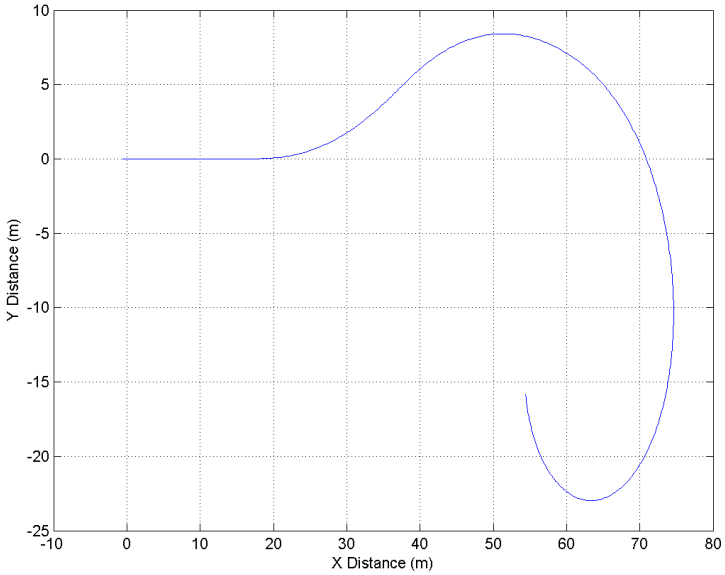

Figure 6.30: Path traced by vehicle in a fishhook stability maneuver. The turn to the left followed by the rapid steering reversal to the right is designed to destabilize the vehicle and induce rollover.

vehicle does not rollover. The RSM reaches zero in this condition, properly indicating the lift-off condition. In the 65kph case the vehicle does in fact rollover. The RSM correctly predicts this case although the difference between true rollover and wheel lift-off is indistinguishable by this measure.

One flaw in the RSM is the slight time lag exhibited by the metric. It can be seen from the plots that the RSM prediction lags the wheel forces by approximately 0.5s. This lag is due to the dynamics of the interaction between the sprung and unsprung masses as reflected in the roll angle and roll rate and is accentuated in an extreme maneuver such as the fishhook. In the intended implementation of the IMM, however, this lag becomes much less significant as the RSM is used predictively and not calculated in real-time as in these results.

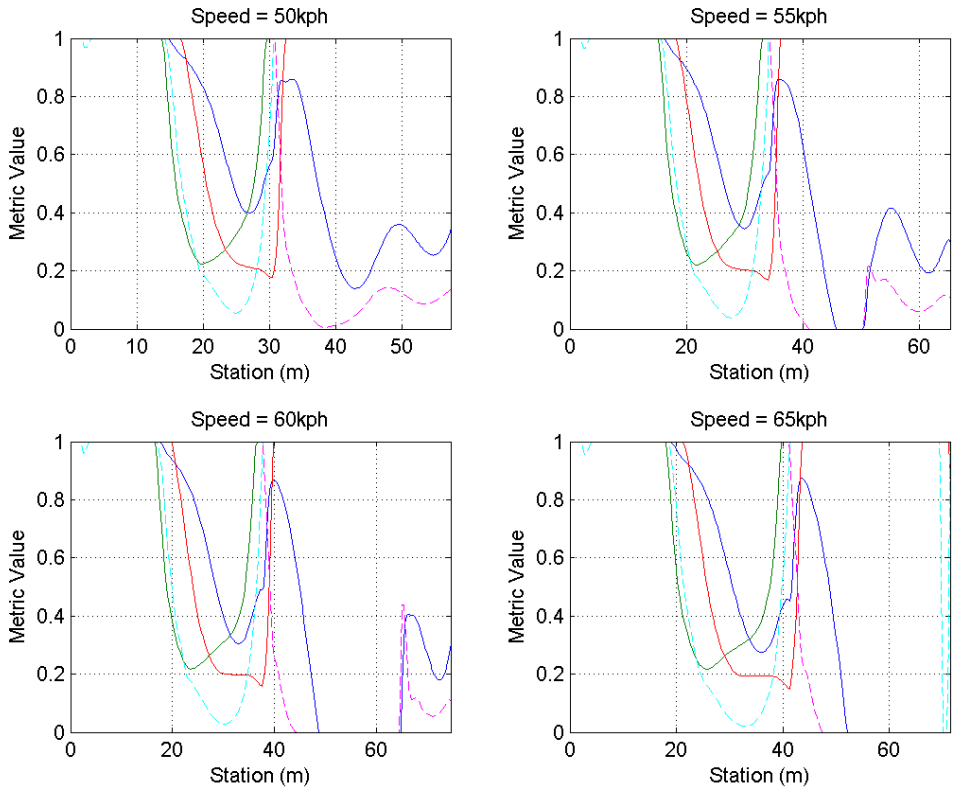

Figure 6.31: Plot of metric values for the fishhook test at varying speeds. Note that the DSM (green) and DCM (red) decrease during the initial steering maneuver while the RSM (blue) reaches its lowest value after the steering reversal. As can be seen from the normalized wheel forces (dashed lines), the vehicle experiences wheel liftoff at 55kph and above and actually rolls over at 65kph. Both cases are predicted by the RSM.

Double Lane Change

Directional controllability will be validated using a double-lane change maneuver which requires a vehicle to make an 'S-turn' as if it were changing lanes on a roadway to avoid an obstacle as shown in Figure 6.32. Such maneuvers are common for autonomous vehicles in obstacle avoidance situations. To achieve loss of directional control, the COF was lowered and the speed increased until the vehicle was no longer able to complete the maneuver.

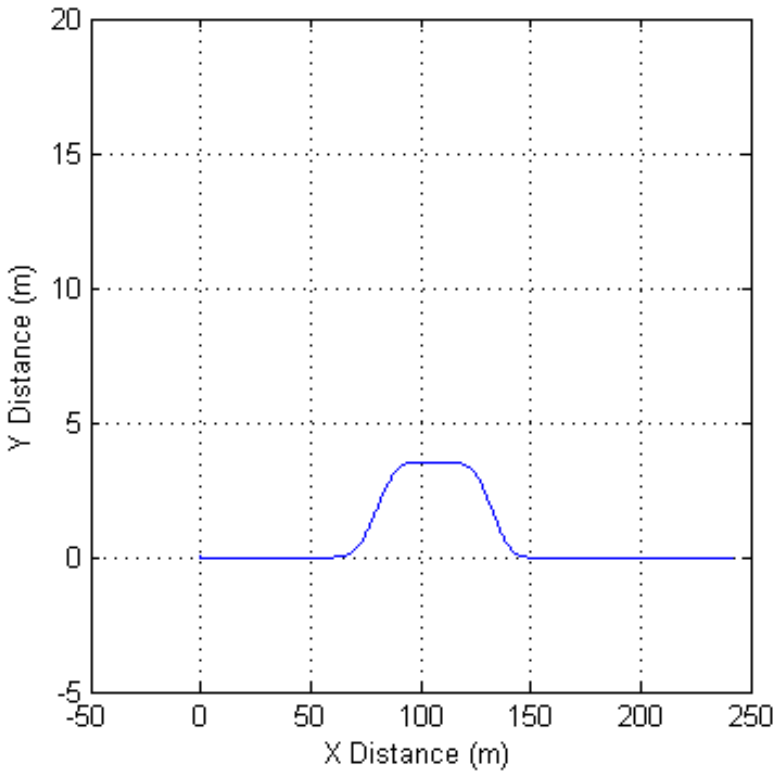

Figure 6.32: Double-lane change stability maneuver. This maneuver requires the vehicle to change to the left-hand lane and then return to the right-hand lane. Similar maneuvers are common obstacle avoidance maneuvers for autonomous vehicles.

Results of the double-lane change test are displayed in Figure 6.33. The two upper plots display the capability of the vehicle to execute the prescribed maneuver in a high friction situation. In both cases, the metric values remain high as the vehicle is not ap-

proaching its dynamic limits. In the extremely low friction situation depicted in the lower plots, the vehicle encounters significantly more difficulty in completing the maneuver. At 35kph the vehicle is operating at the edge of controllability and requires corrective action from the closed-loop steering controller to complete the maneuver; this is indicated by the low values of both the DSM and DCM. At 65kph the vehicle is no longer capable of completing the maneuver as the front tires have saturated and are incapable of generating the required lateral force; as a result the vehicle enters a slide and plows straight ahead despite the actions of the controller. The entry into the slide is correctly predicted by the DCM as would be expected in this condition. Note that while both directional metrics are low, the lower values of the DCM correctly indicate that directional controllability will be lost before directional stability.

Directional Stability

To test yaw stability, the vehicle was simulated in conditions with maximum steer angle and a constant 1/3 throttle setting. These conditions should cause the vehicle to enter a spin before a slide. To induce directional stability loss instead of rollover, the simulations were run using a COFof 0.5. As shown in Figure 6.34, the vehicle is unable to complete the maneuver under these conditions due to the loss of yaw stability. Spin entry is correctly predicted by the DSM as its value is much lower than the DCM at the time of spin entry at time 2s. After the vehicle enters the spin, the metric values fluctuate widely as the vehicle is in an unstable state.

The results indicate that the metrics are capable of successfully predicting the conditions for which they are designed. When used to mask an IMM, carefully chosen metric values should enable an autonomous vehicle to remain safely within its stable dynamic operating envelope.

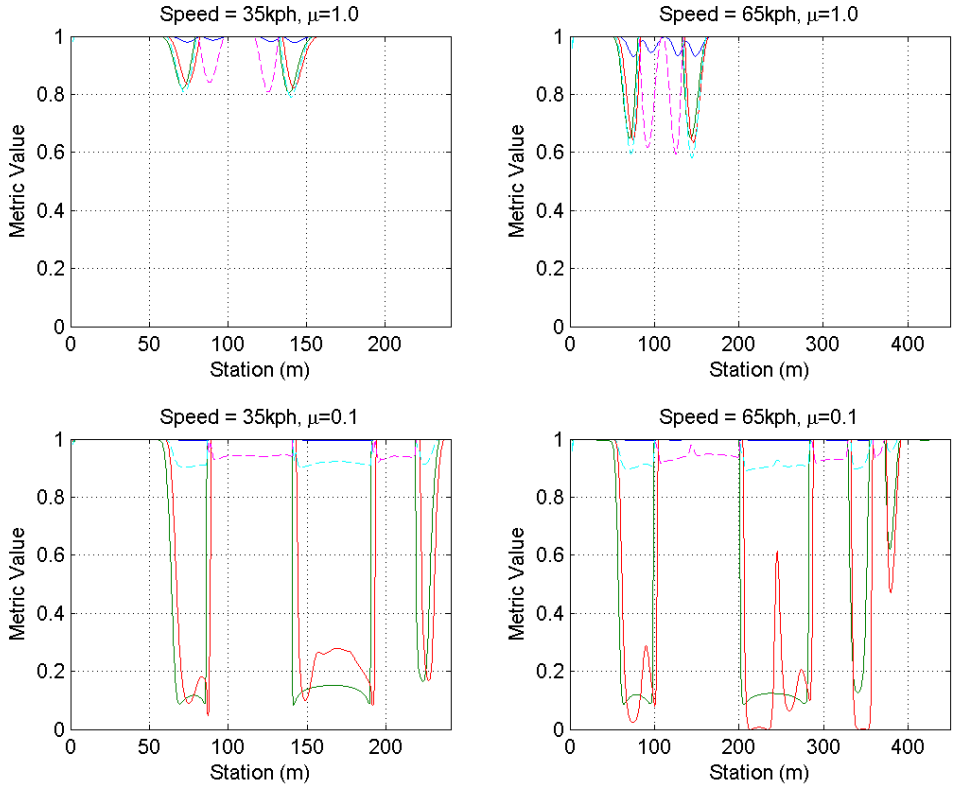

Figure 6.33: Metric values for the double-lane change test at varying speeds and COFs. Note that while the vehicle is able to complete the maneuver easily at $\mu = 1$, it reaches the limits of stability at 35kph and enters a slide at 65kph. Both of these conditions are indicated by the DSM (green) and DCM (red), with slide entry occurring as the DCM reaches zero. As indicated by the RSM (blue) and wheel weights (dashed) the vehicle remains stable in the roll plane throughout all of the maneuvers.

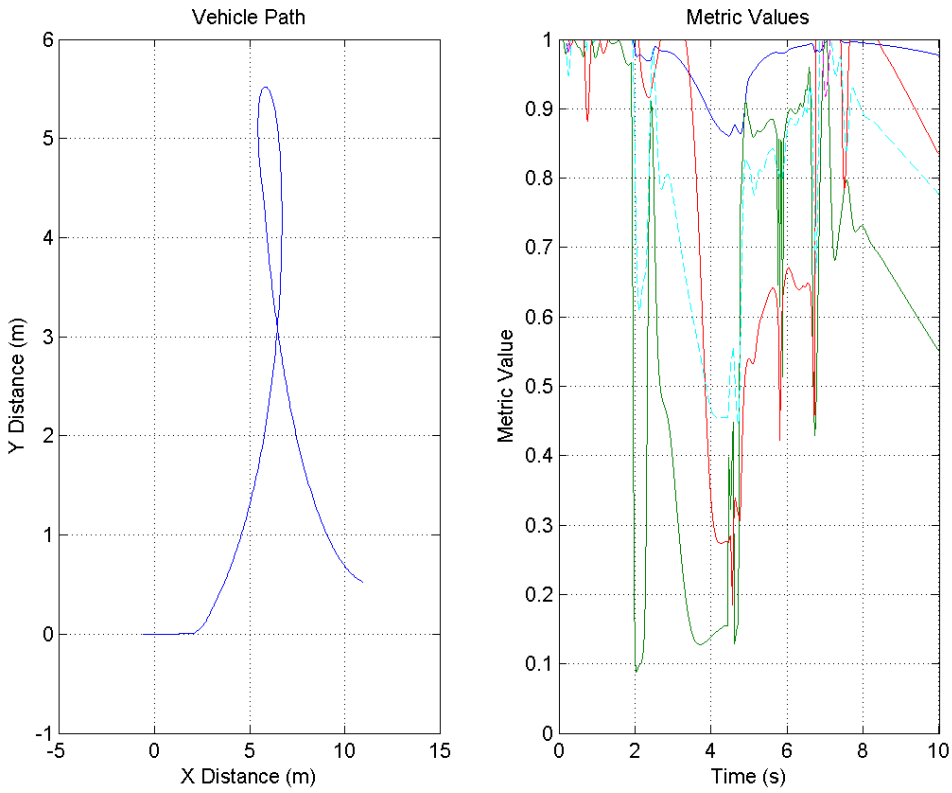

Figure 6.34: Path of the vehicle (left) and metric values (right) for the yaw stability test. Note that the DSM (green) indicates that the vehicle is loosing yaw stability while the DCM (red) indicates that directional controllability still exists. This results in the vehicle entering a spin. At the low friction conditions of this test ($\mu = 0.5$), the RSM (blue) and wheel weights (dashed) indicate that the vehicle remains stable in the roll plane throughout all of the maneuvers.

6.3.2 Map Superposition

The primary issue with map superposition to create the manifolds is that it relies on the unproven assumption that linear superposition applies. This assumption can be tested by comparing the results of multi-variable weighted averages to the results of manifolds calculated directly from the desired variables using the MATLAB FMM implementation. To demonstrate the validity of this assumption, manifolds were superimposed and compared for each of the CG variables independently as well as for a case in which all three variables were superimposed. Results are shown in Figures 6.35-6.39.

The results show that superposition of the manifolds across the CG variables yields an estimated FMM that closely matches the results of a FMM that is calculated directly for the same values. As shown in Figure 6.39, the superposition error is generally less than 10% of the full scale value for both the lateral force and moment coefficients. To generate the data in this figure, 294 separate FMM diagrams were calculated to span the space defined by the CG offsets defined by: $x_{CG} = [0.1, 0, -0.1, -0.2, -0.3, -0.4, -0.5]m$, $y_{CG} = [-0.3, -0.2, -0.1, 0, 0.1, 0.2, 0.3]m$, and $z_{CG} = [-0.1, 0, 0.1, 0.2, 0.3, 0.4]m$. There appears to be little correlation between error and specific offset variables and the error scales roughly linearly with total CG offset.

A close examination of Figures 6.35-6.38 shows that the majority of the error occurs near the limits of the diagram. In the central area, which accounts for the vast majority of actual operation time on most vehicles, the results from the superposition technique are nearly identical to the direct calculation results. Additionally, as can be seen in Appendix B, the outer portions of the IMM are typically not available for operation due to the metric constraints. Thus, the true error in the usable portion of the IMM is likely to be lower than what is shown in Figure 6.39. When the computational constraints discussed in Section 6.3.3 are considered, the superposition technique appears to be an excellent compromise between computational complexity and accuracy.

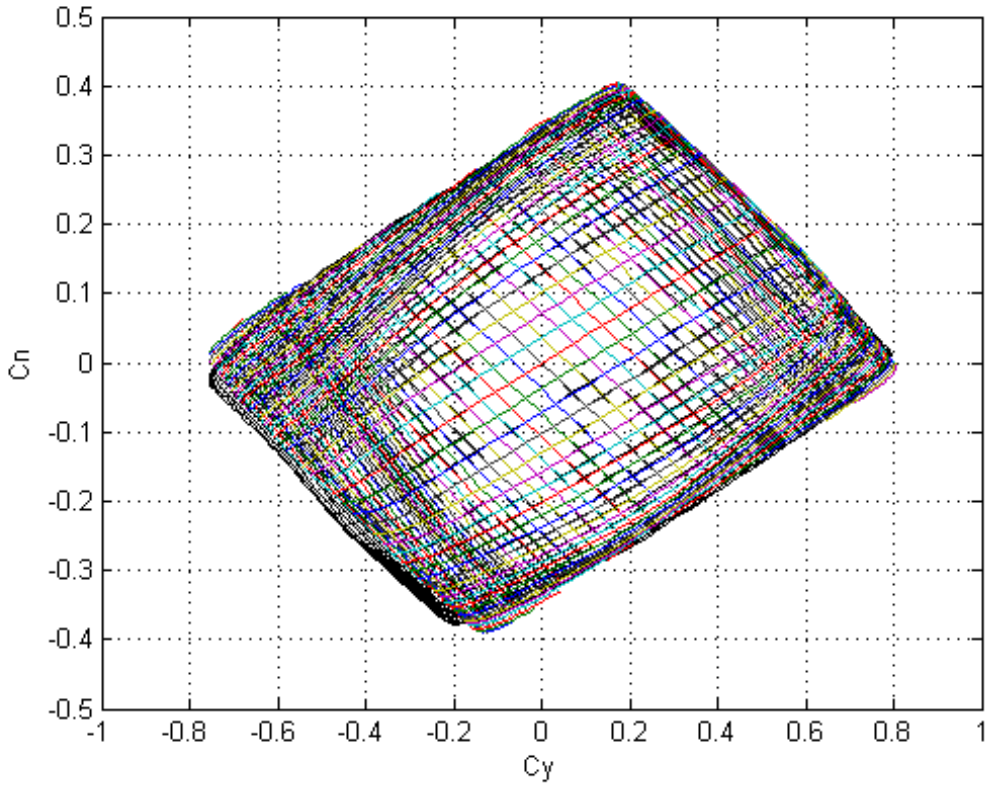

Figure 6.35: Superimposed FMM (color) vs. directly solved FMM (black) for offsets in x_{CG} and y_{CG}. This example shows an x_{CG} offset of -0.2m and a y_{CG} offset of 0.2m from the empty vehicle conditions at $A_x = 0$ and $\mu = 0.88$. Note that the superimposed FMM closely overlays the directly calculated version.

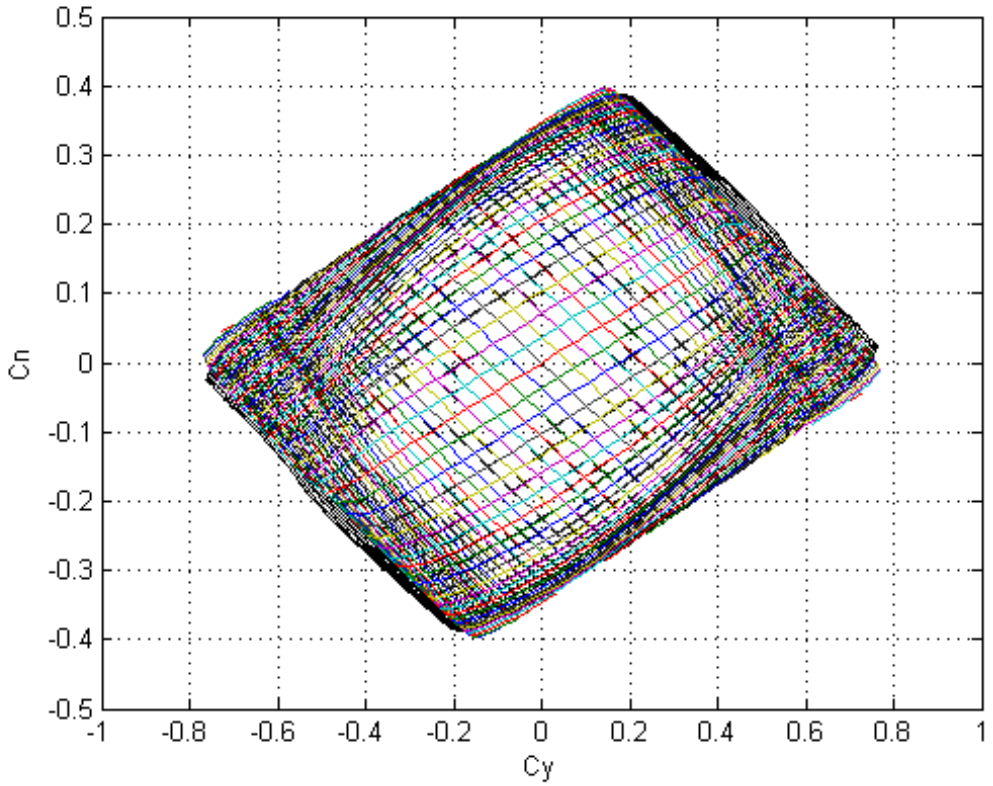

Figure 6.36: Superimposed FMM (color) vs. directly solved FMM (black) for offsets in x_{CG} and z_{CG}. This example shows an x_{CG} offset of -0.2m and a z_{CG} offset of 0.2m from the empty vehicle conditions at $A_x = 0$ and $\mu = 0.88$. Note that the superimposed FMM closely overlays the directly calculated version.

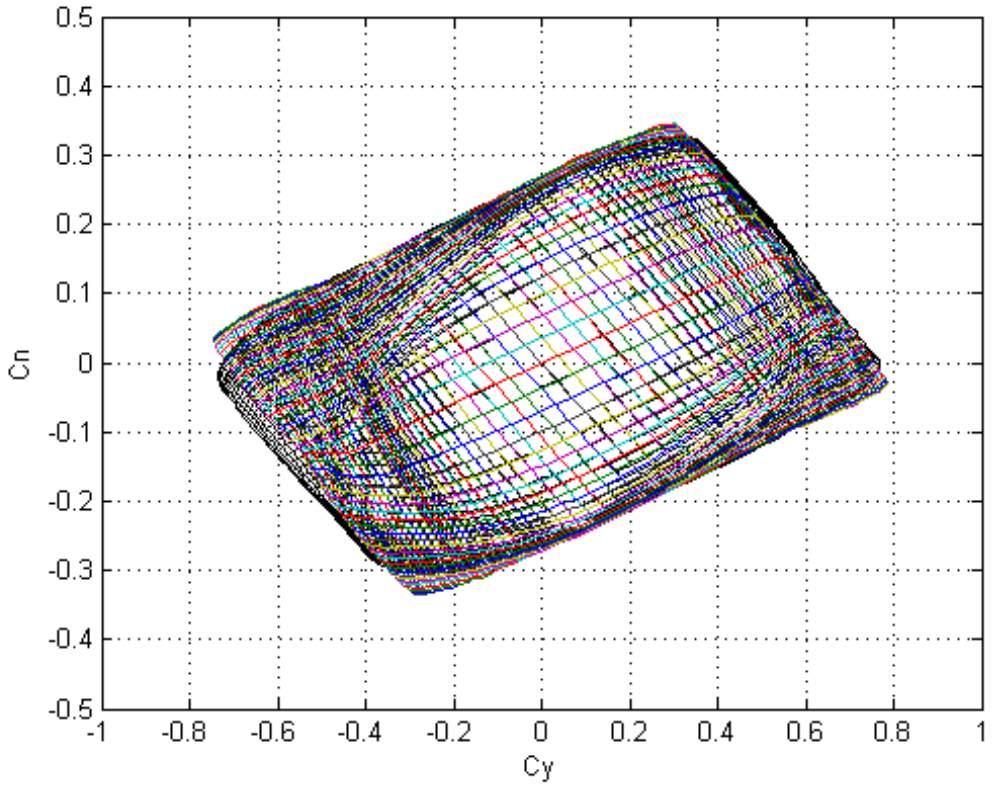

Figure 6.37: Superimposed FMM (color) vs. directly solved FMM (black) for offsets in y_{CG} and z_{CG}. This example shows an y_{CG} offset of 0.2m and a z_{CG} offset of 0.2m from the empty vehicle conditions at $A_x = 0$ and $\mu = 0.88$. Note that the superimposed FMM closely overlays the directly calculated version.

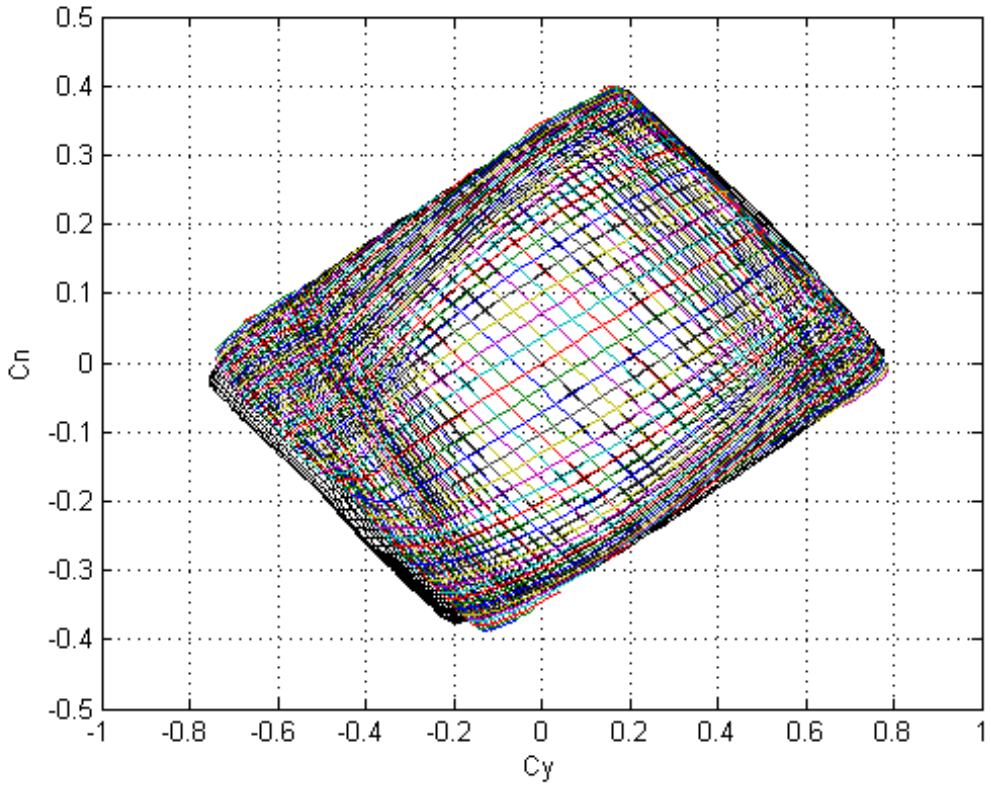

Figure 6.38: Superimposed FMM (color) vs. directly solved FMM (black) for offsets in x_{CG}, y_{CG}, and z_{CG}. This example shows an x_{CG} offset of -0.2m, a y_{CG} offset of 0.2m, and a z_{CG} offset of 0.2m from the empty vehicle conditions at $A_x = 0$ and $\mu = 0.88$. Note that the superimposed FMM closely overlays the directly calculated version.

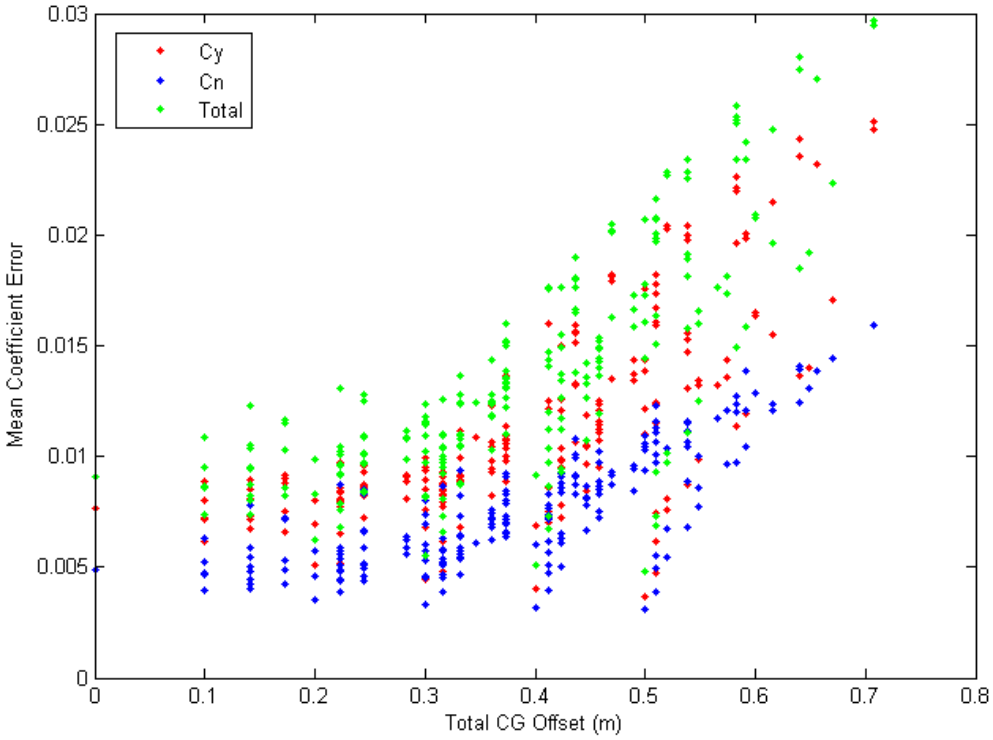

Figure 6.39: Plot of superposition vs. direct calculation error for 294 possible combinations of x_{CG}, y_{CG}, and z_{CG} positions. The abscissa shows the total Pythagorean CG offset while the ordinate shows the mean error in C_y, C_n, and total error coordinates. Note that the error is roughly constant below 0.3m total offset and then increases roughly linearly beyond this point.

6.3.3 Computational Analysis

One important goal of this method is to be able to calculate the manifolds in real time using reasonable computing resources. To test the computational requirements, each component was executed 100 times on a Dell Latitude D630 laptop with a 2.5GHz Intel Core2 Duo processor and 4GB of physical RAM using MATLAB 7.11.0 (R2010b) on Windows XP SP3.

The results, as shown in Table 6.7, show that the initial calculation of the FMM is the most computationally intensive part of the algorithm by several orders of magnitude. It should also be noted that the time given is for only a single instance of the FMM and that calculation of the full data set for a vehicle can take many hours. Additionally, the time required to calculate the FMM is non-deterministic due to the numerical solution technique; it is generally not possible to predict the number of iterations required for each operating point and the time can vary as a result. The extremely long computational times are the prime motivator behind both the precalculation concept and the superposition technique.

Table 6.7: Operation Computational Time

Operation	Time (s)
FMM Calculation	55-70
Force Estimation	0.003
COF Calculation	0.001
FMM Superposition	0.002
Metric Masking	0.004
IMM Conversion	0.07

The more important aspect of the computational time is the rate at which the real-time parts of the algorithm can be executed. The estimation parts of the algorithm require approximately 4ms to execute allowing theoretical iteration rates as high as 250Hz indicating that realistic computational rates in the range of 50-100Hz should be possible. The

IMM generation requires approximately 74ms yielding a theoretical loop rate in the range of 13.5Hz. Allowing for computational overhead, this indicates that the total algorithm could possibly be executed as fast as 10Hz and should definitely be able to run at 5Hz. No specific attempt was made to optimize run-time execution rates on the code, besides standard best practices, and it is likely that these algorithms can be further optimized. Given that the base dynamics of the vehicle are typically below 5Hz, a claim of real-time operation can be justified.

6.4 Results Summary

The results have shown that the proposed methods are capable of producing an IMM with variable mass, CG location, and tire/ground COF in real time. Using proprioceptive sensors that are either common to autonomous and unmanned vehicles or are reasonable to retrofit, it has been shown to be possible to estimate the mass and CG location from a combination of static measurements and simple, low-risk maneuvers. It is then possible to use a UKF based force estimator to estimate the horizontal and vertical wheel forces to a degree of accuracy sufficient for use in the friction estimator. The pneumatic trail based friction estimator shows capability to successfully estimate the terrain COF, provided that sufficient excitation is available.

The IMM can be calculated using linear superposition techniques to form the required combination of the mass, CG, and friction variables. The error on this approximation has been shown to be a reasonable when the large difference in computational time between superposition and direct calculation is taken into account. Finally, the proposed stability metrics have been shown to successfully predict rollover, slides, and spin-out instability conditions and can be used to mask the IMM to predict safe operating ranges. A computational analysis indicates that the proposed algorithm can be run in real-time and if

implemented on a real vehicle would be capable of providing accurate and useful information on the safe operating manifold of the vehicle to autonomous navigation systems.

Chapter 7

Conclusions

The only thing new in the world is the history you don't know.

–Harry S Truman, 1962 [109]

Current unmanned and autonomous ground vehicles largely rely on *a priori* assumptions of both the condition of the vehicle and the terrain on which they are operating. As a result of these assumptions, the vehicles do not, in general, have the capability to adapt their understanding of the maneuvers which are within their dynamic capability to execute. While improvement of an autonomous controller's ability to perceive its environment and develop motion plans are important to the expansion of autonomy, improved world models and motion plans cannot be utilized safely if the vehicle does not understand its own capabilities. The ability to predict the safe maneuvering envelope of UGVs in realistic conditions in which the load configuration of the vehicle and the state of the terrain are unknown is crucial to enable UGVs to fulfill real missions with an acceptable level of safety.

7.1 Conclusions

The methodology developed in this work attempts to address a gap in current research in autonomous systems. The concept of the Instantaneous Maneuvering Manifold is designed to provide a method for representing the vehicle's allowable operating envelope in a manner that can be transmitted to and used by an autonomous motion planning system. The IMM not only represents the current operating state of the vehicle but also the other operating points that can be reached safely given the current vehicle configuration and terrain state. The ability to simultaneously predict operating points beyond the current state is an important aspect of this technique. In order to develop long-term motion plans it is necessary for the motion planner to be able to search the total operating space and not just have knowledge of the current state.

The manifold can be defined by the possible operating point of the vehicle in terms of the steering angle and body slip angle and is bounded by a set of metrics that define the dynamic limitation in terms of rollover and directional stability and controllability. High fidelity closed form solutions to the relevant equations are difficult to derive, complex, and must be solved across the entire operating space. These equations can more easily be solved numerically for each operating point; this, however, is infeasible to perform in real-time. Instead the manifolds can be precalculated, stored, and accessed in real-time as needed. Additionally, this method abstracts the actual vehicle model from the representation of the manifold allowing the vehicle model to be changed or updated without affecting the remainder of the methodology.

Manifolds can be calculated across the space of possible vehicle configurations, but calculating all possible combinations of the vehicle variables is also computationally difficult. Fortunately, it has been shown that IMMs for specific sets of variables can be formulated using the principle of linear superposition of the forces and moments that compose them. The effects of each variable on the manifold can be isolated and linearly

superimposed to generate the resultant IMM. This technique has been shown to be capable of generating IMMs in a computationally effective manner while achieving acceptable levels of error.

The stability metrics have been shown to successfully predict the dynamic operating limits of the vehicle. The RSM relies on an energy approach and is able to predict wheel lift-off before rollover occurs. The DCM and DSM are capable of predicting impending entry into either a slide or a spin, respectively, by analyzing the utilized and available forces at the front and rear wheels. The metrics can be largely precalculated, with the exception of the kinetic energy portion of the RSM, and the superposition principle can be applied to create an appropriate metric mask for a given set of vehicle parameters. Once an appropriate set of metric limits are set, the mask can then be applied to the IMM to eliminate components beyond the operating range that has been deemed safe.

Before one can calculate manifolds for vehicles with differing parameters, it is first necessary to know those parameters. To this end, an estimator was developed that is capable of determining the 3D location of the CG based on measurements from an INS and suspension position sensors. This method requires the vehicle to execute a maneuver to excite the roll dynamics; it then numerically optimizes the relevant equations to achieve a best estimate of CG location. Due to this optimization and the use of suspension position sensors, the estimator is capable of determining the CG from a low-speed, non-hazardous maneuver with accuracies of typically less than 10%.

The other variable required for manifold calculation is the tire/ground coefficient of friction. As look-ahead friction sensors are not available, in order to calculate the COF it is necessary to first know the magnitudes of the horizontal and vertical forces generated by the tires. These forces are not directly measurable without complex and expensive wheel hub sensors, so an UKF based estimator was developed. The UKF is used to estimate the vertical forces on each of the wheels independently as well the lateral and longitudinal

forces at each axle. Unlike in many works, the estimator is specifically designed to work in the type of combined-slip conditions that occur in realistic driving scenarios and has been shown to be capable of estimating the forces under this type of drive cycle.

Friction estimation was performed by using the output of the force estimator to drive an estimator based on pneumatic trail. To date, pneumatic- trail-based methods have shown the best capability of tire force based approaches to estimate COF a relatively low excitation levels. The use of the combined-slip force estimator to drive the friction estimator also effectively extends the usage of this method to combined slip conditions and expands its usability. The friction estimator is highly dependent on the excitation level of the input signals. During low-magnitude maneuvers, the vehicle does not use enough of the available force to effectively estimate the true value of the COF; this limitation is mostly due to the physics of tire-ground interaction and has no obvious methodological solution. However, when sufficient excitation is available, the estimator showed the ability to achieve COF estimates and to rapidly detect changes in the COF.

In an attempt to stabilize the friction estimates, a Bayesian histogram filter was implemented as part of the friction estimator. This filter combines knowledge of friction estimate from the pneumatic trail with an estimate of the excitation level in a probabilistic manner. The BHF is thus capable of both holding estimates with gradually degrading probabilities during periods of low excitation and rejecting spurious estimates that greatly exceed the excitation. The application of this technique to friction estimation is novel and provides a much more stable estimate of the COF without removing the ability to rapidly detect changes.

The overall methodology has been shown to be capable of addressing the issue of determining the allowable operating space for an autonomous vehicle with varying cargo and varying terrain conditions. The method of precalculating FMMs, superimposing them to form IMM estimates, and applying stability metric masks appears to be an effective

technique for estimating an entire operating manifold in real-time. It has also been shown to be possible to estimate the CG position and tire/ground coefficient of friction. Although it is limited by the physics of excitation for the friction estimation, the estimation structure can provide reasonable estimates of the relevant variables in realistic, combined-slip driving conditions. The final result is a methodology that has the potential the greatly increase the ability of autonomous ground vehicles to operate safely and controllably in realistic operating conditions by incorporating predictive and adaptive advanced vehicle dynamics knowledge.

7.2 Future Work

Although the techniques proposed in this work begin to address one of the fundamental problems facing autonomous ground vehicles, many areas of research exist as opportunities for future work.

The most obvious aspect of the future work is to validate this methodology on a real vehicle. The results presented in this dissertation are all based on TruckSIM simulations. While the VehicleSIM model at the heart of TruckSIM is well developed and validated, it is still not a replacement for real vehicle testing. The stability metrics should be evaluated (which would likely require a vehicle equipped with outriggers), and the capability and robustness of the state estimators evaluated. It would also be desirable to further validate the model used to generate the FMMs and to expand it to improve its accuracy, which can be done easily due to the inherent abstraction of the FMM technique. Unfortunately, temporal and resource constraints prevented this type of live vehicle validation from occurring previously.

Another aspect of future work would be the expansion of the allowable terrain constraints. The current methodology is restricted to a smooth, planar surface. It would be

highly desirable to expand the model to allow for large scale changes in both bank and grade. Incorporation of these aspects would require expansion of the state estimator to include states for the terrain grade and bank angles and of the IMM formulation algorithm to include superposition of terrain effects. Additionally, the robustness of the estimators to small-scale stochastic terrain inputs should be evaluated and improved as necessary.

Further work can also be done to integrate the IMM concept into an actual autonomous motion planner algorithm. The variables that define the IMM should be usable in this fashion, but reformulation of the methods of storage and representation may be required. In particular, one of the limitations of the current implementation is that the method for storing the FMM and metric information as arrays of double precision numbers at each operating point requires an excessive amount of storage and memory. This could be improved by use of data compression techniques, but it may be more desirable from a motion planner implementation standpoint to represent the data in the form of sets of curves or clothoids.

For future use in extremely high-speed work, such as racing environments, it may be necessary to further compensate for some of the more extreme dynamic effects of vehicle motion. An example of this would be the phase lag that occurs in roll motion between the sprung and unsprung masses. In conditions such as those tested in this work these effects are typically small enough to be neglected, but they would be expected to be more significant as the vehicle approaches its ultimate handling limits. One possible approach for this type of dynamic compensation would be to develop and observer capable of calculating a virtual Instant Center of Gravity (ICG). Analogous to a kinematic Instant Center, the ICG could represent the effective state of the roll angle and weight distribution due to the dynamics and be used in place of the actual CG values during the manifold superposition and metric calculation. Due to the quasi-static nature of the current implementation, it is believed that this expansion would yield more accurate manifold and metric information

in highly dynamic environments.

The most important area of potential future work would be the development of more advanced sensors and techniques for estimation of the tire/ground COF. Current techniques relying on estimates derived from wheel forces are extremely limited due to the need for relatively high excitation levels in high friction conditions. This results in a Catch-22 situation where the vehicle cannot verify its ability to operate safely at higher speed until it is able to obtain an accurate friction measurement by operating at higher speed. This is clearly not an acceptable situation and is one of the primary limitations in this work. The greatest impact of future research would be development of look-ahead friction sensors that are capable of predicting the COF at a distance in front of the vehicle. It may be possible to do this via terrain characterization using sensors such as computer vision or RADAR. Predictive friction estimation would further increase the capability of motion planning software to use the IMM to formulate safe predicted trajectories.

References

[1] B. Franklin and W. T. Franklin, *Memoirs of the Life and Writings of Benjamin Franklin*. London: A. J. Valpy, 1818.

[2] C. Urmson, J. Anhalt, M. Clark, T. Galatali, J. P. Gonzalez, J. Gowdy, A. Gutierrez, S. Harbaugh, M. Johnson-Roberson, H. Kato, P. Koon, K. Peterson, B. Smith, S. Spiker, E. Tryzelaar, and W. Whittaker, "High speed navigation of unrehearsed terrain: Red team technology for grand challenge 2004," Robotics Institute, Carnegie Mellon University, Tech. Rep., 2004.

[3] S. Thrun, W. Burgard, and D. Fox, *Probabilistic Robotics*. MIT Press, 2006.

[4] G. T. McWilliams, M. A. Brown, R. D. Lamm, C. J. Guerra, P. A. Avery, K. C. Kozak, and B. Surampudi, "Evaluation of autonomy in recent ground vehicles using the autonomy levels for unmanned systems (ALFUS) framework," in *Proceedings of Performance Metrics for Intelligent Systems*, 2007.

[5] K. Kluge and M. Morgenthaler, "Multi-horizon reactive and deliberative path planning for autonomous cross-country navigation," *Unmanned Ground Vehicle Technology*, vol. 6, pp. 461–472, 2004.

[6] DARPA. (2008) DARPA grand challenge website. United States Department of Defense. [Online]. Available: http://www.darpa.mil/grandchallenge/

[7] C. Urmson, J. Anhalt, D. Bartz, M. Clark, T. Galatali, A. Gutierrez, S. Harbaugh, J. Johnston, H. Kato, P. L. Koon, W. Messner, N. Miller, A. Mosher, K. Peterson, C. Ragusa, D. Ray, B. K. Smith, J. M. Snider, S. Spiker, J. C. Struble, J. Ziglar, and W. R. L. Whittaker, "A robust approach to high-speed navigation for unrehearsed desert terrain," *Journal of Field Robotics*, vol. 23, no. 8, pp. 467–508, August 2006.

[8] R. Frezza, A. Beghi, and G. Notarstefano, "Almost kinematic reducibility of a car model with small lateral slip angle for control design," in *Proc. IEEE International Symposium on Industrial Electronics ISIE 2005*, vol. 1, 2005, pp. 343–348.

[9] A. Scheuer and T. Fraichard, "Continuous-curvature path planning for car-like vehicles," in *IEEE/RSJ International Conference on Intelligent Robots and Systems*, 1997.

[10] W. Milliken and D. Milliken, *Race Car Vehicle Dynamics*. Warrendale, Pa.: SAE International, 1995.

[11] R. S. Westfall, *The Life of Isaac Newton*. Cambridge University Press, 1994, p. 106.

[12] C. Bottasso, C. Chang, A. Croce, D. Leonello, and L. Riviello, "Adaptive planning and tracking of trajectories for the simulation of maneuvers with multibody models," *Computer Methods in Applied Mechanics and Engineering.*, vol. Computational Multibody Dynamics, pp. 7052–7072, 2006.

[13] E. Frazzoli, "Real-time motion planning for agile autonomous vehicles," in *Proceedings of American Control Conference*, 2001.

[14] A. Bacha, C. Bauman, R. Faruque, M. Fleming, C. Terwelp, C. Reinholtz, D. Hong, A. Wicks, T. Alberi, D. Anderson, S. Cacciola, P. Currier, A. Dalton, J. Farmer, J. Hurdus, S. Kimmel, P. King, A. Taylor, D. V. Covern, and M. Webster, "Odin: Team VictorTangos entry in the DARPA Urban Challenge," *Journal of Field Robotics*, vol. 25, no. 8, pp. 467–492, 2008.

[15] J. Y. Wong, *Theory of Ground Vehicles*, 4th ed. Wiley, 2008.

[16] C. Urmson, "Navigation regimes for off road autonomy," Ph.D. dissertation, Carnegie Mellon University, 2005.

[17] P. Currier, "Development of an automotive ground vehicle platform for autonomous urban operations," Master's thesis, Virginia Polytechnic Institute and State University, 2008.

[18] H. Abdellatif and B. Heimann, "Accurate modelling and identification of vehicle's nonlinear lateral dynamics," in *Preprints of the 16th IFAC World Congress*, 2005.

[19] R. N. Jazar, *Vehicle Dynamics Theory and Application*. Springer, 2008.

[20] A. B. Will and S. H. Zak, "Modelling and control of an automated vehicle," *Vehicle System Dynamics*, vol. 27:3, pp. 131–155, 1997.

[21] T. A. Wenzel, "State and parameter estimation for vehicle dynamic control," Ph.D. dissertation, Coventry University, UK, 2005, british Libary Shelfnumber XN092803 DSC.

[22] T. A. Wenzel, K. J. Burnham, M. V. Blundell, and R. A. Williams, "Dual extended kalman filter for vehicle state and parameter estimation," *Vehicle System Dynamics*, vol. 44, no. 2, pp. 153–171, 2006.

[23] J. Wang, J. Steiber, and B. Surampudi, "Autonomous ground vehicle control system for high-speed and safe operation," in *American Control Conference*, 2008, pp. 218–223.

[24] T. A. Wenzel, K. J. Burnham, M. V. Blundell, and R. A. Williams, "Kalman filter as a virtual sensor: applied to automotive stability systems," *Transactions of the Institute of Measurement and Control*, vol. 29, no. 2, pp. 95–115, 2007.

[25] M. Sayers, "Standard terminology for vehicle dynamics simulations," The University of Michigan Transportation Research Institute (UMTRI), Tech. Rep., 1996.

[26] H. B. Pacejka, *Tire and Vehicle Dynamics*, 2nd ed. SAE International, 2006.

[27] W. Hirschberg, G. Rill, and H. Weinfurter, "User-appropriate tyre-modelling for vehicle dynamics in standard and limit situations," *Vehicle System Dynamics*, vol. 38, no. 2, pp. 103–125, 2003.

[28] M. S. Grewal and A. P. Andrews, *Kalman Filtering Theory and Practice Using MATLAB*, 2nd ed. Wiley, 2001.

[29] A. Vahidi, S. A., and P. H., "Recursive least squares with forgetting for online estimation of vehiclemass and road grade: Theory and experiments," *Vehicle System Dynamics*, vol. 43, no. 1, pp. 31–55, 2005.

[30] D. Wesemeier and R. Isermann, "Identification of vehicle parameters using stationary driving maneuvers," *Control EngineeringPractice*, vol. 17, pp. 1426–1431, 2008.

[31] R. Anderson and D. M. Bevly, "Estimation of slip angles using a model based estimator and GPS," in *Proceeding of the American Control Conference*, 2004, pp. 2122–2127.

[32] J. Ryu, E. J. Rossetter, and J. C. Gerdes, "Vehicle sideslip and roll parameter estimation using GPS," in *AVEC 2002 6th Int. Symposium on Advanced Vehicle Control*, 2002.

[33] J. Ryu and J. C. Gerdes, "Estimation of vehicle roll and road bank angle," in *Proceeding of the 2004 American Control Conference*, 2004.

[34] L. R. Ray, "Nonlinear state and tire force estimation for advanced vehicle control," *IEEE Transactions on Control Systems Technology*, vol. 3, no. 1, pp. 117–124, 1995.

[35] M. C. Best, T. J. Gordon, and P. J. Dixon, "An extended adaptive Kalman filter for real-time state estimation of vehicle handling dynamics," *Vehicle System Dynamics*, vol. 34, pp. 57–75, 2000.

[36] G. Hodgson and M. C. Best, "A parameter identifying a kalman filter observer for vehicle handling dynamics," *Proceedings IMechE*, vol. 220, no. Part D: J. Automobile Engineering, pp. 1063–1072, 2006.

[37] B. Samadi, R. Kazemi, K. Y. Nikravesh, and M. Kabganian, "Real-time estimation of vehicle state and tire-road friction forces," in *Proceedings of the American Control Conference*, 2001.

[38] A. Jazwinski, *Stochastic Processes and Filtering Theory*. New York Academic Press, 1970, vol. 64.

[39] P. J. Venhovens and K. Naab, "Vehicle dynamics estimation using Kalman filters," *Vehicle System Dynamics*, vol. 32, no. 2, pp. 171–184, 1999.

[40] E. Wan and A. Nelson, *Kalman Filtering and Neural Networks*. John Wiley & Sons, 2001.

[41] S. Brunke and M. Campbell, "Estimation architecture for future autonomous vehicles," *Proceedings of the American Control Conference*, vol. 2, pp. 1108–1114, May 2002.

[42] Y. U. Yim and S.-Y. Oh, "Modeling of vehicle dynamics from real vehicle measurements using a neural network with two-stage hybrid learning for accurate long-term prediction," *IEEE Transactions on Vehicular Technology*, vol. 53, no. 4, pp. 1076–1084, 2004.

[43] U. Kiencke and A. Daiss, "Observation of lateral vehicle dynamics," *Control Engineering Practice*, vol. 5, no. 8, pp. 1145–1150, 1997.

[44] H. S. Bae, J. Ryu, and J. C. Gerdes, "Road grade and vehicle parameter estimation for longitudinal control using gps," in *IEEE Conference on Intelligent Transportation Systems*, 2001.

[45] J. Stephant, A. Charara, and D. Meizel, "Virtual sensor: application to vehicle sideslip angle and transversal forces," *IEEE Transactions on Industrial Electronics*, vol. 51, no. 2, pp. 278–289, 2004.

[46] S. Solmaz, M. Akar, R. Shorten, and J. Kalkkuhl, "Realtime multiple-model estimation of center of gravity position in automotive vehicles," *Vehicle System Dynamics*, vol. 46, pp. 763–788, 2008.

[47] M. Ouladsine, H. Shraim, L. Fridman, and H. Noura, "Vehicle parameter estimation and stability enhancement using the principles of sliding mode," in *Proceedings of the 2007 American Control Conference*, 2007.

[48] J.-O. Hahn, R. Rajamani, and L. Alexander, "GPS-based real-time identification of tire-road friction coefficient," *IEEE Transactions on Control Systems Technology*, vol. 10, no. 3, pp. 331–343, 2002.

[49] J. Wang, L. Alexander, and R. Rajamani, "Friction estimation on highway vehicles using longitudinal measurements," *Journal of Dynamic Systems, Measurement, and Control*, vol. 126, pp. 265–275, June 2004.

[50] Y.-H. J. Hsu, "Estimation and control of lateral tire forces using steering torque." Ph.D. dissertation, Stanford University, 2009.

[51] L. Li, F.-Y. Wang, and Q. Zhou, "Integrated longitudinal and lateral tire/road friction modeling and monitoring for vehicle motion control," *IEEE Transactions on Intelligent Transportations Systems*, vol. 7, no. 1, pp. 1–19, March 2006.

[52] J. S. Putney, "Reactive navigation of an autonomous ground vehicle using dynamic expanding zones," Master's thesis, Virginia Polytechnic Institute and State University, 2006.

[53] D. Odenthal, T. Bunte, and J. Ackermann, "Nonlinear steering and braking control for vehicle rollover avoidance," in *in European Control Conference*, 1999.

[54] R. Whitehead, B. Clark, M. Breland, K. Lambert, D. Bevly, and G. Flowers, "Scaled vehicle electronic stability control," ESV International Collegiate Student Safety Technology Design Competition, North American Regional Review, 2005.

[55] K. Lambert, "A study of vehicle properties that influence rollover and their effect on electronic stability controllers," Master's thesis, Auburn University, 2007.

[56] E. Papadopoulos and D. A. Rey, "The force-angle measure of tipover stability margin for mobile manipulators," *Vehicle System Dynamics*, vol. 33, pp. 29–48, 2000.

[57] S. C. Peters and K. Iagnemma, "An analysis of rollover stability measurement for high-speed mobile robots," in *Proc. IEEE International Conference on Robotics and Automation ICRA 2006*, 2006, pp. 3711–3716.

[58] B.-C. Chen and H. Peng, "Rollover warning for articulated heavy vehicles based on a time-to-rollover metric," *ASME Journal Of Dynamic Systems, Measurement, And Control*, vol. 127, pp. 406–414, 2005.

[59] H. Yu, L. Guvenc, and U. Ozguner, "Heavy duty vehicle rollover detection and active roll control," *Vehicle System Dynamics*, vol. 46, pp. 451–470, 2008.

[60] E. Dahlberg, "A method for determining the rollover threshold of commercial vehicles," SAE, Tech. Rep. 2000-01-3492, 2000.

[61] R. C. Hoffman, J. L. Stein, L. S. Louca, and K. Huh, "Using the milliken moment method and dynamic simulation to evaluate vehicle stability and controllability," *Int. J. Vehicle Design*, vol. 48, no. 1/2, pp. 132–148, 2008.

[62] S. Anwar, "Yaw stability control of an automotive vehicle via generalized predictive algorithm," in *Proc. American Control Conference the 2005*, 2005, pp. 435–440.

[63] R. Karbalaei, A. Ghaffari, R. Kazemi, and S. H. Tabatabaei, "Design of an integrated AFS/DYC based on fuzzy logic control," in *Proc. ICVES Vehicular Electronics and Safety IEEE International Conference on*, 2007, pp. 1–6.

[64] S. Zhao, Y. Li, L. Zheng, and S. Lu, "Vehicle lateral stability control based on sliding mode control," in *Proc. IEEE International Conference on Automation and Logistics*, 2007, pp. 638–642.

[65] A. Nishio, K. Tozu, H. Yamaguchi, K. Asano, and Y. Amano, "Development of vehicle stability control system based on vehicle sideslip angle estimation," *Vehicle Dynamics and Simulation*, vol. SP-1602, pp. 1–10, 2001.

[66] E. K. Liebemann, K. Meder, J. Schuh, and G. Nenninger, "Safety and performance enhancement: The Bosch electronic stability control (ESP)," Robert Bosch GmbH, Tech. Rep. 05-0471, 2004.

[67] R. M. DeSantis, "Path-tracking for car-like robots with single and double steering," *IEEE Transactions on Vehicular Technology*, vol. 44, no. 2, pp. 366–377, 1995.

[68] E. Freund and R. Mayr, "Nonlinear path control in automated vehicle guidance," *IEEE Transactions on Robotics and Automation*, vol. 13, no. 1, pp. 49–60, 1997.

[69] A. Alleyne, "A comparison of alternative obstacle avoidance strategies for vehicle control," *Vehicle System Dynamics*, vol. 27:5, pp. 371–392, 1997.

[70] H. Peng and M. Tomizuka, "Lateral control of front-wheel-steering rubber-tire vehicles," UC Berkeley, Tech. Rep. UCB-ITS-PRR-90-5, 1990.

[71] B. L. Boada, M. J. L. Boadam, and V. Diaz, "Fuzzy-logic applied to yaw moment control for vehicle stability," *Vehicle System Dynamics*, vol. 43:10, pp. 753–770, 2005.

[72] P. Kachroo, M. Tomizuka, and A. M. Agogino, "A comprehensive strategy for longitudinal vehicle control with fuzzy supervisory expert system," in *Proc. IEEE International Conference on Systems, Man and Cybernetics Intelligent Systems for the 21st Century*, vol. 1, 1995, pp. 765–770 vol.1.

[73] J. K. Hedrick, "Nonlinear controller design for automated vehicle applications," in *Proc. Control '98. UKACC International Conference on (Conf. Publ. No. 455)*, vol. 1, 1998, pp. 23–32 vol.1.

[74] D. Smith, R. Benton, and J. Starkey, "Nonlinear-gain-optimized controller development and evaluation for automated emergency vehicle steering," *Int. J. of Vehicle Design*, vol. 24, no. 1, pp. 79–99, 2000.

[75] S. Javid, M. Eghtesad, A. Khayatian, and H. Asadi, "Experimental study of dynamic based feedback linearization for trajectory tracking of a four-wheel autonomous ground vehicle," *Autonomous Robots*, vol. 19, pp. 27–40, 2005.

[76] M. Eghtesad and D. S. Necsulescu, "Experimental study of the dynamic based feedback linearization of an autonomous wheeled ground vehicle," *Robotics and Autonomous Systems*, vol. 47, pp. 47–63, 2004.

[77] P. Falcone, F. Borrelli, J. Asgari, H. E. Tseng, and D. Hrovat, "A model predictive control approach for combined braking and steering in autonomous vehicles," in *Proc. Mediterranean Conference on Control & Automation MED '07*, 2007, pp. 1–6.

[78] B. Kim, D. Necsulescu, and J. Sasiadek, "Model predictive control of an autonomous vehicle," in *Proc. IEEE/ASME International Conference on Advanced Intelligent Mechatronics*, vol. 2, 2001, pp. 1279–1284 vol.2.

[79] A. D. Rodic and M. K. Vukobratovic, "Advanced control and stability of autonomous road vehicles: Part i synthesis of a hybrid neuro-dynamic controller," *International Journal of Computer Applications in Technology*, vol. 15, no. 6, pp. 233–247, 2002.

[80] ——, "Advanced control and stability of autonomous road vehicles: Part ii practical stability of road vehicles," *International Journal of Computer Applications in Technology*, vol. 15, no. 6, pp. 248–263, 2002.

[81] D. Q. Mayne, J. B. Rawlings, C. V. Rao, and P. O. M. Scokaert, "Constrained model predictive control: Stability and optimality," *Automatica*, vol. 36, pp. 789–814, 2000.

[82] A. Lincoln, *The Collected Works of Abraham Lincoln*. Rutgers University Press, 1953, vol. 1, p. 489.

[83] S. J. Singh and D. H. Shin, "Position based path tracking for wheeled mobile robots," in *IEEE/RSJ International Workshop on Intelligent Robots and Systems*, 1989.

[84] K. Watanabe, M. Kitano, and A. Fugishima, "Handling and stability performance of four-track steering vehicles," *Journal of Terramechanics*, vol. 32, pp. 285–302, 1995.

[85] K. Watanabe, J. Yamakawa, M. Tanaka, and T. Sasaki, "Turning characteristics of mult-axle vehicles," *Journal of Terramechanics*, vol. 44, pp. 81–87, 2007.

[86] Y. He, A. Khajepour, J. McPhee, and X. Wang, "Dynamic modelling and stability analysis of articulated frame steer vehicles," *Int. J. Vehicle Systems*, vol. 12, no. 1, pp. 28–59, 2005.

[87] E. Sampo, A. Sorniotti, and A. Crocombe, "Chassis torsional stiffness: Analysis of the influence on vehicle dynamics," in *SAE 2010 World Congress & Exhibition*, April 2010.

[88] L. L. Thompson, P. H. Soni, S. Raju, and E. H. Law, "The effects of chassis flexibility on roll stiffness of a winston cup race car," in *Motorsports Engineering Conference Proceedings*, vol. 1, no. P-340/1, 1998.

[89] N. Lyu and K. Saitou, "Decomposition-based assembly synthesis of space frame structures using joint library," *ASME Journal of Mechanical Design*, vol. 128, pp. 57–65, January 2006.

[90] T. Muro, "Wear rate characteristics of heavy dump truck tyres," *Journal of Terramechanics*, vol. 26, pp. 11–23, 1989.

[91] G. Komandi, "Establishment of soil-mechanical parameters which determine traction on deforming soil," *Journal of Terramechanics*, vol. 27, no. 2, pp. 115–124, 1990.

[92] Mechanical Simulation Corp., *TruckSim Documentation*, 8th ed., December 2009.

[93] U. Kiencke and L. Nielsen, *Automotive Control Systems*, 2nd ed. Springer, 2005.

[94] MathWorks, Inc. (2010, November) Equation solving: Optimization algorithms and examples (optimization toolbox). Online Resource. [Online]. Available: http://www.mathworks.com/help/toolbox/optim/ug/brnoyhf.html

[95] A. Einstein, "Letter to Max Born," December 1926.

[96] S. Thrun, M. Montemerlo, H. Dahlkamp, D. Stavens, A. Aron, J. Diebel, P. Fong, J. Gale, M. Halpenny, G. Hoffmann, K. Lau, C. Oakley, M. Palatucci, V. Pratt, and Pascal Stang and Sven Strohband, C. Dupont, L.-E. Jendrossek, C. Koelen, C. Markey, C. Rummel, J. van Niekerk, E. Jensen, and Philippe Alessandrini and Gary Bradski, B. Davies, S. Ettinger, A. Kaehler, and A. N. and Pamela Mahoney, "Stanley: The robot that won the DARPA Grand Challenge," *Journal of Field Robotics*, vol. 23, pp. 661–692, 2006.

[97] R. Aldridge and B. T. Newill. (2011) Brigham young university creates racecar tire testing apparatus with NI products. BYU. [Online]. Available: http://sine.ni.com/cs/app/doc/p/id/cs-799

[98] P. Huizenga. (2011) Ten questions with Chris Alston Sr. - dragzine.com. [Online]. Available: http://www.dragzine.com/features/interviews/ten-questions-with-chris-alston-sr/

[99] Kistler. (2011, March) Kistler - tire development. [Online]. Available: http://www.kistler.com/IT_en-it/vehicles_3_reifenentwicklung/Tire-Development.html

[100] S. S. Haykin, Ed., *Kalman Filtering and Neural Networks*, ser. Adaptive and learning systems for signal processing, communications, and control. Wiley, 2001.

[101] M. W. Spong and M. Vidyasagar, *Robot Dynamics and Control*. Wiley, 2004.

[102] R. Rajamani, D. Piyabongkarn, V. Tsourapas, and J. Lew, "Real-time estimation of roll angle and CG height for active rollover prevention applications," in *2009 American Control Conference*, June 2009.

[103] I. Novatel, *SPAN-CPT User Manual*, om-20000122 rev 2 ed., September 2008.

[104] Oregon Health and Science University. (2011) Rebel: Recursive bayesian estimation library and toolkit for matlab. [Online]. Available: http://choosh.csee.ogi.edu/rebel/

[105] R. Rajamani, D. Piyabongkarn, J. Y. Lew, and J. A. Grogg, "Algorithms for real-time estimation of individual wheel tire-road friction coefficients," in *Proceedings of the 2006 American Control Conference*, 2006.

[106] J. W. Jones, *Personal reminiscences, anecdotes, and letters of Gen. Robert E. Lee*. D. Appleton and Company, 1875, p. 170.

[107] B. Johansson, "Untripped SUV rollover detection and prevention," Master's thesis, Lund Institute of Technology, 2004.

[108] G. S. Patton, *War As I Knew It*. Mariner Books, 1947.

[109] M. Miller, *Plain Speaking : An Oral Biography of Harry S Truman*. Berkley, 1974, p. 26.

Acronyms and Abbreviations

ABS Anti-lock Brake System

AWD All Wheel Drive

BHF Bayesian Histogram Filter

CG Center of Gravity

COF Coefficient of Friction

CTC Center of Tire Contact

CUT Compact Utility Truck

DARPA Defense Advanced Research Projects Agency

DCM Directional Controllability Metric

DEKF Dual Extended Kalman Filter

DGC DARPA Grand Challenge

DI Dynamic Index

DOF Degree of Freedom

DSC Dynamic Stability Control

DSM Directional Stability Metric

DUC DARPA Urban Challenge

EKF Extended Kalman Filter

FASM Force-Angle Stability Metric

FMM Force-Moment Method

FWD Front Wheel Drive

GPS Global Positioning System

ICG Instant Center of Gravity

IMM Instantaneous Maneuvering Manifold

IMU Inertial Measurement Unit

INS Inertial Navigation System

KF Kalman Filter

KKF Kinematic Kalman Filter

MMM Milliken Moment Method

MPC Model Predictive Controller

OEM Original Equipment Manufacturer

PDF Probability Density Function

PI Proportional-Integral

PID Proportional-Integral-Derivative

PES Pose-Estimation System

RSM Rollover Stability Metric

RWD Rear Wheel Drive

SAE Society of Automotive Engineers

SI Stability Index

SPS Suspension Position Sensor

TTR Time to Rollover

UAV Unmanned Aerial Vehicle

UGV Unmanned Ground Vehicle

UKF Unscented Kalman Filter

Nomenclature

α_n	Slip angle of tire-n
β	Body slip angle
ΔW_x	Longitudinal weight transfer
δ	Steering angle at front wheels
δ	Steering angle of front wheels
$\dot{\kappa}$	Path curvature rate
ℓ	Wheelbase length
η_B	Front/rear brake proportionality
η_D	Front/rear drive torque proportionality
κ	Path curvature
μ	Tire-ground coefficient of friction
ω_n	Rotational velocity of wheel-n
ϕ	Sprung mass roll angle
ψ	Sprung mass pitch angle
σ_n	Standard deviation of variable n
τ	Steering torque
θ	Yaw angle
A_y	Lateral acceleration
C_α	Linear tire cornering stiffness
C_S	Linear tire traction coefficient

c_{ϕ_n} Roll damping coefficient of axle-n

c_{ψ} Pitch damping coefficient

C_{rr} Linear tire rolling resistance coefficient

E_{crit} Critical rollover energy

E_{roll} Total roll energy

F_y Total lateral force

F_{x_n} Longitudinal force generated by tire-n

F_{y_n} Lateral force generated by tire-n

F_{z_n} Vertical load on wheel-n

I_n Moment of inertia about n-axis

k_{ϕ_n} Roll stiffness coefficient of axle-n

k_{ψ} Pitch stiffness coefficient

M Mass of total vehicle

m_c $Mass of cargo beyond empty vehicle mass$

m_s Mass of sprung mass

m_{us_n} Mass of unsprung mass of axle-n

N Total yawing moment

$p(x)$ Prior probability distribution of x

R_{e_n} Effective rolling radius of wheel-n

S_n Slip ratio of tire-n

t_m Mechanical trail

t_n Track width of axle-n

t_p Pneumatic trail

t_{p_0} Maximum pneumatic trail

T_{roll} Roll kinetic energy

U_{roll} Roll potential energy

V_x x-velocity of vehicle

V_y y-velocity of vehicle

W Weight of total vehicle

w Weight of sprung mass

x x displacement in vehicle frame

x_{CG} Longitudinal CG offset from vehicle frame

y y displacement in vehicle frame

y_{CG} Lateral CG offset from vehicle frame

z z displacement in vehicle frame

z_{CG} Vertical CG offset from vehicle frame

z_{RC} Roll center height from vehicle frame

z_{wn} Suspension displacement for wheel-n

Appendix A

Vehicle Properties

Key values from the Compact Utility Truck TruckSIM model that was used for verification purposes are provided in Table A.1.

Table A.1: Simulated Test Vehicle Parameters

Symbol	Parameter Name	Value
C_α	Linear tire cornering stiffness	16000N/rad
C_S	Linear tire traction coefficient	28000N
c_ϕ	Roll damping coefficient	16000Ns/rad
I_x	Moment of inertia about x-axis	640kg-m^2
I_x	Moment of inertia about y-axis	1040kg-m^2
I_x	Moment of inertia about z-axis	1150kg-m^2
k_ϕ	Roll stiffness coefficient	48000N/rad
ℓ	Wheelbase of vehicle	1.923m
M_e	Mass of the empty total vehicle	1160kg
m_{s_e}	Mass of the empty sprung mass	1000kg
t_F	Track width of front axle	1.26m
t_R	Track width of rear axle	1.26m
R_e	Rolling radius of tire	0.263m
x_{CG_e}	Longitudinal empty vehicle CG offset	1.373m
y_{CG_e}	Lateral empty vehicle CG offset	0.0m
z_{CG_e}	Vertical empty vehicle CG offset	0.463m
z_{RC_F}	Front roll center height	0.3m
z_{RC_R}	Rear roll center height	0.3m

Appendix B

Maneuvering Manifolds

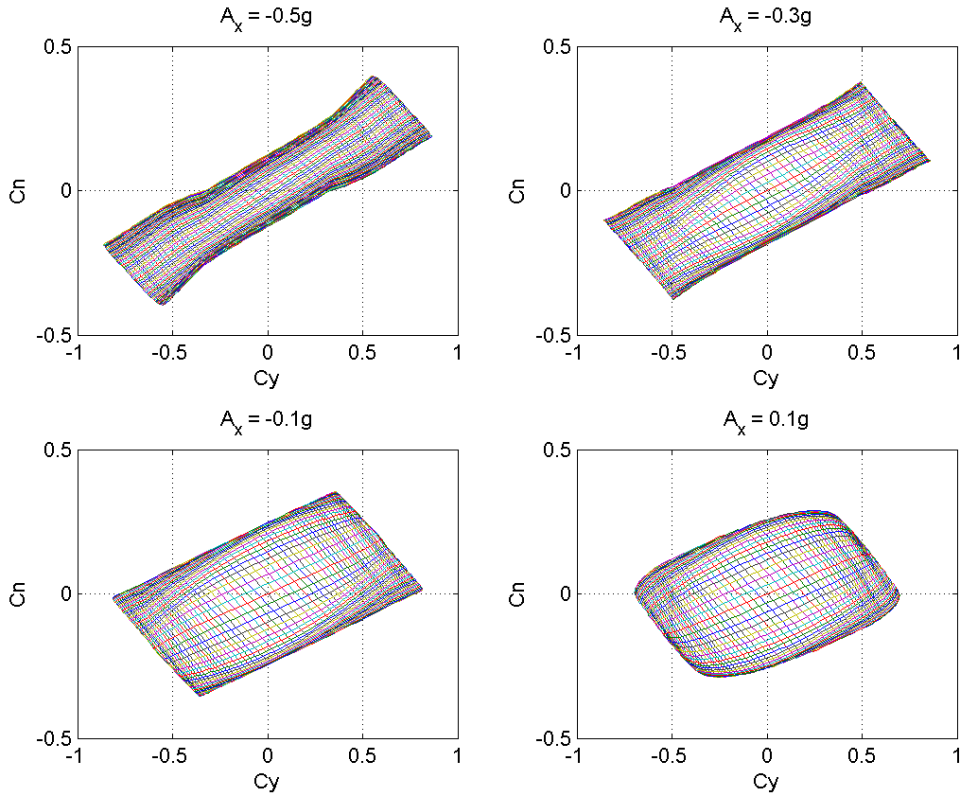

Figure B.1: Effects of longitudinal acceleration on the FMM diagram for the empty vehicle at $\mu = 0.88$. Note that heavy braking tends to accentuate the understeer tendencies of the vehicle while positive acceleration brings the diagram closer to a neutral steer configuration.

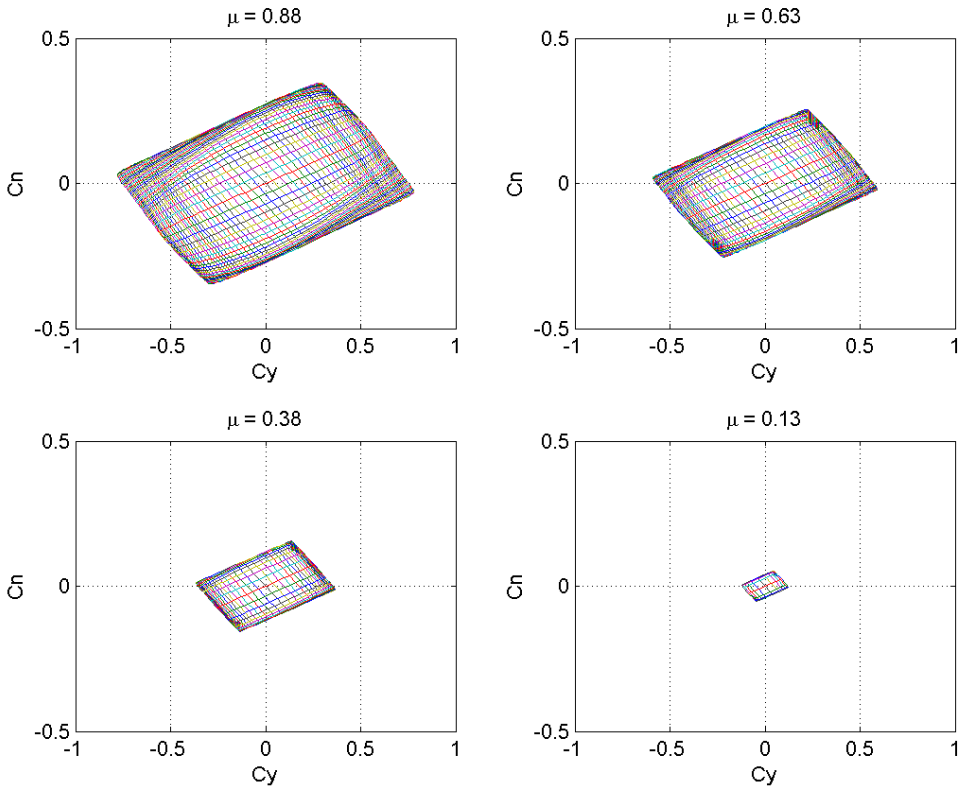

Figure B.2: Effects of the COF on the FMM diagram for the empty vehicle at $A_x = 0$. Note the vast difference in the overall size of the stable operating area as the friction coefficient decreases.

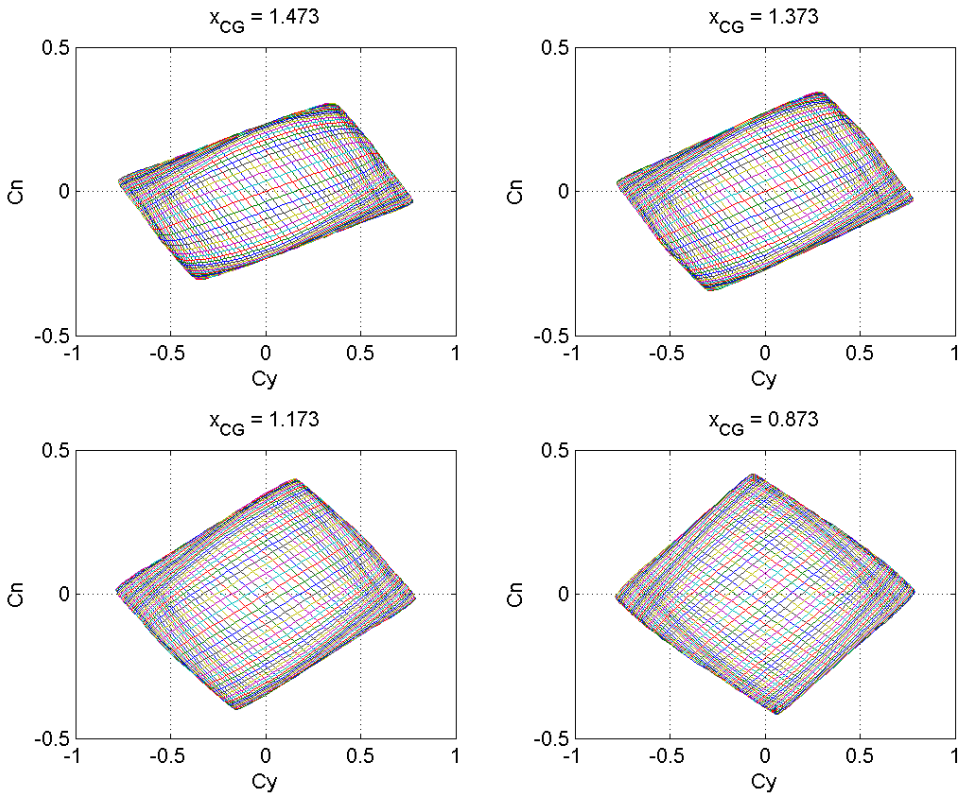

Figure B.3: Effects of changes in x_{CG} on the FMM diagram for the empty vehicle at $A_x = 0$ and $\mu = 0.88$. Note that variation in the longitudinal CG location tends to tilt the diagram, indicating a change in the understeer/oversteer characteristics.

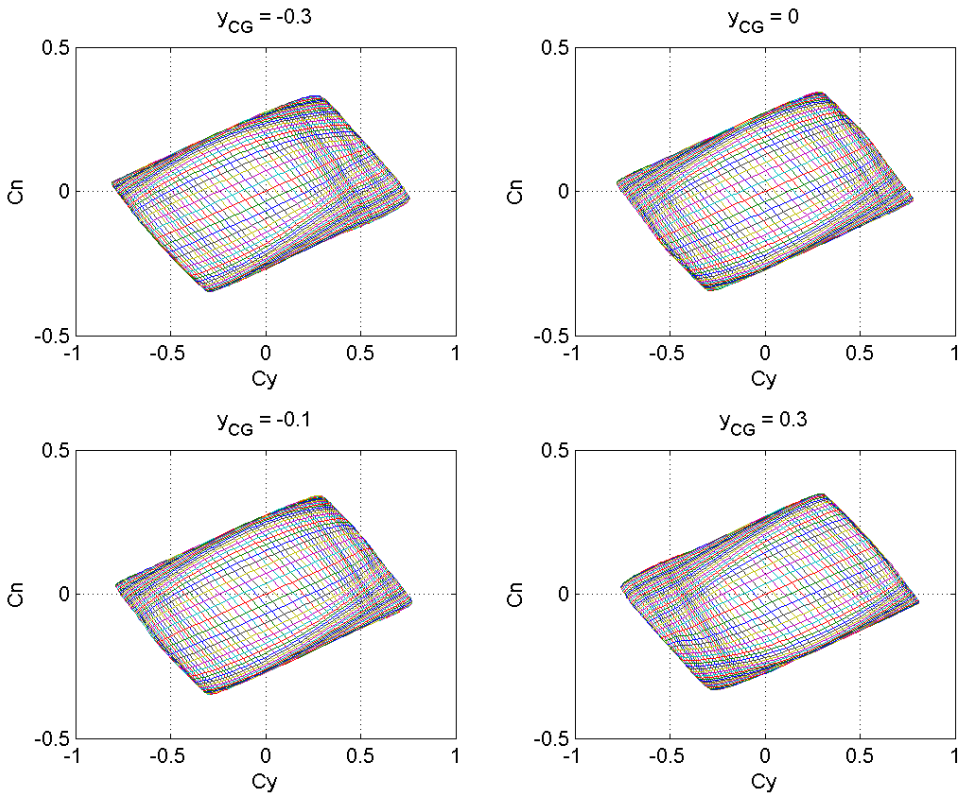

Figure B.4: Effects of changes in y_{CG} on the FMM diagram for the empty vehicle at $A_x = 0$ and $\mu = 0.88$. Note that variation in the lateral CG location has a limited effect, mostly skewing the diagram near the limits.

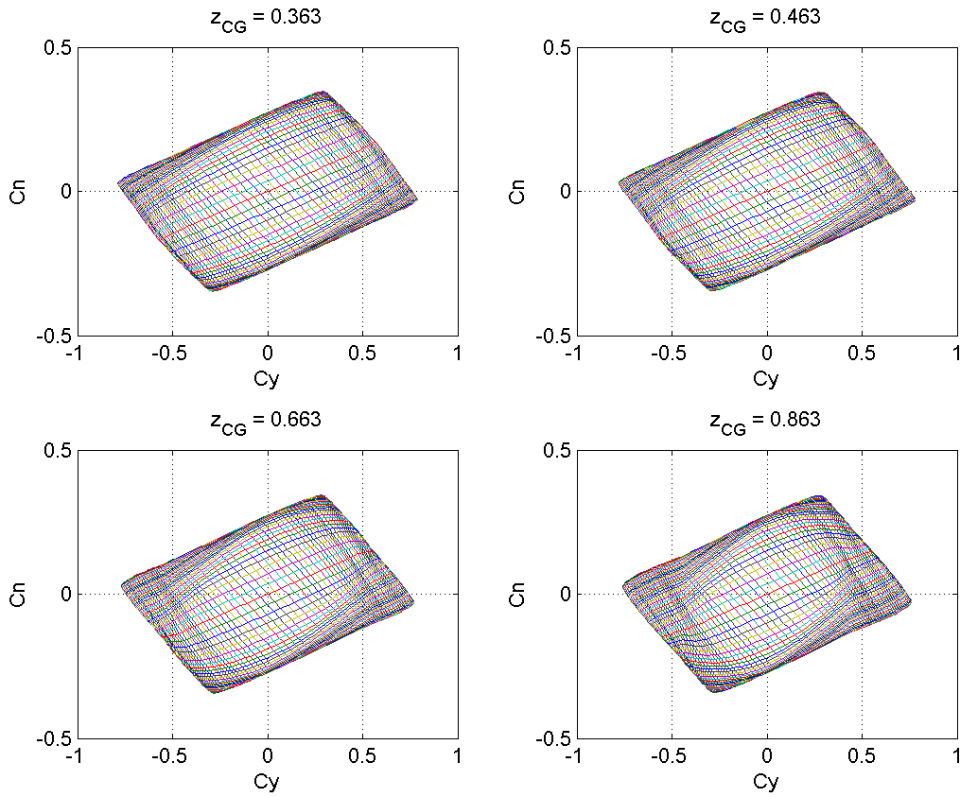

Figure B.5: Effects of changes in z_{CG} on the FMM diagram for the empty vehicle at $A_x = 0$ and $\mu = 0.88$. Note that variation in the vertical CG location tends to tilt the diagram, indicating a change in the understeer/oversteer characteristics.

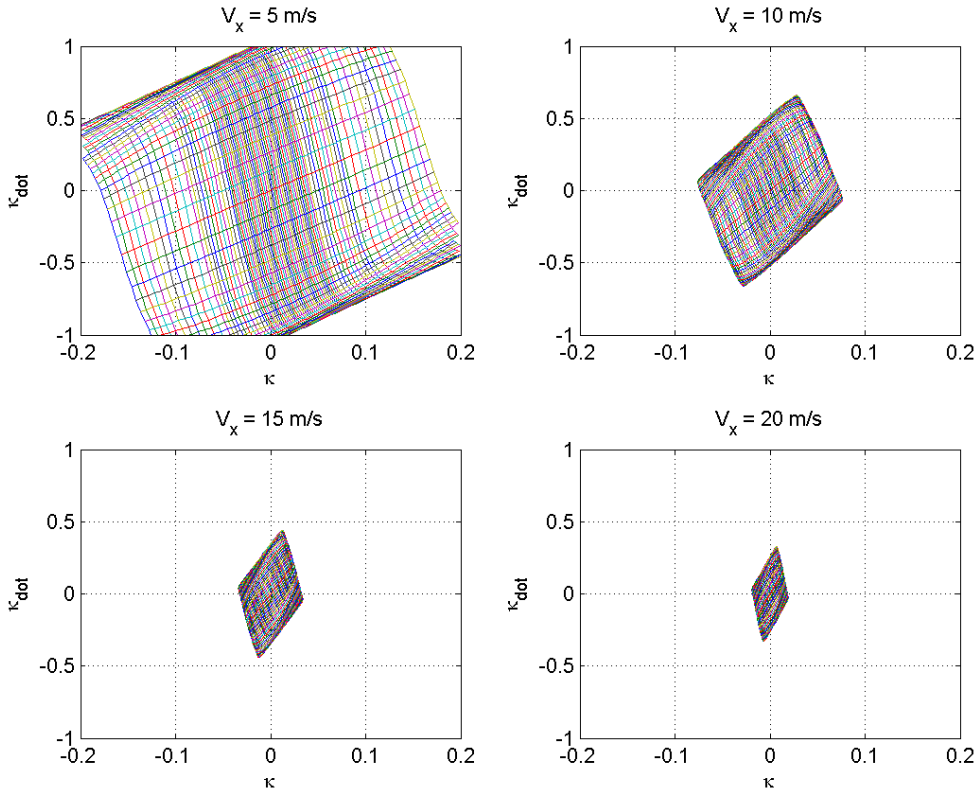

Figure B.6: Effects of longitudinal velocity on the IMM for the empty vehicle at $A_x = 0$ and $\mu = 0.88$. Note that these plots are expressed in curvature and curvature rate coordinates. The change in the manifold size indicates a decrease in the vehicle's ability to execute tighter turns (higher curvatures) as speed increases.

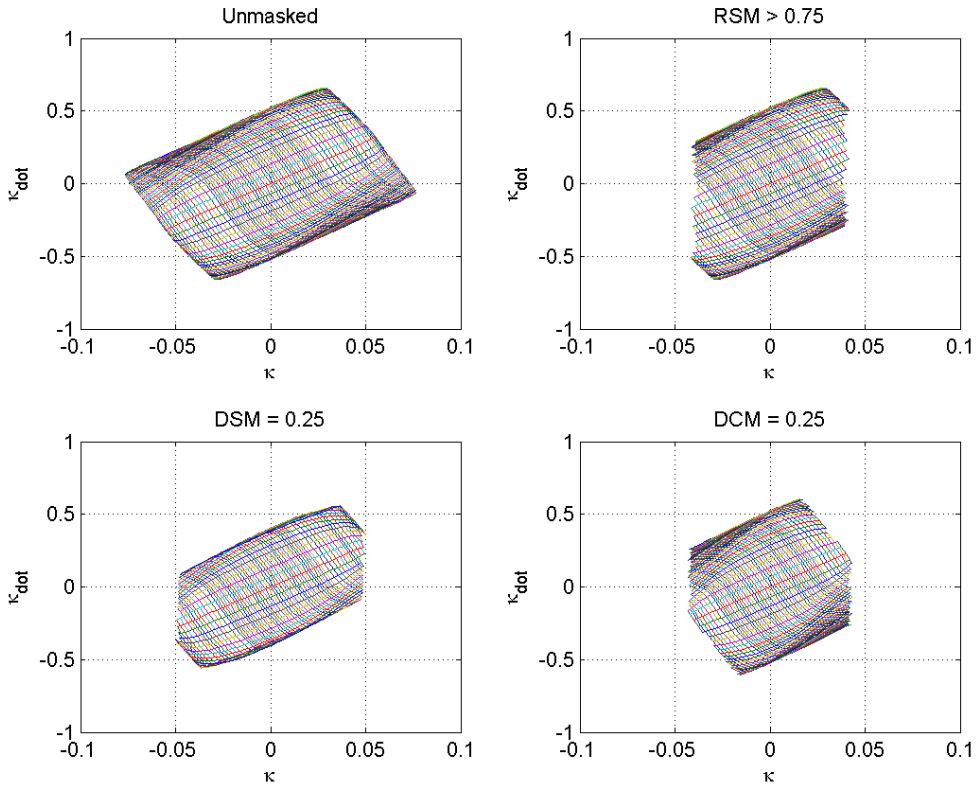

Figure B.7: Effects of metric masking on the IMM for the empty vehicle at $V_x = 10$, $A_x = 0$, and $\mu = 0.88$. Note the change in the manifold size that indicates the safe operating area at the given metric values. The combined metric mask would be the union of the three plots shown here.